

# **Quantum Chemical Calculations of EPR Parameters for Transition Metal Complexes**

Von der Fakultät Chemie der Universität Stuttgart zur Erlangung der Würde  
eines Doktors der Naturwissenschaften (Dr.rer.nat.) genehmigte  
Abhandlung

Vorgelegt von

**Markéta Munzarová**

aus Brno

|                             |                      |
|-----------------------------|----------------------|
| Hauptberichter:             | Prof. Dr. M. Kaupp   |
| Mitberichter:               | Prof. Dr. W. Kaim    |
| Prüfungsvorsitzender:       | Prof. Dr. E. Roduner |
| Tag der mündlichen Prüfung: | 16. 8. 2001          |

**Max-Planck-Institut für Festkörperforschung Stuttgart  
Institut für Anorganische Chemie der Universität Stuttgart**

**2001**



## Abstract

This thesis reports a series of theoretical studies of electron paramagnetic resonance (EPR) parameters for 3d transition metal complexes. The work focusses on the validation of various approaches based on density functional theory (DFT), on the interpretation of the EPR parameters in terms of electronic structure, and on the understanding of the physical mechanisms underlying the EPR magnetic interactions.

The performance of several DFT approaches for the calculation of EPR hyperfine coupling constants has been evaluated critically by comparison with experimental data and coupled-cluster results for 21 first-row transition metal systems. Isotropic couplings and coupling anisotropies for both metal and ligand nuclei have been calculated and discussed. While both gradient-corrected and hybrid functionals allow the calculation of isotropic metal hyperfine coupling constants to within ca. 10-15% for the less critical cases, none of the functionals investigated performs well for all complexes. Gradient-corrected functionals tend to underestimate the important core-shell spin polarization. While this may be improved by exact-exchange mixing in some cases, the accompanying spin contamination may even lead to a deterioration of the results for other complexes. We also identify cases, where essentially none of the functionals performs satisfactorily. In the absence of a "universal functional", the functionals to be applied to the calculation of hyperfine couplings in certain areas of transition metal chemistry have to be carefully selected. Desirable, improved functionals should provide sufficiently large spin polarization for core and valence shells without exaggerating it for the latter.

To obtain an in-depth understanding of the challenging points in the DFT description of the hyperfine interactions, a detailed quantum chemical analysis of the underlying principles of hyperfine coupling in 3d transition metal complexes has been carried out. The explicit evaluation of one- and two-electron integrals for some atomic systems has been used to understand the spin polarization of the core shells. While spin polarization enhances the exchange interaction of the 2s and 2p shells with the singly occupied orbitals, the opposite spin polarization of the 3s and 3p shells arises from the

required orthogonality to the  $2s$  and  $2p$  shells, respectively. Core-shell spin-polarization in molecules is found to be proportional to the spin population in the valence  $3d$  orbitals but to depend little on other details of bonding. In contrast, the spin polarization of the valence shell depends crucially on the overlap between the singly occupied and certain doubly occupied valence orbitals. Large overlap leads to pronounced spin polarization of these orbitals and, among other things, likely to spin contamination when using UHF wave functions or hybrid density functionals. The role of core- and valence-shell spin-polarization for dipolar hyperfine couplings in transition metal complexes is discussed. It is demonstrated that great care should be exercised in deriving spin populations or even orbital compositions from dipolar couplings alone.

A new DFT implementation of electronic  $g$ -tensors within the deMon code including all relevant perturbation operators has been validated in a further part of this thesis. In contrast to the good performance for main-group species, the overall  $g$ -shifts obtained for the  $3d$  transition metal complexes are underestimated typically by  $\sim 40\text{-}50\%$  upon inclusion of both one-electron and two-electron spin-orbit operators. We attribute this to a systematic underestimation of the paramagnetic contributions and expect that the inclusion of Hartree-Fock exchange in the density functional should improve the performance of the method.

In the last part of this work, DFT calculations of electronic  $g$ -tensors and metal hyperfine coupling tensors have been carried out for a series of four vanadyl complexes with structures ranging from nearly trigonal bipyramidal to nearly square pyramidal. The EPR spectroscopic parameters have been rationalized in terms of electronic and geometrical structures. Using all relevant perturbation operators together with local or gradient-corrected density functionals,  $\Delta g$ -tensor components are underestimated systematically by ca.  $40\%$ . Good agreement with experiment is obtained for hyperfine tensor components calculated with hybrid functionals. The rhombicity of the hyperfine tensor is reproduced well at all levels of theory applied. It is mainly determined by the SOMO composition. The latter explains the increasing rhombicity of the  $A$ -tensor with increasing square-pyramidal-to-trigonal-bipyramidal distortion along the series of complexes studied. The orientational dependence of the principal tensor components on the local vanadium coordination is much more pronounced for the  $g$ -tensor than for the  $A$ -tensor.

## Acknowledgments

It is a pleasure to thank those who made it possible for me to write this thesis. I would particularly like to acknowledge my advisor, Professor Martin Kaupp (University of Würzburg), for the remarkable research cooperation and the continuous support of my interest in science. The years of our joint work would perhaps never have become a reality without the kind help of Professor Emil Roduner, University of Stuttgart, to whom I would like to express my sincere gratitude. Professor Wolfgang Kaim, University of Stuttgart, is acknowledged for reviewing and commenting the thesis.

The major part of my graduate studies took place at Max-Planck-Institute for Solid State Research in Stuttgart, Germany. I would like to thank Professors Hans Georg von Schnering and Martin Jansen, the heads of a solid state chemistry department, for placing the facilities at my disposal.

Many thanks are due to my coworkers and friends Drs. Juha Vaara (Helsinki), Bernd Schimmelpfennig (Stockholm), Vladimir G. Malkin, and Olga L. Malkina (Bratislava), and Daniel Sebastiani (Mainz). Besides the many useful discussions we have had, they created a very stimulating and encouraging working atmosphere that has been vital to me. Special thanks are due to Juha Vaara, Vladimir G. Malkin, and Daniel Sebastiani for reviewing and commenting chapters of this thesis.

Part of the work reported in this thesis has been done at Masaryk University in my home city of Brno. Docent Pavel Kubáček, my advisor there, is thanked not only for the support and research cooperation directly related to the work reported here, but also for encouraging my interest in quantum chemistry since the beginning of my undergraduate studies. I would like to thank my colleague Petr Holub for his help in many technical questions.

The last period of my graduate studies - an exchange stay at Cornell University - has not been directly related to the subject of this thesis, but it certainly left its mark on it and on me. I am grateful to Professor Roald Hoffmann and all members of his group for the many stimulating discussions, and for the privilege of sharing a truly exciting atmosphere of scientific cooperation and friendship.

I am grateful to my parents, sisters and brothers who have supported and believed in me over many years. The walls between scholarship and family life are often more permeable than they appear. I am grateful to Dominik, my partner in life, love and intellectual pursuits, for his help, support, and understanding over the years of my graduate studies. This thesis, that has been so much shaped by our joint discussions, is dedicated to him.

Brno, June 15 2001

Markéta Munzarová

## List of Abbreviations

|         |   |
|---------|---|
| AMFI    | one-center mean-field approximation to SO integrals   |
| ANO     | atomic natural orbital (basis set)  |
| BH      | hybrid functional for exchange including 50% of exact exchange and 50% of Becke's GGA for exchange    |
| BHLYP   | exchange-correlation functional with BH functional for exchange and LYP GGA for correlation           |
| BHPW91  | exchange-correlation functional with BH functional for exchange and PW91 GGA for correlation          |
| BHP86   | exchange-correlation functional with BH functional for exchange and P86 GGA for correlation           |
| BLYP    | exchange-correlation functional with Becke's GGA functional for exchange and LYP GGA for correlation  |
| BPW91   | exchange-correlation functional with Becke's GGA functional for exchange and PW91 GGA for correlation |
| BP86    | exchange-correlation functional with Becke's GGA functional for exchange and P86 GGA for correlation  |
| B3      | Becke's three-parameter hybrid functional for exchange  |
| B3LYP   | exchange-correlation functional with B3 functional for exchange and LYP GGA for correlation           |
| B3PW91  | exchange-correlation functional with B3 functional for exchange and PW91 GGA for correlation          |
| CC      | coupled cluster (theory)  |
| CCSD    | CC with single and double substitutions   |
| CCSD(T) | CCSD with triple substitutions  |
| CGTO    | contracted Gaussian type orbital  |
| CI(SD)  | configuration interaction (with single and double excitations)  |
| DFT     | density functional theory   |
| DZ      | double- $\zeta$ (basis)   |
| ECP     | effective core potential  |

|          |   |
|----------|---|
| EPR      | electron paramagnetic resonance (spectroscopy)                          |
| GGA      | generalized gradient approximation                                      |
| GIAO     | gauge-including atomic orbital  |
| GTO      | Gaussian type orbital   |
| HF       | Hartree-Fock (theory)   |
| HFC(C)   | hyperfine coupling (constant)   |
| HOMO     | highest occupied MO   |
| IGLO     | individual gauge for localized orbitals (method)                        |
| KS       | Kohn-Sham (theory)  |
| LCAO     | linear combination of atomic orbitals                                   |
| L(S)DA   | local (spin) density approximation                                      |
| LYP      | Lee-Yang-Parr (correlation functional)                                  |
| MCSCF    | multiconfigurational SCF (theory)                                       |
| MO       | molecular orbital   |
| MP2      | second-order Møller-Plesset many-body (perturbation) theory             |
| MRCI     | multireference configuration interaction                                |
| NMR      | nuclear magnetic resonance (spectroscopy)                               |
| NR       | nonrelativistic (approach)  |
| PT       | perturbation theory   |
| PW91     | Perdew-Wang (correlation functional)                                    |
| P86      | Perdew 1986 (correlation functional)                                    |
| QR       | quasi-relativistic (approach)   |
| ROHF/KS  | restricted open-shell HF/KS (method)                                    |
| R/U CCSD | restricted/unrestricted CCSD  |
| SCF      | self consistent field   |
| SO       | spin-orbit (integral, contribution, Hamiltonian)                        |
| SOMO     | singly-occupied MO  |
| SOS-DFPT | sum-over-states density-functional perturbation theory                  |
| SQP-5    | five-coordinate, square pyramidal (structure)                           |
| SOO      | spin-other-orbit  |
| SSO      | spin-same-orbit   |
| STO      | Slater type orbital   |
| SVWN     | exchange-correlation functional with Dirac exchange and VWN correlation |



|        |   |
|--------|---|
| TBP-5  | five-coordinate, trigonal bipyramidal (structure)           |
| TZ     | triple- $\zeta$ (basis)                                     |
| UDFT   | uncoupled DFT   |
| UHF/KS | unrestricted HF/KS (method)                                 |
| VS     | valence shell   |
| VWN    | Vosko-Wilk-Nusair (correlation functional)                  |
| ZORA   | Zero order regular approximation (for relativistic effects) |



# Content

|          |  |           |
|----------|--|-----------|
| <b>1</b> | <b>ZUSAMMENFASSUNG .....</b>   | <b>13</b> |
| 1.1      | KRITISCHE UNTERSUCHUNG VON DICHTEFUNKTIONAL- UND <i>COUPLED CLUSTER</i> METHODEN ZUR BERECHNUNG VON EPR-HYPERFEIN-KOPPLUNGSKONSTANTEN FÜR ÜBERGANGSMETALLVERBINDUNGEN <sup>1</sup> ..... | 15        |
| 1.2      | MECHANISMEN DER EPR-HYPERFEINKOPPLUNG IN ÜBERGANGSMETALLVERBINDUNGEN .....   | 17        |
| 1.3      | DFT-BERECHNUNG ELEKTRONISCHER <i>g</i> -TENSOREN IN ÜBERGANGSMETALLKOMPLEXEN MIT HILFE VON MEAN-FIELD SPIN-BAHN-OPERATOREN .....   | 19        |
| 1.4      | DFT-BERECHNUNG DER EPR-PARAMETER FÜR VANADYL-SCHIFF-BASE-KOMPLEXE .....  | 20        |
| <b>2</b> | <b>INTRODUCTION .....</b>  | <b>25</b> |
| 2.1      | BACKGROUND AND MOTIVATION .....  | 25        |
| 2.2      | OBJECTIVES OF THE STUDY .....  | 26        |
| <b>3</b> | <b>ELECTRON PARAMAGNETIC RESONANCE PARAMETERS .....</b>  | <b>29</b> |
| 3.1      | ELECTRON SPIN: A THEORETICAL RATIONALE .....   | 29        |
| 3.1.1    | <i>Pauli Spin Matrices</i> .....   | 30        |
| 3.1.2    | <i>The Dirac Equation</i> .....  | 30        |
| 3.1.3    | <i>Pauli Reduction of the Dirac Equation</i> .....   | 32        |
| 3.2      | THE BREIT-PAULI HAMILTONIAN FOR MANY-PARTICLE SYSTEMS .....  | 35        |
| 3.3      | THE SPIN HAMILTONIAN .....   | 40        |
| 3.3.1    | <i>The Concept of the Spin Hamiltonian</i> .....   | 40        |
| 3.3.2    | <i>Spin Hamiltonian Parameters from Condensed-Phase EPR</i> .....  | 43        |
| 3.3.3    | <i>Spin Hamiltonian Parameters from Gas-Phase Spectroscopy</i> .....   | 44        |
| 3.4      | PERTURBATION EXPRESSIONS FOR THE ELECTRON ZEEMAN AND HYPERFINE INTERACTION TERMS .....   | 45        |
| 3.4.1    | <i>Rayleigh-Schrödinger Perturbation Theory</i> .....  | 46        |
| 3.4.2    | <i>Operators Relevant for the Electron Zeeman Effect and for the Hyperfine Interaction</i> ....  | 49        |
| 3.4.3    | <i>Perturbation-Theory Expressions for the Electronic <i>g</i>-Tensor</i> .....  | 54        |
| 3.4.4    | <i>Perturbation-Theory Expressions for the <i>A</i>-Tensor</i> .....   | 56        |
| 3.5      | QUALITATIVE AND SEMI-QUANTITATIVE RELATIONSHIPS BETWEEN THE SPIN HAMILTONIAN PARAMETERS AND ELECTRONIC STRUCTURE .....   | 58        |
| <b>4</b> | <b>COMPUTATIONAL METHODS .....</b>   | <b>63</b> |
| 4.1      | APPROXIMATIONS TO THE SOLUTION OF THE SCHRÖDINGER EQUATION .....   | 64        |
| 4.2      | THE HARTREE-FOCK APPROXIMATION .....   | 65        |
| 4.2.1    | <i>The Hartree Approximation</i> .....   | 65        |
| 4.2.2    | <i>The Hartree-Fock Approximation</i> .....  | 66        |
| 4.2.3    | <i>The Unrestricted Hartree-Fock Method</i> .....  | 69        |
| 4.2.4    | <i>The Restricted Open-Shell Hartree-Fock Method</i> .....   | 73        |
| 4.3      | THE CONFIGURATION INTERACTION METHOD .....   | 75        |
| 4.4      | THE COUPLED-CLUSTER METHOD .....   | 76        |
| 4.5      | DENSITY FUNCTIONAL THEORY .....  | 78        |
| 4.5.1    | <i>The Hohenberg-Kohn Theorems</i> .....   | 78        |
| 4.5.2    | <i>The Kohn-Sham Method</i> .....  | 79        |
| 4.5.3    | <i>Exchange-Correlation Functionals</i> .....  | 82        |
| 4.6      | BASIS SETS AND PSEUDOPOTENTIALS .....  | 84        |

|          |   |            |
|----------|---|------------|
| <b>5</b> | <b>A CRITICAL VALIDATION OF DENSITY FUNCTIONAL AND COUPLED-CLUSTER APPROACHES FOR THE CALCULATION OF EPR HYPERFINE COUPLING CONSTANTS IN TRANSITION METAL COMPLEXES .....</b> | <b>89</b>  |
| <b>6</b> | <b>DENSITY FUNCTIONAL CALCULATIONS OF ELECTRONIC <i>G</i>-TENSORS FOR TRANSITION METAL COMPLEXES: A VALIDATION STUDY .....</b>  | <b>111</b> |
| <b>7</b> | <b>MECHANISMS OF EPR HYPERFINE COUPLING IN TRANSITION METAL COMPLEXES .....</b>   | <b>129</b> |
| <b>8</b> | <b>A DENSITY FUNCTIONAL STUDY OF EPR-PARAMETERS FOR VANADYL COMPLEXES CONTAINING SCHIFF BASE LIGANDS.....</b>   | <b>145</b> |
| <b>9</b> | <b>CONCLUSIONS.....</b>   | <b>183</b> |

# 1 Zusammenfassung

## Quantenchemische Untersuchungen der EPR-Parameter von Übergangsmetallverbindungen

Elektronenspinresonanz (*Electron Paramagnetic Resonance*, EPR) ist im Laufe der Jahre zu einer Standard-Methode zur Untersuchung von Systemen mit ungepaarten Elektronen geworden. Die Messung der Hyperfeinkopplung sowie des *g*-Tensors ist eines der aussagekräftigsten Analyseverfahren in der strukturellen Chemie paramagnetischer Systeme. Mit ihrer Hilfe kann die Elektronenstruktur in der Umgebung eines magnetischen Atomkerns mit sehr großer Genauigkeit ermittelt werden. Ein wichtiger Anwendungsbereich von EPR liegt in der Strukturaufklärung von Übergangsmetallverbindungen, mit vielen Fragestellungen z. B. aus dem Gebiet der bioanorganischen Chemie und der Materialforschung. Im Gegensatz zu den zahlreichen experimentellen EPR-Daten von Übergangsmetall-Komplexen waren die quantenchemischen Berechnungen in letzten Jahren vor allem auf organische Verbindungen bzw. einfache Hauptgruppensysteme konzentriert. Der Grund ist die Komplexität der Elektronenkorrelation, die bei der quantitativen Berechnung von Hyperfeinkopplungen von sehr großer Bedeutung ist. Die Korrelations-Effekte sind bei Verbindungen der Übergangsmetalle besonders stark. Die sehr aufwendigen *post*-Hartree-Fock *ab initio* Rechnungen sind jedoch wegen der grossen Zahl der Elektronen bislang nicht auf Übergangsmetall-Komplexe anwendbar.

Zur Berücksichtigung der Elektronenkorrelation finden neben den *post*-Hartree-Fock Verfahren in den letzten Jahren zunehmend Näherungsmethoden der Dichtefunktionaltheorie (DFT) Verwendung. Diese zeichnen sich durch günstige Skalierungseigenschaften mit der Größe des Systems aus, bei gleichzeitiger impliziter Behandlung der Korrelation. In den letzten Jahren wurden zahlreiche DFT-Berechnungen von Hyperfeinkopplungen an (meist kleinen) Übergangsmetall-Komplexen durchgeführt, unter Verwendung der lokalen Dichtenäherung sowie einigen gradientenkorrigierten Austausch-Korrelations-Funktionalen (siehe Literatur in 1). In

diesen Arbeiten wurde jedoch nur eine kleine Zahl von Dichtefunktionalen und Basissätzen untersucht, und nur ein sehr begrenzter Satz von Bindungsverhältnissen wurde betrachtet. Weitere, systematische Validierungen sind deswegen erforderlich, um auf die Eignung der Dichtefunktionalmethoden für die Berechnung von EPR-Parametern schließen zu können. Eines der Ziele der vorliegenden Arbeit ist daher eine kritische Untersuchung von Dichtefunktionalmethoden zur Berechnung von EPR-Hyperfeinkopplungskonstanten für Übergangsmetallverbindungen (siehe Abschnitt 1.1).

Das Verständnis der Leistungsfähigkeit der DFT-Methoden hängt sehr eng mit den Mechanismen der Hyperfeinkopplung zusammen. Die Hyperfeinkopplung entsteht durch die Fermi-Kontakt Wechselwirkung zwischen einem ungepaarten Elektron und einem magnetischen Kern, und ist proportional der Wahrscheinlichkeit, das ungepaarte Elektron am Kernort zu finden. Das ungepaarte Elektron kann zur Spindichte am Kern nur dann direkt beitragen, wenn das einzeln besetzte Molekülorbital (MO) einen nichtverschwindenden Metall-*s*-Charakter hat. Dies ist in Übergangsmetall-Komplexen oft nicht der Fall. Die Spindichte am Kern entsteht dann indirekt, durch die Spinpolarisation der gepaarten Elektronen, in MOs mit einem Metall-*s*-Charakter. Die Mechanismen der Spinpolarisation in Übergangsmetallverbindungen wurden in dieser Arbeit untersucht und in der Zusammenhang mit der Leistungsfähigkeit der DFT-Methoden zur EPR-Berechnungen dargestellt (siehe Abschnitt 1.2).

Im Kontrast zur theoretischen Behandlung der Hyperfeinkopplung, wo eine gute Wissensbasis von *ab initio* Berechnungen vorhanden ist, sind quantitative Berechnungen von EPR *g*-Tensoren erst seit kurzem möglich. In den letzten Jahren sind einige Hartree-Fock-, *post*-Hartree-Fock-, sowie DFT-Implementierungen realisiert worden (siehe Literatur in 5). Ein Teil der vorliegenden Arbeit ist eine Validierungsuntersuchung einer neuen Implementierung der DFT-Berechnungen von elektronischen *g*-Tensoren im Rahmen des deMon Programmes<sup>5</sup> (siehe Abschnitt 1.3).

Ein weiteres Vorhaben dieser Arbeit war die Anwendung von DFT-Berechnungen von EPR-Parametern auf Fragen aus der bioanorganischen Chemie. Ein interessantes Thema ist hier die biochemische Funktion von Vanadium, die mit der Fähigkeit des Vanadates, eine vierfachkoordinierte, tetraedrische Geometrie, sowie eine fünffachkoordinierte, trigonal-bipyramidale (TBP-5) Geometrie einzunehmen, oft verbunden ist. Die trigonal-bipyramidale Koordination scheint bei den Komplexen des Vanadiums (IV) und Vanadiums (V) auf sterisch eingeschränkte Systeme begrenzt zu

sein, da in der Abwesenheit von sehr sperrigen Liganden quadratisch-pyramidale (SQ-5) oder verzerrte quadratisch-pyramidale Komplexe gebildet werden. Um diese Einschränkungen zu untersuchen, haben Cornman et. al. kürzlich einen Satz von Vanadyl-Komplexen synthetisiert, in denen die Geometrie in der Umgebung Vanadiums von annähernd SQ-5 zu annähernd TBP-5 umgestaltet wurde.<sup>2</sup> EPR-Untersuchungen haben gezeigt, daß die Komponenten des Hyperfeinkopplungstensors sehr empfindlich Änderungen in der Koordination des Vanadiums auf dem Weg von der quadratisch-pyramidalen zur trigonal-bipyramidalen Struktur reagieren. In der vorliegenden Arbeit wurde eine detaillierte DFT-Untersuchung der Hyperfeinkopplung sowie der *g*-Tensoren für einige der vom Cornman et. al. studierten Komplexe<sup>2</sup> durchgeführt (siehe Abschnitt 1.4). Weitere Berechnungen wurden für einen anderen Komplex von Oxovanadium mit Schiff-Base-Liganden, bis(2-methylquinoline-8-olate)oxovanadium(IV), gemacht. Für diesen Komplex konnte die relative Orientierung der Hauptkomponenten der Hyperfein- (*A*-) und *g*-Tensoren experimentell bestimmt worden<sup>3</sup> und ermöglichte so eine weitere Validierung der Theorie.

## **1.1 Kritische Untersuchung von Dichtefunktional- und *coupled cluster* Methoden zur Berechnung von EPR-Hyperfein-Kopplungskonstanten für Übergangsmetallverbindungen<sup>1</sup>**

Die Leistungsfähigkeit verschiedener Dichtefunktionalmethoden für die Berechnung von EPR-Hyperfeinkopplungskonstanten wurde durch Vergleich mit experimentellen Daten und *coupled cluster* Ergebnissen für einen repräsentativen Satz von 21 Übergangsmetallverbindungen untersucht. Die Isotropie sowie die Anisotropie der Metall-Kopplung und die Ligand-Kopplungen wurden berechnet und interpretiert.

Sowohl gradientenkorrigierte als auch Hybrid-Austausch-Korrelations-Funktionale ergeben für einfachere Systeme (z.B. ScO, TiN, TiO, VO, MnO, MnF) eine gute Übereinstimmung der berechneten isotropen Metall-Kopplungen mit dem Experiment (bei typischen Abweichungen von etwa 10-15%); keines der verwendeten Funktionale ist jedoch in der Lage, alle Verbindungen zu beschreiben. Gradientenkorrigierte Funktionale unterschätzen die wichtige Spinpolarisation von

Rumpforbitalen. Dies kann für manche Verbindungen korrigiert werden, indem man sogenannte HF/DFT-Hybrid-Funktionale verwendet, bei denen ein Teil des Austauschpotentials durch exakten Hartree-Fock-Austausch ersetzt wird. Allerdings bereitet dieser Ansatz bei vielen Verbindungen Probleme, die mit der Spinkontamination der Wellenfunktion verbunden sind, d.h. mit der Beimischung von Zuständen höherer Spinmultiplizität. In einigen besonders schwierigen Fällen ( $\text{MnO}_3$ ,  $[\text{Mn}(\text{CN})_5\text{NO}]^{2-}$ ) liefert keines der untersuchten Funktionale eine vernünftige Übereinstimmung mit dem Experiment.

Das Hauptproblem der DFT-Beschreibung der Hyperfeinkopplung, die kleine Spinpolarisation von Rumpforbitalen, ist in vielen Fällen der dominante Mechanismus, der die Spindichte am Kernort bildet. Die Spinpolarisation entsteht vor allem durch die Austausch-Wechselwirkungen zwischen dem einzeln besetzten Metall- $3d$ -Orbital und den doppelt besetzten Metall- $3s$  und  $-2s$  Rumpforbitalen. Die Beschreibung der Austausch-Wechselwirkungen unterscheidet sich natürlich sehr von den Energiegrößen, die heutzutage zur Bestimmung der freien Parameter in Austausch-Korrelations-Funktionalen benutzt werden.

Das andere Problem besteht in der Spinpolarisation von Valenzorbitalen, die viel größer als bei den Rumpforbitalen ist und zur Spinkontamination der Wellenfunktion führen kann. In einigen Komplexen entstand die Spinkontamination, sobald ein Teil des Austauschpotentials  $v_x$  durch exakten Hartree-Fock-Austausch ersetzt wurde. Dies reduzierte die Qualität der Resultate deutlich. In manchen Fällen, wo die Spinpolarisation von Rumpforbitalen durch gradientenkorrigierte Funktionale unterschätzt wird, und wo die Beimischung des exakten Austausches erwünscht wäre, um die Spinpolarisation zu vergrößern, macht das dramatische Anwachsen von Spinkontamination die Verbesserung der Ergebnisse durch die HF/DFT-Hybrid-Funktionale unmöglich. In manchen Grenzfällen ist die Spinkontamination schon bei reinen gradientenkorrigierten Funktionalen von Bedeutung. Die Spinkontamination bei den HF/DFT-Hybrid-Funktionalen hängt mit der gut bekannten Begünstigung höherer Spin-Multiplizitäten im Rahmen der Hartree-Fock-Methode zusammen. Offensichtlich kann die Spinkontamination in Übergangsmetall-Komplexen dank der Existenz tiefliegender angeregten Zustände ganz erheblich wachsen.

Keines der momentan zur Verfügung stehenden Austausch-Korrelations-Funktionale liefert über den gesamten Bereich eine hinreichende Spinpolarisation von



Rumpforbitalen, ohne die Spinpolarisation der Valenzorbitalen zu überschätzen. In dieser Hinsicht ist bei der Anwendung von Dichtefunktionalmethoden Vorsicht angebracht, d.h. das anzuwendende Funktional muss derzeit der Stereochemie und der Elektronenzahl des Komplexes entsprechend ausgewählt werden. Die Wahl verschiedener Funktionale für verschiedene Bindungsverhältnisse ist natürlich aus theoretischer Sicht nicht ganz zufriedenstellend, doch spiegelt dies in gewisser Weise den derzeitigen Stand der Näherungen der Dichtefunktional-Methoden wider. Verbesserte Austausch-Korrelations-Funktionale sollten eine zuverlässige Beschreibung der Spinpolarisation von Rumpf- sowie Valenzorbitalen ergeben. Im allgemeinen läßt sich sagen, daß die Hyperfeinkopplung, vor allem für die Übergangsmetall-Komplexe, ein anspruchsvoller Test für die theoretische Methoden darstellt und zur Verbesserung der Dichtefunktionalen sowie der Entwicklung alternativer Ansätze führen kann.

Die sehr aufwendigen *coupled-cluster* (CCSD and CCSD(T)) Methoden, die an einer kleineren Auswahl von Komplexen untersucht wurden, zeigen eine sehr gute Leistungsfähigkeit, auch wenn die UHF Referenz-Wellenfunktion leicht spinkontaminiert ist. Allerdings steigt der Aufwand dieser Methoden mit der Größe des Systems sehr schnell an. Selbst für die di-, tri- und tetraatomaren Komplexe, die in dieser Arbeit auf *coupled-cluster* Niveau studiert wurden, konnten aufgrund des hohen Rechenaufwands keine CCSD-Berechnungen mit größeren Basissätzen mehr durchgeführt werden. Weniger aufwendige Ansätze sind erwünscht, und verbesserte Dichtefunktionale könnten hier eine sehr praktische Alternative bieten.

## **1.2 Mechanismen der EPR-Hyperfeinkopplung in Übergangsmetallverbindungen<sup>4</sup>**

Es wurde eine detaillierte quantenchemische Analyse der Prinzipien durchgeführt, die der Hyperfeinkopplung in *3d*-Übergangsmetallkomplexen zugrundeliegen. Für ausgewählte atomare Systeme wurden die Ein- und Zweielektronen-Integrale für optimierte ROHF- und UHF-Orbitale explizit berechnet, um die Spinpolarisation von Rumpforbitalen zu verstehen. Die Spinpolarisation erhöht die Austausch-Wechselwirkung zwischen den *2s*- und *2p*- Orbitalen und den einfach besetzten

Orbitalen. Die gegensätzliche Spinpolarisation der  $3s$ - und  $3p$ -Orbitale entsteht wegen der erforderlichen Orthogonalität der  $3s$ - ( $3p$ -) Orbitale zu den  $2s$ - ( $2p$ -) Orbitalen. Dies hat die gegensätzliche Beiträge der  $3s$ - und  $2s$ -Orbitale zur Isotropie sowie der  $3p$ - und  $2p$ -Orbitale zur Anisotropie der Metall-Kopplung zur Folge. Die Änderungen in dem Verhältnis zwischen den Beiträgen der  $3s$ - und  $2s$ -Orbitale (sowie der  $3p$ - und  $2p$ -Orbitale) zur Spindichte in der ersten Übergangsmetallreihe läßt sich auf die Knotenstruktur der Orbitalen zurückverfolgen. Analoge Regeln sind bei den Komplexen der zweiten und dritten Übergangsmetallreihen zu erwarten.

Die in dieser Arbeit durchgeführte Analyse ist teilweise mit den traditionellen Erklärungen der Spinpolarisation konsistent, in denen z.B. die Spinpolarisation in Hauptgruppensystemen entsteht durch die Austausch-Wechselwirkungen zwischen dem einzeln besetzten Orbital und der  $\alpha$ -Komponente der doppelt besetzten Orbitale. Um ein volles Verständnis zu bekommen, muß man jedoch auch die komplementäre Spinpolarisationen von  $\beta$ -Komponenten, sowie die Änderungen in der Coulomb-Abstoßung zwischen den Elektronen und der Elektron-Kern Wechselwirkung, betrachten.

Die Spinpolarisation der Rumpforbitale in molekularen Systemen ist proportional der Spin-Population der  $3d$ -Valenzorbitale; ihre Abhängigkeit von den anderen Bindungs-Parametern ist jedoch sehr klein. Die Spinpolarisation von Valenzorbitalen hängt hingegen sehr stark von der Überlappung zwischen einzeln und doppelt besetzten Orbitalen ab. Eine grosse Überlappung führt zu starker Spinpolarisation und u. a. zur Spinkontamination der Wellenfunktion. Dies passiert gerade für die Systeme, bei denen die Verwendung von Hybrid-Dichtefunktionalen zum dramatischen Anwachsen von Spinkontamination und zur erheblichem Verschlechterung der Resultate führt.<sup>4</sup>

Die Bedeutung der Rumpf- und Valenz-Spinpolarisation für die Anisotropie des Kopplungstensors in Übergangsmetall-Komplexen wurde ebenfalls untersucht. Ganz im Gegensatz zur impliziten Annahme in vielen qualitativen sowie quantitativen Schemas, die von Experimentalisten häufig benutzt werden, können sowohl die Rumpforbitale als auch die Valenzorbitale zur Anisotropie des Kopplungstensors erheblich beitragen. Dies unterscheidet die Übergangsmetall-Komplexe von den Hauptgruppensystemen, wo meistens selbst die Betrachtung des einzeln besetzten Orbitals für die Berechnungen der Kopplungsanisotropie ausreichend ist. Die Bedeutung von Spinpolarisation für die Übergangsmetall-Kopplungsanisotropie entsteht dank den stark polarisierbaren ‘semi-

*core* *p*-Orbitalen (hauptsächlich die *3p*-Orbitalen für die erste Übergangsmetallreihe), die eine sehr ähnliche radiale Ausdehnung wie die Valenz-*d*-Schale aufweisen. Die Spinpolarisation beeinflusst nicht nur die doppelt besetzten Orbitale, sondern auch das einzeln besetzte Orbital selbst. Für beispielsweise  $\text{TiF}_3$  und  $\text{MnO}_3$  hat die Spinpolarisation eine interessante *3d/4s* Rehybridisierung des einzeln besetzten Orbitals zur Folge. Letzteres ist ein weiterer Grund, warum die Versuche, von der Anisotropie des Kopplungstensors auf die Spinpopulation oder gar die Zusammensetzung der Orbitale zu schließen, oft zu falschen Ergebnissen führen. Explizite quantenchemische spin-polarisierte Berechnungen sollten hier bevorzugt werden.

Die Ergebnisse dieser Arbeit können außer zum Verständnis der Mechanismen der EPR-Hyperfeinkopplung in Übergangsmetallverbindungen auch zur Identifizierung von Fehlern in theoretischen Ansätzen dienen, und darüberhinaus hoffentlich zur Entwicklung verbesserter Methoden führen.

### **1.3 DFT-Berechnung elektronischer *g*-Tensoren in Übergangsmetallkomplexen mit Hilfe von Mean-Field Spin-Bahn-Operatoren<sup>5</sup>**

Eine neue störungstheoretische DFT-Methode zur Berechnung elektronischer *g*-Tensoren im Programm "deMon" wurde für einen Satz von 14 Übergangsmetallverbindungen validiert. Die atomare Natur der verwendeten Mean-Field Spin-Bahn-Operatoren erlaubte eine weitergehende Analyse und Interpretation atomarer Beiträge zum beobachteten *g*-Tensor.

Im Gegensatz zu den guten Ergebnissen für Hauptgruppensysteme sind die Abweichungen vom Experiment für die Übergangsmetallkomplexe relativ groß. Die Verwendung von Zweielektronen-Spin-Bahn-Operatoren verschlechtert ganz erheblich die Übereinstimmung mit dem Experiment. Die Zweielektronen-Operatoren reduzieren die *g*-Verschiebungen um ~40-50%, so dass ein linearer Fit mit einer Richtwert von 0.59 erhalten wird wenn sowohl die die Einelektronenterme wie auch die Zweielektronenterme eingerechnet werden. Diese Beobachtung entspricht überraschenderweise den von Bühl et al.<sup>6,7</sup> berichteten Ergebnissen in einer

Validierungsuntersuchung von GGA-Dichtefunktionalmethoden für die Berechnung von NMR chemischen Verschiebungen für *3d*-Übergangsmetallkernen. UDFT-GIAO-Berechnungen mit Hilfe gradientenkorrigierter Funktionale haben ein Richtwert von  $\sim 0.6$  im Vergleich mit dem Experiment ergeben. Letzteres läßt sich auf die systematische Unterschätzung der paramagnetischen Anteile von ungefähr 40% zurückverfolgen.

In Übereinstimmung mit dem Vorschlag von Patchkowskii and Ziegler<sup>8</sup> wird dies auf die Unfähigkeit der lokalen/gradientenkorrigierten Dichtefunktionalen zurückgeführt, die jeweiligen Störungsmatrixelemente sowie die Energienenner gut zu beschreiben. Bühl berichtete eine Verbesserung der Richtwert bis beinahe 1.0 bei der Anwendung von HF/DFT-Hybrid-Funktionalen (B3LYP bzw. B3PW91).<sup>7</sup> Vom Gesichtspunkt der formalen Ähnlichkeit des Shieldingtensors und des *g*-Tensors ist eine Verbesserung der Ergebnisse bei der Anwendung von HF-DFT-Hybridfunktionalen auch für die *g*-Tensoren zu erwarten. Vorläufige Ergebnisse haben bestätigt, daß die Anwendung von HF/DFT-Hybrid-Funktionalen tatsächlich zur Verbesserung der Ergebnissen führen soll.<sup>9</sup>

#### **1.4 DFT-Berechnung der EPR-Parameter für Vanadyl-Schiff-Base-Komplexe<sup>10</sup>**

DFT-Untersuchungen der EPR-Hyperfeinkopplungstensoren und *g*-Tensoren für Vanadyl-Schiff-Base Komplexe wurden durchgeführt. Folgende Komplexe wurden untersucht: [N,N'-ethylenbis(*o-tert*-butyl-*p*-methyalsalicylaldiminato)] oxovanadium(IV), bis(*N*-methyalsalicylaldiminato)] oxovanadium(IV), bis(*N*-methyl-*o-tert*-butyl-*p*-methyalsalicylaldiminato) oxovanadium(IV), und bis(2-methylquinolin-8-olat) oxovanadium(IV).

Die Hauptkomponenten der *A*- und *g*-Tensoren wurden berechnet und interpretiert. Zusätzlich liefert die Rechnung die Orientierung der *A*- und *g*-Tensoren relativ zum Molekülgerüst, die experimentell in diesen Fällen nicht zugänglich ist. Die Orientierung des *A*-Tensors relativ zum *g*-Tensor ist experimentell einfacher zu erhalten und konnte für bis(2-methylquinolin-8-olat) oxovanadium(IV) bestimmt werden.

Während in diesem Fall einige Unklarheiten bezüglich der Zuordnung der Komponenten besteht, stimmen theoretische und experimentelle Resultate miteinander überein. Beide ergeben eine ganz erhebliche Rotation zwischen den senkrechten Komponenten beider Tensoren (Theorie:  $41^\circ$ , Experiment:  $28^\circ$ ).

Die Orientierungs-Abhängigkeit des  $A$ -Tensors von der lokalen Oxovanadium-Koordination ist relativ klein. Die Orientierung des  $g$ -Tensors hängt hingegen sehr stark von Koordinationsgeometrie des Vanadyls ab. Dies lässt sich durch die verschiedene Beiträge angeregter Zustände zu den  $A$ - und  $g$ -Tensoren verstehen. Der  $A$ -Tensor ist hauptsächlich eine Grundzustands-Eigenschaft, während der  $g$ -Tensor eine Reaktion der Wellenfunktion des Systems auf die Störung durch das externe Magnetfeld beschreibt und so den Effekt angeregter Zustände darstellt. Letzteres hat die Nichtkoinzidenz von  $A$ - und  $g$ -Tensoren für die vorliegende Reihe von Komplexen zur Folge. Die Orientierung der  $A$ - und  $g$ -Tensoren relativ zum Molekülgerüst bzw. die experimentell einfacher zu erhaltende Orientierung des  $A$ -Tensors relativ zum  $g$ -Tensor kann als ein sehr empfindlicher Test der lokalen Koordination und Symmetrie des Oxovanadiums dienen.

Der experimentell gefundene Zusammenhang zwischen der Anisotropie des  $A$ -Tensors und der lokalen Oxovanadium-Koordination wurde auf der DFT-Niveau reproduziert, analysiert und mit Hilfe der  $V-3d_z^2$  Beiträge zum einzeln besetzten Orbital (überwiegend  $V-3d_{x^2-y^2}$ ) interpretiert. Letztere Beiträge sind dank der Verzerrung der SQ-5 Koordination zur TBP-5 Koordination möglich. Für den bis(*N*-methyl-*o*-(*tert*-butyl-*p*-methylsalicylaldiminato) oxovanadium(IV) Komplex, der überdies eine erhebliche Verzerrung von der  $C_2$ -Symmetrie aufweist, sind auch die voneinander verschiedenen Metall- $d_{xz}$ , Metall- $d_{yz}$  Beimischungen in das einzeln besetzte Orbital von Bedeutung. Der Zusammenhang zwischen der Anisotropie des  $A$ -Tensors und der lokalen Metall-Koordination sollte für die EPR-unterstützte strukturelle Charakterisierung biochemisch relevanter Komplexe im Allgemeinen von Bedeutung sein.

Die vorliegende Arbeit dient nicht nur zur Interpretation experimenteller Trends in magnetischen Wechselwirkungen, sondern auch als eine weitere Validierungsuntersuchung von Dichtefunktionalmethoden zur Berechnung von EPR-Parametern für Übergangsmetallverbindungen. Die hier untersuchte Vanadyl-Komplexe weisen ein einzeln besetzte Orbital auf, welches relativ wenig mit den doppelt besetzten

Metall-Valenzorbitalen überlappt. In Übereinstimmung mit den vorigen Ergebnissen<sup>1</sup> ist die Spinkontamination bei den HF/DFT-Hybrid-Funktionalen kein großes Problem. Die Hybrid-Austauschfunktionale führen zu besserer Übereinstimmung der berechneten Hyperfeinkopplung mit dem Experiment als die gradientenkorrigierten Funktionale, dank einer verbesserten Behandlung von Spinpolarisation der Rumpforbitale. Alle hier untersuchte Dichtefunktionale, inklusiv die BP86-Gradientenkorrigerung, reproduzieren den experimentellen Trend in der Anisotropie des  $A$ -Tensors unter der SQ-5  $\rightarrow$  TBP-5 Verzerrung sehr gut. Dies läßt sich auf die Tatsache zurückführen, daß die Anisotropie des  $A$ -Tensors hauptsächlich durch das einzeln besetzte Orbital bestimmt wird und relativ wenig von der Spinpolarisation abhängt.

Wie bereits in unserer Validierungsuntersuchung der DFT-Methode zur Berechnung elektronischer  $g$ -Tensoren gefunden,<sup>5</sup> unterschätzen die lokale Dichtenäherung sowie die gradientenkorrigierten Austausch-Korrelations-Funktionale systematisch die paramagnetischen Anteile zu ungefähr 40%. Eine Verbesserung der Ergebnisse ist jedoch bei Anwendung von HF-DFT-Hybridfunktionalen zu erwarten.<sup>9</sup>

## Literatur

---

- <sup>1</sup> Munzarová, M.; Kaupp, M. *J. Phys. Chem. A* **1999**, *103*, 9966.
- <sup>2</sup> Cornman, C. R.; Geiser-Bush, K. M.; Rowley, S. P.; Boyle, P. D. *Inorg. Chem.* **1997**, *36*, 6401-6408.
- <sup>3</sup> Collison, D.; Gahan, B.; Mabbs, F. *J. Chem. Soc. Dalton* **1987**, 111.
- <sup>4</sup> Munzarová, M. L.; Kubáček, P.; Kaupp, M. *J. Am. Chem. Soc.* **2000**, *122*, 11900.
- <sup>5</sup> Malkina, O. L.; Vaara, J.; Schimmelpfennig, B.; Munzarová, M.; Malkin, V. G.; Kaupp, M. *J. Am. Chem. Soc.* **2000**, *122*, 9206.
- <sup>6</sup> Bühl, M.; Malkina, O. L.; Malkin, V. G. *Helv. Chim. Acta* **1996**, *79*, 742.
- <sup>7</sup> Bühl, M.; *Chem. Phys. Lett.* **1997**, *267*, 251.
- <sup>8</sup> Patchkovskii, S.; Ziegler T. *J. Chem. Phys.* **1999**, *111*, 5730.
- <sup>9</sup> Reviakine, R.; Malkin, V. G.; Malkina, O. L.; Arbouznikov, A.; Kaupp, M. *unveröffentlichte Ergebnisse*.
- <sup>10</sup> Munzarová, M. L.; Kaupp, M., eingereicht bei *J. Phys. Chem.*





*In the course of coming into contact with empirical material, physicists have gradually learned how to pose a question properly. Now, proper questioning often means that one is more than half the way towards solving the problem.*

*Werner Heisenberg (1901-1976)*

## **2 Introduction**

### **2.1 Background and Motivation**

Electron paramagnetic resonance spectroscopy (EPR) is a branch of magnetic resonance spectroscopy dealing with molecules in which the total spin quantum number  $S$  is different from zero. In such molecules, the probability of finding at any point an electron with spin “up“ minus the probability of finding there an electron with spin “down”, the spin density, is generally nonzero. Associated with this net electronic spin is a magnetic moment giving rise to two degenerate energy levels. In the presence of an external magnetic field, this degeneracy is lifted due to the electronic Zeeman interaction, and the levels are split by an amount proportional to the field strength. The basic EPR experiment consists of observing a transition between these two energy levels. Most of the EPR spectra, however, do not consist of a single line but do have a hyperfine structure that arises due to interactions between the electronic spin density and nuclear spins in the radical.

Most of the nondynamic information obtained from EPR is an information on the spin density distribution. This in turn provides information on the structure of the molecule observed. An important intermediate in the interpretation of the EPR spectra is the spin Hamiltonian, a model that summarizes the experimental data in terms of small number of parameters. Within the spin Hamiltonian concept, the electronic Zeeman interaction between the net electronic spin and the external magnetic field is parametrized by the electronic  $g$ -tensor; the hyperfine interaction between the electron and nuclear spins is described by the hyperfine  $A$ -tensor.

The hyperfine structure is often considered to be the most important part of information obtained from an EPR spectrum, due to a very direct connection between the spin density at (near the) nucleus and the isotropic (anisotropic) part of the hyperfine tensor. Since the early days of EPR, the interpretation of hyperfine coupling has been an example of a particularly fruitful interaction between theory and experiment. Substantial qualitative understanding has been obtained for organic free radicals as well as for transition metal complexes. Quantitative theoretical studies of the hyperfine coupling have, however, concentrated largely on organic molecules or on other light main group systems. This is understandable, as the accurate inclusion of electron-correlation effects is mandatory for quantitative calculations of electron-nuclear hyperfine interactions. To achieve this in traditional post-Hartree-Fock *ab initio* calculations is far from trivial, and such treatments are not easily applicable to larger transition metal compounds. Yet, recent interest in applications of EPR to transition metal complexes in catalysis, bioinorganic chemistry, or materials research make the quantitative theoretical treatment of such systems highly desirable.

An alternative theoretical approach has been provided by recent developments in density functional theory (DFT) that includes electron correlation approximately, at moderate computational cost. A number of Kohn-Sham DFT studies on transition metal hyperfine coupling have appeared. However, only a limited number of density functionals and basis sets have been employed, and only a relatively small set of molecules and electronic-structure situations was covered. In order to be able to judge in detail the ability of the available DFT approaches to describe the hyperfine coupling for transition metal systems, further systematic studies were needed.

## **2.2 Objectives of the Study**

The primary objective of the work reported in this thesis was to perform a validation study of density functional approaches for the calculations of EPR hyperfine coupling for a series of first-row transition metal complexes. The author's aim was to compare the results obtained for a series of density functionals with experiment, to identify functionals suitable for further application calculations, and to employ these

calculations for the interpretation of spectra of chemically interesting systems. Throughout the validation study, the author has learned much about the mechanisms of transfer of the spin density from the valence shell to the transition metal nuclei. These interpretational aspects became subjects of a separate study. The final objective was to validate a new DFT implementation of electronic  $g$ -tensor calculations within the deMon code for a series of  $3d$  transition metal complexes, as well as to apply the new methods.

The present thesis consists of an introductory part (Chapters 1 through 3), four commented papers summarizing the author's work in the field of theoretical studies of EPR parameters (Chapters 4 through 7), and a conclusion part (Chapter 8). The topics introduced in this chapter (Chapter 1) are dealt with in more detail in subsequent chapters. Chapter 2 describes the theory of the spectral parameters of electron paramagnetic resonance. The concept of the EPR spin Hamiltonian is introduced, followed by a discussion of the perturbation theory approach to the calculation of two of its parameters,  $g$ - and  $A$ -tensors. Chapter 3 is devoted to an overview of *ab initio* computational methods employed in this thesis for obtaining the field-free description of the molecular ground state. Chapter 4 reports the results of the extensive evaluation of DFT methods for the prediction of hyperfine coupling constants for both metals and ligands in  $3d$  transition metal complexes. The results of the validation study of new DFT methods for the calculation of electronic  $g$ -tensors for a set of  $3d$ -transition metal complexes are reported in Chapter 5. Chapter 6 describes the results of a detailed study of the mechanisms of EPR hyperfine coupling in transition metal complexes. Finally, a DFT application study of  $g$ - and  $A$ -tensors for a series of vanadyl complexes is reported in Chapter 7. A number of general conclusions are given in Chapter 8.

SI conventions are assumed throughout this thesis and recommended symbols are employed, with three small exceptions.  $4\pi\epsilon_0$  ( $\epsilon_0$  being the permittivity of free space) is often denoted by the single symbol  $\kappa_0$ ;  $\beta_e$  has been retained for the Bohr magneton (recommended symbol  $\mu_B$ ), and  $\beta_N$  for the nuclear magneton (recommended symbol  $\mu_N$ ). Instead of  $\mu_0/4\pi$  ( $\mu_0$  being the permeability of free space), we have used the equivalent combination  $1/\kappa_0 c^2$ ,  $c$  being the velocity of light.

Atomic units are employed throughout Chapter 3 of this thesis and the original papers. We note that in atomic units,  $e$ ,  $\hbar$ ,  $m$  and  $\kappa_0$  all take unit values and may thus be

dropped from all equations provided the symbols occurring are reinterpreted as the numerical (i.e. dimensionless) measures of the quantities they represent.

*The electron is not as simple as it looks.*

*William Lawrence Bragg (1890-1971)*

### **3 Electron Paramagnetic Resonance Parameters**

This chapter discusses the theory of the spectral parameters of electron paramagnetic resonance. We introduce the concept of the EPR spin Hamiltonian and explain the perturbation-theory (PT) approach to the calculation of two of its parameters: the  $g$ - and  $A$ -tensors. Our approach is based on a PT treatment of the Breit-Pauli Hamiltonian. The conceptual sequence from the relativistic Dirac Hamiltonian through the Breit-Pauli Hamiltonian to the EPR spin Hamiltonian is sketched, following refs 1, 2, 3, and 4. A unified theoretical treatment of  $g$ - and  $A$ -tensors is provided up to second-order perturbation theory. Important links between the spin Hamiltonian parameters and qualitative aspects of electronic structure are established, following the discussion in refs 5 and 6.

#### **3.1 Electron Spin: A Theoretical Rationale**

The technique of electron paramagnetic resonance spectroscopy may be regarded as a fascinating extension of the famed Stern-Gerlach experiment. In one of the most fundamental experiments on the structure of matter, Stern and Gerlach in 1922 showed that an electron magnetic moment in an atom can take only discrete orientations in a magnetic field, despite the sphericity of the atom.<sup>7</sup> As a theoretical rationalization of this striking observation that could not be explained along the lines of quantum mechanics, Uhlenbeck and Goudsmith postulated in 1925 that electrons possessed an intrinsic angular momentum – *electron spin*.<sup>8</sup> This would give rise to an intrinsic magnetic momentum of the electron, independent of any translational motion.

### 3.1.1 Pauli Spin Matrices

The concept of electron spin has been incorporated into quantum mechanics in 1927 by Pauli<sup>9</sup> who postulated that a full characterization of electronic behavior requires, in addition to a spatial function  $\phi(\mathbf{r})$ , a parameter of electron spin  $\sigma$ . The electron spin was suggested to be a combination of degenerate but orthogonal functions

$$\alpha = \begin{bmatrix} 1 \\ 0 \end{bmatrix} ; \quad \beta = \begin{bmatrix} 0 \\ 1 \end{bmatrix} . \quad (3.1)$$

It can be obtained as an expectation value of the operator  $\sigma = (\sigma_x, \sigma_y, \sigma_z)$ , where

$$\sigma_x = \begin{bmatrix} 0 & 1 \\ 1 & 0 \end{bmatrix}, \quad \sigma_y = \begin{bmatrix} 0 & -i \\ i & 0 \end{bmatrix}, \quad \sigma_z = \begin{bmatrix} 1 & 0 \\ 0 & -1 \end{bmatrix} \quad (3.2)$$

are the Pauli spin matrices.

### 3.1.2 The Dirac Equation

The Pauli treatment of spin inspired Dirac in his effort to develop a theory, in which the electron spin and magnetic moment would arise naturally: *“The question remains as to why Nature should have chosen this particular model for the electron instead of being satisfied with the point-charge. One would like to find some incompleteness in the previous methods of applying quantum mechanics to the point-charge electron that, when removed, the whole of the duplexity phenomena [spin effects] follow without arbitrary assumptions.”*<sup>10</sup> This goal has been achieved when Dirac rederived quantum mechanics within Einstein’s special relativity theory, providing thus a formalism in which it was possible to explain all magnetic effects known at the time and predict numerous additional phenomena.

Using Einstein’s relationship between total energy, momentum, and a rest mass  $m$  of a free particle, a relativistic version of the free-particle Schrödinger equation

$$-\frac{\hbar}{i} \frac{\partial \Psi}{\partial t} = \pm c \sqrt{-\hbar^2 \nabla^2 + m^2 c^2} \Psi \quad . \quad (3.3)$$

can be obtained. It is, however, not clear how to interpret the square root in the relativistic Hamiltonian. Dirac circumvented this problem by setting

$$\sqrt{-\hbar^2 \nabla^2 + m^2 c^2} = \frac{\hbar}{i} \nabla \cdot \boldsymbol{\alpha} + \boldsymbol{\beta} mc \quad (3.4)$$

where  $\beta$  is some scalar and  $\alpha = (\alpha_x, \alpha_y, \alpha_z)$ . Equation (3.4) can only be satisfied if

$$[\alpha_i, \alpha_j] = 0 \quad , \quad i \neq j \quad ; \quad [\alpha_i, \beta] = 0 \quad ; \quad \alpha_i^2 = \beta^2 = 1 \quad . \quad (3.5)$$

In the simplest possible solution of the system (3.5),  $\alpha_i$  and  $\beta$  are (4x4) matrices, the explicit form of which can be found elsewhere.<sup>3</sup> The important fact is that the (4x4) nature of the operators implies a four-component relativistic wave function

$$\boldsymbol{\Psi}(\mathbf{r}, t) = \begin{bmatrix} \Psi_1(\mathbf{r}, t) \\ \Psi_2(\mathbf{r}, t) \\ \Psi_3(\mathbf{r}, t) \\ \Psi_4(\mathbf{r}, t) \end{bmatrix} \quad . \quad (3.6)$$

The Dirac equation

$$-\frac{\hbar}{i} \frac{\partial \boldsymbol{\Psi}}{\partial t} = \left( \frac{\hbar c}{i} \nabla \cdot \boldsymbol{\alpha} + \boldsymbol{\beta} mc^2 \right) \boldsymbol{\Psi} \quad (3.7)$$

thus represents a set of four partial differential equations. Of its four solutions, only two correspond to normal electronic behavior. They account for the existence of the  $\alpha$  and  $\beta$  spin states postulated by Pauli (see next section), and for a number of other relativistic quantum effects. The two other solutions were found to describe a particle not known at the moment of Dirac's publication - with electronic properties except for an opposite charge. Four years later, the discovery of the positron – a particle perfectly matching this description – upheld the triumph of Dirac theory.

### 3.1.3 Pauli Reduction of the Dirac Equation

The Dirac equation can be solved exactly only for the most simple systems. It is thus desirable to generate approximations that are more easily solved but still contain the essential features of the Dirac formalism. A common approach to such approximations is looking for the relationships between the fully relativistic Dirac theory of the electron and the nonrelativistic theory where spin is treated in the Pauli sense. There are two categories of reasons for wishing to establish a connection between these two theories. Firstly, understanding of a theory often depends to a large extent on a model in terms of which the predictions of the theory can be interpreted. There is a natural tendency to base new models on revisions of previous models, in this case to relate relativistic quantum mechanics to nonrelativistic quantum mechanics (and in turn, to classical mechanics). Secondly, in many cases relativistic effects are relatively small compared to the total quantities involved; it is thus advantageous from the computational point of view to treat them as perturbations with respect to the nonrelativistic case. The reduction of the fully relativistic theory with four-component wave functions to a non-relativistic theory with two-component wave functions is traditionally done using either the Foldy-Wouthuysen transformation or the partitioning approach.<sup>1</sup> To demonstrate how Dirac theory accounts for the electronic Zeeman effect, we develop here the latter approach – the *Pauli reduction* of the Dirac equation, as applied to a free electron in a magnetic field.

For the description of the effect of a uniform magnetic field  $\mathbf{B}$  on an electron, we will use field-dependent momentum and energy operators

$$\begin{aligned} \mathbf{p} = -\frac{\hbar}{i}\nabla &\quad \rightarrow \quad \boldsymbol{\pi} = -\frac{\hbar}{i}\nabla + \frac{e}{c}\mathbf{A} \\ W = -\frac{\hbar}{i}\frac{\partial}{\partial t} &\quad \rightarrow \quad -\frac{\hbar}{i}\frac{\partial}{\partial t} + e\phi \end{aligned} \quad . \quad (3.8)$$

Here  $\phi$  and  $\mathbf{A}$  are the scalar and vector potentials, from which the electric field strength  $E$  and magnetic flux density  $\mathbf{B}$ , respectively, may be derived within classical



electromagnetic theory. Consequently, one obtains the field dependent version of the Dirac equation

$$-\frac{\hbar}{i} \frac{\partial \Psi}{\partial t} = (c\boldsymbol{\pi} \cdot \boldsymbol{\alpha} + \beta mc^2 - e\phi) \Psi \quad . \quad (3.9)$$

Because one is generally interested in the two electronic solutions only, it is desirable to reduce the (4x4) system of equations (2.9) to a (2x2) system by writing  $\Psi$  in terms of two two-row spinors:

$$\Psi = \begin{bmatrix} \Psi_u \\ \Psi_l \end{bmatrix} ; \quad \Psi_u = \begin{bmatrix} \Psi_1 \\ \Psi_2 \end{bmatrix} ; \quad \Psi_l = \begin{bmatrix} \Psi_3 \\ \Psi_4 \end{bmatrix} \quad . \quad (3.10)$$

Partitioning  $\alpha$  and  $\beta$  accordingly, one obtains

$$\boldsymbol{\alpha} = \begin{bmatrix} \mathbf{0} & \boldsymbol{\sigma} \\ \boldsymbol{\sigma} & \mathbf{0} \end{bmatrix} , \quad \beta = \begin{bmatrix} \mathbf{1} & \mathbf{0} \\ \mathbf{0} & -\mathbf{1} \end{bmatrix} \quad . \quad (3.11)$$

Here  $\mathbf{1}$  and  $\mathbf{0}$  are (2x2) unity and zero matrices, respectively; and the components  $\sigma_x$ ,  $\sigma_y$ ,  $\sigma_z$  of the operator  $\sigma$  are the Pauli spin matrices (3.2).

Within this formalism, the Dirac equation can be written as

$$\begin{aligned} mc^2 \Psi_u + c\boldsymbol{\sigma} \cdot \boldsymbol{\pi} \Psi_l &= W \Psi_u \\ c\boldsymbol{\sigma} \cdot \boldsymbol{\pi} \Psi_u - mc^2 \Psi_l &= W \Psi_l \quad . \end{aligned} \quad (3.12)$$

The total energy  $W$  can be separated into a sum of the rest mass  $mc^2$  and all additional energy  $\varepsilon$ , so that (3.12) becomes

$$c\boldsymbol{\sigma} \cdot \boldsymbol{\pi} \Psi_l = \varepsilon \Psi_u \quad (3.13)$$

$$c\boldsymbol{\sigma} \cdot \boldsymbol{\pi} \Psi_u = (\varepsilon + 2mc^2) \Psi_l \quad . \quad (3.14)$$

If we express  $\Psi_l$  in terms of  $\Psi_u$  using (3.14) and substitute it into (3.13), we obtain

$$\frac{c^2(\boldsymbol{\sigma}\cdot\boldsymbol{\pi})^2}{\varepsilon + 2mc^2}\boldsymbol{\Psi}_u = \varepsilon\boldsymbol{\Psi}_u \quad . \quad (3.15)$$

In most conventional systems, the dominating term in the total energy is the rest mass ( $W \approx mc^2 \gg \varepsilon$ ). Therefore, we can make the approximation  $\varepsilon + 2mc^2 \approx 2mc^2$  (*first Pauli limit*), in which (3.15) becomes

$$\frac{1}{2m}(\boldsymbol{\sigma}\cdot\boldsymbol{\pi})^2\boldsymbol{\Psi}_u = \varepsilon\boldsymbol{\Psi}_u \quad . \quad (3.16)$$

The latter expression can be rewritten as

$$\frac{1}{2m}(\boldsymbol{\sigma}\cdot\boldsymbol{\pi})^2\boldsymbol{\Psi}_u = \frac{1}{2m}\left[\boldsymbol{\pi}^2 + \frac{e\hbar}{c}\boldsymbol{\sigma}\cdot\mathbf{B}\right]\boldsymbol{\Psi}_u = \left[\frac{\boldsymbol{\pi}^2}{2m} + \beta_e\boldsymbol{\sigma}\cdot\mathbf{B}\right]\boldsymbol{\Psi}_u = \varepsilon\boldsymbol{\Psi}_u \quad , \quad (3.17)$$

which is identical to Pauli's empirical incorporation of electron spin into quantum mechanics.

If we expand  $\boldsymbol{\sigma}$  and expect the magnetic field  $\mathbf{B}$  to be oriented in the z-direction, we obtain a system of equations

$$\begin{bmatrix} \frac{\boldsymbol{\pi}^2}{2m} + \beta_e B & 0 \\ 0 & \frac{\boldsymbol{\pi}^2}{2m} - \beta_e B \end{bmatrix} \begin{bmatrix} \Psi_1 \\ \Psi_2 \end{bmatrix} = \varepsilon \begin{bmatrix} \Psi_1 \\ \Psi_2 \end{bmatrix} \quad (3.18)$$

with two nontrivial solutions

$$\Psi_1 = 0 \quad ; \quad \Psi_2 \propto |n, l, m_l\rangle \quad ; \quad \varepsilon = 2n\beta_e B + \frac{l^2\hbar^2}{2m} - e\phi \quad (3.19)$$

$$\Psi_1 \propto |n, l, m_l\rangle \quad ; \quad \Psi_2 = 0 \quad ; \quad \varepsilon = (2n+2)\beta_e B + \frac{l^2\hbar^2}{2m} - e\phi \quad . \quad (3.20)$$

Thus, when subjected to a magnetic field  $\mathbf{B}$ , two electronic states with identical spatial distribution vary in energy by an amount of  $2\beta_e B$ . Pauli's approach, therefore, very closely approximates the Zeeman resonance condition for a free electron

$$h\nu = g_e \beta_e \mathbf{S} \cdot \mathbf{B} \quad , \quad (3.21)$$

where  $\mathbf{S}$  is the electron spin angular momentum vector and  $g_e$  is the spectroscopic splitting factor. Dirac's relativistic theory predicts  $g_e$  to be equal to 2 for a free electron. The discrepancy between this and the experimental value (2.002319304386) is attributed primarily to quantum electrodynamic effects.

In the first Pauli limit, eq (3.15) adopts a form where the terms proportional to  $1/c^{2n}$  disappear, cf. (3.16). A transformation of eq (3.15) that keeps the terms proportional to  $1/c^2$  is called the *second Pauli limit* of the reduced Dirac equation. The resulting expression, called the *Breit-Pauli Hamiltonian*, provides tremendous insight into electromagnetic behavior of a free electron by accounting explicitly for the familiar spin-orbit coupling, the Darwin term, and the relativistic correction to the kinetic energy.

### 3.2 The Breit-Pauli Hamiltonian for Many-Particle Systems

The extension of the approach described above to many-particle systems is based on, first, a generalization of the Dirac Hamiltonian to two particles, and then its application to a many-particle system in which all pairwise interactions are taken as additive. Here we present the terms of the Breit-Pauli Hamiltonian for a many-electron molecule in the absence of any external electric charges. The fixed-nucleus approximation is employed. We follow ref 2 in writing the Hamiltonian in the form

$$H = H_e + H_N + H_{eN} \quad . \quad (3.22)$$

The pure electronic term is then

$$H_e = \sum_{m=1}^{12} H_m^e \quad , \quad (3.23)$$

where (using  $\kappa_0$  to denote  $4\pi\epsilon_0$ )

$$H_1^e = \sum_i \frac{\boldsymbol{\pi}_i^2}{2m_e} , \quad (3.24)$$

$$H_2^e = -e \sum_i \phi_i , \quad (3.25)$$

$$H_3^e = g_e \beta_e \sum_i \left(1 - \frac{\pi_i^2}{2m_e \kappa_0 c^2}\right) \mathbf{s}_i \cdot \mathbf{B} , \quad (3.26)$$

$$H_4^e = - \sum_i \frac{\pi_i^4}{8m_e^3 c^2} , \quad (3.27)$$

$$H_5^e = - \frac{g_e \beta_e}{4m_e c^2} \sum_i \left[ \mathbf{s}_i \cdot \boldsymbol{\pi}_i \times \mathbf{E}_i - \mathbf{s}_i \cdot \mathbf{E}_i \times \boldsymbol{\pi}_i \right] , \quad (3.28)$$

$$H_6^e = - \frac{\hbar \beta_e}{4m_e c^2} \sum_i \operatorname{div} \mathbf{E}_i , \quad (3.29)$$

$$H_7^e = - \frac{e^2}{2\kappa_0} \sum'_{ij} \frac{1}{r_{ij}} , \quad (3.30)$$

$$H_8^e = - \frac{2\pi \beta_e^2}{\kappa_0 c^2} \sum'_{ij} \delta(\mathbf{r}_i - \mathbf{r}_j) , \quad (3.31)$$

$$H_9^e = - \frac{g_e \beta_e^2}{\hbar \kappa_0 c^2} \sum'_{ij} r_{ij}^{-3} \left[ 2\mathbf{s}_i \cdot \mathbf{r}_{ij} \times \boldsymbol{\pi}_j + \mathbf{s}_j \cdot \mathbf{r}_{ij} \times \boldsymbol{\pi}_i \right] , \quad (3.32)$$

$$H_{10}^e = - \frac{\beta_e^2}{\hbar^2 \kappa_0 c^2} \sum'_{ij} r_{ij}^{-3} \left[ r_{ij}^2 \boldsymbol{\pi}_i \cdot \boldsymbol{\pi}_j + \mathbf{r}_{ij} \cdot (\mathbf{r}_{ij} \cdot \boldsymbol{\pi}_i) \boldsymbol{\pi}_j \right] , \quad (3.33)$$

$$H_{11}^e = -\frac{g_e^2 \beta_e^2}{2\kappa_0 c^2} \sum'_{ij} r_{ij}^{-5} \left[ 3(\mathbf{s}_j \cdot \mathbf{r}_{ij})(\mathbf{s}_i \cdot \mathbf{r}_{ij}) - r_{ij}^2 \mathbf{s}_i \cdot \mathbf{s}_j \right] , \quad (3.34)$$

$$H_{12}^e = -\frac{4\pi g_e^2 \beta_e^2}{3\kappa_0 c^2} \sum'_{ij} \mathbf{s}_i \cdot \mathbf{s}_j \delta(\mathbf{r}_i - \mathbf{r}_j) . \quad (3.35)$$

The pure nuclear term is

$$H_N = \sum_{m=1}^{12} H_m^N , \quad (3.36)$$

where (within the fixed-nucleus approximation)

$$H_1^N = -e \sum_N Z_N \phi_N , \quad (3.37)$$

$$H_2^N = -\beta_N \sum_N g_N \mathbf{I}_N \cdot \mathbf{B} , \quad (3.38)$$

$$H_3^N = \frac{e^2}{2\kappa_0} \sum'_{N,N'} \frac{Z_N Z_{N'}}{R_{NN'}} , \quad (3.39)$$

$$H_4^N = -\frac{\beta_N^2}{2\kappa_0 c^2} \sum'_{N,N'} g_N g_{N'} R_{NN'}^{-5} \left[ 3(\mathbf{I}_N \cdot \mathbf{R}_{NN'}) (\mathbf{I}_{N'} \cdot \mathbf{R}_{NN'}) - R_{NN'}^2 \mathbf{I}_N \cdot \mathbf{I}_{N'} \right] . \quad (3.40)$$

Finally, the electron-nuclear term is

$$H_{eN} = \sum_{m=1}^6 H_m^{eN} , \quad (3.41)$$

where

$$H_1^{eN} = -\frac{e^2}{\kappa_0} \sum_{i,N} \frac{Z_N}{r_{iN}} , \quad (3.42)$$

$$H_2^{eN} = \frac{g_e \beta_e \beta_N}{\kappa_0 c^2} \sum_{i,N} g_N r_{iN}^{-5} \left[ 3(\mathbf{s}_i \cdot \mathbf{r}_{iN})(\mathbf{I}_N \cdot \mathbf{r}_{iN}) - r_{iN}^2 \mathbf{s}_i \cdot \mathbf{I}_N \right] , \quad (3.43)$$

$$H_3^{eN} = \frac{8\pi}{3} \frac{g_e \beta_e \beta_N}{\kappa_0 c^2} \sum_{i,N} g_N \mathbf{s}_i \cdot \mathbf{I}_N \delta(\mathbf{r}_i - \mathbf{r}_N) , \quad (3.44)$$

$$H_4^{eN} = \frac{2\beta_e \beta_N}{\hbar \kappa_0 c^2} \sum_{i,N} g_N r_{iN}^{-3} \left[ \mathbf{I}_N \cdot \mathbf{r}_{iN} \times \boldsymbol{\pi}_i \right] , \quad (3.45)$$

$$H_5^{eN} = \frac{g_e \beta_e^2}{\hbar \kappa_0 c^2} \sum_{i,N} Z_N r_{iN}^{-3} \left[ \mathbf{s}_i \cdot \mathbf{r}_{iN} \times \boldsymbol{\pi}_i \right] , \quad (3.46)$$

$$H_6^{eN} = \frac{2\pi \beta_e^2}{\kappa_0 c^2} \sum_{i,N} Z_N \delta(\mathbf{r}_i - \mathbf{r}_N) . \quad (3.47)$$

In the above,  $\mathbf{s}_i$  is the spin angular momentum vector of electron  $i$  and  $\mathbf{I}_N$  is the spin angular momentum of nucleus  $N$ .  $\phi$  is the external electric potential and  $\mathbf{E}_i$  is the external electric field. The vectors

$$\mathbf{r}_{iN} = \mathbf{r}_i - \mathbf{r}_N \quad (3.48)$$

$$\mathbf{r}_{iO} = \mathbf{r}_i - \mathbf{r}_O \quad (3.49)$$

$$\mathbf{r}_{ij} = \mathbf{r}_i - \mathbf{r}_j \quad (3.50)$$

define the position of electron  $i$  with respect to the position of nucleus  $N$  (eq (3.48)), the position of some arbitrarily chosen gauge origin  $O$  (eq (3.49)), and the other integration variable  $\mathbf{r}_j$  (eq (3.50)), respectively.  $g_N$  is the nuclear g-value (that must be found experimentally) and  $Z_N$  is the proton number of nucleus  $N$ . All signs are explicitly taken care of in the formulae (3.23)-(3.47), so  $e$  and  $Z_N$  should be regarded as positive numbers.

The terms in the Breit-Pauli Hamiltonian can be interpreted as follows<sup>1,11</sup>:

The pure electronic terms:

- (3.24) The electron's kinetic energy,
- (3.25) the energy of the interaction between the electron and the external electric field;
- (3.26) the electron Zeeman interaction between  $\mathbf{s}_i$  and  $\mathbf{B}$ ;
- (3.27) relativistic correction to the electron's kinetic energy;
- (3.28) the one-electron spin-orbit interaction;
- (3.29) the Darwin correction to the electric field interaction;
- (3.30) electron-electron Coulomb interaction (electron repulsion);
- (3.31) two-electron Darwin operator;
- (3.32) two-electron spin-orbit interaction
- (3.33) the orbit-orbit interaction between electrons
- (3.34) electron spin-spin dipolar interaction;
- (3.35) electron spin-spin contact interaction.

The pure nuclear terms

- (3.37) Energy of interaction between the nuclei and the external electric field;
- (3.38) nuclear Zeeman term;
- (3.39) nuclear-nuclear Coulomb interaction;
- (3.40) nuclear dipole-dipole interaction.

The electron-nuclear terms:

(3.42) Electron-nuclear Coulomb interaction (Coulomb attraction);

(3.43) dipolar hyperfine interaction;

(3.44) Fermi contact hyperfine interaction;

(3.45) orbital hyperfine interaction;

(3.46) electron-electron spin-orbit hyperfine correction;

(3.47) electron-nuclear Darwin term.

### 3.3 The Spin Hamiltonian

#### 3.3.1 The Concept of the Spin Hamiltonian

The form of the Breit-Pauli Hamiltonian suggests the possibility of constructing a “phenomenological“ Hamiltonian that contains only spin operators and applied fields, together with numerical parameters that serve as „coupling constants“. Indeed, the results of magnetic resonance experiments are most commonly interpreted in terms of a spin Hamiltonian referring to a model spin system whose behavior may be determined by solving

$$H_S \Theta = E \Theta \quad (3.51)$$

in a basis of electron-nuclear spin functions, referring to spins of various nuclei  $\mathbf{I}_N$  and to the *total* electron spin  $\mathbf{S}$ . With a proper choice of coupling constants, the eigenvalues of (3.51) fit the observed energy levels. The spin Hamiltonian is conventionally written in the form<sup>1</sup>

$$H_S = \mathbf{S} \cdot \mathbf{g} \cdot \mathbf{B} + \sum_N \mathbf{S} \cdot \mathbf{A}_N \cdot \mathbf{I}_N + \mathbf{S} \cdot \mathbf{D} \cdot \mathbf{S} \\ + \sum_N \mathbf{I}_N \cdot (1 - \sigma_N) \cdot \mathbf{B} + \sum_{M,N} \mathbf{I}_M \cdot (\bar{\mathbf{D}}_{MN} + \mathbf{K}_{MN}) \cdot \mathbf{I}_N \quad . \quad (3.52)$$



The last two terms in expansion (3.52) correspond to the *nuclear Zeeman* and *nuclear spin-spin coupling* terms, respectively. The following parameters are involved: the *nuclear magnetic shielding tensors*  $\sigma_N$ , which describe the magnetic shielding effects of the electrons on the nuclei; the *classical dipolar interaction tensors*  $\bar{\mathbf{D}}_{MN}$ , which describe the direct couplings of the nuclear magnetic dipole moments; and the reduced *indirect nuclear spin-spin coupling tensors*  $\mathbf{K}_{MN}$ , which describe the indirect coupling of the nuclear dipoles, mediated by the surrounding electrons. These terms are of importance in NMR but are not normally so in EPR.<sup>1</sup>

The crucial parameters of electron paramagnetic resonance are introduced in the first three terms of (3.52). The  $\mathbf{S} \cdot \mathbf{D} \cdot \mathbf{S}$  term involves the *zero field splitting tensor*  $\mathbf{D}$  that describes the electron-spin-electron-spin dipolar interaction in systems with more than one unpaired electron. Our interest in this thesis concentrates on the *electron Zeeman term*,  $\mathbf{S} \cdot \mathbf{g} \cdot \mathbf{B}$ , and the *hyperfine interaction term*,  $\mathbf{S} \cdot \mathbf{A}_N \cdot \mathbf{I}_N$ , of (3.52). The former term involves the *electronic g-tensor*  $\mathbf{g}$  that parameterizes the interaction between the total electron spin and the magnetic field; the latter term introduces the *hyperfine tensor*  $\mathbf{A}_N$  that parameterizes the interaction between the total electron spin and the magnetic nucleus  $N$ .

The tensor components can be obtained as formal second derivatives of the total energy:

The Cartesian  $uv$ -components of the  $g$ -tensor are given by

$$g_{uv} = \frac{1}{\beta_e} \frac{\partial^2 E}{\partial B_u \partial S_v} \Big|_{\mathbf{B}=\mathbf{S}=0} ; \quad (3.53)$$

the Cartesian  $uv$ -components of the  $A$ -tensor are given by

$$A_{N,uv} = \frac{\partial^2 E}{\partial I_{N,u} \partial S_v} \Big|_{\mathbf{I}_N=\mathbf{S}=0} . \quad (3.54)$$

Before giving the explicit expressions for the  $\mathbf{g}$  and  $\mathbf{A}$  tensors (Section 2.4), we will discuss the forms adopted by  $H_S$  in different media to obtain a feeling for the actual parameters. The spectral observables obtained from the resonance experiment correspond to the time average of the components of the second rank EPR tensors  $\mathbf{T} = \mathbf{g}$ ,

**A**, along the direction of the external magnetic field. The latter is chosen to be the  $z'$  axis of the laboratory coordinate system  $(x', y', z')$ .

The transformation equation for a general second rank tensor between any two Cartesian coordinate systems  $(\alpha, \beta, \gamma)$  and  $(a, b, c)$  is given by

$$T_{ab} = \sum_{\alpha\beta} \cos\theta_{\alpha a} \cos\theta_{\beta b} T_{\alpha\beta} \quad , \quad (3.55)$$

where  $\theta_{\alpha a}$  is the angle between the  $\alpha$  and  $a$  axes. From this follows that

$$T_{z'z'} = \sum_{\alpha\beta} \cos\theta_{\alpha z'} \cos\theta_{\beta z'} T_{\alpha\beta} \quad , \quad (3.56)$$

and, for the time average,

$$\langle T_{z'z'} \rangle = T_{iso} + T_{aniso} = \frac{1}{3} \sum_{\alpha} \langle T_{\alpha\alpha} \rangle + \frac{2}{3} \sum_{\alpha\beta} S_{\alpha\beta} \langle T_{\alpha\beta} \rangle \quad , \quad (3.57)$$

where  $\alpha$  and  $\beta$  denote any of the molecule-fixed coordinates  $(x, y, z)$ . The symmetric, traceless matrix **U** represents the *orientation tensor* with respect to the magnetic field

$$U_{\alpha\beta} = \frac{1}{2} \langle 3 \cos\theta_{\alpha z'} \cos\theta_{\beta z'} - \delta_{\alpha\beta} \rangle \quad , \quad (3.58)$$

that carries the information on the probability distribution of molecular orientation with respect to **B**. Equation (3.57) defines the decomposition of the EPR tensors in their *isotropic* and *anisotropic* parts,

$$T_{iso} = \frac{1}{3} \text{Tr} \mathbf{T} = \frac{1}{3} (\langle T_{xx} \rangle + \langle T_{yy} \rangle + \langle T_{zz} \rangle) \quad (3.59)$$

and

$$T_{aniso} = \frac{2}{3} \mathbf{U} \cdot \langle \mathbf{T} \rangle \quad , \quad (3.60)$$

respectively. The angle brackets in the formulas given above indicating the time averaging will be dropped throughout the following discussion.

### 3.3.2 Spin Hamiltonian Parameters from Condensed-Phase EPR

In *liquids* with low viscosity, the orientation of the molecules is not ordered and the tumbling of the molecules is isotropic. The spectral observables are reduced to their isotropic parts: the  $\mathbf{g}$  tensor to the *g-factor*<sup>12</sup> (*g-value*<sup>13</sup>)

$$g = \frac{1}{3} \text{Tr } \mathbf{g} \quad , \quad (3.61)$$

the  $\mathbf{A}$  tensor to the *isotropic hyperfine coupling constant* (HFCC)

$$A_{iso} = \frac{1}{3} \text{Tr } \mathbf{A} \quad . \quad (3.62)$$

Much more information on the spin Hamiltonian parameters can be obtained from *solid-state EPR spectroscopy*. In the ideal case, the measurement is being performed for a *single crystal sample* where the orientation of the molecules with respect to the applied magnetic field is well defined. It is often difficult to make single crystals large enough; a *powder sample* must be used then, for which the orientation of the molecules with respect to the magnetic field is not known.

For *single crystal samples*, the elements of the matrix  $(\mathbf{g} \cdot \mathbf{g}^T)$ ,  $(\mathbf{A} \cdot \mathbf{A}^T)$  can be obtained by the successive rotations of the sample with respect to the magnetic field. Any of the  $(\mathbf{g} \cdot \mathbf{g}^T)$ ,  $(\mathbf{A} \cdot \mathbf{A}^T)$  matrices can be transformed to diagonal form by moving from the laboratory coordinate system to a *principal-axes system*. Once the diagonal elements of the  $(\mathbf{g} \cdot \mathbf{g}^T)$ ,  $(\mathbf{A} \cdot \mathbf{A}^T)$  tensors in the principal-axes system, the *principal values*, are found, one wishes to obtain the matrices  $\mathbf{g}$ ,  $\mathbf{A}$  themselves. Two kinds of problems are encountered here: of matrix antisymmetry and of signs. If  $\mathbf{g}$  is an antisymmetric matrix, then its principal axes system is not an orthogonal one. Such a “true”  $\mathbf{g}$  tensor is obtainable from theory only and is not directly comparable to the symmetric tensor derived from the experimental  $(\mathbf{g} \cdot \mathbf{g}^T)$  matrix. EPR experiments on *powder samples or*

*polycrystalline substances* provide information on the isotropic and anisotropic components of the  $\mathbf{A}$  and  $\mathbf{g}$  tensors in the principal axes system as well. However, the orientation of the principal axes system with respect to the molecular framework can be obtained from *single-crystal* EPR experiments only.

Symmetry concepts are extensively applied in the interpretation of solid-state EPR spectra. From the point of view of local symmetry, three categories are used for the specification:

- (1) *Cubic*: Anisotropy of EPR properties is absent.
- (2) *Uniaxial* (often shortened as “axial”): linear rotational symmetry about a unique axis is contained; anisotropy is observable except with the field  $\mathbf{B}$  in the plane perpendicular to the unique axis. Two principal values of the  $g$  and  $A$ - tensors are equal but differ from the third one, they are conventionally labeled as  $(g_{\perp}, g_{\perp}, g_{\parallel})$ ;  $(A_{\perp}, A_{\perp}, A_{\parallel})$ .
- (3) *Rhombic*. Three unequal principal values are contained in each parameter matrix.

The solid-state measurements provide the most complete information about the spin Hamiltonian parameters. However, the environmental effects can influence the values of the parameters due to both structural and electronical effects. This complicates the comparison of our calculated data with experiment. In general, we cannot aim at a better agreement between our calculation on isolated species with condensed-phase experiment than 10-15%. This comparison is further complicated by the fact that neither solid nor liquid-state EPR measurements provide the signs of the spin Hamiltonian parameters.

### 3.3.3 Spin Hamiltonian Parameters from Gas-Phase Spectroscopy

By definition, atoms and molecules in the gas-phase differ from those in the condensed phase in that they are almost perfectly free to perform translational and rotational motion. Literally free molecular rotation does allow observation of the quantized rotational energy levels. The ensuing rotation-magnetic interactions significantly influence the spectra so that more information on spin Hamiltonian parameters can be obtained than in liquids. On the other hand, due to the complexity of

the rotational-magnetic patterns, gas-phase microwave spectra have been resolved for monoatomic, diatomic, and very simple polyatomic species only.

Most of the experimental data for the diatomics we refer to in this thesis have been obtained using the gas-phase spectroscopy. The hyperfine parameters have been determined from the analysis of the rotational level splittings. The relative positions of the energy levels were obtained either directly by monitoring the absorption/emission (“pure” microwave rotational spectroscopy) or indirectly (through fluorescence or laser beam deflection).<sup>14</sup> The accuracy of such measurements is usually very high, e.g. in the kHz range ( $\sim 1$  ppm) for the hyperfine parameters when using microwave optical double resonance.<sup>15</sup> Unlike the situation in liquids, the spin Hamiltonian parameters are not averaged by the molecular tumbling, so that, e.g., for diatomics all of the  $g_{\parallel}$ ,  $g_{\perp}$ ,  $A_{\parallel}$ ,  $A_{\perp}$  parameters can be determined. The set of total angular-momentum vectors  $\mathbf{F}$  of molecules can be thought of as randomly oriented, but each is fixed in its direction until disturbed by a collision, which is a relatively rare event on the EPR time scale in most studies. In molecular beam studies such interactions between molecules are completely absent. The quantum number  $M_F$  thus remains constant and can be measured after an external magnetic field is applied, i.e., once the quantization direction is specified.<sup>12</sup> Missing or weak intermolecular perturbations, together with the great accuracy of the measurement, make gas-phase data the most reliable for comparison with our computed data on isolated molecules. Moreover, unlike in the condensed phase, the sign of the hyperfine coupling constants is obtainable from the gas-phase experiments.

### **3.4 Perturbation Expressions for the Electron Zeeman and Hyperfine Interaction Terms**

In the preceding two sections, we have shown that it is possible, from a relativistic theory, to derive operators necessary for a complete description of the electronic Zeeman and hyperfine effects, and that these effects enter the concept of the spin Hamiltonian as the  $\mathbf{g}$  and  $\mathbf{A}$  tensors. The next step to be taken is to discuss which of the many terms of the Breit-Pauli Hamiltonian are needed for a treatment of the  $\mathbf{g}$  and  $\mathbf{A}$  tensors, and to give the explicit expressions for these parameters. Conceptually, the

simplest approach would be to determine the eigenvalues of the Schrödinger equation involving all the necessary terms of the Breit-Pauli Hamiltonian (3.22), and to calculate the  $\mathbf{g}$  and  $\mathbf{A}$  tensors using relations (3.53), (3.54). Unfortunately, even the regular time-independent Schrödinger equation without any magnetic operators can be solved exactly only for some one-electron systems. Variational approaches that are conventionally applied to find solutions for problems not involving the effects of the magnetic field<sup>2</sup> prove prohibitively difficult when many magnetic operators are required.

Since the magnetic effects are generally very small compared to the total molecular energy, it is very convenient to adopt a different, perturbational treatment. The philosophy of perturbation theory (PT) approaches is the partitioning of the total molecular Hamiltonian into a zeroth-order part ( $H_0$ ), which has known eigenfunctions and eigenvalues, and a remaining part – the perturbation ( $V$ ). The exact energy is then expressed as a sum of contributions of increasing complexity, and converges quickly if the partitioning of the Hamiltonian leaves the perturbation  $V$  small. In our case, the natural choice for  $H_0$  is the magnetic-field-free part of the total Hamiltonian, leaving the field-dependent parts to represent the perturbation  $V$ . The perturbation approach breaks the problem down into two separate tasks. The first step (that we will deal with in Chapter 3) involves a description of the field-free problem. Here we concentrate on the second step - quantifying the changes (perturbations) in the description that are induced by a magnetic field, and that enter the  $\mathbf{A}$  and  $\mathbf{g}$  tensors. We start with recapitulating the basic features of the PT approach.

### 3.4.1 Rayleigh-Schrödinger Perturbation Theory

The general problem is to solve the eigenvalue equation

$$H |\Phi_i\rangle = (H^{(0)} + V) |\Phi_i\rangle = E_i |\Phi_i\rangle \quad , \quad (3.63)$$

supposing that we have solved the electronic Schrödinger equation

$$H^{(0)} |\Psi_i^{(0)}\rangle = E_i^{(0)} |\Psi_i^{(0)}\rangle \quad (3.64)$$

for a set of eigenfunctions  $|\Psi_i^{(0)}\rangle$  (below denoted as  $|i\rangle$ ) and eigenvalues  $E_i^{(0)}$ . The exact eigenfunctions and eigenvalues of the perturbed system with Hamiltonian  $H$  can be written in terms of a Taylor series in the ordering parameter  $\lambda$ :

$$E_i = E_i^{(0)} + \lambda E_i^{(1)} + \lambda^2 E_i^{(2)} + \dots \quad (3.65)$$

$$|\Phi_i\rangle = |\Psi_i^{(0)}\rangle + \lambda |\Psi_i^{(1)}\rangle + \lambda^2 |\Psi_i^{(2)}\rangle + \dots \quad (3.66)$$

If we choose the eigenfunctions of  $H^{(0)}$  to be normalized and the wave function  $\Phi_i$  to be intermediately normalized ( $\langle i | \Phi_i \rangle = 1$ ), we obtain by multiplication of eq (3.66) by  $|i\rangle$

$$\langle i | \Phi_i \rangle = \langle i | i \rangle + \lambda \langle i | \Psi_i^{(1)} \rangle + \lambda^2 \langle i | \Psi_i^{(2)} \rangle + \dots = 1 \quad (3.67)$$

As (3.67) holds for all values of  $\lambda$ , one sees that

$$\langle i | \Psi_i^{(n)} \rangle = 0 \quad n = 1, 2, 3, \dots \quad (3.68)$$

Thus, substituting eqs (3.65), (3.66) into eq 0 and equating the coefficients of  $\lambda^n$  gives

$$E_i^{(0)} = \langle i | H^{(0)} | i \rangle \quad (3.69)$$

$$E_i^{(1)} = \langle i | V | i \rangle \quad (3.70)$$

$$E_i^{(2)} = \langle i | V | \Psi_i^{(1)} \rangle \quad (3.71)$$

The zeroth- and first-order energies are thus defined in terms of the zeroth-order wave function. Expanding  $|\Psi_i^{(1)}\rangle$  in terms of eigenfunctions of  $H^{(0)}$ , we obtain a similar expression for the second-order energy:

$$E_i^{(2)} = \sum_{n \neq i} \frac{\langle i|V|n\rangle\langle n|V|i\rangle}{E_i^{(0)} - E_n^{(0)}} \quad (3.72)$$

The details of the derivation of these and higher-order contributions can be found elsewhere.<sup>16</sup>

In section 2.3, the spin Hamiltonian parameters have been defined as energy derivatives. In non-degenerate perturbation theory, the first- and second-order energy derivatives with respect to a perturbation  $\mathbf{x}$ , known as the *first- and second-order molecular properties*, are given by

$$\frac{\partial E(\mathbf{x})}{\partial x_i} = \langle 0 | \frac{\partial H}{\partial x_i} | 0 \rangle \quad (3.73)$$

$$\frac{\partial^2 E(\mathbf{x})}{\partial x_i \partial x_j} = \langle 0 | \frac{\partial^2 H}{\partial x_i \partial x_j} | 0 \rangle + 2 \sum_{n \neq 0} \frac{\langle 0 | \frac{\partial H}{\partial x_i} | n \rangle \langle n | \frac{\partial H}{\partial x_j} | 0 \rangle}{E_0 - E_n} \quad (3.74)$$

where the derivatives are taken at  $\mathbf{x}=0$  (e.g., zero field and zero magnetic moments). The first derivative of a first-order property eq (3.73) is thus simply the expectation value of the first-order Hamiltonian (this is a consequence of the *Hellmann-Feynman theorem*) and requires only a knowledge of the unperturbed state  $|0\rangle$ . The second derivative of the second order property eq (3.74) contains an expectation-value term analogous to the first-order properties but also a sum-over-states contribution from each excited state  $|n\rangle$  of energy  $E_n$ . For magnetic properties, the expectation-value contribution to the second-order property is known as the *diamagnetic* part, the sum-over-states contribution is referred to as the *paramagnetic* part.<sup>17</sup> To arrive at the explicit expressions for  $A$  and  $g$ -tensors, we must consider the relevant terms of the Breit-Pauli Hamiltonian, as we do in the next section.



### 3.4.2 Operators Relevant for the Electron Zeeman Effect and for the Hyperfine Interaction

In order to establish a connection between the terms of the Breit-Pauli Hamiltonian (3.22) and the parameters of the spin Hamiltonian (3.52), the form of the latter operator should be discussed briefly. We first note that (3.52) contains only terms bilinear in the magnetic operators  $\mathbf{B}$ ,  $\mathbf{I}$ , and  $\mathbf{S}$ . No terms linear in (only one of the)  $\mathbf{B}$ ,  $\mathbf{I}$ , or  $\mathbf{S}$  are involved, as any of the corresponding operators is pure imaginary and is characteristic of the spatial components of time-odd interactions. The requirement of time-reversal invariance of the nonvanishing energy terms thus enforces the absence of terms linear in  $\mathbf{B}$ ,  $\mathbf{I}$ , or  $\mathbf{S}$  from the spin Hamiltonian. The exclusion of terms involving powers higher than second of  $\mathbf{B}$ ,  $\mathbf{I}$ , and  $\mathbf{S}$  or their combination from the spin Hamiltonian is not rigorous, but is a convenient and usually good approximation.<sup>1</sup> Such terms would clearly arise if we went higher than to second order in perturbation theory. In order to retain gauge invariance of the results for both the  $\mathbf{g}$  and the  $\mathbf{A}$  tensor, it is necessary to include all relevant contributions to these tensors up to a certain order of the fine-structure constant  $\alpha$ . Below, we give the operators of the Breit-Pauli Hamiltonian relevant for the 2<sup>nd</sup>-order perturbation theory expressions up to  $O(\alpha^2)$  for both the  $\mathbf{g}$ - and the  $\mathbf{A}$ -tensor, including also the spin-orbit terms ( $\sim O(\alpha^4)$ ) for the latter.

The main contribution to the  $\mathbf{g}$ -tensor up to  $O(\alpha^2)$  involves the *electron Zeeman interaction*  $H_3^e$ , given by (3.25). The part of  $H_3^e$  that depends on  $\mathbf{s}_i$  and  $\mathbf{B}(i)$  only (corresponding to the term “1” in the brackets following the summation)

$$H_{SZ} = g_e \beta_e \sum_i \mathbf{s}_i \cdot \mathbf{B} \quad (3.75)$$

is usually referred to as the *spin-Zeeman operator*. The part corresponding to the field-independent part of  $\pi_i$

$$H_{RMC-SZ} = -\frac{g_e \beta_e}{2m_e^2 \kappa_0 c^2} \sum_i p_i^2 \mathbf{s}_i \cdot \mathbf{B} \quad (3.76)$$

is called the *spin-Zeeman relativistic mass correction operator*, where  $p_i^2 = \mathbf{p}_i \cdot \mathbf{p}_i$  is the square of linear momentum operator for electron  $i$ . Both  $H_{SZ}$  and  $H_{RMC-SZ}$  give first-order contributions to the electronic  $g$ -tensor.  $H_{SZ}$  results in the free-electron  $g$ -tensor ( $g_e \mathbf{1}$ ), whereas  $H_{RMC-SZ}$  contributes in first order to the  $\Delta \mathbf{g}$  tensor that is defined as

$$\Delta \mathbf{g} = \mathbf{g} - g_e \mathbf{1} \quad . \quad (3.77)$$

The main second-order contributions to both the  $g$ - and  $A$ -tensors (and the dominant contributions to the components  $\Delta \mathbf{g}$ , the  $g$ -shifts) arise from the one-electron spin-orbit interaction term ( $H_5^{eN}$ ) of the Breit-Pauli Hamiltonian.  $H_5^{eN}$  involves the field-dependent momentum  $\pi_i$ , and, for the purposes of practical calculations, it is necessary to expand it into field-dependent and field-independent parts. By retaining only the field-independent part of  $\pi_i$ ,  $H_5^{eN}$  reduces to

$$H_{SO(1e)} = \frac{2g_e\beta_e^2}{\hbar\kappa_0c^2} \sum_N Z_N \sum_i \frac{\mathbf{s}_i \cdot \mathbf{l}_{iN}}{r_{iN}^3} \quad . \quad (3.78)$$

$H_{SO(1e)}$  thus describes the interaction between the spin  $g_e\beta_e\mathbf{s}_i$  and orbital  $\beta_e\mathbf{l}_{iN}$  magnetic moments of the electron. The angular momentum operators  $\mathbf{l}_{iN}$ ,  $\mathbf{l}_{iO}$ , and  $\mathbf{l}_{ij}$  employed here and below for the sake of shortening the expressions are defined in the following fashion:

$$\mathbf{l}_{iN} = \mathbf{r}_{iN} \times \mathbf{p}_i \quad (3.79)$$

and correspond to the different vectors defined in eqs (3.48)-(3.50). It is the term (3.78), rather than eq (3.28), which is normally equated with the concept of the *one-electron spin-orbit coupling*, and we will retain such a naming throughout this thesis.

The other part of  $H_5^{eN}$ , involving the field-dependent part of  $\pi_i$ , is given by

$$H_{GC-SO(1e)} = -\frac{g_e\beta_e^2e}{2\hbar\kappa_0c^2} \sum_N Z_N \sum_i \frac{[\mathbf{s}_i \cdot \mathbf{B}(\mathbf{r}_{iN} \cdot \mathbf{r}_{iO}) - \mathbf{s}_i \cdot \mathbf{r}_{iN} (\mathbf{r}_{iO} \cdot \mathbf{B})]}{r_{iN}^3} \quad . \quad (3.80)$$

Due to its origin in  $H_5^{eN}$ , the  $H_{GC-SO(1e)}$  term may be regarded as the portion of the spin-orbit coupling which is dependent on the external field  $\mathbf{B}$ , and is called the *one-electron spin-orbit gauge correction*.<sup>18</sup> *Gauge correction* refers to the dependence of this term on the origin  $O$  of the computational coordinate system.  $H_{GC-SO(1e)}$  contributes in the first order PT to the electronic  $g$ -tensor.

From equation (3.32), it is possible to derive the two-electron analogues of  $H_{SO(1e)}$  and  $H_{GC-SO(1e)}$  - the *two-electron spin-orbit coupling term*

$$H_{SO(2e)} = -\frac{g_e \beta_e^2}{\hbar \kappa_0} \sum_{ij} \frac{(\mathbf{s}_i + 2\mathbf{s}_j) \cdot \mathbf{l}_{ij}}{r_{ij}^3}, \quad (3.81)$$

and the *two-electron spin-orbit gauge correction term*

$$H_{GC-SO(2e)} = \frac{g_e \beta_e^2 e}{2\hbar \kappa_0 c^2} \sum_{ij} \frac{[(\mathbf{s}_i + 2\mathbf{s}_j) \cdot \mathbf{B}](\mathbf{r}_{ij} \cdot \mathbf{r}_{iO}) - [(\mathbf{s}_i + 2\mathbf{s}_j) \cdot \mathbf{r}_{ij}](\mathbf{r}_{iO} \cdot \mathbf{B})}{r_{ij}^3}. \quad (3.82)$$

These terms may be regarded as conceptually identical to their one-electron analogues (3.78), (3.80). In this case, however, the magnetic interactions take place under an electric field arising from electron-electron Coulomb repulsion, rather than electron-nuclear attraction. The corresponding one- and two-electron terms thus have opposite signs.  $H_{SO(2e)}$  - analogously to  $H_{SO(1e)}$  - gives second-order contributions to both the  $g$ - and  $A$ -tensors;  $H_{GC-SO(2e)}$  - like  $H_{GC-SO(1e)}$  - contributes to the  $g$ -tensor in the first order.

The second-order contributions to the  $g$ -tensor involving  $H_{SO(1e)}$  and  $H_{SO(2e)}$  arise as cross terms between any of the spin-orbit operators and the *orbital Zeeman operator*

$$H_{OZ} = -\frac{e}{m_e} \sum_i \mathbf{A}(\mathbf{r}_i) \cdot \mathbf{p}_i = -\frac{\beta_e}{\hbar} \mathbf{B} \sum_i \mathbf{l}_{iO}. \quad (3.83)$$

$H_{OZ}$  is obtained from the operator  $H_1^e$  upon the expansion of the field-dependent momentum  $\pi$  (cf. (3.8)).<sup>3</sup> It reflects the interaction between the external field  $\mathbf{B}$  and the orbital magnetic moment  $\boldsymbol{\mu}_l = \beta_e \mathbf{l}$ .

The dominant, first-order contributions to the  $A$ -tensor are the *Fermi-contact operator* corresponding to nucleus  $N$  (from  $H_3^{eN}$ , (3.44))

$$H_{FC}^N = \frac{8\pi}{3} \frac{g_e g_N \beta_e \beta_N}{\kappa_0 c^2} \sum_i \delta(\mathbf{r}_{iN}) \mathbf{s}_i \cdot \mathbf{I}_N \quad , \quad (3.84)$$

and the *spin-dipolar operator* (from  $H_2^{eN}$ , (3.43))

$$H_{SD}^N = \frac{g_e g_N \beta_e \beta_N}{\kappa_0 c^2} \sum_i \mathbf{s}_i \cdot \frac{3\mathbf{r}_{iN} \mathbf{r}_{iN} - \mathbf{1} r_{iN}^2}{r_{iN}^5} \cdot \mathbf{I}_N \quad . \quad (3.85)$$

If second-order contributions to the  $A$ -tensor are to be considered, then for consistency certain additional but small first-order contributions should be included. These are analogous to the “gauge correction” terms contributing to  $\Delta \mathbf{g}$  but with the vector potential due to the nuclear moment replacing that due to the uniform external field. The vector potential due to the magnetic nucleus  $N$  is given by

$$\mathbf{A}_N(\mathbf{r}_i) = \frac{g_N \beta_N}{\kappa_0 c^2} \frac{\mathbf{I}_N \times \mathbf{r}_{iN}}{r_{iN}^3} \quad . \quad (3.86)$$

From the 1-electron part of the spin-orbit (SO) Hamiltonian  $H_5^{eN}$ , cf. eq (3.46), we obtain *the one-electron spin-orbit hyperfine correction term*

$$H_{HC-SO(1e)}^N = \frac{e}{2m_e} \frac{g_e g_N \beta_e \beta_N}{\kappa_0^2 c^4} \sum_i \sum_{N,N'}' \frac{Z_{N'}}{r_{iN}^3 r_{iN'}^3} \times [(\mathbf{r}_{iN} \cdot \mathbf{r}_{iN'}) (\mathbf{s}_i \cdot \mathbf{I}_N) - (\mathbf{s}_i \cdot \mathbf{r}_{iN'}) (\mathbf{I}_N \cdot \mathbf{r}_{iN})] \quad . \quad (3.87)$$

From the spin-spin and the spin-other-orbit parts of the 2-electron SO Hamiltonian  $H_9^e$ , cf. eq (3.32), arise the *spin-spin-orbit hyperfine correction term*

$$H_{HC-SSO}^N = \frac{e}{2m_e} \frac{g_e g_N \beta_e \beta_N}{\kappa_0^2 c^4} \sum_{i,j}' \sum_N \frac{1}{r_{ij}^3 r_{iN}^3} \times [(\mathbf{r}_{ji} \cdot \mathbf{r}_{iN}) (\mathbf{s}_i \cdot \mathbf{I}_N) - (\mathbf{s}_i \cdot \mathbf{r}_{iN}) (\mathbf{I}_N \cdot \mathbf{r}_{ji})] \quad , \quad (3.88)$$

and the *spin-other-orbit hyperfine correction term*

$$H_{HC-SOO}^N = \frac{e}{2m_e} \frac{g_e g_N \beta_e \beta_N}{\kappa_0^2 c^4} \sum_{i,j} \sum_N \frac{1}{r_{ij}^3 r_{iN}^3} \times [(\mathbf{r}_{ji} \cdot \mathbf{r}_{jN})(\mathbf{s}_i \cdot \mathbf{I}_N) - (\mathbf{r}_{ji} \cdot \mathbf{I}_N)(\mathbf{r}_{jN} \cdot \mathbf{s}_i)] \quad . \quad (3.89)$$

The latter two terms are usually treated together as the two-electron hyperfine correction term

$$H_{HC-SO(2e)}^N = H_{HC-SOO}^N + H_{HC-SOO}^N \quad . \quad (3.90)$$

Second-order contributions to the hyperfine tensor arise as cross-terms between any of the spin-orbit operators (3.78), (3.81), and the *paramagnetic nuclear spin - electron orbit operator*

$$H_{PSO}^N = \frac{e}{m_e} \frac{g_N \beta_N}{\kappa_0 c^2} \sum_i \frac{\mathbf{l}_{iN}}{r_{iN}^3} \quad . \quad (3.91)$$

$H_{PSO}^N$  is obtained by expanding the kinetic-energy term  $H_1^e$ , cf. eq (3.24), considering the contribution given by the magnetic dipole of the nucleus  $N$  to the field-dependent momentum  $\pi$ .

To summarize, the second-order expressions for the  $g$ -tensor up to  $O(\alpha^2)$  involve the following 7 operators:<sup>1,3</sup> the spin-Zeeman operator  $H_{SZ}$ , the spin-Zeeman relativistic mass correction operator  $H_{RMC-SZ}$ , the one-electron and the two-electron gauge correction terms  $H_{GC-SO(1e)}$ ,  $H_{GC-SO(2e)}$ , the one-electron and the two-electron spin-orbit coupling operators  $H_{SO(1e)}$ ,  $H_{SO(2e)}$ , and the orbital Zeeman operator  $H_{OZ}$ . First-order contributions are given by  $H_{SZ}$ ,  $H_{RMC-SZ}$ ,  $H_{GC-SO(1e)}$  and  $H_{GC-SO(2e)}$ , second-order contributions arise from cross-terms between  $H_{OZ}$  and any of the  $H_{SO(1e)}$ ,  $H_{SO(2e)}$  terms.

The second-order expressions for the  $A$ -tensor up to  $O(\alpha^2)$  including the spin-orbit terms up to  $O(\alpha^4)$  involve the Fermi-contact operator  $H_{FC}^N$ , the spin-dipolar operator  $H_{SD}^N$ , the one-electron and the two-electron spin-orbit hyperfine correction terms  $H_{HC-SO(1e)}^N$  and  $H_{HC-SO(2e)}^N$ , the one-electron and the two-electron spin-orbit coupling

operators  $H_{SO(1e)}$ ,  $H_{SO(2e)}$ , and the paramagnetic nuclear spin - electron orbit operator  $H_{PSO}^N$ .

### 3.4.3 Perturbation-Theory Expressions for the Electronic $g$ -Tensor

As discussed above, the perturbation  $V$  is in the case of  $g$ -tensor calculations given by

$$V = H_{SZ} + H_{RMC-SZ} + H_{GC-SO(1e)} + H_{GC-SO(2e)} + H_{SO(1e)} + H_{SO(2e)} + H_{OZ} . \quad (3.92)$$

The perturbation treatment can be simplified as follows:

- (1) The 0<sup>th</sup> order contribution  $E_i^{(0)}$  does not contribute to the Zeeman splitting and can thus be ignored.
- (2) It can be shown that the operators  $H_{SO(1e)}$ ,  $H_{SO(2e)}$ , and  $H_{OZ}$  do not contribute to  $E_i^{(1)}$ .<sup>1,3</sup> The first-order perturbation can thus be written as

$$V^{(1)} = H_{SZ} + H_{RMC-SZ} + H_{GC-SO(1e)} + H_{GC-SO(2e)} . \quad (3.93)$$

- (3) Recall that we look for contributions to the Zeeman splitting bilinear in the magnetic field  $\mathbf{B}$  and effective electronic spin  $\mathbf{S}$ . We can therefore exclude from the 2<sup>nd</sup>-order contributions operators  $H_{SZ}$ ,  $H_{RMC-SZ}$ ,  $H_{GC-SO(1e)}$  and  $H_{GC-SO(2e)}$ , which have quadratic dependence on  $\mathbf{S}$  or  $\mathbf{B}$ . Thus,

$$V^{(2)} = H_{SO(1e)} + H_{SO(2e)} + H_{OZ} . \quad (3.94)$$

The requirement of the bilinearity in  $\mathbf{B}$  and  $\mathbf{S}$  further restricts the 2<sup>nd</sup>-order contributions to two cross terms: between  $H_{SO(1e)}$  and  $H_{OZ}$ , and between  $H_{SO(2e)}$  and  $H_{OZ}$ .

The second-order expressions up to  $O(\alpha^2)$  for the  $g$ -tensor components can be obtained using the expression (3.74) for second-order molecular properties. We recall that the spin-Zeeman operator  $H_{SZ}$  results in the free-electron  $g$ -tensor ( $g_e \mathbf{1}$ ) and does

not contribute to the  $g$ -shifts. The Cartesian  $uv$ -components of the  $\Delta\mathbf{g}$  tensor involve contributions from the spin-Zeeman relativistic mass correction operator  $H_{RMC-SZ}$

$$\Delta\mathbf{g}_{RMC-SZ,uv}^{(1)} = -\frac{g_e\beta_e}{2m_e^2\kappa_0c^2}\delta_{uv}\langle 0|\sum_i(-\frac{1}{2}\nabla_i^2)s_{iz}|0\rangle, \quad (3.95)$$

the one-electron gauge correction term  $H_{GC-SO(1e)}$

$$\Delta\mathbf{g}_{GC-SO(1e),uv}^{(1)} = -\frac{g_e\beta_e^2e}{2\hbar\kappa_0c^2}\frac{1}{\langle S_Z\rangle}\sum_N Z_N\langle 0|\sum_i\frac{r_{iN}^2\delta_{uv}-(\mathbf{r}_{iN})_u(\mathbf{r}_{iN})_v}{r_{iN}^3}s_{iz}|0\rangle, \quad (3.96)$$

the two-electron gauge correction term  $H_{GC-SO(2e)}$

$$\Delta\mathbf{g}_{GC-SO(2e),uv}^{(1)} = \frac{g_e\beta_e^2e}{2\hbar\kappa_0c^2}\frac{1}{\langle S_Z\rangle}\langle 0|\sum_{ij}\frac{\mathbf{r}_{ij}\cdot(2\mathbf{r}_j-\mathbf{r}_i)\delta_{uv}-(2\mathbf{r}_j-\mathbf{r}_i)_u(\mathbf{r}_{ij})_v}{r_{ij}^3}s_{iz}|0\rangle, \quad (3.97)$$

the cross terms between the one-electron spin-orbit coupling operator  $H_{SO(1e)}$  and the orbital Zeeman operator  $H_{OZ}$

$$\Delta\mathbf{g}_{SO/OZ(1e),uv}^{(2)} = \frac{2g_e\beta_e^3}{\hbar^2\kappa_0c^2}\frac{1}{\langle S_Z\rangle}\sum_N Z_N\sum_n\left\{\frac{\langle 0|\sum_i\frac{1}{r_{iN}^3}\times(\mathbf{l}_{iN})_us_{iz}|n\rangle\langle n|\sum_j(\mathbf{l}_{jN})_v|0\rangle}{E_0^{(0)}-E_n^{(0)}}+\text{c.c.}\right\}, \quad (3.98)$$

and the cross terms between the two-electron spin-orbit coupling operator  $H_{SO(2e)}$  and the orbital Zeeman operator  $H_{OZ}$

$$\Delta\mathbf{g}_{SO/OZ(2e),uv}^{(2)} = \frac{2g_e\beta_e^3}{\hbar^2\kappa_0c^2}\frac{1}{\langle S_Z\rangle}\sum_N Z_N\sum_n\left\{\frac{\langle 0|\sum_{ij}[\mathbf{r}_{ij}\times(\nabla_i-2\nabla_j)]_us_{iz}|n\rangle\langle n|\sum_k(\mathbf{r}_k\times\nabla_k)_v|0\rangle}{E_0^{(0)}-E_n^{(0)}}+\text{c.c.}\right\}, \quad (3.99)$$

where “+ c.c.” indicates addition of the complex conjugate of the preceding term.

The total result for  $\Delta g_{uv}$  up to  $O(\alpha^2)$  is the sum of contributions

$$\Delta g_{uv} = \Delta g_{RMC-SZ,uv}^{(1)} + \Delta g_{GC-SO(1e),uv}^{(1)} + \Delta g_{GC-SO(2e),uv}^{(1)} + \Delta g_{SO/OZ(1e),uv}^{(2)} + \Delta g_{SO/OZ(2e),uv}^{(2)} \quad (3.100)$$

In the application calculations reported in this thesis, all contributions given in (3.100) except for  $\Delta g_{GC-SO(2e),uv}^{(1)}$  have been included. The latter term has been neglected due to its general smallness (see refs 3 and 19) and the lack of computationally efficient approximations thereto.

### 3.4.4 Perturbation-Theory Expressions for the $A$ -Tensor

The perturbation  $V$  is in the case of  $A$ -tensor calculations given by

$$V = H_{FC}^N + H_{SD}^N + H_{HC-SO(1e)}^N + H_{HC-SO(2e)}^N + H_{SO(1e)}^N + H_{SO(2e)}^N + H_{PSO}^N \cdot \quad (3.101)$$

Along similar lines as for the  $g$ -tensor, the first- and second-order contributions to the  $A$ -tensor up to  $O(\alpha^2)$  including the spin-orbit terms up to  $O(\alpha^4)$  can be obtained.

The contribution from the Fermi-contact hyperfine operator  $H_{FC}^N$  is given by

$$A_{FC,uv}^{N(1)} = \frac{8\pi}{3} \frac{g_e g_N \beta_e \beta_N}{\kappa_0 c^2} \frac{1}{\langle S_Z \rangle} \langle 0 | \sum_i \delta(\mathbf{r}_{iN}) s_{iz} | 0 \rangle. \quad (3.102)$$

The contribution of the spin-dipolar hyperfine operator  $H_{SD}^N$  is equal to

$$A_{SD,uv}^{N(1)} = \frac{g_e g_N \beta_e \beta_N}{\kappa_0 c^2} \frac{1}{\langle S_Z \rangle} \langle 0 | \sum_i \frac{\delta_{uv}(\mathbf{r}_{iN}^2) - 3(\mathbf{r}_{iN})_u(\mathbf{r}_{iN})_v}{r_{iN}^5} s_{iz} | 0 \rangle. \quad (3.103)$$

The one-electron spin-orbit hyperfine correction term  $H_{HC-SO(1e)}^N$  contributes as

$$A_{HC-SO(1e),uv}^{N(1)} = \frac{e}{2m_e} \frac{g_e g_N \beta_e \beta_N}{\kappa_0^2 c^4} \frac{1}{\langle S_Z \rangle} \langle 0 | \sum_i \sum_{N'(\neq N)} \frac{Z_{N'}}{r_{iN}^3 r_{iN'}^3} \times [(\mathbf{r}_{iN} \cdot \mathbf{r}_{iN'}) \delta_{uv} - (\mathbf{r}_{iN})_u (\mathbf{r}_{iN'})_v] s_{iz} | 0 \rangle. \quad (3.104)$$



The two-electron spin-orbit hyperfine correction term  $H_{HC-SO(2e)}^N$  (cf. eq (3.90)) contributes as

$$A_{HC-SO(2e),uv}^{N(1)} = \frac{e}{2m_e} \frac{g_e g_N \beta_e \beta_N}{\kappa_0^2 c^4} \frac{1}{\langle S_Z \rangle} \cdot \langle 0 | \sum_{i,j} ' \frac{1}{r_{ij}^3 r_{iN}^3} \times [\mathbf{r}_{ij} \cdot (2\mathbf{r}_{jN} - \mathbf{r}_{iN}) \delta_{uv} - (2\mathbf{r}_{jN} - \mathbf{r}_{iN})_u (\mathbf{r}_{iN})_u (\mathbf{r}_{ij})_v] s_{jz} | 0 \rangle. \quad (3.105)$$

Finally, two second-order contributions to the  $A$ -tensor are obtained as cross terms between any of the spin-orbit operators  $H_{SO(1e)}$ ,  $H_{SO(2e)}$ , and the paramagnetic nuclear spin - electron orbit operator  $H_{PSO}^N$ :

$$A_{SO(1e)/PSO,uv}^{N(2)} = \frac{e}{m_e} \frac{2g_e g_N \beta_e^2 \beta_N}{\hbar \kappa_0^2 c^4} \frac{1}{\langle S_Z \rangle} \cdot \sum_n \left\{ \frac{\langle 0 | \sum_i \sum_{N'} Z_{N'} \frac{1}{r_{iN'}^3} (\mathbf{1}_{iN'})_u \times s_{jz} | n \rangle \langle n | \sum_j \frac{1}{r_{jN}^3} (\mathbf{1}_{jN})_v | 0 \rangle}{E_0^{(0)} - E_n^{(0)}} + \text{c.c.} \right\}, \quad (3.106)$$

$$A_{SO(2e)/PSO,uv}^{N(2)} = \frac{e}{m_e} \frac{2g_e g_N \beta_e^2 \beta_N}{\hbar \kappa_0^2 c^4} \frac{1}{\langle S_Z \rangle} \cdot \sum_n \left\{ \frac{\langle 0 | \sum_{i,j} ' \frac{1}{r_{ij}^3} [\mathbf{r}_{ij} \times (2\nabla_i - \nabla_j)]_u \times s_{jz} | n \rangle \langle n | \sum_k \frac{1}{r_{kN}^3} (\mathbf{1}_{kN})_v | 0 \rangle}{E_0^{(0)} - E_n^{(0)}} + \text{c.c.} \right\}. \quad (3.107)$$

The total result for  $A_{uv}^N$  up to  $O(\alpha^2)$  including the spin-orbit terms up to  $O(\alpha^4)$  is the sum of contributions

$$A_{uv}^N = A_{FC,uv}^{N(1)} + A_{SD,uv}^{N(1)} + A_{HC-SO(1e),uv}^{N(1)} + A_{HC-SO(2e),uv}^{N(1)} + A_{SO(1e)/PSO,uv}^{N(2)} + A_{SO(2e)/PSO,uv}^{N(2)}. \quad (3.108)$$

The density-functional calculations of the  $A$ -tensor reported in this thesis are nonrelativistic. Only the Fermi-contact contribution  $A_{FC,uv}^{N(1)}$  and the spin-dipolar

contribution  $A_{SD,uv}^{N(1)}$  have thus been included. Rough semiempirical estimates of spin-orbit contributions to the HFCCs has been obtained along the perturbation theoretical approach of Abragam and Pryce.<sup>20</sup>

### 3.5 Qualitative and Semi-Quantitative Relationships between the Spin Hamiltonian Parameters and Electronic Structure

The phenomenon of hyperfine coupling is often considered to be the most important interaction in EPR spectroscopy. This is mainly due to a very simple qualitative connection between the hyperfine tensor components and the electronic and geometrical structure of the paramagnetic species. First-order contributions to the hyperfine tensor directly reflect the spin density at the point of the magnetic nucleus (isotropic part) and the anisotropy of the spin density distribution in the proximity of the magnetic nucleus (anisotropic part). The spin density distribution throughout the molecule is dominated by the direct contribution of the singly-occupied molecular orbital(s) (SOMO). For many transition-metal complexes, the SOMOs are mainly – if not for symmetry reasons purely – metal  $d$  orbitals. As a result, the direct contribution to the  $A_{\text{iso}}$  given by the SOMOs is negligible, and negative spin density arises at the nucleus due to the spin polarization of the doubly occupied molecular orbitals. When significant admixture of the outer  $s$  orbital into the SOMO occurs, the spin density at the nucleus may become positive. Simple semi-quantitative estimates of the  $s$  character of the SOMO from the  $A_{\text{iso}}$  are often employed that are based on known values of spin-polarization and direct contributions to the hyperfine coupling for unit occupations of metal  $d$  and  $s$  orbitals, respectively.<sup>21</sup> Estimates of the  $d$  character of the SOMO are being obtained from the anisotropic hyperfine tensor components, completely neglecting the spin polarization contributions to the hyperfine coupling anisotropy.<sup>21,22,23</sup> Such estimates are very useful for establishing simple *qualitative* bonding schemes from the spin Hamiltonian parameters, or vice versa. As we discuss in Chapter 7, any *quantitative* usage of such orbital composition estimates should be used with great care.

The interpretation of electronic  $g$ -tensor components is more complex. The dominant contributions to  $g$ -shifts are given by the SO coupling.<sup>3,24</sup> Thus, not only the

composition of the singly-occupied orbital, but also compositions and relative energies of the virtual and doubly-occupied orbitals determine the  $g$ -tensor. The definitive work in understanding spin Hamiltonian parameters of transition metal complexes on the basis of the crystal-field theory has been done by Abragam and Pryce<sup>20</sup> and by Abragam and Bleaney.<sup>5</sup> This approach is very informative and useful when very ionic complexes, especially in sites of very high symmetry, are involved. The interest of the author in Chapter 8 was rather in understanding  $g$ - and  $A$ -tensor components for less symmetrical complexes, where both  $\sigma$  and  $\pi$  bonding plays an important role. The most suitable way to obtain such understanding, and to relate it to the results of quantum chemical calculations, is the molecular orbital approach discussed in great detail by Mabbs and Collison<sup>6</sup> that is introduced briefly in Chapter 8. This approach also enables us to make a rough semiempirical estimate of SO to the hyperfine coupling that are not accounted for yet in our present DFT calculations of HFCCs.

## References

---

- <sup>1</sup> Harriman, J. E. *Theoretical Foundations of Electron Spin Resonance*, Academic Press: New York, 1978.
- <sup>2</sup> McWeeny, R. *Methods of Molecular Quantum Mechanics*, Academic Press: New York, 1996.
- <sup>3</sup> Lushington, G. H. Ph.D. Thesis, The University of New Brunswick, Canada, 1996.
- <sup>4</sup> Vaara, J; Dissertation; Report Series in Physical Sciences 7; University of Oulu Press: Oulu, 1997.
- <sup>5</sup> Abragam, A.; Bleaney, B. *Electron Paramagnetic Resonance of Transition Ions*; Clarendon Press: Oxford, 1970.
- <sup>6</sup> Mabbs, F. E.; Collison, D. *Electron Paramagnetic Resonance of d Transition Metal Compounds*, Elsevier: Amsterdam, 1992.
- <sup>7</sup> Gerlach, W.; Stern, O. *Z. Phys.* **1922**, 9, 349.
- <sup>8</sup> Uhlenbeck, G.; Goudsmit, S.; *Naturwiss.* **1925**, 13, 593; *Nature* **1926**, 117, 263.
- <sup>9</sup> Pauli, W. *Z. Phys.* **1927**, 43, 601.
- <sup>10</sup> Dirac, P. A. M. *Proc. Roy. Soc. (London)* **1928**, A117, 610.
- <sup>11</sup> Maxwell, J. C. *Phil. Trans. Roy. Soc. (London)* **1865**, 155.
- <sup>12</sup> Weil, J. A.; Bolton, J. R.; Wertz, J. E.; *Electron Paramagnetic Resonance: Elementary Theory and Practical Applications*, Willey & Sons: New York, 1994.
- <sup>13</sup> Atherton, N. M. *Principles of Electron Spin Resonance*, Prentice Hall: New York, 1993.
- <sup>14</sup> Carrington, A. *Microvawe Spectroscopy of Free Radicals*; Academic Press: New York, 1974.
- <sup>15</sup> Childs, W. J. *Phys. Reports* **1992**, 211, 114. Childs, W. J.; Steimle, T. C. *J. Phys. Chem.* **1988**, 88, 6168. Fletcher, D. A.; Surlock, C. T.; Jung, K. Y.; Steimle, T. C. *J. Chem. Phys.* **1993**, 99, 4288.
- <sup>16</sup> Szabo, A.; Ostlund, N. S. *Modern Quantum Chemistry*, Dover: Mineola, NY, 1996.
- <sup>17</sup> Helgaker, T.; Jaszunski, M.; Ruud, K. *Chem. Rev.* **1999**, 99, 293.

- 
- <sup>18</sup> This gauge-correction term is also related to the spin-Zeeman interaction, cf. ref 3.
- <sup>19</sup> Schreckenbach, G.; Ziegler, T. *J. Phys. Chem. A* **1997**, *101*, 3388.
- <sup>20</sup> Abragam, A.; Pryce, M. H. L. *Proc. Roy. Soc. A.* **1951**, *205*, 135.
- <sup>21</sup> Symons, M. C. R. *Chemical and Biochemical Aspects of Electron-Spin Resonance Spectroscopy*; Van Nostrand: New York, 1978.
- <sup>22</sup> Varberg, T. D.; Field, R. W.; Merer, A. J. *J. Chem. Phys.* **1991**, *95*, 1563.
- <sup>23</sup> Balfour, W. J. Merer, A. J.; Niki, H. *J. Chem. Phys.* **1993**, *99*, 3288.
- <sup>24</sup> Lushington, G. H.; Grein, F. *Theor. Chimica Acta* **1996**, *93*, 259. Bruna, P.; Lushington, G. H.; Grein, F. *Chem. Phys.* **1997**, *225*, 1.



*It seems that if one is working from the point of view of getting beauty in one's equations, and if one has really a sound insight, one is on a sure line of progress.*

*Paul Adrien Maurice Dirac (1902-84)*

## 4 Computational Methods

In the previous Chapter, the electronic  $g$ -tensor and the hyperfine  $A$ -tensor have been related to the field-free description of the system's electronic structure. In this respect, a crucial role is played by the molecular ground state  $|0\rangle$  that is needed for determining both the first-order, diamagnetic contributions and, as a reference state, also the second-order, paramagnetic contributions to the spin-Hamiltonian parameters. This chapter provides an overview of *ab initio* computational methods used in this thesis for obtaining the field-free description of the molecular ground state. First, the Hartree-Fock approach is introduced as a basic one-electron approximation and discussed in both its spin-restricted and spin-unrestricted forms for open-shell systems. Then, the philosophy of the post-Hartree-Fock approaches is discussed for the cases of the Configuration Interaction (CI) and the Coupled Cluster (CC) methods. The crucial concept of spin polarization is introduced at two levels: at the spin-unrestricted one-electron (unrestricted Hartree-Fock) level, and at the spin-restricted correlated level (CI based on a spin-restricted reference wave function). Next, the theorems of the density-functional theory and the Kohn-Sham approach are presented, followed by a discussion of the various exchange-correlation functionals. Finally, basis sets and the pseudopotential approximation used in the present applications are described. The discussion of the wave function approaches in this Chapter is based on refs 1,2 and 3, that of the density functional approaches on refs 4 and 5.

## 4.1 Approximations to the Solution of the Schrödinger Equation

The starting point for a nonrelativistic quantum mechanical description of stationary molecular properties is the time-independent Schrödinger equation

$$H \Psi(\mathbf{r}_i, \mathbf{R}_N) = E \Psi(\mathbf{r}_i, \mathbf{R}_N), \quad (4.1)$$

where the Hamiltonian operator for a system of electrons and nuclei described by position vectors  $\mathbf{r}_i$  and  $\mathbf{R}_N$ , respectively, is

$$H^{(0)} = -\sum_i \frac{1}{2} \nabla_i^2 - \sum_N \frac{1}{2M_N} \nabla_N^2 - \sum_i \sum_N \frac{Z_N}{r_{iN}} + \sum_i \sum_{j>i} \frac{1}{r_{ij}} + \sum_N \sum_{M>N} \frac{Z_M Z_N}{R_{MN}}. \quad (4.2)$$

The exact solution of the Schrödinger equation requires a complete description of the interparticle interactions and is impossible for systems with more than two particles. The central issue of quantum chemistry is thus an approximation of the many particle problem by a set of single-particle problems, often followed by a subsequent inclusion of many-particle interactions using variational or perturbational techniques. The first common step in such reduction is the Born-Oppenheimer approximation, which separates the fast electronic movements from the slow nuclear movements by supposing that one can consider the electrons to be moving in the field of fixed nuclei. The true molecular wave function is then approximated as

$$\psi(q_i; q_N) = \psi_e(q_i; q_N) \psi_N(q_N), \quad (4.3)$$

where  $q_i$  and  $q_N$  stand for the electronic and nuclear coordinates, respectively, and  $\psi_e$  is the eigenstate of the electronic Hamiltonian

$$H_{elec}^{(0)} = -\sum_i \frac{1}{2} \nabla_i^2 - \sum_i \sum_N \frac{Z_N}{r_{iN}} + \sum_i \sum_{j>i} \frac{1}{r_{ij}}. \quad (4.4)$$

This leaves us with an electronic Schrödinger equation



$$H_{elec}^{(0)} \Psi_{elec}(\mathbf{r}_i, \mathbf{R}_N) = E_{elec} \Psi_{elec}(\mathbf{r}_i, \mathbf{R}_N), \quad (4.5)$$

where the Hamiltonian  $H_{elec}^{(0)}$  has only a parametric dependence on the nuclear positions.

## 4.2 The Hartree-Fock Approximation

### 4.2.1 The Hartree Approximation

The electronic Schrödinger equation (4.5) for many-electron atoms and molecules cannot be solved analytically. The mathematical difficulties are brought about by the last term in the Hamiltonian (4.4) that describes the instantaneous Coulomb repulsion of every pair of electrons. A fundamental approximation of quantum chemistry is to replace any of these interactions with a repulsion which the particular electron would feel when moving in a time-averaged field of the other electron. This approach has been introduced by Hartree, who assumed that each electron in a multielectron system is described by its own wave function and is thus subject to the Coulomb potential due to the remaining electrons:

$$V_{i,coul}(\mathbf{r}_1) = \sum_{j \neq i} \int d\mathbf{r}_2 \frac{1}{r_{12}} |\psi_j(\mathbf{r}_2)|^2 . \quad (4.6)$$

It is convenient to define a *Coulomb operator*

$$J_i(\mathbf{r}_1) = \int d\mathbf{r}_2 |\psi_i(\mathbf{r}_2)|^2 r_{12}^{-1} \quad (4.7)$$

that represents the average potential at  $\mathbf{r}_1$  arising from the charge distribution due to the  $i$ -th electron.

The one-electron wave functions for a many-electron system are then obtained by solving a system of equations of the form

$$\left[ h(1) + \sum_{j \neq i} J_j(\mathbf{r}_1) \right] \psi_i(\mathbf{r}_1) = \varepsilon_i \psi_i(\mathbf{r}_1) \quad , \quad (4.8)$$

where

$$h(1) = -\frac{1}{2} \nabla^2 - \sum_N \frac{Z_N}{r_{1N}} \quad (4.9)$$

is the operator of kinetic energy and potential energy for the attraction to the nuclei, corresponding to a single electron chosen to be the first electron. This is must be done iteratively, since the orbitals  $\psi_i$  that solve the problem appear in the operator  $J$ . Consequently, the Hartree method is a nonlinear “self-consistent-field” method. One begins with a guessed set of orbitals  $\psi_i$ , constructs the set of operators  $J_i$  as given by (4.7), then finds new set of orbitals from (4.8), constructs a new set of operator  $J_i$ , etc. The total Hartree wave function is given by a simple product of the one-electron wave functions. The correlations between the movements of different electrons are thus completely neglected. In addition, such wave function does not fulfill the Pauli’s requirement of antisymmetry with respect to an exchange of two particles.

#### 4.2.2 The Hartree-Fock Approximation

The symmetry requirements have been included in the Hartree method in a generalization due to Fock and Slater. Within this so-called *Hartree-Fock theory*, the Hartree product is substituted by a determinantal wave function (*Slater determinant*) of the form

$$\Psi_{\text{HF}}(\mathbf{x}_1, \mathbf{x}_2, \dots, \mathbf{x}_N) = \frac{1}{\sqrt{N!}} \begin{vmatrix} \chi_a(\mathbf{x}_1) & \chi_b(\mathbf{x}_1) & \dots & \chi_k(\mathbf{x}_1) \\ \chi_a(\mathbf{x}_2) & \chi_b(\mathbf{x}_2) & \dots & \chi_k(\mathbf{x}_2) \\ \dots & \dots & \dots & \dots \\ \chi_a(\mathbf{x}_N) & \chi_b(\mathbf{x}_N) & \dots & \chi_k(\mathbf{x}_N) \end{vmatrix} \quad , \quad (4.10)$$

where

$$\mathbf{x}_i = (\mathbf{r}_i, \sigma_i) \quad (4.11)$$

and the one-electron wave functions

$$\chi_i(\mathbf{x}_j) = \psi_i(\mathbf{r}_j) \omega_i(\sigma_j) \quad (4.12)$$

depend on both spatial  $\mathbf{r}_i$  and spin  $\sigma_i$  coordinates.

It is useful to introduce a shorthand notation, which includes the normalization constant and only shows the diagonal elements of the determinant,

$$\Psi_{\text{HF}}(\mathbf{x}_1, \mathbf{x}_2, \dots, \mathbf{x}_N) = \left| \chi_i(\mathbf{x}_1) \chi_j(\mathbf{x}_2) \dots \chi_k(\mathbf{x}_N) \right\rangle \quad (4.13)$$

Provided that we always choose the electron labels to be in the order  $\mathbf{x}_1, \mathbf{x}_2, \dots, \mathbf{x}_N$ , eq (4.13) can be further shortened to

$$\Psi_{\text{HF}}(\mathbf{x}_1, \mathbf{x}_2, \dots, \mathbf{x}_N) = \left| \chi_i \chi_j \dots \chi_k \right\rangle \quad (4.14)$$

The energy of the Slater determinant can be minimized using the variational condition

$$\delta \langle \Psi_{\text{HF}} | H_{\text{elec}} | \Psi_{\text{HF}} \rangle = 0 \quad (4.15)$$

( $H_{\text{elec}}$  refers to eq (4.4)), and we require that all orbitals are normalized. Using the rules for matrix elements between determinantal wave functions, condition (4.15) results in the *Hartree-Fock* (HF) equations:

$$\left[ h(1) + \sum_j \int d\mathbf{r}_2 \frac{1}{r_{12}} |\psi_j(\mathbf{r}_2)|^2 \right] \psi_i(\mathbf{r}_1) - \sum_j \delta(m_{s_i}, m_{s_j}) \left[ \int d\mathbf{r}_2 \frac{1}{r_{12}} \psi_j^*(\mathbf{r}_2) \psi_i(\mathbf{r}_2) \right] \psi_j(\mathbf{r}_1) = \varepsilon_i \psi_i(\mathbf{r}_1) \quad (4.16)$$

The term  $\delta(m_{s_i}, m_{s_j})$  results from an integration over the spin coordinates and indicates that the corresponding summation runs only over electrons with the same spin as that of

the electron  $i$ . The eigenvalue  $\varepsilon_i$  appears here as the Lagrange multiplier ensuring the normalization of the orbitals.

The Hartree-Fock equation (4.16) can be written as an eigenvalue equation

$$\left[ h(1) + \sum_j J_j(\mathbf{r}_1) - \sum_j \delta(m_{s_i}, m_{s_j}) K_j(\mathbf{r}_1) \right] \psi_i(\mathbf{r}_1) = \varepsilon_i \psi_i(\mathbf{r}_1) \quad , \quad (4.17)$$

if we define an *exchange operator*  $K_j(\mathbf{r}_1)$  by its effect when operating on an orbital  $\psi_i(\mathbf{r}_1)$ ,

$$K_j(\mathbf{r}_1) \psi_i(\mathbf{r}_1) = \left[ \int d\mathbf{r}_2 \psi_j^*(\mathbf{r}_2) r_{12}^{-1} \psi_i(\mathbf{r}_2) \right] \psi_j(\mathbf{r}_1) \quad . \quad (4.18)$$

The solution of the Hartree-Fock equations proceeds is found using the self-consistent-field approach.

The Hartree-Fock equation (4.17) differs from the Hartree equation (4.8) by the fact that the summation of the Coulomb operators runs over all values of  $j$  (including  $j=i$ ), and by the presence of the exchange operators. These are nonlocal operators and arise from the determinantal form of the wave function. Had we used a product trial wave function this term would be missing and we would have obtained Hartree's equation. The presence of the nonlocal term ensures that the Hartree-Fock equation represents an eigenvalue problem for a Hermitian operator, and the eigenfunctions corresponding to different eigenvalues are thus orthogonal. On the contrary, the Hartree equation does not correspond to a single eigenvalue problem, as the potential (4.6) is different for different one-electron wave functions, and the orthogonality of the orbitals is thus not enforced.

The nonclassical exchange term incorporates in the HF theory not only the antisymmetry properties, but also a correlation of electrons with the same spin. The probability of finding two electrons with the same spin simultaneously at the same place is zero. A Fermi hole is said to exist around each electron, which keeps electrons of the same spin separated.

Up to now, we have discussed the HF method independently of the particular spin state of the atom or molecule. A closed-shell system with  $N$  electrons can be described by two sets of spin-orbitals:

$$\begin{aligned} \psi_1(\mathbf{r})\alpha, \psi_2(\mathbf{r})\alpha, \dots, \psi_{\frac{N}{2}}(\mathbf{r})\alpha & ; \\ \psi_1(\mathbf{r})\beta, \psi_2(\mathbf{r})\beta, \dots, \psi_{\frac{N}{2}}(\mathbf{r})\beta & . \end{aligned} \quad (4.19)$$

If we denote a spin-orbital by its spatial part only, using a bar or lack of a bar to indicate whether it has the  $\beta$  or  $\alpha$  spin function, we can write a singlet closed-shell Slater determinant as

$$\Psi_{\text{HF}}(\mathbf{x}_1, \mathbf{x}_2, \dots, \mathbf{x}_N) = \left| \psi_1 \bar{\psi}_1 \psi_2 \bar{\psi}_2 \dots \psi_{\frac{N}{2}} \bar{\psi}_{\frac{N}{2}} \right\rangle . \quad (4.20)$$

In this work, however, we will be handling exclusively open-shell systems with  $N^\alpha$  electrons of  $\alpha$  spin and  $N^\beta$  electrons of  $\beta$  spin,  $N^\alpha > N^\beta$ . For this purpose, two modifications of the HF method are used: the unrestricted HF method and the restricted-open-shell HF method.

### 4.2.3 The Unrestricted Hartree-Fock Method

The Hartree-Fock equation (4.17) has the form of a Schrödinger equation for a particle moving in a nonlocal potential. For an open-shell system, the presence of the exchange term in (4.17) makes the potential depend on the spin of the particular electron  $i$ . Consequently, one has to solve two sets of equations

$$f^\alpha(\mathbf{r}_1) \psi_i^\alpha = \varepsilon_i^\alpha \psi_i^\alpha , \quad (4.21)$$

$$f^\beta(\mathbf{r}_1) \psi_i^\beta = \varepsilon_i^\beta \psi_i^\beta , \quad (4.22)$$

where the *Fock operators*  $f^\alpha(\mathbf{r}_1)$ ,  $f^\beta(\mathbf{r}_1)$  are given by

$$f^\alpha(\mathbf{r}_1) = h(1) + \sum_j^{N^\alpha} [J_j^\alpha(\mathbf{r}_1) - K_j^\alpha(\mathbf{r}_1)] + \sum_j^{N^\beta} J_j^\beta(\mathbf{r}_1) \quad , \quad (4.23)$$

$$f^\beta(\mathbf{r}_1) = h(1) + \sum_j^{N^\beta} [J_j^\beta(\mathbf{r}_1) - K_j^\beta(\mathbf{r}_1)] + \sum_j^{N^\alpha} J_j^\alpha(\mathbf{r}_1) \quad . \quad (4.24)$$

The unrestricted Coulomb and exchange operators are defined in analogy to our previous definitions (4.7) and (4.18) of the restricted Coulomb and exchange operators:

$$J_j^\alpha(\mathbf{r}_1) = \int d\mathbf{r}_2 \psi_j^{\alpha*}(\mathbf{r}_2) r_{12}^{-1} \psi_j^\alpha(\mathbf{r}_2) \quad , \quad (4.25)$$

$$K_j^\alpha(\mathbf{r}_1) \psi_i^\alpha(\mathbf{r}_1) = \left[ \int d\mathbf{r}_2 \psi_j^{\alpha*}(\mathbf{r}_2) r_{12}^{-1} \psi_i^\alpha(\mathbf{r}_2) \right] \psi_j^\alpha(\mathbf{r}_1) \quad . \quad (4.26)$$

The definitions of  $J_j^\beta$  and  $K_j^\beta$  are strictly analogous to the above. Equations (4.23) and (4.24) are coupled through the Coulomb operators and must thus be solved by a simultaneously. The exchange interactions of the  $\alpha$ -spin electrons are different from those of their  $\beta$ -counterparts. As a result, even within an electron “pair”, both the spatial parts  $\psi_i^\alpha(\mathbf{r})$ ,  $\psi_i^\beta(\mathbf{r})$  and the energies of the optimized spin-orbitals  $\psi_i^\alpha(\mathbf{r})\alpha$ ,  $\psi_i^\beta(\mathbf{r})\beta$  are slightly different. Thus, an *unrestricted Hartree-Fock* (UHF) wave function for an open-shell system can be written as

$$\Psi^{\text{UHF}}(\mathbf{x}_1, \mathbf{x}_2, \dots, \mathbf{x}_N) = \left| \psi_1^\alpha \bar{\psi}_1^\beta \psi_2^\alpha \bar{\psi}_2^\beta \dots \psi_{N^\beta}^\alpha \bar{\psi}_{N^\beta}^\beta \psi_{N^\beta+1}^\alpha \dots \psi_{N^\alpha}^\alpha \right\rangle \quad . \quad (4.27)$$

The total energy corresponding to an UHF wave function may be written as

$$E^{\text{UHF}} = \sum_i h_{ii}^\alpha + \sum_i h_{ii}^\beta + \frac{1}{2} \sum_i \sum_j (J_{ij}^{\alpha\alpha} - K_{ij}^{\alpha\alpha}) + \frac{1}{2} \sum_i \sum_j (J_{ij}^{\beta\beta} - K_{ij}^{\beta\beta}) + \sum_i \sum_j J_{ij}^{\alpha\beta} \quad , \quad (4.28)$$

with  $\alpha$  and  $\beta$  denoting spin, where  $h_{ii}^\alpha$ ,  $h_{ii}^\beta$ ,  $J_{ij}^{\alpha\alpha}$ ,  $J_{ij}^{\beta\beta}$ ,  $J_{ij}^{\alpha\beta}$ ,  $K_{ij}^{\alpha\alpha}$ ,  $K_{ij}^{\beta\beta}$  are matrix elements of the corresponding operators involving the spatial orbitals  $\psi_i^\alpha(\mathbf{r})$ ,  $\psi_i^\beta(\mathbf{r})$ ,  $\psi_j^\alpha(\mathbf{r})$ , and  $\psi_j^\beta(\mathbf{r})$ . The expectation values of the one-electron operator  $h$

$$h_{ii}^{\alpha} = \langle \psi_i^{\alpha} | h | \psi_i^{\alpha} \rangle \quad \text{and} \quad h_{ii}^{\beta} = \langle \psi_i^{\beta} | h | \psi_i^{\beta} \rangle \quad (4.29)$$

represent the average kinetic and nuclear-attraction energy of the unrestricted orbitals  $\psi_i^{\alpha}$  and  $\psi_i^{\beta}$ , respectively.

Matrix elements

$$J_{ij}^{\alpha\beta} = \langle \psi_i^{\alpha} | J_j^{\beta} | \psi_i^{\alpha} \rangle = \langle \psi_j^{\beta} | J_i^{\alpha} | \psi_j^{\beta} \rangle =: \langle \psi_i^{\alpha} \psi_j^{\beta} | \psi_i^{\alpha} \psi_j^{\beta} \rangle \quad , \quad (4.30)$$

$$J_{ij}^{\alpha\alpha} = \langle \psi_i^{\alpha} | J_j^{\alpha} | \psi_i^{\alpha} \rangle = \langle \psi_j^{\alpha} | J_i^{\alpha} | \psi_j^{\alpha} \rangle =: \langle \psi_i^{\alpha} \psi_j^{\alpha} | \psi_i^{\alpha} \psi_j^{\alpha} \rangle \quad , \quad (4.31)$$

and

$$J_{ij}^{\beta\beta} = \langle \psi_i^{\beta} | J_j^{\beta} | \psi_i^{\beta} \rangle = \langle \psi_j^{\beta} | J_i^{\beta} | \psi_j^{\beta} \rangle =: \langle \psi_i^{\beta} \psi_j^{\beta} | \psi_i^{\beta} \psi_j^{\beta} \rangle \quad (4.32)$$

express the classical Coulomb repulsion between the charge clouds  $|\psi_i(\mathbf{r}_1)|^2$  and  $|\psi_j(\mathbf{r}_2)|^2$  for electrons of different or the same spin and are referred to as the *Coulomb integrals*.

Finally, matrix elements

$$K_{ij}^{\alpha\alpha} = \langle \psi_i^{\alpha} | K_j^{\alpha} | \psi_i^{\alpha} \rangle = \langle \psi_j^{\alpha} | K_i^{\alpha} | \psi_j^{\alpha} \rangle =: \langle \psi_i^{\alpha} \psi_j^{\alpha} | \psi_j^{\alpha} \psi_i^{\alpha} \rangle \quad (4.33)$$

and

$$K_{ij}^{\beta\beta} = \langle \psi_i^{\beta} | K_j^{\beta} | \psi_i^{\beta} \rangle = \langle \psi_j^{\beta} | K_i^{\beta} | \psi_j^{\beta} \rangle =: \langle \psi_i^{\beta} \psi_j^{\beta} | \psi_j^{\beta} \psi_i^{\beta} \rangle \quad , \quad (4.34)$$

the so-called *exchange integrals*, represent the exchange interaction energy of the two electrons with parallel spins. There is no exchange interaction between electrons of opposite spin.

The summations in eq (4.28) are not restricted to pairs of different spin orbitals. Therefore, the (unphysical) electrostatic interaction of an electron with itself is

accounted for in the Coulomb part and again subtracted in the exchange part. This allows a unique orbital decomposition of the total electron repulsion energy into exchange and Coulomb parts.<sup>a</sup> The Coulomb part may be interpreted as the classical electrostatic energy of a charge cloud of density  $\rho(r)$ , whereas the exchange part includes all nonclassical effects, (see ref 4, pp 34,39).

The total spin density corresponding to an UHF wave function is given by:

$$Q^{UHF}(\mathbf{r}) = \sum_{i=N^{\beta}+1}^{N^{\alpha}} |\psi_i^{\alpha}(\mathbf{r})|^2 + \sum_{j=1}^{N^{\beta}} \left( |\psi_j^{\alpha}(\mathbf{r})|^2 - |\psi_j^{\beta}(\mathbf{r})|^2 \right) . \quad (4.35)$$

The first sum represents the direct contribution from the unpaired electrons, the second sum is the spin polarization contribution from the remaining “paired” electrons. The inclusion of the spin polarization is a crucial property of the UHF method. As will be shown below, it provides a one-electron-level understanding of the spin-density transfer from the valence space to the nucleus. At the same time, the spin polarization leads to a serious drawback of the UHF method, namely that the UHF wave functions do not correspond to pure spin states. A nominal doublet state, e.g., contains small amounts of quartet, sextet and higher spin states. Before evaluating spin properties from an UHF wave function, the spin contaminants are often eliminated using spin-projection techniques. However, the justification for doing so is doubtful. A strong argument against using the spin projection is that the UHF method yields the correct diagrams in a perturbation theory development of the exact wave function, whereas the spin-projected UHF does not do so.<sup>6</sup>

---

<sup>a</sup> When self interaction is not accounted for, the decomposition of the electron repulsion energy into Coulomb and exchange parts may be arbitrary. E.g., for a  $p$ -shell fully occupied with six electrons, both the total Coulomb and the total exchange energy depends on the orbital basis (angular momentum eigenfunctions or real functions). The reason is that

$$\begin{aligned} \langle p_x p_y | p_x p_y \rangle &= \langle p_x p_z | p_x p_z \rangle = \langle p_y p_z | p_y p_z \rangle \\ &= \langle p_1 p_0 | p_1 p_0 \rangle = \langle p_{-1} p_0 | p_{-1} p_0 \rangle \neq \langle p_{-1} p_1 | p_{-1} p_1 \rangle . \end{aligned}$$



#### 4.2.4 The Restricted Open-Shell Hartree-Fock Method

The spin-contamination problem in the HF description of open-shell systems can be avoided using a more complicated *restricted open-shell Hartree-Fock* (ROHF) method. Whereas at the UHF level of theory, MOs  $\psi_i^\alpha(\mathbf{r})$  and  $\psi_i^\beta(\mathbf{r})$  are allowed to differ, within the ROHF method they are required to be identical for every  $i \leq N^\beta$ . We are thus looking for a Slater determinant of the form

$$\Psi^{\text{ROHF}}(\mathbf{x}_1, \mathbf{x}_2, \dots, \mathbf{x}_N) = \left| \psi_1 \bar{\psi}_1 \psi_2 \bar{\psi}_2 \dots \psi_{N^\beta} \bar{\psi}_{N^\beta} \psi_{N^\beta+1} \dots \psi_{N^\alpha} \right\rangle \quad (4.36)$$

which minimizes the total electronic energy.

To achieve this, the  $N^\beta$  electron pairs (i.e. the closed shell) are treated separately from the  $N^\alpha - N^\beta$  unpaired (open-shell) electrons and the virtual orbitals. This approach results in two sets of equations:

$$f^c(\mathbf{r}_1) \psi_i^c = \varepsilon_i^c \psi_i^c \quad , \quad (4.37)$$

$$f^o(\mathbf{r}_1) \psi_i^o = \varepsilon_i^o \psi_i^o \quad . \quad (4.38)$$

The *Fock operators*  $f^c(\mathbf{r}_1)$ ,  $f^o(\mathbf{r}_1)$  are defined as

$$f^c(\mathbf{r}_1) = h(1) + 2 \sum_j^{N^\beta} [J_j(\mathbf{r}_1) - K_j(\mathbf{r}_1) + \kappa L_j^o(\mathbf{r}_1) - \lambda M_j^o(\mathbf{r}_1)] \quad (4.39)$$

$$\begin{aligned} f^o(\mathbf{r}_1) = & h(1) + \sum_{j \in c}^N [J_j(\mathbf{r}_1) - K_j(\mathbf{r}_1)] \\ & + \sum_{\substack{j \neq i \\ j \in o}} [\kappa' J_j(\mathbf{r}_1) - \lambda' K_j(\mathbf{r}_1)] + \sum_{j \neq i} [\kappa L_j^c(\mathbf{r}_1) - \lambda M_j^c(\mathbf{r}_1)] \quad . \end{aligned} \quad (4.40)$$

where

$$L_j^o(\mathbf{r}_1) = \nu \sum_{\substack{m=1 \\ m \in o}}^N |\psi_m\rangle \langle \psi_m| J_j(\mathbf{r}_1) \quad , \quad (4.41)$$

$$M_j^o(\mathbf{r}_1) = \nu \sum_{\substack{m=1 \\ m \in o}}^N |\psi_m\rangle \langle \psi_m| K_j(\mathbf{r}_1) \quad , \quad (4.42)$$

$$L_j^c(\mathbf{r}_1) = \sum_{\substack{m=1 \\ m \in c}}^N |\psi_m\rangle \langle \psi_m| J_j(\mathbf{r}_1) \quad , \quad (4.43)$$

$$M_j^c(\mathbf{r}_1) = \sum_{\substack{m=1 \\ m \in c}}^N |\psi_m\rangle \langle \psi_m| K_j(\mathbf{r}_1) \quad (4.44)$$

are necessary in order to preserve the orthogonality of the ROHF solutions. The quantities  $\kappa$ ,  $\kappa'$ ,  $\lambda$ ,  $\lambda'$  and  $\nu$  are dependent on the particular spin state and are described elsewhere. In ROHF theory, the treatment yields a single-determinant expression that satisfies all spin and symmetry requirements.<sup>7</sup>

The total energy corresponding to an ROHF wave function is given by:

$$E^{ROHF} = 2 \sum_{i=1}^{N^\beta} h_{ii} + \sum_{i=N^\beta+1}^{N^\alpha} h_{ii} + \sum_{i=1}^{N^\alpha} \sum_{j=1}^{N^\beta} (2J_{ij} - K_{ij}) + \frac{1}{2} \sum_{i=N^\beta+1}^{N^\alpha} \sum_{j=N^\beta+1}^{N^\alpha} (J_{ij} - K_{ij}) \quad . \quad (4.45)$$

The spin density in this model is the sum of probability distributions of the open-shell orbitals

$$Q^{ROHF}(\mathbf{r}) = \sum_{i=N^\beta+1}^{N^\alpha} |\psi_i(\mathbf{r})|^2 \quad . \quad (4.46)$$

The closed-shell (doubly-occupied) orbitals do not contribute to  $Q(\mathbf{r})$ , as the contributions of the  $\alpha$  spin-orbitals are always exactly cancelled by the contributions of the  $\beta$  spin-orbitals. Spin-polarization contributions can be included in the ROHF wave function using the configuration interaction approach.

### 4.3 The Configuration Interaction Method

The Hartree-Fock method is a one-electron approximation. As such it describes the electron-repulsion interactions in an averaged way and does not include important electron-correlation effects. The exact wave function for the ground as well as the excited states of the system can be written as a linear combination of all possible  $N$ -electron Slater determinants formed from a complete set of spin-orbitals. Since any determinant can be described in reference to the HF determinant  $|\text{HF}\rangle$ , we can write (within the second quantization formalism):

$$\Phi = \left( 1 + \sum_{iu} c_i^u a_u^\dagger a_i + \sum_{iu,jv} c_{ij}^{uv} a_u^\dagger a_v^\dagger a_i a_j + \dots \right) |\text{HF}\rangle, \quad (4.47)$$

where the creation and annihilation operators  $a_u^\dagger$  and  $a_i$  create a particle in the virtual orbital  $u$  and annihilate a particle in the occupied orbital  $i$ , respectively. The summations over  $i,j,\dots$  and  $u,v,\dots$  run over all occupied spin-orbitals and virtual spin-orbitals, respectively. The lowest eigenvalue of the Hamiltonian matrix with elements  $\langle \Psi_k | H | \Psi_l \rangle$  formed from the complete set  $\{ |\Psi_k\rangle \} = \{ |\text{HF}\rangle, a_u^\dagger a_i |\text{HF}\rangle, a_u^\dagger a_v^\dagger a_i a_j |\text{HF}\rangle, \dots \}$  is the exact nonrelativistic ground state energy of the system within the Born-Oppenheimer approximation.

In practical calculations, various approximations to the full wave function of eq (4.47) are obtained by working with a finite (rather than complete) set of spin-orbitals and truncating the expansion at some excitation level. The values of the coefficients  $c_{ij\dots m}^{uv\dots z}$  are optimized using the variational principle, as the resulting total energy is always an upper bound to the exact energy. This is the so-called configuration interaction (CI) method. A serious drawback of truncated CI methods is that they are not size consistent: the total energy of a system composed of non-interacting molecules does not scale linearly with the number of the molecules.

The CI formalism improves the HF description of the spin density distribution by including the electron-correlation effects. Particularly, it augments the ROHF spin density with the spin-polarization contributions. As the spin density is a one-electron property, for a CI wave function it can be written as a sum over matrix elements

between configurations belonging to the same excitation class or differing in one excitation<sup>8</sup>

$$\begin{aligned}
Q^{CI}(\mathbf{r}) = & \sum_{i,u} c_0 c_i^u \langle i | \delta(\mathbf{x}-\mathbf{r}) | u \rangle + \sum_{i,u} c_i^u c_i^u \sum_a \langle a | \delta(\mathbf{x}-\mathbf{r}) | a \rangle + \sum_{i,u<v} c_i^u c_i^v \langle u | \delta(\mathbf{x}-\mathbf{r}) | v \rangle \\
& + \sum_{i<j,u} c_i^u c_j^u \langle i | \delta(\mathbf{x}-\mathbf{r}) | j \rangle + \sum_{i<j,u<v} c_i^u c_{ij}^{uv} \langle j | \delta(\mathbf{x}-\mathbf{r}) | v \rangle + \dots \quad .
\end{aligned}
\tag{4.48}$$

The first term in eq (4.48) represents the contribution arising from matrix elements between the ROHF determinant and singly excited determinants. The second term gives the contributions of diagonal matrix elements, the third and fourth terms provide contributions of nondiagonal matrix elements between singly-excited determinants. The sum over  $a$  in the second term runs over all occupied orbitals in the wave function  $a_u^\dagger a_i | \text{ROHF} \rangle$ . The last term gives the single-double contributions. Further contributions arise from double-double, double-triple excitations, etc. The most important contributions come from the singly and doubly excited determinants. To obtain accurate isotropic HFCCs, however, one has to take into account also higher than double excitations. As the higher excitations contribute mainly indirectly, by influencing the coefficients of the lower excitations, it is sufficient to include their effect perturbatively.<sup>8</sup>

#### 4.4 The Coupled-Cluster Method

In the coupled-cluster method, the trial many-electron wave function is written as

$$\Phi_{\text{CCA}} = \exp(T_1 + T_2 + \dots) | \text{HF} \rangle \quad ,
\tag{4.49}$$

where

$$\begin{aligned}
T_1 &= \left(\frac{1}{1!}\right)^2 \sum_{iu} c_i^u a_u^\dagger a_i \quad , \\
T_2 &= \left(\frac{1}{2!}\right)^2 \sum_{iu,jv} c_{ij}^{uv} a_u^\dagger a_v^\dagger a_i a_j \quad , \\
T_3 &= \dots \quad .
\end{aligned}
\tag{4.50}$$

The total energy  $E^{CC}$  is found by projecting the Schrödinger equation  $(e^{-T} H e^T - E)|HF\rangle = 0$  to the HF reference state  $(|HF\rangle)^\dagger$  as

$$E = \langle HF | H e^T | HF \rangle \quad , \tag{4.51}$$

and the cluster amplitudes  $c$  are found similarly by projecting to states of the corresponding excitation level, e.g., for the single particle-hole pair amplitudes  $c_i^u$

$$\langle HF | a_i^\dagger a_u e^{-T} H e^T | HF \rangle = 0 \quad . \tag{4.52}$$

This process leads to a non-linear system of equations to be solved iteratively.

In practical calculations, the CC wave functions are truncated at certain excitation level, and the cluster expansion (4.49) ensures that – unlike for the CI methods – the size consistence is retained. The present work uses the CCSD truncation that includes the *singles* and *doubles* operators  $T_1, T_2$  in  $e^T$ , and the CCSD(T) truncation which is an approximate form of the CC method including the *singles*, *doubles*, and *triples* operators  $T_1, T_2$ , and  $T_3$  in  $e^T$ .<sup>9</sup> The price paid for the size consistency is that truncated CC methods are not variational.

The expressions for the total energy and the spin density within the CC method are given elsewhere.<sup>1,10</sup>

## 4.5 Density Functional Theory

### 4.5.1 The Hohenberg-Kohn Theorems

The quantum chemistry methods discussed above use the many-electron wave function, and consequently the external potential  $v(\mathbf{r})$  and the number of electrons  $N$ , which specify the electronic Hamiltonian, as the source for the determination of all electronic properties. The basic theorem of the density functional theory states that the electron density  $\rho(\mathbf{r})$  can be used as the basic variable instead. The external potential  $v(\mathbf{r})$  is determined, within a trivial additive constant, by the electron density  $\rho(\mathbf{r})$  (*the first Hohenberg-Kohn theorem*). Obviously,  $\rho(\mathbf{r})$  determines also  $N$ .

The total electronic energy can thus be written as

$$E[\rho] = T[\rho] + V_{ne}[\rho] + V_{ee}[\rho] = \int \rho(\mathbf{r}) v(\mathbf{r}) d\mathbf{r} + F_{HK}[\rho] \quad , \quad (4.53)$$

where  $T[\rho]$  represents the kinetic energy,  $V_{ne}[\rho]$  and  $V_{ee}[\rho]$  the potential energy due to the nuclei and the electrons, respectively, and

$$F_{HK}[\rho] = T[\rho] + V_{ee}[\rho] \quad (4.54)$$

is a universal functional of the electronic density, which does not depend on the particular system.

The electron-electron repulsion term  $V_{ee}[\rho]$  can be partitioned as

$$V_{ee}[\rho] = J[\rho] + \text{nonclassical term} \quad , \quad (4.55)$$

where

$$J[\rho] = \frac{1}{2} \iint \frac{1}{r_{12}} \rho(\mathbf{r}_1) \rho(\mathbf{r}_2) d\mathbf{r}_1 d\mathbf{r}_2 \quad (4.56)$$

is the classical self-repulsion energy of a distribution  $\rho(\mathbf{r})$ , i.e. the Coulomb energy defined above, cf. eqs (4.25), (4.28).

The second Hohenberg-Kohn theorem represents the energy variational principle. For a trial density  $\tilde{\rho}(\mathbf{r})$  such that  $\tilde{\rho}(\mathbf{r}) \geq 0$  and

$$\int \tilde{\rho}(\mathbf{r}) d\mathbf{r} = N \quad , \quad (4.57)$$

the energy  $E[\tilde{\rho}(\mathbf{r})]$  is always an upper bound to the exact energy  $E_0$ :

$$E_0 \leq E[\tilde{\rho}(\mathbf{r})] \quad . \quad (4.58)$$

The latter requires that the ground-state density satisfies the stationary principle

$$\delta \left\{ E[\rho] - \mu \left[ \int \rho(\mathbf{r}) d\mathbf{r} - N \right] \right\} = 0 \quad (4.59)$$

which gives the Euler-Lagrange equation

$$\mu = \frac{\delta E[\rho]}{\delta \rho(\mathbf{r})} = v(\mathbf{r}) + \frac{\delta F_{HK}[\rho]}{\delta \rho(\mathbf{r})} \quad . \quad (4.60)$$

The Lagrange multiplier  $\mu$  is the *chemical potential* and has been introduced in order to constrain the minimization (4.58) by the normalization condition (4.57). If we knew the exact  $F_{HK}[\rho]$ , (4.58) would be an exact equation for the ground-state electron density.

#### 4.5.2 The Kohn-Sham Method

Due to the unfortunate (but challenging) fact that the functional  $F_{HK}[\rho]$  is hard to come by in explicit form, accurate calculational implementations of the density-functional theory are far from easy to achieve. Approximate forms of  $F_{HK}[\rho]$  are required and can be constituted using a direct approach, whereby one constructs explicit approximate forms for  $T[\rho]$  and  $V_{ee}[\rho]$ . Unfortunately, there are seemingly insurmountable difficulties in going beyond the crude level of approximation of  $T[\rho]$ .

An ingenious indirect approach to the kinetic energy functional has been developed within the *Kohn-Sham* (KS) method. It introduces a (hypothetical) non-interacting reference system with exactly the same electron density as that of the real system.<sup>11</sup> The exact wave function of the noninteracting system is a Slater determinant formed from  $N$  spin-orbitals (Kohn-Sham orbitals)  $\psi_i(\mathbf{x})$ . The exact kinetic energy for the reference system

$$T_S = \sum_i^N \langle \psi_i | -\frac{1}{2} \nabla^2 | \psi_i \rangle \quad (4.61)$$

can be – by virtue of the first Hohenberg-Kohn theorem – considered a functional of the charge density

$$\rho(\mathbf{r}) = \sum_i |\psi_i(\mathbf{x})|^2 \quad . \quad (4.62)$$

The quantity  $T_S[\rho]$  is of course not equal to the true kinetic energy of the interacting system  $T[\rho]$ . The very clever idea of Kohn and Sham is to set up a problem of interest in such a way that  $T_S[\rho]$  is its kinetic-energy component, exactly.

To produce the desired separation out of  $T_S[\rho]$  as the kinetic energy component, we rewrite (4.54) as

$$F_{HK}[\rho] = T_S[\rho] + J[\rho] + E_{xc}[\rho] \quad (4.63)$$

where

$$E_{xc}[\rho] \equiv T[\rho] - T_S[\rho] + V_{ee}[\rho] - J[\rho] \quad . \quad (4.64)$$

The defined quantity  $E_{xc}[\rho]$  is called the *exchange-correlation energy*; it contains the difference between  $T$  and  $T_S$  (presumably fairly small), and the nonclassical part of  $V_{ee}[\rho]$ .

The Euler equation (4.60) now becomes



$$\mu = v_{\text{eff}}(\mathbf{r}) + \frac{\delta T_s[\rho]}{\delta \rho(\mathbf{r})} \quad (4.65)$$

where the Kohn-Sham (KS) effective potential is defined by

$$v_{\text{eff}}(\mathbf{r}_1) = v(\mathbf{r}_1) + \frac{\delta J[\rho]}{\delta \rho(\mathbf{r}_1)} + \frac{\delta E_{\text{xc}}[\rho]}{\delta \rho(\mathbf{r}_1)} = v(\mathbf{r}_1) + \int \frac{\rho(\mathbf{r}_2)}{r_{12}} d\mathbf{r}_2 + v_{\text{xc}}(\mathbf{r}_1) \quad (4.66)$$

with the *exchange-correlation potential*

$$v_{\text{xc}}(\mathbf{r}_1) = \frac{\delta E_{\text{xc}}[\rho]}{\delta \rho(\mathbf{r}_1)} . \quad (4.67)$$

The Kohn-Sham treatment runs as follows. Equation (4.65) represents a conventional DFT approach when applied to a system of *noninteracting* electrons moving in the external potential  $v_{\text{eff}}(\mathbf{r})$ . Therefore, for a given  $v_{\text{eff}}(\mathbf{r})$ , one obtains the  $\rho(\mathbf{r})$  that satisfies (4.65) simply by solving the  $N$  one-electron equations

$$\left[ -\frac{1}{2}\nabla^2 + v_{\text{eff}}(\mathbf{r}) \right] \psi_i = \varepsilon_i \psi_i \quad (4.68)$$

and setting

$$\rho(\mathbf{r}) = \sum_i \psi_i(\mathbf{x}) \quad (4.69)$$

Here,  $v_{\text{eff}}(\mathbf{r})$  depends on  $\rho(\mathbf{r})$  through (4.67); hence, (4.66), (4.68), and (4.69) must be solved self-consistently.

The total Kohn-Sham energy is given by

$$E = \sum_i^N h_{ii} - \frac{1}{2} \iint \frac{\rho(\mathbf{r}_1)\rho(\mathbf{r}_2)}{r_{12}} d\mathbf{r}_1 d\mathbf{r}_2 + E_{\text{xc}}[\rho] - \int v_{\text{xc}}(\mathbf{r}_1)\rho(\mathbf{r}_1) d\mathbf{r}_1 , \quad (4.70)$$

where

$$\sum_i^N h_{ii} = \sum_i^N \langle \psi_i | -\frac{1}{2} \nabla^2 + v_{eff}(\mathbf{r}) | \psi_i \rangle = T_s[\rho] + \int v_{eff}(\mathbf{r}) \rho(\mathbf{r}) d\mathbf{r} \quad . \quad (4.71)$$

The KS equations are formally very similar to the HF equations. Nevertheless, in HF theory, electron correlation effects are by definition neglected and can be accounted for only using multi-determinantal trial wave functions. On the contrary, the more general local potential  $v_{xc}$  in the KS equations ensures that the Kohn-Sham theory is in principle exact, as it fully incorporates the exchange-correlation effects. Kohn-Sham equations can be improved by improving approximations to  $E_{xc}[\rho]$ . In this sense, Kohn-Sham theory represents the best one-electron approach. A crucial advantage is that KS theory is typically computationally much less expensive than the correlated methods based on HF, and enables thus the treatment of larger systems.

The methods for the treatment of the open-shell systems within the KS theory - the unrestricted Kohn-Sham (UKS) and the restricted open-shell Kohn-Sham (ROKS) methods - are analogous to the HF-based approaches introduced in sections 4.2.3 and 4.2.4. The expressions for the UKS and ROKS spin densities are identical to those given by (4.35) and (4.46), respectively, where the optimized Kohn-Sham orbitals are considered instead of the optimized Hartree-Hock orbitals.

### 4.5.3 Exchange-Correlation Functionals

The explicit form of the exchange-correlation functional  $E_{xc}[\rho]$  that specifies the Kohn-Sham potential (4.66) is not known and represents the greatest challenge in DFT. Various approximations have been suggested for  $E_{xc}[\rho]$ , the simplest one being the *local density approximation* (LDA)

$$E_{xc}^{LDA}[\rho] = \int \rho(\mathbf{r}) \varepsilon_{xc}(\rho) d\mathbf{r} \quad , \quad (4.72)$$

where  $\varepsilon_{xc}(\rho)$  is the exchange and correlation energy per particle in a uniform electron gas of density  $\rho(\mathbf{r})$ . Thus, we associate with the density  $\rho(\mathbf{r})$  the exchange and correlation energies and potentials that a homogenous electron gas of equal, but

constant density would have, and assume that the exchange-correlation functionals depend only on the *local* value of  $\rho(\mathbf{r})$ .

The exchange part of the LDA functional is

$$E_x^{LDA}[\rho] = -\frac{3}{4} \left( \frac{3}{\pi} \right)^{1/3} \int \rho^{4/3}(\mathbf{r}) d\mathbf{r} . \quad (4.73)$$

$E_c^{LDA}$  can not be written in a such an explicit form, but highly accurate numerical values are available for this property on the basis of Monte Carlo calculations of the homogeneous electron gas.<sup>12</sup> On the basis of these results, various authors have presented analytical expressions of  $E_c^{LDA}$  based on sophisticated interpolation schemes. The most widely used representation of  $E_c^{LDA}$  is due to Vosko, Wilk, and Nusair (VWN).<sup>13</sup> The exchange (4.73) together with the VWN correlation functional forms the so-called SVWN functional, used in our deMon calculations.

The local density approximation provides, however, only moderate accuracy and is thus insufficient for most applications in chemistry. The logical first step in the going beyond LDA is to consider functionals that are functions of both the local density,  $\rho(\mathbf{r})$ , and the gradient of the density,  $\nabla\rho(\mathbf{r})$ . Functionals that include the gradients of the charge density are collectively known as *generalized gradient approximations* (GGA). These functionals are the workhorses of current density functional theory (they have been extensively applied throughout this thesis) and can generally be written as

$$E_{xc}^{GGA}[\rho_\alpha, \rho_\beta] = \int f(\rho_\alpha, \rho_\beta, \nabla\rho_\alpha, \nabla\rho_\beta) d\mathbf{r} . \quad (4.74)$$

Finally, there is a great interest recently in applications of exchange-correlation functionals that include some exact, nonlocal exchange. Such *hybrid functionals* have also been used for the calculations employed in this thesis. These, as well as the generalized gradient approximations, are discussed in detail elsewhere.<sup>5</sup>

## 4.6 Basis Sets and Pseudopotentials

Practical electronic structure calculations of polyatomic molecules typically use the linear-combination-of-atomic-orbitals (LCAO) approximation

$$|\psi_k\rangle = \sum_{\mu} c_{\mu}^k |\chi_{\mu}\rangle, \quad (4.75)$$

where  $\{\chi_{\mu}\}$  is the basis set of atomic orbitals.

The most common LCAO basis functions employed presently in quantum chemistry are Gaussian type orbitals (GTOs) centered on atomic nuclei. In spherical coordinates, their form is

$$\chi_{\mu}(r, \theta, \varphi) = Y_{lm}(\theta, \varphi) r^{n-1} e^{-\zeta r^2}, \quad (4.76)$$

where  $Y_{lm}$  are the spherical harmonics;  $\zeta$  is the so-called *exponent* of the GTO. Due to their convenient mathematical properties, GTOs are more popular than the physically more correct Slater type orbitals (STO). The better physical behavior of STOs at  $r=0$  and at large  $r$  is simulated by working with fixed linear combinations of *primitive gaussian functions*  $\chi_{\mu}$ . These linear combinations lead to *contracted Gaussian functions* (CGTOs); each of them being specified by a set of exponents and another set of contraction coefficients which are not allowed to change during the calculation. Depending on the number of CGTOs used per atomic shell, basis sets are referred to as single- $\zeta$  (1 CGTO), double- $\zeta$  (DZ, 2 CGTOs), triple- $\zeta$  (TZ, 3 CGTOs), etc. The flexibility of a basis set is improved by adding functions of higher angular momentum than corresponds to occupied orbitals in the ground state of the particular atom. These are called the *polarization functions* and are *p*-type functions for H and He, *d*-type functions for the first-row atoms Li-F, etc. *Diffuse functions* are those with very small exponents and allow the charge distribution to be spread widely in the space.

For the purposes of this work, we have constructed a (15s11p6d)/[9s7p4d]<sup>b</sup> basis as a standard medium-size basis set for the 3*d* transition metal atoms. Our starting point was the DZ basis of Schäfer et al.,<sup>14</sup> to which we added the most diffuse functions (a 1s2p1d set) from the ECP valence basis of Dolg et al.<sup>15</sup> IGLO-III basis sets<sup>16</sup> were used for the main group atoms.

Hyperfine properties reflect the spatial coincidence of the spin density and the magnetic nuclei; proper treatment of the core electrons is thus necessary. In structure optimizations, however, the role of the core electrons is negligible in comparison to the valence electrons. Instead of the explicit treatment of the core electrons, their influence on the valence electrons can be simulated by using an effective core potential (ECP).<sup>17</sup> The properties of the valence pseudo-orbitals obtained in an ECP calculation are at the same time required to be the same as those obtained in an all-electron treatment. Our structure optimizations employed small-core ECPs and (8s7p6d)/[6s5p3d] GTO valence basis sets of the Stuttgart group for the transition metals.<sup>18</sup> For the first-row ligand atoms, ECPs with (4s4p1d)/[2s2p1d] basis sets have been used.<sup>19</sup> For hydrogen, a (4s1p)/[2s1p] basis<sup>20</sup> has been employed.

---

<sup>b</sup> The notation (15s11p6d)/[9s7p4d] indicates a contraction of the basis set and has the following meaning: The numbers in parentheses are the total numbers of primitive gaussian functions, the numbers in square brackets are those of CGTOs.

## References

---

- <sup>1</sup> Szabo, A.; Ostlund, N. S. *Modern Quantum Chemistry*, Dover: New York, 1996.
- <sup>2</sup> Bethe, H. A.; Jackiw, R. *Intermediate Quantum Mechanics*, Perseus Books: Massachusetts, 1997.
- <sup>3</sup> Levine, I. N. *Quantum Chemistry*, Prentice Hall: New Jersey, 2000.
- <sup>4</sup> Parr, R. G.; Yang, W. *Density-functional theory of atoms and molecules*, Oxford University Press: New York, 1989.
- <sup>5</sup> Koch, W.; Holthausen, M. C. *A Chemist's Guide to Density Functional Theory*; Wiley-VCH: Weinheim, 2000.
- <sup>6</sup> Chipman, D. M. *Theor. Chim. Acta* **1992**, 82, 93.
- <sup>7</sup> Csizmadia, L. G. *Theory and Practice of MO calculations*, Elsevier: Amsterdam, 1976; Roothaan, C. C. J. *Rev. Mod. Phys.* **1960**, 32, 179.
- <sup>8</sup> Engels, B.; Eriksson, L.; Lunell, S. *Adv. Quantum Chem.* **1996**, 27, 297.
- <sup>9</sup> Noga, J.; Bartlett, R. J. *J. Chem. Phys.* **1987**, 86, 7041.
- <sup>10</sup> Perera, S. A.; Salemi, L. M.; Bartlett, R.J.; *J. Chem. Phys.* **1997**, 106, 4061; Bartlett, R.J.; Stanton, J. F., in *Reviews in Computational Chemistry; Vol. 5*; Lipkowitz, K. B., Boyd, D. B; Eds.; VCH: New York; 1994; pp. 95-165.
- <sup>11</sup> Such reference systems exists always when the density is noninteracting  $v$ -representable, cf. ref 4.
- <sup>12</sup> Ceperley, D. M.; Alder B. J. *Phys. Rev. Lett.* **1980**, 45, 566.
- <sup>13</sup> Vosko, S. J.; Wilk L.; Nusair, M. *Can. J. Phys.* **1980**, 58, 1200.
- <sup>14</sup> Schäfer, A.; Horn, H.; Ahlrichs, R. *J. Chem. Phys* **1992**, 97, 2571.
- <sup>15</sup> Dolg, M.; Wedig, U.; Stoll, H.; Preuss, H. *J. Chem. Phys.* **1987**, 86, 866.
- <sup>16</sup> Kutzelnigg, W.; Fleischer, U.; Schindler, M. In *NMR-Basic Principles and Progress*, Vol. 23. Springer-Verlag: Heidelberg, 1990; p. 165.
- <sup>17</sup> Szasz, L. *Pseudopotential Theory of Atoms and Molecules*; Willey: New York, 1985.
- <sup>18</sup> Dolg, M.; Wedig, U.; Stoll, H.; Preuss, H. *J. Chem. Phys.* **1987**, 86, 866.

---

<sup>19</sup> a) Bergner, A.; Dolg, M.; Küchle, W.; Stoll, H.; Preuss, H. *Mol. Phys.* **1993**, *80*, 1431. b) d-Type polarization functions have been taken from: *Gaussian Basis Sets for Molecular Calculations*, Huzinaga, S., Ed.; Elsevier: New York, 1984.

<sup>20</sup> Dunning, T. H.; Hay, H. *In Methods of Electronic Structure Theory, Vol. 3 of Modern Theoretical Chemistry*, Schaefer III, H. F., Ed.; Plenum Press: New York, 1977.





*I think that there is a moral to this story, namely that it is more important to have beauty in one's equations than to have them fit experiment .... If there is not complete agreement between the results of one's work and experiment, one should not allow oneself to be too discouraged, because the discrepancy may well be due to minor features that are not properly taken into account and that will get cleared up with further developments of the theory.*

*Paul Adrien Maurice Dirac (1902-84)*

## **5 A Critical Validation of Density Functional and Coupled-Cluster Approaches for the Calculation of EPR Hyperfine Coupling Constants in Transition Metal Complexes**

### *Introduction*

Hyperfine coupling constants (tensors) are considered to be the most important part of the information obtained from an EPR spectrum, due to a very direct connection between the magnitude of the hyperfine coupling and the electronic structure of the paramagnetic species. In spite of the richness of experimental data on the hyperfine coupling in transition metal complexes, previous theoretical studies of HFCCs concentrated largely on light main group systems for which the post-Hartree-Fock *ab initio* treatment of electron correlation is still applicable. Recent developments in density functional theory provided an alternative by including electron correlation approximately, at moderate computational cost, and enabled thus calculations on systems of larger size and/or including heavier elements like transition metals. The following paper represents the first extensive evaluation of DFT methods for the prediction of hyperfine coupling constants for both metals and ligands in 3d transition metal complexes. Results obtained for a series of 21 complexes using eight different density functionals have been compared with reliable experimental data and results from elaborate coupled cluster calculations. The author of this thesis performed all of the calculations included in the study and contributed significantly to the preparation of the manuscript.

## *Results*

In the present study, no generally valid hierarchy of the tested functionals for the calculation of hyperfine coupling constants of transition-metal complexes could be established, since the performance of a given functional varies significantly for different classes of complexes. The subtleties of the electronic structures, the degree of spin contamination as well as other factors seem to be responsible for these variations. On the other hand, for a significant number of complexes a ca. 10-15% agreement with experiment has been achieved with essentially all of the functionals. In other subsets of molecules, the analysis of the electronic structure suggests the range of functionals that might be most appropriate.

## *Conclusions and outlook*

The present study has shown that the functionals to be applied to the calculation of hyperfine couplings in certain areas of transition metal chemistry have to be carefully selected. Desirable, improved functionals should provide sufficiently large spin polarization for core and valence shells without exaggerating it for the latter, and thus introducing spin contamination. Generally, hyperfine coupling constants, in particular for transition metal systems, may turn out to be a particularly fruitful testing ground for new DFT (or alternative) approaches. As noted in a very recent study by Neese<sup>1</sup>, the relatively poor performance of DFT for some of the hyperfine couplings might be connected to the wrong behavior of the state-of-the-art exchange-correlation potentials close to the nucleus where they show an unphysical divergence.<sup>2</sup> The connection between the performance of DFT and the relative size of spin polarization contributions to the HFCCs established became a motivation for a detailed analysis of mechanisms of EPR hyperfine coupling in *3d* metal complexes (Chapter 7).

The study reported in here does not include scalar relativistic and spin-orbit effects, except for a rough semi-empirical estimate of SO contributions to HFCCs for some of the complexes. Recently, the zero order regular approximation for relativistic effects (ZORA) has been employed for the calculation of EPR parameters for Ni

complexes by Stein et al.<sup>3</sup> The authors discuss in detail the relation between their results for  $[\text{Ni}(\text{CO})_3\text{H}]$  and the nonrelativistic results obtained for this complex in the following paper. A detailed evaluation of the density functional approach in the ZORA formalism has been reported recently by Belanzoni et al.<sup>4</sup> In the spin-orbit coupled equations, only spin-restricted density functionals have been applied as the current implementation of the ZORA approach does not yet allow the simultaneous inclusion of spin-orbit and spin-polarization effects.<sup>4</sup> An approach that would allow such simultaneous inclusion is currently being developed in our group.

## References

---

- <sup>1</sup> Neese, F. *J. Phys. Chem. A* **2001**, *105*, 4290.
- <sup>2</sup> (a) Van Leeuwen, R.; Baerends, E. J.; *Phys. Rev. A*. **1994**, *49*, 2421. (b) Baerends, E. J.; Gritsenko, O. V.; Van Leeuwen, R. In *Chemical Applications of Density Functional Theory*; Laird B. B., Ross, R. B., Ziegler, T., Eds.; American Chemical Society: Washington DC, 1996, p 20ff.
- <sup>3</sup> Stein, M.; van Lenthe, E.; Baerends, E. J.; Lubitz, W. *J. Phys. Chem. A* **2001**, *105*, 416.
- <sup>4</sup> Belanzoni, P.; van Lenthe, E.; Baerends, E. J. *J. Chem. Phys.* **2001**, *114*, 4421.

# A Critical Validation of Density Functional and Coupled-Cluster Approaches for the Calculation of EPR Hyperfine Coupling Constants in Transition Metal Complexes

Markéta Munzarová and Martin Kaupp\*

Max-Planck-Institut für Festkörperforschung, Heisenbergstrasse 1, D-70569 Stuttgart, Germany

Received: July 7, 1999; In Final Form: September 27, 1999

The performance of various density functional approaches for the calculation of electron paramagnetic resonance (EPR) hyperfine coupling constants in transition metal complexes has been evaluated critically by comparison with experimental data and high-level coupled-cluster results for 21 systems, representing a large variety of different electronic situations. While both gradient-corrected and hybrid functionals allow the calculation of isotropic metal hyperfine coupling constants to within ca. 10–15% for the less critical cases (e.g., ScO, TiN, TiO, VO, MnO, MnF), none of the functionals investigated performs well for all complexes. Gradient-corrected functionals tend to underestimate the important core–shell spin polarization. While this may be improved by exact-exchange mixing in some cases, the accompanying spin contamination may even lead to a deterioration of the results for other complexes. We also identify cases, where essentially none of the functionals performs satisfactorily. In the absence of a "universal functional", the functionals to be applied to the calculation of hyperfine couplings in certain areas of transition metal chemistry have to be carefully selected. Desirable, improved functionals should provide sufficiently large spin polarization for core and valence shells without exaggerating it for the latter (and thus introducing spin contamination). Coupling anisotropies and coupling constants for ligand nuclei are also discussed. The computationally much more demanding coupled cluster (CCSD and CCSD(T)) methods, which have been applied to a subset of complexes, show good performance, even when a UHF reference wave function is moderately spin-contaminated.

## 1. Introduction

Electron paramagnetic resonance (EPR) spectroscopy represents one of the most powerful experimental tools for studying the molecular and electronic structure of compounds containing unpaired electrons. Since the early days of this technique, a large number of EPR spectra for transition metal complexes have been measured. A wealth of experimental data on electronic g-tensors and hyperfine coupling constants (HFCCs) is thus available.<sup>1–8</sup> Quantitative theoretical studies of HFCCs have, however, concentrated largely on organic molecules or on other light main group systems. This is understandable, as the accurate inclusion of electron-correlation effects is mandatory for quantitative calculations of electron–nuclear hyperfine interactions. To achieve this in traditional post-Hartree–Fock *ab initio* calculations is far from trivial, and such treatments are not easily applicable to larger transition metal complexes. CAS–SCF and MR–SDCI calculations have been done on ScO, TiN, and VN by Mattar et al.,<sup>9–11</sup> as well as on VO<sub>x</sub> (*x* = 1, 2, 3) by Knight et al.<sup>12</sup> To our knowledge, no other transition metal systems have been treated at comparable levels.

Recent developments in density functional theory (DFT) do in principle provide an alternative, as DFT includes electron correlation approximately, at moderate computational cost. A number of Kohn–Sham DFT studies on transition metal HFCCs have appeared, using local-spin-density approximations (LSDA), generalized-gradient approximations (GGA), as well as hybrid functionals including exact exchange. Hyperfine parameters have been computed for VN by Mattar and Doleman,<sup>11</sup> for TiN and TiO by Engels et al.,<sup>13</sup> for CuC<sub>2</sub>H<sub>2</sub> and Cu(CO) by Barone et al.,<sup>14,15</sup> for a ruthenium complex by Aarnts et al.,<sup>16</sup> for TiF<sub>3</sub> by

Belanzoni et al.<sup>17,18</sup> and by van Lenthe et al.,<sup>19</sup> and for a series of molybdenum(V) oxyhalide anions by Swann and Westmoreland.<sup>20</sup> During the course of the present study, Knight et al. reported DFT results on MO (*M* = Sc, Y, La).<sup>21</sup> A number of earlier calculations employed the X<sub>α</sub> method.<sup>22–24</sup> Reasonable agreement between experiment and theory for the isotropic HFCCs has been found when significant metal *s*-character in the singly occupied molecular orbitals (SOMOs) leads to a dominance of direct contributions to the spin density at the nucleus. The description is expected to be considerably more complicated when spin-polarization effects become large, a situation that should apply for many transition metal systems.<sup>1</sup>

In the studies mentioned, only a limited number of exchange–correlation functionals and basis sets have been employed, and only a relatively small set of molecules and electronic structure situations was encompassed. Further systematic studies are thus needed, if one wants to be able to judge in detail the ability of the available DFT approaches to describe HFCCs for transition metal systems. Here we present a critical validation study, including twenty-one first-row transition metal complexes and eight different state-of-the-art exchange–correlation potentials  $\nu_{xc}$ . Throughout this work, we have learned much about the mechanisms of spin polarization and related phenomena for HFCCs in transition metal complexes. These interpretational aspects will be covered in more detail elsewhere<sup>25</sup> (including numerical results), but will be touched upon briefly in this work whenever needed for an understanding of the performance of different functionals.

After outlining roughly the nonrelativistic theoretical formalism of hyperfine couplings in section 2 (mainly to connect to the rather different types of experimental information available), we will discuss problems connected with the selection of

\* Corresponding author e-mail: kaupp@vsibm1.mpi-stuttgart.mpg.de

experimental data (section 3). Information on molecular structures, basis sets, and theoretical approaches used is given in section 4. After a description of coupled cluster results for a subset of the complexes (section 5), which we employ as reference data, basis set effects are examined in section 6. Then the performance of different exchange–correlation functionals is compared systematically for the metal HFCCs (section 7), followed by a brief discussion of ligand HFCCs (section 8). A number of general conclusions are provided in section 9.

## 2. Theoretical Formalism

The theory of EPR hyperfine couplings is covered in detail in text books,<sup>1,3–8,26</sup> and we summarize only those points which are important for the comparison between computed and experimental quantities. The hyperfine coupling parameters describe the interactions of unpaired electrons with various magnetic nuclei. The  $3 \times 3$  hyperfine interaction tensor  $A$  can be separated into its isotropic and anisotropic (dipolar) components.<sup>6</sup> In the first-order approximation (neglecting spin–orbit effects; cf. discussion in section 4), isotropic hyperfine splittings  $A_{\text{iso}}(\text{N})$  are equal to the Fermi contact term  $A_{\text{FC}}$  and they are related to the spin densities  $\rho^{\alpha-\beta}(R_{\text{N}})$  at the corresponding nuclei by<sup>4</sup>

$$A_{\text{iso}}(\text{N}) = A_{\text{FC}} = \frac{4\pi}{3} \beta_e \beta_N g_e g_N \langle S_Z \rangle^{-1} \rho_N^{\alpha-\beta} \quad (1)$$

where  $\beta_e$  is the Bohr magneton,  $\beta_N$  the nuclear magneton,  $g_e$  the free electron  $g$ -value (2.002 319 31). The  $g$ -value of the nucleus  $\text{N}$  is given by  $g_N = \mu_N / I_N$  ( $\mu_N$  is the nuclear magnetic moment of nucleus  $\text{N}$  in units of  $\beta_N$ , and  $I_N$  is the total nuclear spin for that nucleus).  $\langle S_Z \rangle$  is the expectation value of the  $z$ -component of the total electronic spin. The spin density  $\rho_N^{\alpha-\beta}$  at the position of nucleus  $\text{N}$  ( $R_{\text{N}}$ ) can be expressed as:

$$\rho_N^{\alpha-\beta} = \sum_{\mu,\nu} P_{\mu,\nu}^{\alpha-\beta} \langle \phi_\mu | \delta(R_{\text{N}}) | \phi_\nu \rangle \quad (2)$$

where  $P_{\mu,\nu}^{\alpha-\beta}$  is the spin density matrix. We will in the following abbreviate  $\rho_N^{\alpha-\beta}$  by  $\rho_N$ .

The components  $T_{kl}$  of the anisotropic tensor are in the first-order approximation given by<sup>31</sup>

$$T_{kl}(\text{N}) = \frac{1}{2} \beta_e \beta_N g_e g_N \langle S_Z \rangle^{-1} \sum_{\mu\nu} P_{\mu,\nu}^{\alpha-\beta} \times \langle \phi_\mu | r_N^{-5} (r_N^2 \delta_{kl} - 3r_{N,k} r_{N,l}) | \phi_\nu \rangle \quad (3)$$

where  $r_{\text{N}} = r - R_{\text{N}}$ .  $T$  is always traceless and may be brought to diagonal form. For magnetic nuclei with an electronic environment of axial symmetry (i.e., those located on an at least 3-fold symmetry axis), it has the form  $(-A_{\text{dip}}, -A_{\text{dip}}, 2A_{\text{dip}})$ , where  $A_{\text{dip}}$  is the so-called dipolar coupling constant. From the experimental tensor components ( $A_{\perp}$ ,  $A_{\perp}$ ,  $A_{\parallel}$ ),  $A_{\text{iso}}$  and  $A_{\text{dip}}$  may then be extracted via  $A_{\text{iso}} = (A_{\parallel} + 2A_{\perp})/3$ ,  $A_{\text{dip}} = (A_{\parallel} - A_{\perp})/3$ . Another terminology is used in gas-phase spectroscopy studies.<sup>30</sup> The high-resolution spectra of linear molecules can be described in terms of five parameters ( $a$ ,  $b$ ,  $c$ ,  $d$ ,  $e$ ), of which  $b$  and  $c$  are related to  $A_{\text{iso}}$  and  $A_{\text{dip}}$  as  $A_{\text{iso}} = (b + c/3)$  and  $A_{\text{dip}} = c/3$ .

All transition metal nuclei in the present study are at sites of axial symmetry. Although this is not the case for all ligands, experimentalists in the field prefer to use the “ $A_{\text{dip}}$ ” terminology, even if it is not justified by symmetry. This is often due to the fact that the dipolar ligand splittings are small, and two different “perpendicular” components are not observed in the spectra (at least for complexes such as those considered here, where the

unpaired spin density is mainly localized on the metal). See section 4 for comments on spin–orbit corrections to the hyperfine couplings.

## 3. Selection of Experimental Data

The selection of the molecules used in this study was determined mainly by the availability of experimental data on small systems having a well-resolved hyperfine structure for the metal and, if possible, also for the ligands. We have included examples for all first-row transition metals. Some pairs of isoelectronic molecules have been selected to compare different transition metals in similar electronic surroundings. In the following we will comment on the interpretation of the measured data and on the expected accuracy of different experimental techniques.

**Gas-Phase Data.** For all diatomic oxides and nitrides, and for MnH, literature hyperfine parameters from high-resolution gas-phase molecular spectroscopy have been used. The relative positions of the energy levels were obtained either directly by monitoring of the absorption/emission (“pure” microwave rotational spectroscopy) or indirectly (through fluorescence or molecular beam deflection).<sup>30</sup> The hyperfine parameters have been determined from the analysis of the level splittings. The accuracy of such measurements is usually very high, sometimes in the kHz range for microwave optical double resonance.<sup>27–29</sup>

In most of the gas-phase investigations, the interactions between molecules represent relatively small perturbations which usually affect only the widths of the spectral lines; in molecular beam studies such interactions are completely absent.<sup>30</sup> This makes the gas-phase data most reliable for comparison with our computed data on isolated molecules. Moreover, in these gas-phase experiments, the sign of the HFCCs is known.

**Condensed-Phase EPR Data.** For the remaining systems, the hyperfine parameters had to be taken from condensed-phase EPR spectroscopy. Different trapping sites (mostly inert-gas matrices, but also host crystals and frozen solutions) are thus involved. Obviously, the environment can influence the values of the hyperfine parameters, in particular of the isotropic coupling constants,<sup>31</sup> due to both structural and electronic effects. This complicates the comparison of our calculated data with experiment.

In those few cases where EPR results are available on the same complex from both gas- and condensed-phase measurements, the HFCCs differ typically by a few percent, up to ca. 10% in extreme cases. Thus, e.g., the gas-to-matrix shift for  $A_{\text{iso}}(\text{V})$  of VO is less than 3% of the absolute value (data available are 798 MHz in Ne matrix,<sup>12</sup> 796 MHz in Ar matrix,<sup>32</sup> and 778 MHz in the gas phase<sup>33</sup>). The situation is similar for ScO (cf. matrix values of 2005–2018 MHz<sup>34,21</sup> vs gas-phase value of 1947 MHz<sup>28</sup> for  $A_{\text{iso}}(\text{Sc})$ ). Larger gas-to-matrix shifts have been found for MnO (7%; cf. 448 MHz in matrix<sup>35</sup> vs 480 MHz in the gas phase<sup>36</sup>) and MnH (11%, see ref 37). For charged species, counterion effects may be considerable and have to be kept in mind as a potential source of errors.

In view of these environmental effects, we cannot aim at a better agreement with condensed-phase experiments than ca. 10–15%. Furthermore, the theoretical values should best be compared with the whole range of accurate experimental data available. This is most important for complexes with very small isotropic coupling constants, since these are particularly sensitive to the influence of the surroundings. We note also that the computed structures do not include any rovibrational corrections. On the other hand, the experimental structures also have to be viewed with some error bars. Structural aspects contribute thus

**TABLE 1: Structures Used in the HFCC Calculations<sup>a</sup>**

| molecule                               |                | metal–ligand (intraligand) bond lengths and angles  | source <sup>b</sup>   |
|--|----------------|---|-----------------------|
| ScO                                    | $C_{\infty v}$ | 1.667   | opt                   |
| TiN                                    | $C_{\infty v}$ | 1.567   | opt                   |
| TiO                                    | $C_{\infty v}$ | 1.623   | <i>c</i>              |
| VN                                     | $C_{\infty v}$ | 1.567   | <i>d</i>              |
| VO                                     | $C_{\infty v}$ | 1.589   | <i>e</i>              |
| MnH                                    | $C_{\infty v}$ | 1.731   | <i>f</i>              |
| MnO                                    | $C_{\infty v}$ | 1.648   | <i>g</i>              |
| MnF                                    | $C_{\infty v}$ | 1.839   | opt                   |
| CuO                                    | $C_{\infty v}$ | 1.729   | <i>h</i>              |
| MnF <sub>2</sub>                       | $D_{\infty h}$ | 1.811   | <i>i</i>              |
| TiF <sub>3</sub>                       | $D_{3h}$       | 1.780   | opt                   |
| MnO <sub>3</sub>                       | $D_{3h}$       | 1.579   | opt                   |
| [Cu(CO) <sub>3</sub> ]                 | $D_{3h}$       | 1.796 (1.151)   | opt. MP2 <sup>j</sup> |
| [Cr(CO) <sub>4</sub> ] <sup>+</sup>    | $T_d$          | 2.190 (1.122)   | opt                   |
| [Mn(CN) <sub>4</sub> ] <sup>2-</sup>   | $T_d$          | 2.158 (1.133)   | <i>k</i>              |
| [Ni(CO) <sub>3</sub> H]                | $C_{3v}$       | d(Ni–H) = 1.512, d(Ni–C) = 1.851, d(C–O) = 1.135,<br>∠(H–Ni–C) = 90.87, ∠(Ni–C–O) = 171.29  | opt                   |
| [Co(CO) <sub>4</sub> ]                 | $C_{3v}$       | d(Co–C <sub>ax</sub> ) = 1.875, d(Co–C <sub>eq</sub> ) = 1.847, d(C–O) <sub>ax</sub> = 1.137, d(C–O) <sub>eq</sub> = 1.139<br>∠(C <sub>ax</sub> –Co–C <sub>eq</sub> ) = 99.2, ∠(Co–C–O) = 179.2   | opt                   |
| [Mn(CN) <sub>4</sub> N] <sup>-</sup>   | $C_{4v}$       | d(Mn–N) = 1.504, d(Mn–C) = 1.967, d(C–N) = 1.165,<br>∠(N–Co–C) = 103.97, ∠(Mn–C–N) = 180.00   | opt                   |
| [Mn(CN) <sub>5</sub> NO] <sup>2-</sup> | $C_{4v}$       | d(Mn–C <sub>ax</sub> ) = 2.009, d(Mn–C <sub>eq</sub> ) = 2.025, d(C–N) <sub>ax</sub> = 1.167,<br>d(C–N) <sub>eq</sub> = 1.168, d(Mn–N <sub>nitros</sub> ) = 1.722, d(N–O) <sub>nitros</sub> = 1.169,<br>∠(C <sub>ax</sub> –Mn–C <sub>eq</sub> ) = 86.81, ∠(Mn–C–N) = 180.00 | opt                   |
| [Mn(CO) <sub>5</sub> ]                 | $C_{4v}$       | d(Mn–C <sub>ax</sub> ) = 1.845, d(Mn–C <sub>eq</sub> ) = 1.875, d(C–O) <sub>ax</sub> = 1.143, d(C–O) <sub>eq</sub> = 1.141,<br>∠(C <sub>ax</sub> –Mn–C <sub>eq</sub> ) = 97.01, ∠(Mn–C <sub>eq</sub> –O <sub>eq</sub> ) = 179.95  | opt                   |
| [Fe(CO) <sub>5</sub> ] <sup>+</sup>    | $C_{4v}$       | d(Fe–C <sub>ax</sub> ) = 1.969, d(Fe–C <sub>eq</sub> ) = 1.906, d(C–O) <sub>ax</sub> = 1.125, d(C–O) <sub>eq</sub> = 1.125,<br>∠(C <sub>ax</sub> –Fe–C <sub>eq</sub> ) = 96.11, ∠(Fe–C <sub>eq</sub> –O <sub>eq</sub> ) = 179.94  | opt                   |

<sup>a</sup> Distances in Å, angles in degrees <sup>b</sup> Opt = optimized in this work, otherwise the corresponding experimental reference is given. <sup>c</sup> Hocking, H.; Gerry, M. C.; Merrer, A. J. *Can. J. Phys.* **1979**, *57*, 54. <sup>d</sup> Balfour, J.; Merer, A. J.; Niki, H.; Simard, B.; Hackett, P. A. *J. Chem. Phys.* **1993**, *99*, 3288. <sup>e</sup> Reference 12. <sup>f</sup> Herzberg, H. *Spectra of Diatomic Molecules*; Van Nostrand: Princeton, New Jersey, 1950. <sup>g</sup> Gordon, R. M.; Merer, A. J. *Can. J. Phys.* **1980**, *58*, 642. <sup>h</sup> Merer, A. J. *Ann. Rev. Phys. Chem.* **1989**, *40*, 407. <sup>i</sup> *Landolt-Börnstein Numerical Data and Functional Relationships in Science and Technology, New Series, Group II, Vol. 21*; Madelung, O., Ed.; Springer: Berlin, 1992; p 74. <sup>j</sup> See text. At the DFT level, we obtain d(Cu–C) = 1.880 Å; d(C–O) = 1.140 Å. <sup>k</sup> Reference 53.

also to the uncertainties in the comparison between calculation and experiment.

From the solid-state EPR spectrum, only absolute values of the hyperfine tensor components (e.g.,  $|A_{||}|$  and  $|A_{\perp}|$ ) for an axially symmetric center can be determined. Additional information can be obtained, e.g., from the signs of the components of the nuclear quadrupolar tensor, so that the sign of  $A_{||}$  and/or  $A_{\perp}$  may be deduced.<sup>38</sup> Another possibility is to compare  $|A_{||}|$  and  $|A_{\perp}|$  from the solid-state measurement with the  $|A_{\text{iso}}|$  result obtained via EPR in a solution. Unfortunately, such information is usually not available, and four combinations of  $A_{\text{iso}}$  and  $A_{\text{dip}}$  are possible. To decide which of them is the correct one, theoretical arguments have to be considered. For example, the sign of  $A_{\text{dip}}$  may be estimated from the type of the singly occupied molecular orbital (SOMO) present. Chemically similar complexes may be expected to have the same signs of  $A_{||}$  and  $A_{\perp}$ , etc.

In this study, those signs of  $A_{||}$  and  $A_{\perp}$  are given in the tables (if not known experimentally), for which the resulting value of  $A_{\text{dip}}$  is as close as possible to our theoretical value. This choice is a natural one, since the calculation of the anisotropic coupling parameters is much less sensitive to the theoretical approach, and thus reasonable agreement with experiment is usually found.<sup>13</sup> In the majority of cases, the resulting sign turned out to be consistent with that adopted in the experimental papers. For several particular cases, the choice of sign is further discussed in the footnotes to the tables.

All values of the hyperfine parameters are given in MHz. In those cases where the experimental data have been reported in Gauss, they have been converted to MHz by multiplying with a factor of 2.80238(g/g<sub>e</sub>).<sup>2</sup>

#### 4. Computational Details

Molecular structures used for the hyperfine structure calculations were taken from experiment where available or have otherwise been optimized in unrestricted Kohn–Sham calculations with the B3LYP functional (using the *Gaussian 94* program<sup>39</sup>). The optimizations employed small-core effective-core potentials (ECPs) and (8s7p6d)/[6s5p3d] GTO valence basis sets for the metals,<sup>40</sup> and ECPs with (4s4p1d)/[2s2p1d] basis sets<sup>41</sup> for the ligand atoms (a (4s1p)/[2s1p] hydrogen basis<sup>42</sup> was used for MnH and [Ni(CO)<sub>3</sub>H]). The resulting structure parameters are summarized in Table 1. [Cu(CO)<sub>3</sub>] is a weakly bonded complex with significant dispersion contributions to the bonding. Here the DFT optimizations are known to overestimate the Cu–C distance, and we have therefore resorted to an MP2 optimization with one f-function ( $\alpha = 3.525^{43}$ ) added to the metal basis set.

The following symmetry restrictions have been used in the optimizations:  $D_{3h}$  symmetry was used for TiF<sub>3</sub> and MnO<sub>3</sub> and for [Cu(CO)<sub>3</sub>]. The trigonal planar structures are consistent with hyperfine data<sup>44–47</sup> and IR spectra.<sup>48,49</sup>  $D_{3h}$  symmetry has also been established theoretically for TiF<sub>3</sub> by Belanzoni et al.<sup>17</sup> [Co(CO)<sub>4</sub>] and [Ni(CO)<sub>3</sub>H] have  $C_{3v}$  symmetry.<sup>50,51</sup>  $T_d$  symmetry was used for [Cr(CO)<sub>4</sub>]<sup>+</sup> and [Mn(CN)<sub>4</sub>]<sup>2-</sup>, again in agreement with experimental evidence.<sup>52,53</sup>  $C_{4v}$  symmetry has been imposed for [Mn(CO)<sub>5</sub>] and [Fe(CO)<sub>5</sub>]<sup>+</sup>, consistent with the EPR spectra.<sup>54,55</sup> DFT optimizations performed by Rosa et al.<sup>56</sup> for [Mn(CO)<sub>5</sub>] and by Ricca et al.<sup>57</sup> for [Fe(CO)<sub>5</sub>]<sup>+</sup> have provided structural parameters close to ours. Our optimizations for [Mn(CN)<sub>4</sub>N]<sup>-</sup>, starting from the experimental  $C_{2v}$  structure of [Mn(CN)<sub>4</sub>N]<sup>2-</sup>,<sup>58</sup> converged to a regular square pyramid ( $C_{4v}$ ), in agreement with the observed hyperfine structure.<sup>58</sup> The struc-

ture of  $[\text{Mn}(\text{CN})_5\text{NO}]^{2-}$  was optimized in  $C_{4v}$  symmetry, starting from experimental structure of Pink and Billing.<sup>59</sup> In discussions of the electronic structure of the complexes, we generally refer to the conventional orientation for a given point group.

The all-electron DFT calculations (cf. below for the basis sets) of the hyperfine structure were done with the *Gaussian 94* program.<sup>39</sup> Unless noted otherwise, unrestricted Kohn–Sham calculations were carried out. We have compared eight different combinations of exchange and correlation potentials ( $\nu_x[\rho]$  and  $\nu_c[\rho]$ , respectively), abbreviated as BLYP, BP86, BPW91, B3LYP, B3PW91, BHLYP, BHP86, and BHPW91. The first three combine Becke’s GGA functional for exchange<sup>60</sup> (B) with three different GGAs for correlation (LYP,<sup>61</sup> P86,<sup>62</sup> and PW91<sup>63</sup>). The fourth and fifth combinations use instead for exchange Becke’s three-parameter hybrid functional (B3; this includes ca. 20% exact exchange).<sup>64</sup> Finally, for the last three functionals we have used the “half-and-half” hybrid (BH), incorporating as much as 50% exact exchange.<sup>65</sup> Such functionals are somewhat less popular but have been reported to perform particularly well for certain classes of open-shell main group<sup>66</sup> or transition metal<sup>67</sup> compounds. All functionals were used in their *Gaussian 94* implementation.<sup>39</sup> To obtain further high-level ab initio data to compare with, we have carried out coupled cluster [CCSD and CCSD(T)] calculations for a subset of molecules, using unrestricted Hartree–Fock reference wave functions (unless noted otherwise) and the ACES–II code.<sup>68</sup>

As a medium-size metal basis set for use in larger systems, we have constructed a (15s11p6d)/[9s7p4d] basis. Our starting point was the DZ basis of Schäfer et al.,<sup>69</sup> to which we added the most diffuse functions (a 1s2p1d set) from the ECP valence basis of Dolg et al.<sup>40</sup> IGLO–III basis sets<sup>70</sup> were used for the main group atoms.

Basis-set convergence was tested for several of the smaller complexes. To this end, we used a larger (21s15p10d3f)/[13s10p6d2f] metal basis, constructed from the atomic natural orbital (ANO) basis sets of Roos et al.<sup>71</sup> as follows: the 1s-, 2p-, 3p-, and 3d-ANO coefficients were used to contract s-functions 1–12, p-functions 1–10, p-functions 5–12, and d-functions 1–10, respectively. To this we added, in an uncontracted fashion, s-functions 10–21, p-functions 8–15, and d-functions 6–10. Finally, the 3f set of Bauschlicher et al.<sup>72</sup> has been added in a 21 contraction. For both the smaller and larger metal basis sets, more flexible contractions have furthermore been tested (section 5).

As a somewhat larger basis for the first-row main group atoms, we have constructed a (14s8p3d1f)/[8s6p3d1f] set, starting from the cc-pV5Z basis.<sup>73</sup> To the contracted sets of s-functions 1–11 and p-functions 1–8, s-functions 8–14 and p-functions 4–8 have been added in an uncontracted way, as well as three d-functions and one f-function from the cc-pVQZ basis.<sup>73</sup>

The results we give have been obtained with the default integration grids (int = finegrid option<sup>39</sup>) of the *Gaussian 94* program. For various complexes we have also tested larger angular and radial grids (results not shown). The effect of different grids was generally below 1% of the computed HFCCs, even with the largest, uncontracted basis sets.

The present calculations do not include relativistic corrections. Scalar relativistic effects on the isotropic metal HFCCs may be estimated roughly from hydrogen-like multiplicative correction factors to magnetic s-type hyperfine integrals.<sup>74</sup> These range from 1.036 for Sc to 1.072 for Cu. This suggests that the neglect of scalar relativistic effects may lead maximally to an underestimate of  $\rho_N$  by ca. 4–7% within the first transition metal row (in the case of a pure s-type SOMO). The influence on

TABLE 2: Available Experimental g-Tensor Components<sup>a</sup>

| molecule                               | $g_{\perp}$ | $g_{\parallel}$     |
|--|-------------|---------------------|
| ScO <sup>b</sup>                       | 2.0018(3)   | 2.0018(3)           |
| TiF <sub>3</sub>                       | 1.8808      | 1.9902              |
| VO <sup>c</sup>                        | 1.980       | 2.002               |
| [Cr(CO) <sub>4</sub> ] <sup>+</sup>    | 1.9986      | 1.9986              |
| MnH                                    | 2.001       | 2.0023 <sup>d</sup> |
| MnO <sup>e</sup>                       | 1.995       | 2.0023 <sup>d</sup> |
| MnO <sub>3</sub>                       | 2.0084      | 2.0036              |
| MnF                                    | 1.999       | 2.002 <sup>d</sup>  |
| MnF <sub>2</sub>                       | 1.999       | 2.002 <sup>d</sup>  |
| [Mn(CN) <sub>4</sub> ] <sup>2-</sup>   | 2.003       | 2.003               |
| [Mn(CO) <sub>5</sub> ]                 | 2.043       | 2.004               |
| [Fe(CO) <sub>5</sub> ] <sup>+</sup>    | 2.0832      | 2.008               |
|  | 2.0797      |                     |
| [Mn(CN) <sub>5</sub> NO] <sup>2-</sup> | 2.0311      | 1.9922              |
| [Mn(CN) <sub>4</sub> N] <sup>-</sup>   | 2.0045      | 1.999               |
| [Co(CO) <sub>4</sub> ]                 | 2.1299      | 2.0059              |
| [Ni(CO) <sub>3</sub> H]                | 2.0674      | 2.0042              |
| [Cu(CO) <sub>3</sub> ]                 | 2.0002      | 2.0008              |

<sup>a</sup> See footnotes to Tables 8 and 10 for references. The g-values were usually estimated from the spectra without considering second-order effects. The g-value of the free electron is 2.0023. <sup>b</sup> Reference 21. <sup>c</sup> Reference 12. <sup>d</sup> Assumed in the experimental work. <sup>e</sup> Reference 35.

dipolar couplings is expected to be somewhat less pronounced. Explicit scalar relativistic DFT calculations on TiF<sub>3</sub><sup>19</sup> enhanced  $\rho_N(\text{Ti})$  by ca. 2% and decreased  $A_{\text{dip}}(\text{Ti})$  by a similar amount. Interestingly, these calculations indicated scalar relativistic effects for the (small) <sup>19</sup>F HFCCs on the order of ca. 10–20%. This has to be kept in mind when discussing the ligand HFCCs (section 8).

Spin–orbit effects may manifest themselves in a second-order “pseudocontact” contribution to  $A_{\text{iso}}$  ( $A_{\text{PC}}$ ), and in a second-order contribution to  $A_{\text{dip}}$  ( $A_{\text{dip},2}$ ).<sup>3,8,17,75</sup> When the g-tensor of a system is known, a rough semiempirical estimate of spin–orbit contributions to the HFCCs may be obtained along the lines of the classical perturbation theoretical approach of Abragam and Pryce<sup>76</sup> (more details for specific d-orbital occupations and coordination arrangements are given in ref 8). For example, for a d<sup>1</sup>-system in a trigonally distorted octahedral field (d<sub>z<sup>2</sup></sub>-configuration), we may use equations (9.204)–(9.209) in ref 8 to get

$$A_{\parallel} = A_{\text{FC}} + P \left[ \frac{4}{7} \delta^2 - \frac{1}{7} \Delta g_{\perp} \right]$$

$$A_{\perp} = A_{\text{FC}} + P \left[ -\frac{2}{7} \delta^2 + \frac{15}{14} \Delta g_{\perp} \right] \quad (4)$$

where  $P = (\mu_0/4\pi)2\mu_B\langle r^3 \rangle$ ,  $\delta$  is d<sub>z<sup>2</sup></sub>-orbital coefficient in the SOMO, and  $\Delta g_{\perp} = g_e - g_{\perp}$ . Now, setting  $(2/7)\delta^2 P = A_{\text{dip}}$ , we get

$$A'_{\parallel} = A_{\parallel} - A_{\text{FC}} = A_{\text{dip}} \left[ 2 - \frac{\Delta g_{\perp}}{2\delta^2} \right]$$

$$A'_{\perp} = A_{\perp} - A_{\text{FC}} = A_{\text{dip}} \left[ -1 + \frac{15\Delta g_{\perp}}{4\delta^2} \right] \quad (5)$$

Since  $A'_{\perp} = -A_{\text{dip}} - A_{\text{dip},2} + A_{\text{PC}}$  and  $A_{\text{PC}} = 1/3(A'_{\parallel} + 2A'_{\perp})$ , we get

$$A_{\text{PC}} = \frac{7\Delta g_{\perp} A_{\text{dip}}}{3\delta^2} \quad A_{\text{dip},2} = -\frac{17\Delta g_{\perp} A_{\text{dip}}}{12\delta^2} \quad (6)$$

Using our DFT results for  $A_{\text{dip}}$  (we chose the BPW91 data), together with experimental values of the g-tensor components (Table 2), we may thus approximately estimate the spin–orbit



**TABLE 3: Coupled-Cluster Results (in MHz)**

| molecule                                   | 9s7p4d            |                    |  | 15s10p6d2f    |               | exp <sup>a</sup>              |
|--|-------------------|--------------------|--|---------------|---------------|-------------------------------|
|  | RCCSD             | UCCSD              | UCCSD(T)   | UCCSD         | UCCSD(T)      |                               |
| <i>A</i> <sub>iso</sub> (M)                |                   |                    |  |               |               |                               |
| <sup>2</sup> ScO                           |                   | 1823.1             | 1819.2   | 1837.3        | 1837.1        | 1947.339(2)                   |
| <sup>4</sup> VO                            |                   | 676.6              | 730.4  | 702.1         | 740.8         | 778(2)                        |
| <sup>6</sup> MnO                           | 416.6             | 441.6              | 435.2  | 467.6         | 460.6         | 479.9                         |
| <sup>6</sup> MnF <sub>2</sub>              | 64.4              | 63.0               | 77.3   |               |               | 104(6) <sup>b</sup>           |
| <sup>7</sup> MnH                           |                   | 217.0              | 216.7  | 242.2         | 243.4         | 279.4                         |
| <sup>2</sup> TiF <sub>3</sub>              | -170.9            | -170.5             |  |               |               | -177.1(4) <sup>b</sup>        |
| <sup>2</sup> MnO <sub>3</sub>              | 1492.0            | 1511.3             |  |               |               | 1613(6)                       |
| <sup>2</sup> CuO                           |                   | -498.9             | -515.0   | -538.4        | -552.1        | -483.6(94)                    |
| <i>A</i> <sub>dip</sub> (M)                |                   |                    |  |               |               |                               |
| <sup>2</sup> ScO                           |                   | 23.1               | 23.9   | 23.7          | 24.3          | 24.8                          |
| <sup>4</sup> VO                            |                   | -46.5              | -46.3  | -47.6         | -46.5         | -41.2                         |
| <sup>6</sup> MnO                           | -16.0             | -16.7              | -17.3  | -16.9         | -17.8         | -16.1                         |
| <sup>6</sup> MnF <sub>2</sub>              | 4.2               | 4.1                | 3.5  |               |               | 10(6) <sup>b</sup>            |
| <sup>7</sup> MnH                           |                   | 12.0               | 12.0   | 12.6          | 12.6          | 12.0(8)                       |
| <sup>2</sup> TiF <sub>3</sub>              | -7.5              | -7.5               |  |               |               | -6.6(4) <sup>b</sup>          |
| <sup>2</sup> MnO <sub>3</sub>              | 94.7              | 101.5              |  |               |               | 81(3)                         |
| <sup>2</sup> CuO                           |                   | 34.4               | 34.9   | 44.6          | 46.2          | 24.1                          |
| <i>A</i> <sub>iso</sub> (X)                |                   |                    |  |               |               |                               |
| <sup>2</sup> ScO                           |                   | -17.4              | -23.9  | -17.3         | -23.7         | -20.3(3) <sup>b</sup>         |
| <sup>4</sup> VO                            |                   | 3.8                | 3.8  | 4.2           | 3.4           | 0(4)                          |
| <sup>6</sup> MnO                           | -5.1              | -7.0               | -6.9   | -8.2          | -7.9          |                               |
| <sup>6</sup> MnF <sub>2</sub>              | 9.9               | 9.9                | 9.5  |               |               |                               |
| <sup>7</sup> MnH                           |                   | 13.6               | 13.8   | 15.3          | 17.1          | 20.7(39)                      |
| <sup>2</sup> TiF <sub>3</sub>              | -33.3             | -35.1              |  |               |               | 8.3(4) <sup>c</sup>           |
| <sup>2</sup> MnO <sub>3</sub>              | 4.9               | 7.8                |  |               |               |                               |
| <sup>2</sup> CuO                           |                   | -42.7              | -40.9  | -43.6         | -41.6         |                               |
| <i>A</i> <sub>dip</sub> (X)                |                   |                    |  |               |               |                               |
| <sup>2</sup> ScO                           |                   | 0.4                | -0.1   | 0.7           | -0.1          | 0.4(2) <sup>b</sup>           |
| <sup>4</sup> VO                            |                   | 2.2                | -3.2   | 1.4           | -2.7          | 0(3)                          |
| <sup>6</sup> MnO                           | 9.2               | 11.1               | 8.6  | 11.5          | 8.7           |                               |
| <sup>6</sup> MnF <sub>2</sub>              | -10.3             | -10.2              | -10.6  |               |               |                               |
| <sup>7</sup> MnH                           |                   | 11.8               | 11.8   | 11.9          | 11.8          | 8.4(33)                       |
| <sup>2</sup> TiF <sub>3</sub> <sup>d</sup> | 18.0, 6.1, -24.0  | 18.7, 5.9, -24.6   |  |               |               | <i>e</i>                      |
| <sup>2</sup> MnO <sub>3</sub> <sup>d</sup> | -22.6, -7.7, 30.3 | -27.0, -35.8, 62.8 |  |               |               |                               |
| <sup>2</sup> CuO                           |                   | 57.6               | 55.9   | 57.6          | 55.8          |                               |
|  |                   |                    | $\langle S^2 \rangle_{\text{CC}} / \langle S^2 \rangle_{\text{UHF}}$ |               |               | nominal $\langle S^2 \rangle$ |
| <sup>2</sup> ScO                           |                   | 0.751/0.756        | 0.750/0.756  | 0.751/0.755   | 0.750/0.755   | 0.750                         |
| <sup>4</sup> VO                            |                   | 3.779/4.229        | 3.741/4.229  | 3.782/4.238   | 3.739/4.238   | 3.750                         |
| <sup>6</sup> MnO                           | 8.838/8.750       | 8.828/9.534        | 8.727/9.534  | 8.859/9.532   | 8.722/9.532   | 8.750                         |
| <sup>6</sup> MnF <sub>2</sub>              | 8.752/8.750       | 8.762/8.752        | 8.750/8.762  |               |               | 8.750                         |
| <sup>7</sup> MnH                           |                   | 12.000/12.005      | 12.000/12.005  | 12.001/12.005 | 12.000/12.005 | 12.000                        |
| <sup>2</sup> TiF <sub>3</sub>              | 0.750/0.750       | 0.750/0.753        |  |               |               | 0.750                         |
| <sup>2</sup> MnO <sub>3</sub>              | 0.771/0.750       | 1.068/2.601        |  |               |               | 0.750                         |
| <sup>2</sup> CuO                           |                   | 0.754/0.772        | 0.750/0.772  | 0.754/0.772   | 0.750/0.772   | 0.750                         |

<sup>a</sup> Cf. footnotes to Tables 8 and 10 for sources of experimental data. <sup>b</sup> Ne matrix result. Tables 8–11 also include the Ar matrix results. <sup>c</sup> Reference 44, cf. reference 18 for a revision. <sup>d</sup> Nonaxial tensor. The  $T_{ii}$  components are given in order: (1) along the metal–ligand bond, (2) normal to the metal–ligand bond, in the molecular plane, (3) along the molecular  $z$ -axis. <sup>e</sup> Anisotropy experimentally not well defined, cf. discussion in reference 18.

contributions to the hyperfine parameters from eq 6. The values of  $\delta$  were obtained from the Mulliken population analysis of the SOMO composition. The formulas given here may be used for any axially symmetric system with the SOMO dominated by the metal  $d_z^2$  orbital. This approach is used for TiF<sub>3</sub>, [Mn(CO)<sub>5</sub>], [Fe(CO)<sub>5</sub>]<sup>+</sup>, [Ni(CO)<sub>3</sub>H], and [Co(CO)<sub>4</sub>]. We use related formulae to estimate the spin–orbit contributions for [Mn(CN)<sub>5</sub>NO]<sup>2-</sup>, where the SOMO is a metal  $d_{xy}$  orbital. In essentially all other cases, deviations of the  $g$ -tensors from the free-electron  $g$ -value are sufficiently small to expect negligible spin–orbit effects on the HFCCs (no experimental  $g$ -tensor is available for CuO; for this complex we expect significant SO effects, cf. section 7). We should also note that the assumption of the  $d_z^2$  orbital dominating the SOMO is not entirely appropriate for [Mn(CO)<sub>5</sub>] and [Ni(CO)<sub>3</sub>H] (significant  $4p_z$  character has to be considered), which may lead to a significant error in the estimate (see section 7).

## 5. Coupled-Cluster Results

The CCSD and CCSD(T) calculations carried out on a subset of complexes (ScO, VO, MnO, MnF<sub>2</sub>, MnH, TiF<sub>3</sub>, MnO<sub>3</sub>, and CuO) should provide benchmark data for the validation of the more economical DFT approaches. The results are summarized in Table 3. Both the standard 9s7p4d and the more flexible 15s10p6d2f metal basis sets were used for the diatomics (see also section 6), together with the IGLO–III basis for the ligand atoms. With the available computational resources we could not use the larger basis set for MnF<sub>2</sub>, TiF<sub>3</sub>, or MnO<sub>3</sub> (for the latter two complexes, even the CCSD(T) calculations with the smaller basis exceeded our available resources). While the larger basis should be essentially saturated in the important range of the outermost core shells (cf. section 6), it is probably still incomplete with respect to higher angular-momentum functions necessary for the explicit description of electron correlation.

Disregarding CuO for the moment, the results of the largest CCSD(T)/15s10p6d2f calculations for the isotropic metal coupling constants are only ca. 4–5% below experiment. For the smaller absolute value in MnH, the deviation is ca. 13% (again the computational result is too low). A similar underestimation of the experimental metal HFCCs was also found in the few available previous post-Hartree–Fock studies.<sup>9–12</sup> These results suggest that the coupled-cluster calculations underestimate electron correlation, mainly because of basis-set incompleteness, and therefore may overestimate spin polarization to some extent. Of course we have to remember that scalar relativistic effects and rovibrational corrections have not been considered (cf. section 4). CuO differs from the other cases, as both basis-set extension and inclusion of triple excitations leads to more negative  $A_{\text{iso}}(\text{Cu})$  and thus to inferior agreement with experiment (although still better than with DFT methods, see below). The discrepancy is probably related to the neglect of spin–orbit corrections (see discussion in section 7).

Comparison of CCSD(T) and CCSD results indicates that the perturbative inclusion of triple excitations is particularly notable for MnF<sub>2</sub> and VO, where the positive triples contribution brings the results closer to experiment (note that for VO the triples contribution is less pronounced with the larger basis set). In all other cases, the influence of triple excitations is small. We note that the inclusion of triple excitations brings our CCSD(T) data for VO into better agreement with experiment than the SDCI and MRCI results of Knight et al. (ca. 685–692 MHz with different basis sets, which are comparable to the ones used here).<sup>12</sup>

Use of the smaller 9s7p4d metal basis leads to a reduction of  $A_{\text{iso}}(\text{M})$  by ca. 9% for MnH, by ca. 5% for MnO, by ca. 3% for CuO, and by only ca. 1% for VO and ScO. While this is in part due to some error compensation, it indicates already that the 9s7p4d basis provides a good compromise between computational effort and accuracy. This is confirmed in the DFT calculations (see below). We expect that a larger basis should bring the result for MnF<sub>2</sub> closer to the Ne matrix value. The CCSD results for TiF<sub>3</sub> and MnO<sub>3</sub> with the 9s7p4d metal basis are already in good agreement with experiment (cf. Table 3). Even for the latter system, the coupled cluster wave function corrects quite efficiently the significant spin contamination of the UHF reference (cf.  $\langle S^2 \rangle$  values in Table 3; this behavior of the CC approach was discussed before<sup>77,78</sup>). Despite the remaining contamination, the RCCSD and UCCSD results for  $A_{\text{iso}}(\text{Mn})$  are already quite close. Differences are still apparent for  $A_{\text{dip}}(\text{Mn})$  and for the ligand HFCCs. Spin contamination of the UHF reference wave function for MnO and MnF<sub>2</sub> is lower, and thus the agreement between RCCSD and UCCSD results is even closer. This indicates the relative stability of the CC approach with respect to the quality of the reference wave function.<sup>77,78</sup> A more detailed analysis of different reference wave functions is beyond the scope of the present study.

The small dipolar coupling constants for the metals are reproduced rather accurately for most systems. The less favorable agreement for MnF<sub>2</sub> might be due to matrix effects (cf. Table 8), whereas the description of CuO is generally more complicated, probably due to spin–orbit effects (cf. above and section 7). Except for the latter complex, the dependence of  $A_{\text{dip}}(\text{M})$  on triple excitations and basis set is only moderate, as one might expect. Agreement of the CC results with available experimental ligand isotropic and anisotropic HFCCs may also be considered reasonable in most cases, in view of their smallness in absolute terms (note the significant error bar on the experimental result for VO).

**TABLE 4: Basis-Set Dependence of the HFCC (MHz) in Mn<sup>+</sup>**<sup>a</sup>

| basis                             | $A_{\text{iso}}(\text{Mn})$ |
|-----------------------------------|-----------------------------|
| (15s11p6d)/[9s7p4d] <sup>b</sup>  | 759.2                       |
| 9s7p4d + 1s <sup>c</sup>          | 757.0                       |
| 9s7p4d + 2s <sup>c</sup>          | 744.8                       |
| 9s7p4d + 3s <sup>c</sup>          | 729.5                       |
| 15s11p6d uncontr. <sup>d</sup>    | 728.4                       |
| (21s15p10d3f)/[13s10p6d2f]        | 841.9                       |
| 13s10p6d2f (all p-orb. uncontr.)  | 841.9                       |
| 13s10p10d2f (all d-orb. uncontr.) | 840.8                       |
| 13s10p6d2f + 1s <sup>c</sup>      | 811.0                       |
| 13s10p6d2f + 2s <sup>c</sup>      | 802.6                       |
| 13s10p6d2f + 3s <sup>c</sup>      | 798.5                       |
| 13s10p6d2f + 4s <sup>c</sup>      | 798.3                       |
| 13s10p6d2f + 5s <sup>c</sup>      | 797.6                       |
| 21s10p6d2f (all s-orb. uncontr.)  | 797.8                       |
| 21s15p10d3f uncontr. <sup>d</sup> | 797.4                       |
| exp <sup>f</sup>                  | 757.8 <sup>e</sup>          |

<sup>a</sup> B3PW91 results. <sup>b</sup> Standard 9s7p4d basis. <sup>c</sup> Outermost core s-functions added in an uncontracted way, see text. <sup>d</sup> Fully uncontracted. <sup>e</sup> All s-functions uncontracted. Kasai, P. H. *Acc. Chem. Res.* **1971**, *4*, 329. Ar-matrix isolation. <sup>f</sup> Reference 45 reports a value of 771(14) MHz.

## 6. Basis-Set Study

While the basis-set dependence of the hyperfine parameters for light main group atoms and molecules has already been investigated in detail,<sup>13,15,79,80</sup> systematic basis-set studies are lacking for transition metal systems, except for a comparison of different STO basis-sets for TiF<sub>3</sub> by Belanzoni et al.<sup>17</sup> For several small systems, we have therefore studied the GTO basis-set convergence at the DFT level.

Table 4 examines the B3PW91 results for  $A_{\text{iso}}$  in the <sup>7</sup>Mn<sup>+</sup> cation, using a variety of basis sets. For this high-spin cation with d<sup>5</sup>s<sup>1</sup> configuration, the large positive direct contribution to the HFCC due to the single s-type SOMO should be partially compensated by negative contributions from spin polarization of the core shells, due to the five d-type SOMOs.<sup>81</sup> A better description of this spin polarization should thus reduce the HFCC. From tests with still larger basis sets, we expect the fully uncontracted 21s15p10d3f basis to be converged to within better than ca. 10 MHz. Comparison of the resulting 797 MHz to the 980 MHz obtained at the restricted B3PW91 level (with the same basis) suggests a total spin-polarization contribution of ca. –183 MHz. Remaining differences to experiment (note the two different experimental values available in the literature; footnotes e,f to Table 4) are expected to be largely the result of deficiencies in the exchange–correlation potential,  $\nu_{\text{xc}}$ . Contraction of the basis to 13s10p6d2f increases the HFCC by ca. 43 MHz. Starting from this contraction, we may now examine the influence of partial decontraction. Changes in the p- and d-basis have negligible effects. However, if we add s-function 9 ( $\alpha = 316.3768$ ) in an uncontracted fashion, 30 MHz of the 43 MHz contraction error have been eliminated. Adding s-exponents 8 ( $\alpha = 727.3039$ ) and 7 ( $\alpha = 1755.212$ ) reduces the HFCC by another 8 and 4 MHz, respectively, giving 798.5 MHz for the resulting 15s10p6d2f basis, i.e., almost the value obtained with the fully uncontracted basis (further addition of uncontracted tighter s-functions has thus very little effect). Our MO analyses indicate that this is mainly due to a decrease in the direct SOMO contribution, possibly due to a better description of the nodal structure of the 4s-orbital.

We may also analyze the results obtained with our smaller 9s7p4d standard basis constructed for use in larger systems. Employing this basis fully uncontracted to 15s11p6d, the expected basis-set limit HFCC (for the B3PW91 functional used)

**TABLE 5: Basis-Set Dependence of Hyperfine Parameters (in MHz) in MnO<sup>a</sup>**

| basis set                               |                                      | BP86                        |                             |                            |                            | B3LYP                       |                             |                            |                            | B3PW91                      |                             |                            |                            |
|---|--------------------------------------|-----------------------------|-----------------------------|----------------------------|----------------------------|-----------------------------|-----------------------------|----------------------------|----------------------------|-----------------------------|-----------------------------|----------------------------|----------------------------|
| Mn                                      | O                                    | $A_{\text{iso}}(\text{Mn})$ | $A_{\text{dip}}(\text{Mn})$ | $A_{\text{iso}}(\text{O})$ | $A_{\text{dip}}(\text{O})$ | $A_{\text{iso}}(\text{Mn})$ | $A_{\text{dip}}(\text{Mn})$ | $A_{\text{iso}}(\text{O})$ | $A_{\text{dip}}(\text{O})$ | $A_{\text{iso}}(\text{Mn})$ | $A_{\text{dip}}(\text{Mn})$ | $A_{\text{iso}}(\text{O})$ | $A_{\text{dip}}(\text{O})$ |
| 9s7p4d <sup>b</sup>                     | IGLO-III                             | 526.8                       | -24.4                       | -5.4                       | 8.1                        | 521.8                       | -20.7                       | -8.0                       | 9.9                        | 507.5                       | -20.2                       | -7.3                       | 10.1                       |
| 9s7p4d+3s <sup>c</sup>                  | IGLO-III                             | 507.3                       | -24.5                       | -5.4                       | 8.1                        | 502.5                       | -20.7                       | -8.0                       | 9.9                        | 485.9                       | -20.3                       | -7.6                       | 9.9                        |
| 15s11p6d<br>(uncontr. <sup>d</sup> )    | IGLO-III<br>(uncontr. <sup>d</sup> ) | 507.1                       | -24.9                       | -5.3                       | 8.1                        | 501.9                       | -21.1                       | -7.9                       | 9.9                        | 488.2                       | -20.6                       | -7.2                       | 10.1                       |
| 13s10p6d2f <sup>e</sup>                 | 8s6p3d1f <sup>f</sup>                | 562.5                       | -24.2                       | -5.5                       | 8.3                        | 557.7                       | -20.4                       | -8.0                       | 10.0                       | 543.3                       | -20.0                       | -7.8                       | 10.3                       |
| 13s10p6d2f+2s <sup>g</sup>              | 8s6p3d1f <sup>f</sup>                | 539.9                       | -24.2                       | -5.4                       | 8.3                        | 534.8                       | -20.4                       | -7.7                       | 10.2                       | 518.2                       | -20.0                       | -7.4                       | 10.3                       |
| 13s10p6d2f+2s <sup>g</sup>              | IGLO-III                             | 534.5                       | -24.2                       | -5.3                       | 8.3                        | 532.9                       | -20.4                       | -7.5                       | 10.2                       | 516.3                       | -20.0                       | -7.2                       | 10.3                       |
| 21s15p10d3f<br>(uncontr. <sup>d</sup> ) | 8s6p3d1f<br>(uncontr. <sup>d</sup> ) | 531.5                       | -24.6                       | -5.4                       | 8.4                        | 527.5                       | -20.5                       | -8.0                       | 10.0                       | 513.7                       | -20.1                       | -7.3                       | 10.3                       |

<sup>a</sup> Experimental data:  $A_{\text{iso}}(\text{Mn}) = 479.861(100)$  MHz,  $A_{\text{dip}}(\text{Mn}) = -16.066(59)$  MHz (gas-phase measurement, ref 36). <sup>b</sup> (15s11p6d)/[9s7p4d]. <sup>c</sup> Three outermost core s-functions added, see text. <sup>d</sup> Fully uncontracted. <sup>e</sup> (21s15p10d3f)/[13s10p6d2f]. <sup>f</sup> Larger ligand basis, see Computational Methods. <sup>g</sup> Two outermost core s-functions added, see text.

**TABLE 6: Dependence of Metal HFCCs (in MHz) on the Metal Basis-Set for Selected Systems<sup>a</sup>**

| molecule         |                  | BP86   |                      |                         | B3LYP  |                      |                         | B3PW91 |                      |                         | exp <sup>d</sup> |
|------------------|------------------|--------|----------------------|-------------------------|--------|----------------------|-------------------------|--------|----------------------|-------------------------|------------------|
|                  |                  | 9s7p4d | 12s7p4d <sup>b</sup> | 15s10p6d2f <sup>c</sup> | 9s7p4d | 12s7p4d <sup>b</sup> | 15s10p6d2f <sup>c</sup> | 9s7p4d | 12s7p4d <sup>b</sup> | 15s10p6d2f <sup>c</sup> |                  |
| <sup>2</sup> ScO | $A_{\text{iso}}$ | 1979.6 | 1898.4               | 1932.0                  | 2032.3 | 1948.2               | 1995.6                  | 1930.2 | 1849.9               | 1878.6                  | 1947.339(2)      |
|                  | $A_{\text{dip}}$ | 17.5   | 17.5                 | 18.8                    | 18.7   | 18.7                 | 20.1                    | 18.7   | 18.7                 | 20.1                    | 24.8053(7)       |
| <sup>2</sup> TiN | $A_{\text{iso}}$ | -569.0 | -547.3               | -561.8                  | -584.3 | -559.7               | -578.1                  | -554.2 | -534.1               | -548.1                  | -558.8(11)       |
|                  | $A_{\text{dip}}$ | -4.3   | -4.3                 | -4.7                    | -4.4   | -4.5                 | -4.9                    | -4.7   | -4.6                 | -5.1                    | -5(2)            |
| <sup>4</sup> VO  | $A_{\text{iso}}$ | 821.0  | 789.8                | 815.4                   | 829.5  | 796.5                | 825.5                   | 795.2  | 763.0                | 788.8                   | 778(2)           |
|                  | $A_{\text{dip}}$ | -48.1  | -48.0                | -48.1                   | -49.9  | -49.8                | -50.0                   | -48.2  | -48.2                | -48.1                   | -41.3(8)         |
| <sup>6</sup> MnO | $A_{\text{iso}}$ | 526.8  | 507.3                | 534.5                   | 521.8  | 502.5                | 532.9                   | 507.5  | 485.9                | 516.3                   | 479.861(100)     |
|                  | $A_{\text{dip}}$ | -24.4  | -24.5                | -24.2                   | -20.7  | -20.7                | -20.4                   | -20.2  | -20.3                | -20.0                   | -16.066(59)      |
| <sup>7</sup> MnH | $A_{\text{iso}}$ | 380.0  | 366.7                | 398.1                   | 331.8  | 322.1                | 349.0                   | 329.6  | 322.3                | 351.7                   | 279.4(12)        |
|                  | $A_{\text{dip}}$ | 8.4    | 8.3                  | 9.0                     | 9.8    | 9.7                  | 10.4                    | 10.1   | 10.1                 | 10.9                    | 12.0(8)          |

<sup>a</sup> The IGLO-III basis was used for the ligands. <sup>b</sup> Three outermost core functions added to standard 9s7p4d basis, see text. <sup>c</sup> Two outermost core functions added to 13s10p6d2f basis, see text. <sup>d</sup> See footnotes to Tables 8 and 10 for the sources of experimental data.

is underestimated by ca. 70 MHz (Table 4). This is most probably related to the lack of very large core-shell s-exponents to describe accurately the spin density near the nucleus. Upon contraction, the discrepancy with respect to the 21s15p10d3f basis result decreases, again due to an increased SOMO contribution. The medium-size 9s7p4d basis simulates the largest basis sets quite well, due to error compensation. We find this compensation to be systematic rather than accidental (see below) and take it as a support for the usefulness of this smaller metal basis for applications to larger systems.

Table 5 shows basis-set tests for both metal and ligand isotropic and dipolar HFCCs in MnO, using three different functionals. First of all, we note that the anisotropies show relatively little basis-set dependence. Examination of the effect of the ligand basis set on the isotropic HFCCs indicates that the IGLO-III basis is already rather well converged relative to the larger 8s6p3d1f basis. The effect of the metal basis is very similar to the above results for Mn<sup>+</sup>. Decontraction of the outermost core-shell s-functions decreases  $A_{\text{iso}}(\text{Mn})$ . The smaller 9s7p4d basis compares again well with the fully uncontracted 21s15p10d3f basis (for all functionals), due to error compensation.

Table 6 shows results for  $A_{\text{iso}}(\text{M})$  and  $A_{\text{dip}}(\text{M})$  of a somewhat larger subset of molecules with three different basis sets (9s7p4d, 9s7p4d+3s, 13s10p6d2f+2s), and again with three functionals. As in the two previous cases, a more flexible description of the outermost s-core shell regions (2s, 3s) reduces the absolute value of  $A_{\text{iso}}(\text{M})$  (TiN has a negative HFCC due to the negative  $g_{\text{N}}(\text{Ti})$ ; cf. Table 7). Notably, the contracted 9s7p4d basis gives results that deviate only by ca. 1–2% from the values obtained with the flexible 15s10p6d2f basis. Only for MnH, the deviation is ca. 5%. This gives further justification to our use of the 9s7p4d basis as the standard metal basis set for the remainder of this study.

**TABLE 7: Nuclear g-Values<sup>a</sup>**

| isotope          | g-value  |
|------------------|----------|
| <sup>45</sup> Sc | 1.35883  |
| <sup>47</sup> Ti | -0.31538 |
| <sup>51</sup> V  | 1.47100  |
| <sup>53</sup> Cr | -0.31567 |
| <sup>55</sup> Mn | 1.37960  |
| <sup>57</sup> Fe | 0.18084  |
| <sup>59</sup> Co | 1.31886  |
| <sup>61</sup> Ni | -0.49987 |
| <sup>63</sup> Cu | 1.48187  |
| <sup>1</sup> H   | 5.58556  |
| <sup>13</sup> C  | 1.40480  |
| <sup>14</sup> N  | 0.40375  |
| <sup>17</sup> O  | -0.75748 |
| <sup>19</sup> F  | 5.25760  |

<sup>a</sup> In nuclear magnetons. Taken from Fuller, G. H. *J. Chem. Phys. Ref. Data* **1976**, 5, 835.

## 7. Performance of Different Exchange–Correlation Functionals for Metal HFCCs

**General Trends.** We will start by discussing some general trends before going into more detailed analyses for specific groups of complexes. Table 8 gives isotropic metal HFCCs, Table 9 the dipolar couplings for all 21 molecules and for the eight functionals of this study, in comparison with experiment. The dipolar couplings give us further insight, as they depend less on subtle details of spin polarization but more on the overall quality of our wave functions. Additional insight on spin contamination is provided by the  $\langle S^2 \rangle$  expectation values, which are also included in Table 9.<sup>82</sup>

Figures 1–7 show graphically for groups of related complexes the spin-density at the metal nuclei, and for all functionals, normalized to the number of unpaired electrons. Two general trends hold with very few exceptions: (i) For a given exchange

TABLE 8: Dependence of Isotropic Metal HFCCs on the Exchange–Correlation Functional (in MHz)

|   | BLYP   | BP86   | BPW91  | B3LYP  | B3PW91 | BHLYP  | BHP86  | BHPW91 | exp <sup>a</sup>                    |
|---|--------|--------|--------|--------|--------|--------|--------|--------|-------------------------------------|
| <sup>2</sup> ScO                                    | 2043.5 | 1979.6 | 1933.5 | 2032.3 | 1930.2 | 1904.7 | 1983.1 | 1847.7 | 1947.339(2) <sup>b,c</sup>          |
| <sup>2</sup> TiN                                    | −587.0 | −569.0 | −556.6 | −584.3 | −554.2 | −569.6 | −540.7 | −528.0 | −558.8(11) <sup>b,d</sup>           |
| <sup>3</sup> TiO                                    | −257.5 | −251.0 | −246.3 | −252.8 | −242.4 | −241.9 | −233.2 | −227.0 | −241.0(60) <sup>b,d</sup>           |
| <sup>3</sup> VN                                     | 1432.6 | 1393.5 | 1357.8 | 1388.9 | 1315.4 | 1168.9 | 1124.6 | 1081.7 | 1311.8 <sup>b,e</sup>               |
| <sup>4</sup> VO                                     | 847.8  | 821.0  | 811.9  | 829.5  | 795.2  | 795.0  | 763.3  | 753.4  | 778(2) <sup>b,f</sup>               |
| <sup>6</sup> MnO                                    | 543.1  | 526.8  | 524.0  | 521.8  | 507.5  | 528.5  | 509.8  | 504.7  | 479.861(100) <sup>b,g</sup>         |
| <sup>6</sup> MnF <sub>2</sub>                       | 313.0  | 294.2  | 283.9  | 240.7  | 214.1  | 144.9  | 118.5  | 109.0  | 104(6), 134(6) <sup>h,i</sup>       |
| <sup>7</sup> MnF                                    | 501.9  | 480.6  | 473.9  | 470.5  | 443.6  | 422.3  | 397.4  | 391.5  | 442(6), 443(6) <sup>h,i</sup>       |
| <sup>7</sup> MnH                                    | 380.0  | 380.0  | 385.0  | 331.8  | 329.6  | 277.1  | 271.8  | 276.3  | 279.4(12) <sup>b,j</sup>            |
| <sup>2</sup> TiF <sub>3</sub>                       | −218.0 | −216.6 | −211.6 | −192.2 | −186.1 | −157.8 | −151.9 | −149.4 | −184.8(4), −177.1(4) <sup>h,k</sup> |
| <sup>2</sup> MnO <sub>3</sub>                       | 2042.4 | 2009.3 | 1987.2 | 1735.5 | 1675.9 | 1187.6 | 1141.5 | 1111.7 | 1613(6) <sup>h,l</sup>              |
| <sup>6</sup> [Mn(CN) <sub>4</sub> ] <sup>2−</sup>   | −90.8  | −99.8  | −104.8 | −116.6 | −132.0 | −155.0 | −169.3 | −176.0 | −199(3) <sup>m</sup>                |
| <sup>6</sup> [Cr(CO) <sub>4</sub> ] <sup>+</sup>    | 21.9   | 23.8   | 25.2   | 26.9   | 30.8   | 34.5   | 38.4   | 40.4   | 41.5 <sup>n,o</sup>                 |
| <sup>2</sup> [Mn(CO) <sub>5</sub> ]                 | 6.7    | 2.8    | 0.8    | −2.5   | −12.1  | −21.4  | −32.0  | −37.6  | −2.8, 0.6, 5.6 <sup>p</sup>         |
| <sup>2</sup> [Fe(CO) <sub>5</sub> ] <sup>+</sup>    | 1.1    | 0.0    | −0.6   | −3.2   | −5.3   | −9.3   | −11.7  | −12.3  | −2.2 <sup>q</sup>                   |
| <sup>2</sup> [Mn(CN) <sub>5</sub> NO] <sup>2−</sup> | −134.3 | −145.8 | −153.8 | −223.6 | −259.2 | −304.5 | −351.7 | −364.1 | −219.5 <sup>r</sup>                 |
| <sup>2</sup> [Mn(CN) <sub>4</sub> N] <sup>−</sup>   | −160.1 | −170.4 | −176.0 | −250.1 | −275.0 | −506.7 | −548.5 | −558.5 | −276 <sup>s</sup>                   |
| <sup>2</sup> [Ni(CO) <sub>3</sub> H]                | 24.4   | 22.3   | 23.5   | 33.3   | 33.9   | 51.3   | 54.8   | 56.0   | 9.0(2) <sup>n,t</sup>               |
| <sup>2</sup> [Co(CO) <sub>4</sub> ]                 | −6.4   | −11.3  | −15.7  | −61.4  | −75.4  | −175.4 | −210.0 | −219.7 | −47.8, −52(1) <sup>u</sup>          |
| <sup>2</sup> CuO                                    | −651.8 | −640.0 | −678.1 | −755.2 | −776.4 | −732.4 | −676.4 | −717.3 | −483.6(94) <sup>b,v</sup>           |
| <sup>2</sup> [Cu(CO) <sub>3</sub> ]                 | −19.2  | −7.3   | −7.1   | 4.7    | 13.0   | 45.0   | 68.8   | 67.9   | 71.2 <sup>w</sup>                   |

<sup>a</sup> The numbers in parentheses represent standard deviations. <sup>b</sup> Gas-phase measurement. <sup>c</sup> Reference 28. <sup>d</sup> Reference 29. For the TiO molecule, parameter “c” determining the dipolar contribution has not been resolved. Our B3PW91/9s7p4d result for  $A_{\text{dip}} (= c/3)$  has been used to derive  $A_{\text{iso}} (= b + c/3)$  from the reported sum  $b + c = -231.6(60)$  MHz. <sup>e</sup> Balfour, J.; Merer, A. J.; Niki, H.; Simard, B.; Hackett, P. A. *J. Chem. Phys.* **1993**, *99*, 3288. Our B3PW91/9s7p4d result for  $A_{\text{dip}} (= c/3)$  has been used to derive  $A_{\text{iso}} (= b + c/3)$  from the reported sum  $b + c = 1264.2$  MHz. <sup>f</sup> Reference 33. <sup>g</sup> Reference 36. See also references given therein. <sup>h</sup> EPR in Ne and Ar matrix, respectively. <sup>i</sup> DeVore, C.; Van Zee, J. R.; Weltner, W. Jr. *J. Chem. Phys.* **1978**, *68*, 3522. <sup>j</sup> Reference 37. <sup>k</sup> Reference 44. <sup>l</sup> Reference 45. <sup>m</sup> EPR in solution, ref 53. <sup>n</sup> EPR in Kr matrix. <sup>o</sup> Reference 52. <sup>p</sup> (1) EPR in Ar matrix, ref 54. (2) Solid-state EPR: Ozin, G. A., personal communication cited by Huffadine, A. S.; Peake, B. M.; Robinson B. M.; Simpson, J.; Davson, P. A. *J. Organomet. Chem.* **1976**, *121*, 391. (3) EPR in C<sub>6</sub>D<sub>6</sub> matrix: Howard, J. A.; Morton, J. R.; Preston, K. F. *Chem. Phys. Lett.* **1982**, *83*, 1226. <sup>q</sup> EPR in Cr(CO)<sub>6</sub> host crystal, ref 55. <sup>r</sup> Single-crystal EPR in a host lattice of Na<sub>2</sub>Fe(CN)<sub>5</sub>NO·2H<sub>2</sub>O: Manoharan, T.; Gray, H. B. *Inorg. Chem.* **1966**, *5*, 823. <sup>s</sup> EPR in CH<sub>3</sub>CN at 300 and 10 K, cf. ref 58. Relative signs are known. <sup>t</sup> Reference 51. The sign of the  $A_{\parallel}(+)$  has been determined from the sign of the nuclear quadrupolar coupling tensor component. <sup>u</sup> EPR in solid Kr, ref 50; EPR in CO matrix, cf. ref 88b. <sup>v</sup> Steimle, T.; Namiki, K.; Saito, S. *J. Chem. Phys.* **1997**, *107*, 6109. <sup>w</sup> EPR in Ar matrix, refs 46 and 47.

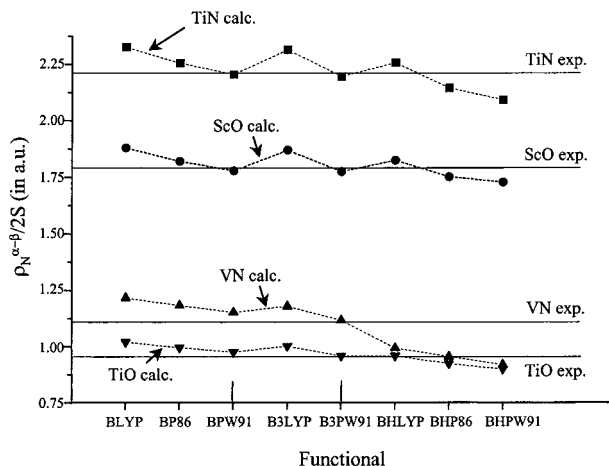


**Figure 1.** Spin density  $\rho_N^{\alpha-\beta}$  at the metal nuclei in <sup>2</sup>ScO, <sup>3</sup>TiO, <sup>2</sup>TiN, and <sup>3</sup>VN, normalized to the number of unpaired electrons. Dependence on  $\nu_{\text{xc}}$ .

functional  $\nu_{\text{x}}[\rho]$ , the computed spin density  $\rho_N$  at the metal nucleus depends on the correlation functional  $\nu_{\text{c}}[\rho]$  as  $\rho_N(\text{LYP}) \geq \rho_N(\text{P86}) \geq \rho_N(\text{PW91})$ . (ii) For a given correlation functional,  $\rho_N$  decreases such as  $\rho_N(\text{B}) \geq \rho_N(\text{B3}) \geq \rho_N(\text{BH})$ , i.e., the spin density is reduced with increasing admixture of exact exchange. The latter trend is consistent with the expectation that the “pure” GGA functionals underestimate spin polarization.<sup>13,14,83,84</sup> As the core–shell contributions to this spin polarization dominate typically in transition metals and contribute overall negatively to  $\rho_N$  (see above), the metal HFCCs tend to be overestimated at the GGA level. It is well known that unrestricted Hartree–Fock wave functions tend to overestimate spin polarization (accompanied by spin contamination). Therefore, the inclusion

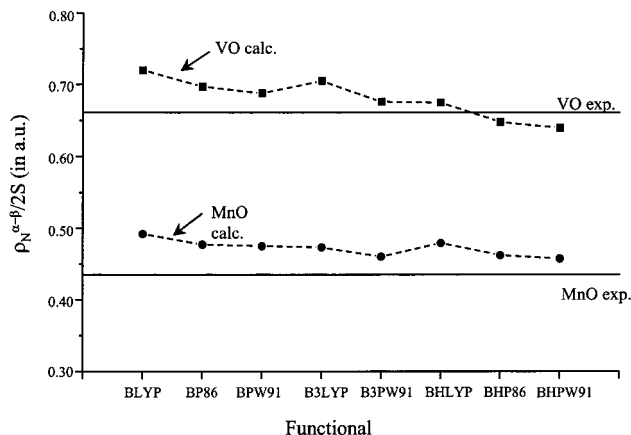


**Figure 2.** Spin density  $\rho_N^{\alpha-\beta}$  at the metal nuclei in <sup>4</sup>VO and <sup>6</sup>MnO, normalized to the number of unpaired electrons. Dependence on  $\nu_{\text{xc}}$ .

of exact exchange into  $\nu_{\text{x}}[\rho]$  is expected to increase spin polarization and thus to decrease  $A_{\text{iso}}(\text{M})$ .

The relative sensitivity of the results to  $\nu_{\text{x}}[\rho]$  and  $\nu_{\text{c}}[\rho]$  depends strongly on the particular system. For ScO, TiN, or TiO, a change in  $\nu_{\text{c}}$  (e.g. BLYP  $\rightarrow$  BP86  $\rightarrow$  BPW91) influences the results considerably more than the change of  $\nu_{\text{x}}$  from B to B3 (Figure 1). For TiF<sub>3</sub>, MnH or MnF<sub>2</sub>, and for several other complexes, the behavior is just the opposite, i.e., the dependence on  $\nu_{\text{x}}$  dominates (e.g., Figures 3 and 4). In other cases, the dependence on  $\nu_{\text{x}}$  and  $\nu_{\text{c}}$  is of comparable magnitude (see, e.g., Figure 2). Except for cases with strong spin contamination (cf. below), the effects of  $\nu_{\text{x}}$  and  $\nu_{\text{c}}$  appear to be roughly additive.

The overall range of variation of the HFCCs for different functionals is also rather diverse in different systems. Thus, for some systems the range of results encompasses only some

**TABLE 9: Dependence of Dipolar Metal HFCCs on the Exchange–Correlation Functional (in MHz)**

| molecule  |                       | BLYP   | BP86   | BPW91  | B3LYP  | B3PW91 | BHLYP  | BHP86  | BHPW91 | exp. <sup>a</sup><br>nominal $\langle S^2 \rangle$ |
|---|-----------------------|--------|--------|--------|--------|--------|--------|--------|--------|--|
| <sup>2</sup> ScO                                    | $A_{\text{dip}}$      | 17.1   | 17.5   | 17.3   | 18.7   | 18.7   | 21.1   | 21.2   | 21.0   | 24.8053(7)   |
|   | $\langle S^2 \rangle$ | 0.751  | 0.752  | 0.752  | 0.751  | 0.752  | 0.751  | 0.752  | 0.753  | 0.750  |
| <sup>2</sup> TiN                                    | $A_{\text{dip}}$      | -4.1   | -4.3   | -4.3   | -4.4   | -4.7   | -5.0   | -5.2   | -5.3   | -5(2)  |
|   | $\langle S^2 \rangle$ | 0.752  | 0.754  | 0.756  | 0.753  | 0.759  | 0.757  | 0.768  | 0.769  | 0.750  |
| <sup>3</sup> TiO                                    | $A_{\text{dip}}$      | -5.0   | -4.7   | -4.7   | -5.0   | -4.7   | -5.1   | -4.9   | -4.9   |  |
|   | $\langle S^2 \rangle$ | 2.009  | 2.011  | 2.014  | 2.012  | 2.017  | 2.016  | 2.020  | 2.024  | 2.000  |
| <sup>3</sup> VN                                     | $A_{\text{dip}}$      | -29.7  | -28.0  | -26.6  | -26.3  | -23.8  | -16.0  | -14.8  | -14.0  |  |
|   | $\langle S^2 \rangle$ | 2.034  | 2.040  | 2.047  | 2.076  | 2.119  | 2.424  | 2.442  | 2.505  | 2.000  |
| <sup>4</sup> VO                                     | $A_{\text{dip}}$      | -49.8  | -48.1  | -47.7  | -49.9  | -48.2  | -50.9  | -49.9  | -48.9  | -41.3(8)   |
|   | $\langle S^2 \rangle$ | 3.784  | 3.791  | 3.798  | 3.799  | 3.815  | 3.817  | 3.817  | 3.841  | 3.750  |
| <sup>6</sup> MnO                                    | $A_{\text{dip}}$      | -24.9  | -24.4  | -24.3  | -20.7  | -20.2  | -16.2  | -16.2  | -16.0  | -16.066(59)  |
|   | $\langle S^2 \rangle$ | 8.783  | 8.788  | 8.794  | 8.827  | 8.848  | 9.034  | 9.059  | 9.078  | 8.750  |
| <sup>6</sup> MnF <sub>2</sub>                       | $A_{\text{dip}}$      | -7.8   | -6.4   | -6.4   | -3.6   | -2.2   | 0.8    | 2.0    | 2.2    | 10(6) or 6(6) <sup>b</sup>                         |
|   | $\langle S^2 \rangle$ | 8.758  | 8.760  | 8.761  | 8.760  | 8.762  | 8.760  | 8.761  | 8.762  | 8.750  |
| <sup>7</sup> MnF                                    | $A_{\text{dip}}$      | 5.6    | 6.2    | 6.2    | 7.0    | 7.6    | 8.4    | 8.7    | 8.7    | 24(6), 16(6)                                       |
|   | $\langle S^2 \rangle$ | 12.002 | 12.003 | 12.003 | 12.003 | 12.003 | 12.003 | 12.003 | 12.003 | 12.000   |
| <sup>7</sup> MnH                                    | $A_{\text{dip}}$      | 7.8    | 8.4    | 8.4    | 9.8    | 10.1   | 10.9   | 11.2   | 11.2   | 12.0(8)  |
|   | $\langle S^2 \rangle$ | 12.003 | 12.004 | 12.004 | 12.003 | 12.004 | 12.002 | 12.003 | 12.004 | 12.000   |
| <sup>2</sup> TiF <sub>3</sub>                       | $A_{\text{dip}}$      | -9.9   | -9.2   | -9.1   | -10.1  | -9.5   | -9.9   | -9.5   | -9.3   | -6.6(4), -8.1(4) <sup>b</sup>                      |
|   | $\langle S^2 \rangle$ | 0.752  | 0.752  | 0.753  | 0.752  | 0.753  | 0.752  | 0.752  | 0.753  | 0.750  |
| <sup>2</sup> MnO <sub>3</sub>                       | $A_{\text{dip}}$      | 95.9   | 95.1   | 95.5   | 124.5  | 125.9  | 178.0  | 174.2  | 171.4  | 81(3)  |
|   | $\langle S^2 \rangle$ | 0.765  | 0.768  | 0.770  | 0.880  | 0.914  | 2.0025 | 1.994  | 2.054  | 0.750  |
| <sup>6</sup> [Mn(CN) <sub>4</sub> ] <sup>2-</sup>   | $A_{\text{dip}}$      | 0.0    | 0.0    | 0.0    | 0.0    | 0.0    | 0.0    | 0.0    | 0.0    | 0 <sup>c</sup>                                     |
|   | $\langle S^2 \rangle$ | 8.762  | 8.764  | 8.765  | 8.762  | 8.766  | 8.763  | 8.765  | 8.766  | 8.750  |
| <sup>6</sup> [Cr(CO) <sub>4</sub> ] <sup>+</sup>    | $A_{\text{dip}}$      | 0.0    | 0.0    | 0.0    | 0.0    | 0.0    | 0.0    | 0.0    | 0.0    | 0.0  |
|   | $\langle S^2 \rangle$ | 8.757  | 8.761  | 8.762  | 8.759  | 8.764  | 8.761  | 8.765  | 8.765  | 8.750  |
| <sup>2</sup> [Mn(CO) <sub>5</sub> ]                 | $A_{\text{dip}}$      | 97.0   | 96.1   | 96.2   | 96.5   | 95.8   | 88.6   | 88.4   | 89.0   | 90(8) - 92(6) <sup>d</sup>                         |
|   | $\langle S^2 \rangle$ | 0.753  | 0.753  | 0.754  | 0.758  | 0.759  | 0.773  | 0.773  | 0.776  | 0.750  |
| <sup>2</sup> [Fe(CO) <sub>5</sub> ] <sup>+</sup>    | $A_{\text{dip}}$      | 18.5   | 18.3   | 18.2   | 19.3   | 19.0   | 19.7   | 19.5   | 19.6   | 15.4   |
|   | $\langle S^2 \rangle$ | 0.757  | 0.757  | 0.756  | 0.763  | 0.764  | 0.770  | 0.770  | 0.771  | 0.750  |
| <sup>2</sup> [Mn(CN) <sub>5</sub> NO] <sup>2-</sup> | $A_{\text{dip}}$      | -97.3  | -98.2  | -96.2  | -58.1  | -56.0  | -30.3  | -30.2  | -29.0  | -115.2   |
|   | $\langle S^2 \rangle$ | 0.868  | 0.850  | 0.866  | 1.440  | 1.464  | 2.091  | 2.077  | 2.086  | 0.750  |
| <sup>2</sup> [Mn(CN) <sub>4</sub> N] <sup>-</sup>   | $A_{\text{dip}}$      | -116.2 | -115.2 | -115.1 | -117.2 | -115.6 | -88.5  | -88.7  | -89.2  | -122.4   |
|   | $\langle S^2 \rangle$ | 0.774  | 0.773  | 0.775  | 0.882  | 0.896  | 1.763  | 1.784  | 1.796  | 0.750  |
| <sup>2</sup> [Ni(CO) <sub>3</sub> H]                | $A_{\text{dip}}$      | -49.8  | -49.6  | -49.6  | -56.9  | -56.5  | -67.8  | -67.2  | -66.8  | -44.0(2)   |
|   | $\langle S^2 \rangle$ | 0.752  | 0.752  | 0.752  | 0.757  | 0.756  | 0.793  | 0.791  | 0.793  | 0.750  |
| <sup>2</sup> [Co(CO) <sub>4</sub> ]                 | $A_{\text{dip}}$      | 153.6  | 152.4  | 151.8  | 147.4  | 146.2  | 101.2  | 93.6   | 84.5   | 110.0  |
|   | $\langle S^2 \rangle$ | 0.762  | 0.761  | 0.763  | 0.788  | 0.789  | 0.930  | 0.957  | 1.005  | 0.750  |
| <sup>2</sup> CuO                                    | $A_{\text{dip}}$      | 42.7   | 41.6   | 41.8   | 33.7   | 33.4   | 22.8   | 20.8   | 21.6   | 24.1   |
|   | $\langle S^2 \rangle$ | 0.762  | 0.761  | 0.762  | 0.767  | 0.768  | 0.768  | 0.765  | 0.767  | 0.750  |
| <sup>2</sup> [Cu(CO) <sub>3</sub> ]                 | $A_{\text{dip}}$      | 65.2   | 65.7   | 64.8   | 65.9   | 65.4   | 58.4   | 58.8   | 58.3   | 81   |
|   | $\langle S^2 \rangle$ | 0.751  | 0.752  | 0.752  | 0.753  | 0.754  | 0.756  | 0.757  | 0.758  | 0.750  |

<sup>a</sup> See corresponding footnotes to Table 8 for the sources of the experimental data. <sup>b</sup> EPR in Ne and Ar matrix, respectively. <sup>c</sup> Not observed (zero due to symmetry). <sup>d</sup> EPR using different solid matrices.

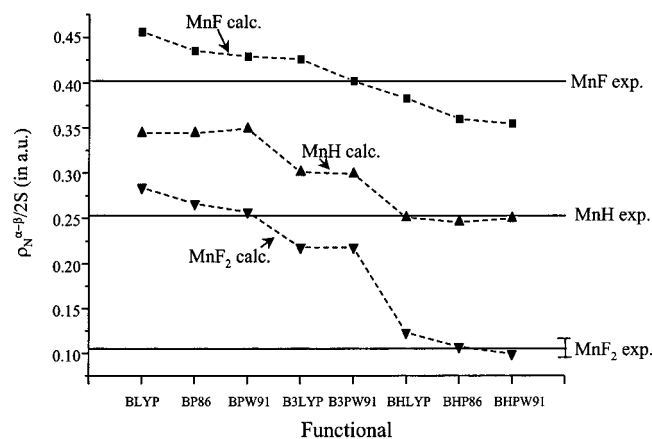


**Figure 3.** Spin density  $\rho_N^{\alpha-\beta}$  at the metal nuclei in <sup>2</sup>TiF<sub>3</sub> and <sup>2</sup>MnO<sub>3</sub>, normalized to the number of unpaired electrons. Dependence on  $\nu_{xc}$ .

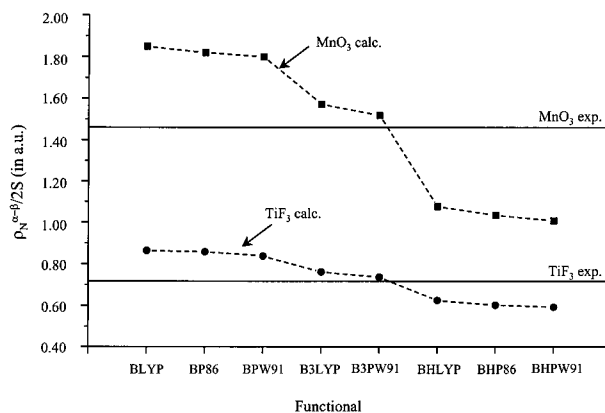


**Figure 4.** Spin density  $\rho_N^{\alpha-\beta}$  at the metal nuclei in <sup>7</sup>MnF, <sup>7</sup>MnH, and <sup>6</sup>MnF<sub>2</sub>, normalized to the number of unpaired electrons. Dependence on  $\nu_{xc}$ .

percent of the value of the HFCC (e.g., for ScO, TiN, TiO, or VO; note that previous studies have concentrated on such species), whereas for others this range may be on the order of the HFCC itself. This relative variation depends of course on the absolute value of the HFCC but also on other features we

will discuss in more detail below. In comparison with experiment (Table 8), or with the coupled-cluster results (Table 3), unfortunately we cannot single out any functional which would be superior to the others. The performance of a given functional is very different for different classes of complexes. Thus, while the B3LYP functional has been particularly popular for HFCCs

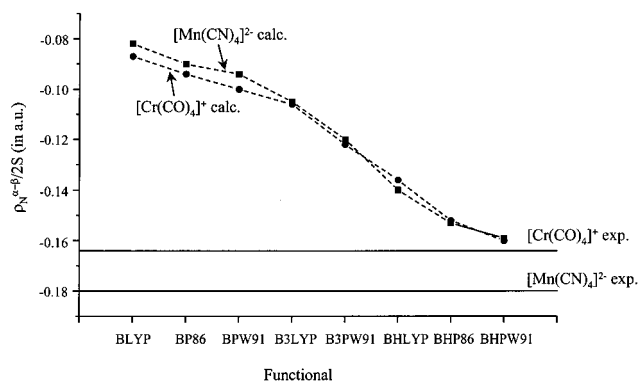


**Figure 5.** Spin density  $\rho_N^{\alpha-\beta}$  at the metal nuclei in  $^{6}\text{[Mn(CN)}_4]^{2-}$  and  $^{6}\text{[Cr(CO)}_4]^{+}$ , normalized to the number of unpaired electrons. Dependence on  $\nu_{xc}$ .

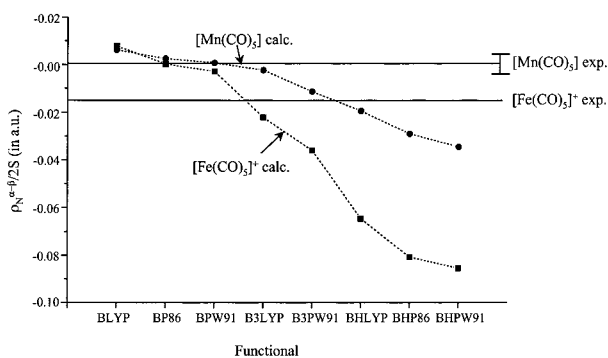


**Figure 6.** Spin density  $\rho_N^{\alpha-\beta}$  at the metal nuclei in  $^2\text{[Mn(CO)}_5]$  and  $^2\text{[Fe(CO)}_5]^{+}$ , normalized to the number of unpaired electrons. Dependence on  $\nu_{xc}$ .

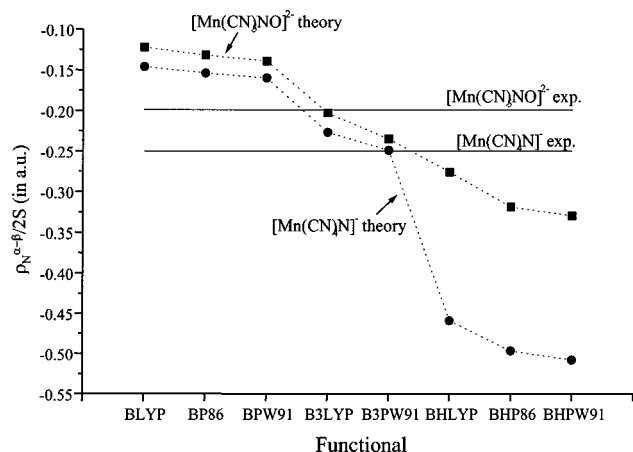


**Figure 7.** Spin density  $\rho_N^{\alpha-\beta}$  at the metal nuclei in  $^2\text{[Mn(CN)}_5\text{NO}]^{2-}$  and  $^2\text{[Mn(CN)}_4\text{N}]^{-}$ , normalized to the number of unpaired electrons. Dependence on  $\nu_{xc}$ .

of organic molecules,<sup>85</sup> no “universal functional” appears to be available yet for the present transition metal systems.<sup>86</sup> The variations in the electronic structure appear to be too large. For the “easier” systems mentioned (ScO, TiN, TiO, and VO), any of the GGA or hybrid functionals gives results within ca. 5–10% of the experimental values. In some cases (e.g., VN,  $\text{MnO}_3$ ,  $[\text{Mn(CN)}_4\text{N}]^{-}$ ,  $[\text{Ni(CO)}_3\text{H}]$ ,  $[\text{Co(CO)}_4]$ ), the spin contamination (cf.  $\langle S^2 \rangle$  in Table 9) for the BH-type hybrid functionals is unacceptably large and leads to a deterioration of the results. In other cases (e.g.,  $[\text{Mn(CN)}_5\text{NO}]^{2-}$ ), spin contamination is even significant with pure GGA functionals. However, interestingly there is also a significant group of complexes (e.g., MnH,  $\text{MnF}_2$ ,  $[\text{Mn(CN)}_4]^{2-}$ ,  $[\text{Cr(CO)}_4]^{+}$ ), where the half-and-half hybrids perform particularly well, without any apparent prob-

lems of spin contamination. Let us therefore discuss the results in more detail, and relate them to the electronic structure of the molecules in question.

**ScO, TiN, TiO, VN, and VO.** This first group of systems exhibits large positive spin density at the metal nucleus, resulting from the dominant participation of the metal 4s orbital in the SOMO, or in one of the SOMOs.  $^2\text{ScO}$  and  $^2\text{TiN}$  are the simplest representatives. Here the  $\sigma$ -type SOMO has predominantly metal 4s character,<sup>9,12,29</sup> with some  $3d_z^2$  and 4p admixture (it is polarized away from the ligand).  $^3\text{TiO}$  and  $^3\text{VN}$  have in addition one  $3d_\delta$ -type SOMO,  $^4\text{VO}$  two  $3d_\delta$ -type SOMOs. The dominance of the direct SOMO contribution to the HFCCs explains the relatively low dependence on  $\nu_x$  (Figures 1, 2, Table 8). The treatment of dynamical correlation via  $\nu_c$  appears to influence the HFCCs mainly via the shape of the SOMO. We find the SOMO to become more diffuse along the series LYP < P86 < PW91 (valence-shell spin polarization is also affected somewhat by  $\nu_c$ ). Addition of exact exchange also renders the SOMO somewhat more diffuse and reduces the HFCC slightly (the spin-polarization contributions are also affected but are not very pronounced).

VN is exceptional within this group, due to the significant onset of spin contamination upon inclusion of exact exchange (in contrast to the isoelectronic TiO!). This leads to a much larger dependence of the HFCC on the exchange functional, and finally to a significant deterioration of the results with BH-type hybrid functionals. This is confirmed by the results for  $A_{\text{dip}}(\text{M})$  (Table 9). The relatively low coupling anisotropy is mainly due to the  $3d_z^2$ -type SOMO and depends relatively little on  $\nu_{xc}$  for ScO, TiN, TiO, and VO. In contrast, for VN the admixture of exact exchange reduces the absolute value of  $A_{\text{dip}}(\text{M})$  significantly, in parallel with the drastic increase in  $\langle S^2 \rangle$  (Table 9). Unfortunately, no experimental  $A_{\text{dip}}(\text{M})$  is available for this system.

$^3\text{TiO}$  and  $^2\text{TiN}$  have been studied recently by Engels et al.,<sup>13</sup> using the PWP86 functional and medium-sized basis sets. For TiN, their results differ only by ca. 1% from our BP86 value, despite their ca. 0.03 Å larger Ti–N distance. Our own test calculations for TiN at the structure used by Engels et al. indicate very small changes (<1 MHz), i.e., a small dependence of the isotropic metal HFCC on bond length. Recently, B3LYP calculations for ScO have been performed by Knight et al.<sup>21</sup> Their value given for  $A_{\text{iso}}(\text{Sc})$  was 1877.5 MHz, ca. 8% lower than the value in Table 8, ca. 6% lower than our result with the larger 15s10p6d2f basis (cf. Table 6), but in excellent agreement with our B3PW91 results. Indeed, we have meanwhile been informed that Knight et al. erroneously reported their B3PW91 data as B3LYP results.<sup>87</sup>

Except for VN, the dipolar coupling constants (Table 9) are small and increase slightly in absolute value with increasing exact-exchange mixing in the functional. While this trend is partly related to an increasing participation of the metal  $4p_z$  orbital in the SOMO, spin polarization should not be disregarded completely. Thus, e.g., a restricted B3PW91 calculation on ScO gives  $A_{\text{dip}}(\text{Sc}) = +12.8$  MHz, quite different from the unrestricted result of +20.0 MHz. This should be compared to the RB3PW91 and UB3PW91 results for the isotropic HFCC of +1910.6 MHz and +1948.8 MHz, respectively. Thus, on a relative basis, spin polarization in ScO is more important for  $A_{\text{dip}}(\text{Sc})$  than for  $A_{\text{iso}}(\text{Sc})$ !

**MnO, MnF<sub>2</sub>, MnF, MnH.** In going to higher spin multiplicities, we may compare  $^6\text{MnO}$  to  $^4\text{VO}$ . MnO has two additional SOMOs, antibonding orbitals with metal- $3d_\pi$  and  $4p_\pi$ , as well as ligand  $2p_\pi$  character. Due to the large number of d-type

SOMOs, spin-polarization effects via the core shells are more pronounced. At first sight surprisingly, the BLYP hybrid functional gives a somewhat larger spin density than B3LYP. This is most likely connected to the significant spin contamination upon exact-exchange mixing (cf. Table 9). The net dependence on  $\nu_{xc}$  may still be considered moderate, with an overall range of less than 10% of the absolute HFCC. The somewhat larger dependence on  $\nu_x$  and the spin contamination are also apparent from the somewhat larger variations in  $A_{\text{dip}}(\text{M})$  compared to the above species (Table 9).

As related high-spin systems, but with lower net  $\rho_{\text{N}}$ , we may compare  ${}^7\text{MnF}$ ,  ${}^7\text{MnH}$ , and  ${}^6\text{MnF}_2$  (cf. Figure 3, Table 8).  ${}^6\text{MnF}_2$  differs from the related  ${}^6\text{MnO}$  by the symmetrical arrangement of two ligands in this linear two-coordinate complex. As a result, the single  $\sigma$ -type SOMO (which is accompanied by two  $3d_{\delta^-}$ - and two  $3d_{\pi^-}$ -type SOMOs) has larger  $3d_z^2$  and less  $4s$  character than for  $\text{MnO}$  and is significantly Mn–F antibonding. The isotropic HFCC is therefore lower, and its significantly larger dependence on  $\nu_x$  is mainly due to valence-shell spin polarization. The overall range of  $A_{\text{iso}}(\text{M})$  values is thus larger than the relatively low HFCC itself. Comparison with experiment suggests the BH-type hybrid functionals to provide the best description (Table 8). Spin contamination is generally low. The absolute value of  $A_{\text{dip}}(\text{M})$  is very small and thus difficult to describe accurately. Moreover, it changes significantly from Ne to Ar matrix (Table 9). Remember that this system was also one of the more difficult examples in the coupled cluster calculations (section 5, Table 3).

${}^7\text{MnF}$  and  ${}^7\text{MnH}$  differ from  ${}^6\text{MnO}$  and  ${}^6\text{MnF}_2$  mainly by having two rather than one singly occupied  $\sigma$ -type orbitals. The metal  $4s$  orbital contributes in an Mn–X bonding way to one of these SOMOs, in an antibonding fashion to the other one (both orbitals are again dominated by the  $3d_z^2$  orbital). As for  $\text{MnF}_2$ , inclusion of exact exchange influences mainly the SOMO and valence-shell spin-polarization contributions in both systems, while the total core polarizations are almost unaffected. The overall dependence on  $\nu_x$  is quite large for  $\text{MnH}$  (but not as large as for  $\text{MnF}_2$ ), somewhat lower for  $\text{MnF}$  (cf. Figure 3). The choice of  $\nu_c$  influences both core and valence shell contributions. For  $\text{MnH}$  these changes cancel each other so that the overall dependence on  $\nu_c$  is low, similar to  $\text{MnF}_2$  but in contrast to  $\text{MnF}$ . The comparison with experiment would suggest BH-type functionals to perform best for  $\text{MnH}$ . On the other hand, all functionals give results within ca. 13% from experiment for  $\text{MnF}$ . Spin contamination does not seem to be a problem for  $\text{MnF}_2$ ,  $\text{MnF}$ , or  $\text{MnH}$ , in contrast to the BH-type results for  $\text{MnO}$  (Table 9).

For these four manganese systems,  $A_{\text{dip}}(\text{M})$  is very small and caused mainly by the  $3d_{xz}$ ,  $3d_{yz}$ ,  $3d_{xy}$ , and  $3d_{x^2-y^2}$  character of the  $\pi$ - and  $\delta$ -type SOMOs. It is notable that the effect of spin polarization is again not negligible (cf. above). For example, the dipolar coupling of  $-15.7$  MHz for  $\text{MnO}$  at the unrestricted BHPW91 level is changed to  $-20.2$  MHz at the restricted level. Similarly, we obtain  $+2.4$  MHz for  $A_{\text{dip}}(\text{Mn})$  in  $\text{MnF}_2$  at the unrestricted,  $-5.9$  MHz at the restricted BHPW91 level.

**TiF<sub>3</sub> and MnO<sub>3</sub>.** Two related molecules with relatively large positive spin densities at the nuclei, but with a significant dependence on  $\nu_{xc}$  are  $\text{TiF}_3$  and  $\text{MnO}_3$  (cf. Figure 4, Table 8). For both systems, the SOMO is dominated by the metal  $3d_z^2$  orbital, interacting with the ligand hybrid orbitals in an antibonding way. Some  $4s$  character is mixed in. The composition of the SOMO is similar for both complexes (Mulliken population analyses, using the BLYP functional, give a  $4s/3d_z^2$

population ratio of 0.18/0.76 for  $\text{TiF}_3$  and of 0.13/0.67 for  $\text{MnO}_3$ ). The larger  $\rho_{\text{N}}$  of  $\text{MnO}_3$  is thus due to the much larger effective charge on the metal. The sensitivity to  $\nu_x$  is already significant for  $\text{TiF}_3$ , but all functionals do still give results within ca. 15% of the experimental value. DFT calculations of Belanzoni et al.<sup>17</sup> (with the BP86 functional and STO basis sets) gave  $-233.9$  MHz for  $A_{\text{iso}}(\text{Ti})$ , somewhat larger than our  $-216.6$  MHz with the same functional. This difference arises mainly from their shorter LSDA Ti–F bond length ( $1.756$  Å vs our  $1.780$  Å). Using their shorter distance, we obtain  $-231.0$  MHz, i.e., closer agreement with their value (note the negative  $g_{\text{N}}(\text{Ti})$ , Table 7). This indicates a much larger structural dependence of  $A_{\text{iso}}(\text{Ti})$  compared to our above discussion for  $\text{TiN}$ , probably due to presence of core–shell spin-polarization contributions.

In view of the significant deviations of the  $g$ -tensor from the free-electron value (Table 2),  $\text{TiF}_3$  is one of the cases where spin–orbit effects have to be considered. Indeed, here we are in the fortunate situation that explicit DFT calculations of these spin–orbit contributions are available, both within a perturbation–theoretical approach,<sup>17</sup> and using the explicitly relativistic two-component zero-order-regular-approximation (ZORA) scheme.<sup>19</sup> Using the BP86 functional, both approaches gave very small positive spin–orbit (pseudocontact) contributions to  $A_{\text{iso}}(\text{Ti})$  (ca. 3–6 MHz), whereas the spin–orbit contributions to  $A_{\text{dip}}(\text{Ti})$  are negative (between  $-2.3$  MHz and  $-2.8$  MHz) and significant relative to the small dipolar coupling. Our own simple semiempirical estimate of the spin–orbit corrections (section 4, eq 6) gives  $+3.4$  MHz for the pseudocontact term and  $-2.1$  MHz for  $A_{\text{dip}}$ , in good agreement with the explicit calculations. The addition of the latter value to the computed  $A_{\text{dip}}$  does not improve the agreement with experiment, but it has to be noted that the matrix does affect the results nonnegligibly (cf. Table 9).

For  $\text{MnO}_3$ , the  $\nu_x$  dependence of  $A_{\text{iso}}$  is particularly pronounced (Table 8 and Figure 4), and is complicated by significant spin contamination (cf.  $\langle S^2 \rangle$ ) and the large dependence of  $A_{\text{dip}}(\text{Mn})$  on  $\nu_x$ , Table 9). The results for  $\text{MnO}_3$  exemplify a dilemma that arises also in other cases (see below): While some admixture of exact exchange increases spin polarization and thus may improve the agreement with experiment relative to the “pure” GGA results, it may lead at the same time to considerable spin contamination (we note that the spin contamination is connected to valence-shell spin polarization.). Thus, despite the superficial similarity with the isoelectronic  $\text{TiF}_3$ , the demands on the functional are much higher for the more covalent, highly oxidized  $\text{MnO}_3$  (cf. also the VN vs TiO comparison above). One could argue that the B3-type functionals do still provide a reasonable description of the wave function for  $\text{MnO}_3$  (with moderate but nonnegligible spin contamination). However, the unusually large variations in  $A_{\text{dip}}(\text{M})$  (Table 9) speak against this. Note that the coupled cluster results for  $A_{\text{iso}}(\text{M})$  (Table 3) agree well with experiment (they are slightly too negative).

**$[\text{Mn}(\text{CN})_4]^{2-}$  and  $[\text{Cr}(\text{CO})_4]^+$ .** As two further high-spin systems, we may examine the two isoelectronic, tetrahedral ions  ${}^6[\text{Mn}(\text{CN})_4]^{2-}$  and  ${}^6[\text{Cr}(\text{CO})_4]^+$ . The five SOMOs correspond to all five metal  $d$  orbitals, corresponding to the  $t_2$  and  $e$  irreducible representations in  $T_d$  symmetry. Due to the absence of any direct  $s$ -type SOMO contribution,  $\rho_{\text{N}}$  is entirely caused by spin polarization and is negative for both systems (see Figure 5; the positive  $A_{\text{iso}}(\text{Cr})$  is due to the negative  $g_{\text{N}}(\text{Cr})$ , cf. Table 7). Spin polarization of the core shells by the  $d$ -type SOMOs dominates (and provides negative  $\rho_{\text{N}}$ ) and is partly compensated by valence-shell spin polarization. Therefore, the dependence

on  $\nu_{xc}$  is particularly large, and it is rather similar for these isoelectronic systems (Figure 5). Even with BH-type hybrid functionals, which provide the best agreement with experiment, the spin polarization apparently is still underestimated slightly. The coupling anisotropy is zero, due to symmetry, and spin contamination is relatively small for all functionals (Table 9).

**[Mn(CO)<sub>5</sub>] and [Fe(CO)<sub>5</sub>]<sup>+</sup>.** Let us now turn to low-spin complexes. For the isoelectronic low-spin d<sup>7</sup> complexes <sup>2</sup>[Mn(CO)<sub>5</sub>] and <sup>2</sup>[Fe(CO)<sub>5</sub>]<sup>+</sup>, the SOMO exhibits metal 3d<sub>z<sup>2</sup></sub> and 4p<sub>z</sub> character and is  $\sigma$ -antibonding with respect to the axial M-CO bond in these square pyramidal (C<sub>4v</sub>) complexes. The metal 4s contribution to the SOMO is small. As the small positive direct SOMO contribution to  $A_{iso}(M)$  (ca. +60 MHz and ca. +14 MHz for M = Mn, Fe, respectively) is furthermore canceled partly by negative core-shell spin-polarization contributions, very small isotropic HFCCs result for these low-spin systems. As a consequence, the description is difficult and the dependence on  $\nu_{xc}$  (particularly on  $\nu_x$ ) is large on a relative scale (Figure 6). This holds in particular for the iron complex. In other words, a larger effective charge at the metal appears to increase the sensitivity to the functional (as found above for other isoelectronic pairs, e.g., VN vs TiO or MnO<sub>3</sub> vs TiF<sub>3</sub>). Based on the comparison to experiment, it is difficult to select any particular functional that would be preferable over the others (the BH-type hybrids might seem to be less preferable, although spin contamination is not very pronounced). We estimate spin-orbit corrections (cf. section 4) of ca. +21.2 MHz for  $A_{iso}(Mn)$  and of ca. -12.8 MHz for  $A_{dip}(Mn)$  in [Mn(CO)<sub>5</sub>], as well as ca. +5.3 MHz for  $A_{iso}(Fe)$  and ca. -3.0 MHz for  $A_{dip}(Fe)$  in [Fe(CO)<sub>5</sub>]<sup>+</sup>. The correction for the manganese complex may be overestimated, as the coefficient of the 3d<sub>z<sup>2</sup></sub> orbital in the SOMO is small ( $\delta^2 = 0.43$ , cf. eq 6) and the neglected contribution from the 4p<sub>z</sub> orbital may be large.

**[Mn(CN)<sub>5</sub>NO]<sup>2-</sup> and [Mn(CN)<sub>4</sub>N]<sup>-</sup>.** The two C<sub>4v</sub> symmetrical systems <sup>2</sup>[Mn(CN)<sub>5</sub>NO]<sup>2-</sup> and <sup>2</sup>[Mn(CN)<sub>4</sub>N]<sup>-</sup> (a low-spin d<sup>5</sup> and a d<sup>1</sup> complex, respectively) both have a single metal 3d<sub>xy</sub>-type SOMO. They also share the unfortunate problem of significant spin contamination, in particular with hybrid functionals (Table 9). Significant core-shell spin polarization dominates the observed negative isotropic HFCCs. This is augmented by valence-shell spin polarization, mainly involving metal d<sub>xz</sub> and d<sub>yz</sub> orbitals. These d-orbitals contribute to the  $\pi$ -components of the Mn-N triple bond in the d<sup>1</sup> system, and to both Mn-N  $\pi$ -bonding and  $\pi$ -antibonding MOs in the d<sup>5</sup> complex. Low-lying excited states involving these  $\pi$ - and  $\pi^*$ -type orbitals are mainly responsible for the spin contamination (i.e., the spin contamination is connected to significant valence-shell spin polarization, as found above for MnO<sub>3</sub>).

Spin contamination is already nonnegligible for the GGA functionals, increases for the B3-type hybrids, and becomes dramatic for the BH-type hybrids. As a consequence, the computed  $A_{dip}$  values appear to be still reasonable for the GGAs but deteriorate significantly for the hybrid functionals (with the exception of the B3-type hybrid results for [Mn(CN)<sub>4</sub>N]<sup>-</sup>). The isotropic HFCCs are not sufficiently negative with the GGAs, are in closer agreement with experiment for the B3-type hybrids, but become much too negative with the BH-type hybrids (Figure 7). We have to conclude that the reasonable  $A_{iso}$  results with the B3-type hybrids are at least in part fortuitous, due to spin contamination. None of the functionals investigated here is thus really adequate to describe all features of the hyperfine coupling in these two complexes. We also note that SCF convergence to a global minimum in parameter space (i.e., in the MO coef-

ficients) was difficult with several of the functionals, in particular for [Mn(CN)<sub>4</sub>N]<sup>-</sup>. It appears that low-lying local minima exist. We have therefore used tighter convergence criteria on the density matrix for these systems than the *Gaussian 94* default values (i.e., 10<sup>-8</sup> au instead of 10<sup>-4</sup> au root-mean-square deviation).

The pure GGA functionals give three positive occupied orbital energies for [Mn(CN)<sub>5</sub>NO]<sup>2-</sup> (no positive eigenvalues are obtained with the BH-type hybrids), indicating that the isolated dianion might not be stable with respect to electron loss (this holds also for the [Mn(CN)<sub>4</sub>]<sup>2-</sup> dianion discussed above). However, we believe that, in connection with the finite basis set, this affects the HFCC results negligibly compared to the more serious problem of spin contamination.

Due to the significant deviations of the g-tensor components from the free-electron value (Table 2) in [Mn(CN)<sub>5</sub>NO]<sup>2-</sup>, we have considered spin-orbit corrections. Our simple estimate gives a pseudocontact term of ca. +6.4 MHz and a spin-orbit contribution to  $A_{dip}$  of -2.8 MHz. Spin-orbit effects are estimated to be small for [Mn(CN)<sub>4</sub>N]<sup>-</sup> (cf. g-tensor in Table 2).

**[Ni(CO)<sub>3</sub>H] and [Co(CO)<sub>4</sub>].** The SOMO of these two trigonal pyramidal (C<sub>3v</sub>) d<sup>9</sup> complexes<sup>88</sup> is of a<sub>1</sub> symmetry and composed of metal 3d<sub>z<sup>2</sup></sub> and 4p<sub>z</sub> contributions, with overall axial metal-ligand  $\sigma$ -antibonding character. In both cases, the SOMO has very little metal 4s character and thus gives only small direct contributions to  $\rho_N$ . These are furthermore compensated partially by the negative core-shell spin polarization. As a result, the isotropic HFCCs are low. Possibly due to the partial 4p<sub>z</sub> character of the SOMO, the dipolar couplings are relatively large (in analogy to the low-spin d<sup>7</sup> complexes [Mn(CO)<sub>5</sub>] and [Fe(CO)<sub>5</sub>]<sup>+</sup> discussed above).

At first sight,  $A_{dip}(M)$  in [Co(CO)<sub>4</sub>] would seem significantly too large with GGA (and B3-type) functionals (Table 9), despite the relatively small spin contamination. However, in view of the very large g-shifts (Table 2), spin-orbit corrections are expected to be particularly significant for this complex. Indeed, our simple estimate (eq 6, section 4) provides a large correction of -42.2 MHz to  $A_{dip}(Co)$ . This would bring both the GGA results and the B3-type hybrid results into good agreement with experiment, whereas the BH-type hybrid results would then be too low. The reduction of the dipolar couplings by inclusion of exact exchange is again accompanied by significant spin contamination, and we do not expect these BH-type functionals to provide a reliable description for this system. In view of its smallness, the isotropic HFCC (Table 8) is difficult to describe. Considering also the estimated spin-orbit correction to  $A_{iso}(Co)$  of +69.5 MHz may suggest that even the B3-type hybrid results are still insufficiently negative. On the other hand, the BH-type hybrid results clearly overshoot the negative spin-polarization contributions dramatically.

Both spin contamination and the dependence of  $A_{dip}(M)$  on  $\nu_{xc}$  are less pronounced for [Ni(CO)<sub>3</sub>H]. The GGA results would seem to agree best with experiment for  $A_{dip}(Ni)$ , whereas the BH-type hybrid results are clearly too negative (and are accompanied by spin-contamination, Table 9). Our estimated spin-orbit correction of +16.4 MHz to  $A_{dip}(Ni)$  would change this picture but may be too large, as the metal 4p<sub>z</sub> orbital contributes significantly to the SOMO (the 3d<sub>z<sup>2</sup></sub> contribution to the SOMO is particularly low for this complex, with  $\delta^2 = 0.28$ , cf. eq 6). The estimated spin-orbit correction to  $A_{iso}(Ni)$  (pseudocontact term) of -26.8 MHz may thus also be too large. In view of these uncertainties about the magnitude of the spin-orbit corrections, either GGA or B3-type hybrid functionals might



be closest to the experimental isotropic HFCC (Table 8), whereas the BH-type hybrids give in any case too large values.

**CuO.** The  $d^9$  complex  ${}^2\text{CuO}$  differs from the previous cases by exhibiting a hole in a degenerate ( $\pi$ -type) MO. In other words, the one-particle description of the  $X^2\Pi$  ground state of CuO assigns three electrons to the  $4\pi$  MO (the two components are built from the O  $2p_x$ , Cu  $3d_{xz}$ , Cu  $4p_x$ , and from the O  $2p_y$ , Cu  $3d_{yz}$ , and Cu  $4p_y$  orbitals, respectively).<sup>89</sup> It is thus clear that a cylindrically symmetrical wave function in a single-determinant framework may be obtained only by using fractional occupations (i.e., 0.5 electrons in each of the two MOs). The integer occupation of one of the two degenerate  $4\pi$  MOs would, e.g., not provide an axially symmetrical hyperfine tensor. On the other hand, one may average calculations with different integer occupations (similar considerations pertain to Kohn–Sham calculations on certain degenerate states of open-shell atoms<sup>90a</sup>). The results for  $A_{\text{dip}}(\text{Cu})$  obtained by this averaging procedure are given in Table 9 (the coupled cluster results in Table 3 were obtained in the same manner). As we were not able to enforce appropriate fractional occupations within the *Gaussian 94* program, we resorted to calculations using the BP86 functional and the deMon code<sup>31,90</sup> to compare integer and fractional occupations (using the same basis set but in addition auxiliary basis sets to fit charge density and exchange–correlation potential<sup>31,90</sup>). Indeed, the dipolar couplings obtained with fractional occupations differed by less than 6 MHz from averaged results with integer occupations (the isotropic couplings also changed by less than 5 MHz). This seems to justify the averaging procedure.

Due to the absence of metal  $4s$  orbital contributions to the SOMO, the isotropic metal HFCC arises exclusively from spin polarization. Interestingly, the  $\nu_x$  dependence for a given  $\nu_c$  is  $\rho_N(\text{B}) > \rho_N(\text{BH}) > \rho_N(\text{B3})$ . On the other hand, we find a significant decrease of  $A_{\text{dip}}(\text{Cu})$  from B to B3 to BH functionals. The latter trend is due to the shift of single-electron density from Cu to O with admixture of exact exchange. For the isotropic HFCCs, stronger core–shell spin polarization accounts for the more negative value with B3-type relative to B-type functionals. Further dramatic decrease of the spin density on Cu reverses the trend and gives a less negative  $A_{\text{iso}}(\text{Cu})$  with BH-type functionals.

The  $A_{\text{iso}}(\text{Cu})$  results are too negative for all functionals, whereas the variation between the functionals is smaller than the discrepancy with respect to experiment. Note that even the coupled cluster calculations give too negative  $A_{\text{iso}}(\text{Cu})$  when considering the trend upon enlarging the basis set (Table 3). Moreover, spin contamination seems to be small. The difference with respect to experiment is thus probably not mainly a problem of describing the spin polarization well. There are three other possible reasons which might account for the too negative isotropic HFCCs, of which we suspect the latter to be decisive: multireference character of the wave function, errors in the bond length, relativistic effects.

*Multireference Character of the Wave Function.* Our coupled cluster wave functions give no large coefficients for configurations other than the given reference configuration. We note also that the single-reference coupled-pair-functional (CPF) calculations by Langhoff and Bauschlicher appear to describe the ground state of CuO adequately (whereas CISD calculations without corrections for higher order excitations perform poorly).<sup>91</sup> Thus, CuO is probably not a priori a multireference case. Moreover, spin contamination is small. This speaks against significant problems of describing the wave function with the current approaches.

*Bond Length Errors.* The isotropic HFCC is extremely dependent on the Cu–O bond length. Shortening the bond by only 0.005 Å (from 1.729 to 1.724 Å) changes  $A_{\text{iso}}(\text{Cu})$  from  $-776$  MHz to  $-747$  MHz, i.e., by ca. 4% (B3PW91 result). Together with the above results for TiN and TiF<sub>3</sub>, this suggests that the dependence of the isotropic HFCCs on bond length increases with an increasing importance of spin polarization (a more systematic study of the interdependence between structural changes and HFCCs in transition metal complexes is beyond the scope of the present study but should be pursued in the future). On the other hand, the experimental bond distance of 1.729 Å appears to be reliable and has been confirmed experimentally<sup>92</sup> and theoretically.<sup>93</sup>

*Relativistic Effects.* Scalar relativistic effects should lead to a larger (negative) spin density at the nucleus and would thus be expected to lead to *more* negative values for  $A_{\text{iso}}(\text{Cu})$ . Spin–orbit effects are difficult to judge, as unfortunately no experimental g-tensor information is available. Our preliminary perturbation–theoretical calculations of the g-tensor indicate a large positive  $\Delta g_{\perp}$ . Thus, we may expect significant spin–orbit contributions to the HFCCs, and we believe that this is the most likely reason for the discrepancies between calculation and experiment.

**[Cu(CO)<sub>3</sub>].** Finally, we look at a very different bonding situation. The wave function in  $[\text{Cu}(\text{CO})_3]$  is derived from the  $3d^{10}4p^1$  configuration of  $\text{Cu}^0$ , and the SOMO is composed of the Cu  $4p_z$  orbital and  $\pi$ -type ligand orbitals. The isotropic metal HFCC is thus exclusively due to spin polarization. Interestingly,  $\rho_N(\text{Cu})$  is positive, whereas we have seen above that core–shell spin polarization due to  $3d$ -type SOMOs always contributes negatively to  $\rho_N(\text{M})$ . Thus, the situation resembles more that known for main-group  $\pi$ -type radicals, with the (slight) difference that we have a very polarizable M-shell below the  $4p_z$ -type SOMO. The description for  $[\text{Cu}(\text{CO})_3]$  is thus considerably more difficult than for  $\text{Cu}(\text{C}_2\text{H}_2)$  or  $\text{Cu}(\text{CO})$  studied previously with DFT methods by Barone et al.,<sup>14,15</sup> where large positive direct contributions from a metal  $4s$ -type SOMO dominate.

Spin contamination is minor, and the dipolar couplings depend relatively little on the functional (however, the BH-type hybrids give ca. 6–7 MHz lower values, cf. Table 9). The experimental  $A_{\text{dip}}(\text{Cu})$  is underestimated. It is possible that this is due to an overestimate of the Cu–C bond length even by the MP2 optimizations used (cf. Table 1). This would be consistent with our finding that test calculations at the larger DFT optimized bond length (also Table 1), give ca. 8 MHz lower dipolar couplings. In other words, structural errors are more likely for this weakly bound complex than for the other systems.

Looking at the isotropic metal HFCC (Table 8), we see that we obviously underestimate core–shell spin polarization with the pure GGA functionals. Even the sign of the HFCC is wrong. The agreement with experiment is improved somewhat with B3-type hybrids, and even more significantly with the BH-type hybrids, without any apparent spin contamination problem. The situation may thus be comparable to that for  $\pi$ -type organic radicals.<sup>15</sup> We also see a surprisingly large difference between the B3LYP functional and the B3PW91 and B3PW91 functionals (likely due to the description of the SOMO).

## 8. Ligand HFCCs

As this work concentrates on complexes with the SOMO mainly localized on the metal, the spin densities at the ligand nuclei are about 1–2 orders of magnitude smaller than those at the metal nuclei. This places of course considerable demand

TABLE 10: Isotropic Ligand HFCCs (in MHz)

|   | isotope                            | BLYP  | BP86  | BPW91 | B3LYP | B3PW91 | BHLYP  | BHP86  | BHPW91 | exp <sup>a</sup>                    |
|---|------------------------------------|-------|-------|-------|-------|--------|--------|--------|--------|-------------------------------------|
| <sup>2</sup> ScO                                    | <sup>17</sup> O                    | -22.8 | -21.3 | -19.8 | -19.9 | -17.0  | -16.5  | -13.3  | -11.6  | -20.3(3) or -18.9(4) <sup>b,c</sup> |
| <sup>2</sup> TiN                                    | <sup>14</sup> N                    | 19.8  | 18.4  | 17.3  | 17.1  | 14.4   | 12.8   | 10.1   | 9.5    | 18.478(1)                           |
| <sup>3</sup> TiO                                    | <sup>17</sup> O                    | -8.2  | -8.2  | -7.3  | -4.9  | -4.3   | -0.2   | 0.6    | 1.6    |                                     |
| <sup>3</sup> VN                                     | <sup>14</sup> N                    | 6.0   | 6.2   | 5.8   | 3.2   | 3.2    | -9.3   | -6.0   | -7.2   |                                     |
| <sup>4</sup> VO                                     | <sup>17</sup> O                    | -2.7  | -3.1  | -2.4  | 1.1   | 1.5    | 6.7    | 7.3    | 8.0    | 0(4) <sup>d</sup>                   |
| <sup>6</sup> MnO                                    | <sup>17</sup> O                    | -6.6  | -5.4  | -5.3  | -8.0  | -7.3   | -9.0   | -9.1   | -8.8   |                                     |
| <sup>6</sup> MnF <sub>2</sub>                       | <sup>19</sup> F                    | 20.4  | 16.1  | 15.4  | 22.6  | 18.5   | 27.9   | 20.4   | 20.8   |                                     |
| <sup>7</sup> MnF                                    | <sup>19</sup> F                    | 78.5  | 69.4  | 67.2  | 79.2  | 72.9   | 82.9   | 79.5   | 77.9   | 68(6) or 75(6) <sup>b</sup>         |
| <sup>7</sup> MnH                                    | <sup>1</sup> H                     | 35.6  | 25.8  | 22.1  | 28.0  | 19.0   | 23.0   | 14.0   | 10.1   | 20.7(39)                            |
| <sup>2</sup> TiF <sub>3</sub>                       | <sup>19</sup> F                    | 8.7   | 5.0   | 1.7   | -5.6  | -12.9  | -14.8  | -23.5  | -24.3  | 8.3(4) or 8.0(4) <sup>b,e</sup>     |
| <sup>2</sup> MnO <sub>3</sub>                       | <sup>17</sup> O                    | -5.1  | -4.1  | -3.5  | 2.6   | 2.6    | 26.2   | 19.1   | 19.0   |                                     |
| <sup>6</sup> [Mn(CN) <sub>4</sub> ] <sup>2-</sup>   | <sup>13</sup> C                    | 3.5   | -0.1  | -0.8  | 0.5   | -3.0   | -1.2   | -4.7   | -5.1   |                                     |
|   | <sup>14</sup> N                    | 1.1   | 0.8   | 0.7   | 1.0   | 0.8    | 1.1    | 0.8    | 0.8    |                                     |
| <sup>6</sup> [Cr(CO) <sub>4</sub> ] <sup>+</sup>    | <sup>13</sup> C                    | -5.0  | -9.2  | -11.5 | -8.4  | -13.4  | -10.4  | -14.6  | -15.4  | -13.5                               |
|   | <sup>17</sup> O                    | -1.6  | -1.2  | -1.1  | -1.8  | -1.4   | -2.1   | -1.7   | -1.6   |                                     |
| <sup>2</sup> [Mn(CO) <sub>5</sub> ]                 | <sup>13</sup> C <sub>ax</sub>      | 0.7   | -1.9  | -3.4  | -34.4 | -37.0  | -72.7  | -72.9  | -73.0  |                                     |
|   | <sup>13</sup> C <sub>eq</sub>      | -15.1 | -18.3 | -19.7 | -21.7 | -26.0  | -27.9  | -31.2  | -32.2  |                                     |
|   | <sup>17</sup> O <sub>ax</sub>      | -8.8  | -8.2  | -8.0  | -8.2  | -7.6   | -6.4   | -6.1   | -5.8   |                                     |
|   | <sup>17</sup> O <sub>eq</sub>      | -2.9  | -2.0  | -2.0  | -3.6  | -2.7   | -4.3   | -3.6   | -3.2   |                                     |
| <sup>2</sup> [Fe(CO) <sub>5</sub> ] <sup>+</sup>    | <sup>13</sup> C <sub>ax</sub>      | 69.7  | 65.6  | 65.0  | 39.0  | 37.0   | 20.5   | 18.8   | 20.2   | 53.5                                |
|   | <sup>13</sup> C <sub>eq</sub>      | -18.5 | -20.3 | -21.3 | -25.1 | -26.9  | -25.2  | -27.0  | -26.9  | -23.0                               |
|   | <sup>17</sup> O <sub>ax</sub>      | -9.6  | -9.2  | -9.1  | -9.9  | -9.6   | -9.3   | -9.2   | -9.0   |                                     |
|   | <sup>17</sup> O <sub>eq</sub>      | -1.9  | -1.4  | -1.4  | -1.7  | -1.3   | -1.2   | -1.0   | -0.8   |                                     |
| <sup>2</sup> [Mn(CN) <sub>5</sub> NO] <sup>2-</sup> | <sup>13</sup> C <sub>ax</sub>      | -44.4 | -41.3 | -43.9 | -83.3 | -88.0  | -136.6 | -133.2 | -130.7 |                                     |
|   | <sup>13</sup> C <sub>eq</sub>      | -41.6 | -40.1 | -42.9 | -80.4 | -85.4  | -133.2 | -132.1 | -128.2 |                                     |
|   | <sup>14</sup> N(NO)                | -12.3 | -9.7  | -10.6 | -29.6 | -27.5  | -55.7  | -50.0  | -49.9  | -10.64                              |
|   | <sup>14</sup> N(CN <sub>ax</sub> ) | 0.5   | 0.4   | 0.4   | 0.7   | 0.6    | 0.9    | 0.4    | 0.6    |                                     |
|   | <sup>14</sup> N(CN <sub>eq</sub> ) | 1.0   | 0.5   | 0.5   | 1.0   | 0.7    | 1.2    | 0.7    | 0.6    |                                     |
|   | <sup>17</sup> O                    | 7.8   | 4.0   | 4.3   | 33.2  | 27.6   | 82.0   | 70.5   | 69.7   |                                     |
| <sup>2</sup> [Mn(CN) <sub>4</sub> N] <sup>-</sup>   | <sup>13</sup> C                    | -28.9 | -28.7 | -30.1 | -53.0 | -55.4  | -135.1 | -134.1 | -136.2 |                                     |
|   | <sup>14</sup> N <sub>ax</sub>      | -3.1  | -1.5  | -1.4  | -8.2  | -5.0   | -31.3  | -21.3  | -19.4  |                                     |
|   | <sup>14</sup> N <sub>eq</sub>      | 1.4   | 0.7   | 0.7   | 1.8   | 1.3    | 3.6    | 2.7    | 2.8    |                                     |
| <sup>2</sup> [Ni(CO) <sub>3</sub> H]                | <sup>1</sup> H                     | 348.2 | 308.7 | 311.8 | 208.0 | 189.3  | -116.2 | -105.5 | -110.0 | 293                                 |
|   | <sup>13</sup> C                    | 17.3  | 12.4  | 11.9  | 5.1   | 4.8    | -8.3   | -10.7  | -10.2  |                                     |
|   | <sup>17</sup> O                    | -3.0  | -2.2  | -2.2  | -3.7  | -3.1   | -4.1   | -3.6   | -3.5   |                                     |
| <sup>2</sup> [Co(CO) <sub>4</sub> ]                 | <sup>13</sup> C <sub>ax</sub>      | 105.8 | 101.0 | 100.4 | 57.3  | 55.6   | 29.7   | 32.8   | 37.7   | 67.2                                |
|   | <sup>13</sup> C <sub>eq</sub>      | 6.2   | 3.2   | 3.1   | 3.0   | 1.5    | 15.6   | 18.8   | 24.7   |                                     |
|   | <sup>17</sup> O <sub>ax</sub>      | -13.7 | -13.1 | -12.9 | -12.7 | -12.1  | -9.0   | -8.8   | -8.3   |                                     |
|   | <sup>17</sup> O <sub>eq</sub>      | -2.9  | -2.4  | -2.4  | -2.9  | -2.7   | -1.2   | -1.3   | -0.7   |                                     |
| <sup>2</sup> CuO                                    | <sup>17</sup> O                    | -20.4 | -6.7  | -5.2  | -32.0 | -18.7  | -55.7  | -39.2  | -37.9  |                                     |
| <sup>2</sup> [Cu(CO) <sub>3</sub> ]                 | <sup>13</sup> C                    | -6.3  | -14.6 | -17.5 | -12.3 | -20.5  | -19.1  | -30.4  | -32.3  | -18.7                               |
|   | <sup>17</sup> O                    | -4.4  | -2.7  | -2.7  | -6.9  | -5.3   | -10.7  | -11.3  | -9.0   | 11.2                                |

<sup>a</sup> Unless stated otherwise, the experimental values are from the sources cited in the corresponding footnotes to Table 8. <sup>b</sup> In Ne or Ar matrix, respectively. <sup>c</sup> Cf. ref 10. <sup>d</sup> In Ne matrix, ref 12. <sup>e</sup> Reference 44, cf. ref 18 for a revision.

on the computational approach to describe the subtle delocalization of spin density to the ligands, as well as spin-polarization effects. We should also mention again that relativistic effects, which are not considered here, may have a nonnegligible influence on the small ligand HFCCs (cf. section 4). The metal HFCCs are our main interest in this work, but we may nevertheless note some trends in the computed ligand HFCCs.

Table 10 summarizes the isotropic ligand HFCCs, Table 11 the dipolar couplings. Concerning the dependence of the isotropic HFCCs on  $\nu_{xc}$ , we note trends very similar to above for the metal HFCCs. Thus, the spin densities  $\rho_N$  at the ligand nuclei (when including their signs) exhibit often the  $\nu_c$  dependence  $\rho_N(\text{LYP}) \geq \rho_N(\text{P86}) \geq \rho_N(\text{PW91})$  for a given  $\nu_x$ , and typically the  $\nu_x$  dependence  $\rho_N(\text{B}) \geq \rho_N(\text{B3}) \geq \rho_N(\text{BH})$  for a given  $\nu_c$  (the negative  $g_N(\text{O})$  needs to be kept in mind, cf. Table 7). A notable exception to this trend is provided by the inverse dependence on  $\nu_x$ , i.e.,  $\rho_N(\text{BH}) \geq \rho_N(\text{B3}) \geq \rho_N(\text{B})$  in the high-spin complexes MnO, MnF<sub>2</sub>, and MnF or in the case of <sup>17</sup>O splitting in CuO and Cu(CO)<sub>3</sub>. Exceptions to the abovementioned trends are also notable when significant spin contamination is connected to orbitals with large contributions on the given ligand (see, e.g., results for VN, MnO<sub>3</sub>, [Co(CO)<sub>4</sub>]), and for the axial nitrogen in [Mn(CN)<sub>4</sub>N]<sup>-</sup> (cf. Table 10). The

relative sensitivity of the results to  $\nu_x$  vs  $\nu_c$  is of course different than it was for the metal HFCCs, as the relevant spin-polarization effects are now those around the ligand nuclei.

As for the isotropic metal HFCCs, the isotropic ligand HFCCs are made up of direct SOMO and indirect spin-polarization contributions. The latter are missing for MnH, where the single hydrogen 1s-AO is directly involved in two of the SOMOs (cf. section 7). The  $A_{\text{iso}}(\text{H})$  in MnH is thus a relatively simple measure of the localization of the two  $\sigma$ -type SOMOs at the H nucleus. Interestingly, the dependence of this  $A_{\text{iso}}(\text{H})$  on  $\nu_{xc}$  in MnH is similar to that of the metal HFCCs in ScO and TiN, which are also dominated by direct SOMO contributions (but with much larger overall  $\rho_N$ ; cf. section 7). The significant difference between LYP and the two other correlation functionals is particularly notable for  $A_{\text{iso}}(\text{H})$  in MnH. This may suggest that the description of dynamical correlation is critical for the charge distribution within the two  $\sigma$ -type SOMOs.

A similar dependence on  $\nu_c$  is apparent for the <sup>13</sup>C HFCCs in [Mn(CN)<sub>4</sub>]<sup>2-</sup> and [Cr(CO)<sub>4</sub>]<sup>+</sup>, but for a different reason: The SOMO contributions are affected very little, and it is valence-shell spin polarization which changes with  $\nu_c$  (core polarizations at carbon are negligible). Experimental data are available only for [Cr(CO)<sub>4</sub>]<sup>+</sup>. The hybrid functionals appear to give better

**TABLE 11: Dipolar Ligand HFCCs (in MHz)<sup>a</sup>**

|   | isotope   | BLYP               | BP86               | BPW91              | B3LYP              | B3PW91             | BHLYP               | BHP86               | BHPW91              | exp <sup>b</sup>            |
|---|---|--------------------|--------------------|--------------------|--------------------|--------------------|---------------------|---------------------|---------------------|-----------------------------|
| <sup>2</sup> ScO                                    | <sup>17</sup> O                                 | 0.2                | -0.2               | -0.2               | 0.6                | 0.2                | 1.4                 | 0.7                 | 0.7                 | 0.4(2), 0.7(3) <sup>c</sup> |
| <sup>2</sup> TiN                                    | <sup>14</sup> N                                 | 0.6                | 0.5                | 0.4                | 0.4                | 0.3                | 0.0                 | -0.1                | -0.3                | 0.055(2)                    |
| <sup>3</sup> TiO                                    | <sup>17</sup> O                                 | -1.1               | -1.5               | -1.6               | -0.6               | -1.0               | 0.7                 | 0.4                 | 0.3                 |                             |
| <sup>3</sup> VN                                     | <sup>14</sup> N                                 | 1.7                | 1.7                | 1.7                | 2.1                | 2.2                | 3.6                 | 3.9                 | 3.9                 |                             |
| <sup>4</sup> VO                                     | <sup>17</sup> O                                 | -2.2               | -2.8               | -3.1               | -1.7               | -2.5               | 0.0                 | -0.3                | -1.1                | 0(3)                        |
| <sup>2</sup> TiF <sub>3</sub>                       | <sup>19</sup> F <sup>d</sup>                    | 20.9, -0.2, -20.7  | 26.9, 5.0, -31.9   | 29.7, 6.4, -35.8   | 19.4, -0.4, -19.0  | 25.2, 4.8, -30.0   | 15.7, 2.2, -13.4    | 19.6, 2.0, -21.6    | 21.6, 2.8, -24.4    | <i>e</i>                    |
| <sup>2</sup> MnO <sub>3</sub>                       | <sup>17</sup> O <sup>d</sup>                    | -23.9, 3.0, 20.9   | -24.2, 2.0, 22.2   | -24.7, 1.5, 23.2   | -34.7, -14.9, 49.6 | -55.3, 18.1, 37.2  | -61.7, -57.2, 118.9 | -61.5, -57.8, 119.3 | -62.1, -57.9, 120.0 |                             |
| <sup>6</sup> [Mn(CN) <sub>4</sub> ] <sup>2-</sup>   | <sup>13</sup> C                                 | 2.1                | 2.0                | 2.0                | 2.0                | 2.0                | 2.1                 | 2.0                 | 2.0                 |                             |
|   | <sup>14</sup> N                                 | -0.1               | -0.1               | -0.1               | -0.1               | -0.1               | -0.1                | -0.1                | -0.1                |                             |
| <sup>6</sup> [Cr(CO) <sub>4</sub> ] <sup>+</sup>    | <sup>13</sup> C                                 | 1.1                | 1.1                | 0.8                | 1.4                | 1.1                | 1.4                 | 1.4                 | 1.4                 | 1.0                         |
|   | <sup>17</sup> O                                 | 1.0                | 0.8                | 1.0                | 0.9                | 0.9                | 0.8                 | 0.8                 | 0.8                 |                             |
| <sup>6</sup> MnO                                    | <sup>17</sup> O                                 | 8.3                | 8.1                | 8.3                | 9.9                | 10.1               | 15.4                | 15.5                | 15.7                |                             |
| <sup>6</sup> MnF <sub>2</sub>                       | <sup>19</sup> F                                 | -19.3              | -18.9              | -18.3              | -15.7              | -15.3              | -11.8               | -11.7               | -11.6               |                             |
| <sup>7</sup> MnF                                    | <sup>19</sup> F                                 | 12.9               | 13.4               | 13.7               | 13.4               | 13.4               | 12.9                | 12.6                | 12.6                | 8(6), 10(6) <sup>c</sup>    |
| <sup>7</sup> MnH                                    | <sup>1</sup> H                                  | 10.9               | 10.9               | 10.9               | 11.2               | 11.2               | 11.8                | 11.8                | 11.8                | 8.4(33)                     |
| <sup>2</sup> [Mn(CO) <sub>5</sub> ]                 | <sup>13</sup> C <sub>ax</sub>                   | 1.6                | 1.2                | 1.6                | 1.1                | 1.1                | 0.7                 | 0.7                 | 0.8                 |                             |
|   | <sup>13</sup> C <sub>eqf</sub>                  | -0.8, -5.8, 6.7    | -0.8, -5.6, 6.5    | -0.8, -5.7, 6.6    | -0.5, -5.6, 6.1    | -0.2, -5.6, 5.8    | -0.3, -5.4, 5.6     | -0.3, -5.4, 5.6     | -0.3, -5.5, 5.7     |                             |
|   | <sup>17</sup> O <sub>ax</sub>                   | -2.0               | -2.0               | -2.1               | -1.7               | -1.8               | -1.7                | -1.7                | -1.9                |                             |
| <sup>2</sup> [Fe(CO) <sub>5</sub> ] <sup>+</sup>    | <sup>17</sup> O <sub>eqf</sub>                  | 7.0, 8.6, -15.6    | 6.9, 8.3, -15.2    | 6.8, 8.3, -15.1    | 6.7, 8.9, -15.6    | 6.3, 8.8, -15.1    | 5.5, 10.6, -16.1    | 5.4, 10.2, -15.6    | 5.1, 10.3, -15.4    |                             |
|   | <sup>13</sup> C <sub>ax</sub>                   | 2.8                | 2.8                | 2.8                | 2.0                | 2.0                | 1.4                 | 1.4                 | 1.4                 | 2.8                         |
|   | <sup>13</sup> C <sub>eqf</sub>                  | 5.0, -3.6, -1.4    | 4.9, -3.5, -1.3    | 5.0, -3.6, -1.4    | 5.4, -3.1, -2.2    | 5.3, -3.1, -2.2    | 5.8, -3.1, -2.7     | 5.7, -3.1, -2.7     | 5.8, -3.0, -2.8     | 4.4, -2.2, -2.2             |
|   | <sup>17</sup> O <sub>ax</sub>                   | -3.0               | -3.0               | -3.0               | -2.6               | -2.7               | -2.7                | -5.0                | -2.8                |                             |
|   | <sup>17</sup> O <sub>eqf</sub>                  | 3.2, 5.1, -8.3     | 3.2, 5.0, -8.2     | 3.2, 4.9, -8.1     | 2.2, 4.8, -7.0     | 2.1, 4.7, -6.9     | 0.9, 4.9, -5.8      | 1.0, 4.8, -5.8      | 0.9, 4.8, -5.6      |                             |
| <sup>2</sup> [Mn(CN) <sub>5</sub> NO] <sup>2-</sup> | <sup>13</sup> C <sub>ax</sub>                   | 1.1                | 1.1                | 1.1                | 2.2                | 2.2                | 3.0                 | 2.9                 | 3.0                 |                             |
|   | <sup>13</sup> C <sub>eqf</sub>                  | 5.1, -3.1, -2.0    | 5.0, -3.1, -1.9    | 5.1, -3.2, -1.9    | 6.3, -4.2, -2.1    | 6.3, -4.2, -2.1    | 6.7, -5.0, -1.7     | 6.6, -5.0, -1.7     | 6.7, -5.0, -1.7     |                             |
|   | <sup>14</sup> N(NO)                             | 7.9                | 7.1                | 7.7                | 17.7               | 17.7               | 23.9                | 23.1                | 23.5                | 2.7                         |
|   | <sup>14</sup> N <sub>ax</sub> (CN)              | -0.6               | -0.6               | -0.6               | -1.2               | -1.3               | -1.8                | -1.8                | -1.7                |                             |
|   | <sup>14</sup> N <sub>eq</sub> (CN) <sup>f</sup> | -2.9, 4.6, -1.7    | -2.9, 4.7, -1.8    | -3.0, 4.7, -1.7    | -3.2, 4.1, -0.9    | -3.4, 4.2, -0.8    | -3.9, 4.4, -0.5     | -3.9, 4.4, -0.5     | -3.9, 4.4, -0.5     |                             |
|   | <sup>17</sup> O                                 | -15.0              | -13.6              | -14.6              | -38.2              | -38.3              | -55.0               | -54.3               | -54.2               |                             |
| <sup>2</sup> [Mn(CN) <sub>4</sub> N] <sup>-</sup>   | <sup>13</sup> C <sub>f</sub>                    | 5.0, -2.7, -2.3    | 5.0, -2.7, -2.3    | 5.1, -2.8, -2.3    | 6.4, -4.4, -2.0    | 6.5, -4.5, -2.0    | 8.7, -3.7, -3.1     | 8.6, -5.0, -3.6     | 8.9, -5.2, -3.7     |                             |
|   | <sup>14</sup> N <sub>ax</sub>                   | 2.4                | 2.4                | 2.5                | 6.6                | 6.9                | 16.9                | 16.9                | 16.6                |                             |
|   | <sup>14</sup> N(CN) <sup>f</sup>                | -3.5, 5.8, -2.3    | -3.5, 5.8, -2.2    | -3.6, 5.8, -2.2    | -3.8, 4.8, -1.0    | -3.9, 4.8, -0.9    | -4.4, 5.9, -1.5     | -4.4, 6.0, -1.6     | -6.2, 7.9, -1.7     |                             |
| <sup>2</sup> [Ni(CO) <sub>3</sub> H]                | <sup>1</sup> H                                  | 2.9                | 2.7                | 2.7                | 6.3                | 6.2                | 17.1                | 16.9                | 17.1                | 5.5                         |
|   | <sup>13</sup> C <sub>f</sub>                    | -2.6, -5.7, 8.3    | -2.7, -5.6, 8.3    | -2.8, -5.7, 8.5    | -3.2, -5.5, 8.7    | -3.3, -5.5, 8.8    | -3.3, -5.3, 8.5     | -3.2, -5.2, 8.5     | -3.3, -5.4, 8.7     |                             |
|   | <sup>17</sup> O <sub>f</sub>                    | -6.2, -8.4, 14.6   | -6.3, -8.2, 14.4   | -6.2, -8.2, 14.4   | -5.3, -8.7, 14.0   | -5.3, -8.6, 13.9   | -3.0, -10.1, 13.1   | -3.1, -9.8, 12.9    | -2.9, -10.0, 12.9   |                             |
| <sup>2</sup> [Co(CO) <sub>4</sub> ]                 | <sup>13</sup> C <sub>ax</sub>                   | 4.2                | 4.0                | 3.9                | 3.4                | 3.3                | 3.8                 | 3.9                 | 4.3                 | 3.6                         |
|   | <sup>13</sup> C <sub>eqf</sub>                  | 8.3, -6.6, -1.7    | 8.1, -6.4, -1.7    | 8.3, -6.6, -1.7    | 9.7, -7.7, -1.9    | 9.7, -7.7, -2.0    | 12.8, -11.8, -1.0   | 12.7, -11.9, -0.8   | 14.0, -13.6, -0.4   |                             |
|   | <sup>17</sup> O <sub>ax</sub>                   | -4.1               | -4.1               | -4.2               | -4.0               | -4.1               | -5.5                | -5.8                | -6.4                |                             |
|   | <sup>17</sup> O <sub>eqf</sub>                  | 2.2, -10.2, 8.0    | 2.4, -10.1, 7.7    | 2.2, -10.0, 7.8    | 0.3, -10.0, 9.6    | 0.3, -10.1, 9.8    | 5.8, -23.7, 17.9    | 6.2, -25.0, 18.8    | 6.9, -38.0, 31.1    |                             |
| <sup>2</sup> CuO                                    | <sup>17</sup> O                                 | -112.1             | -111.9             | -112.6             | -121.2             | -121.2             | -126.1              | -125.8              | -126.2              |                             |
| <sup>2</sup> Cu(CO) <sub>3</sub>                    | <sup>13</sup> C <sup>d</sup>                    | -11.8, -13.8, 25.6 | -11.9, -13.3, 25.2 | -12.2, -13.4, 25.7 | -10.5, -12.5, 23.1 | -11.0, -12.3, 23.3 | -8.2, -10.5, 18.7   | -8.3, -9.6, 17.9    | -8.9, -9.8, 18.8    | -12.3, -12.3, -24.6         |
|   | <sup>17</sup> O <sup>d</sup>                    | 16.2, 15.9, -32.2  | 15.8, 15.5, -31.3  | 15.8, 15.5, -31.3  | 16.5, 16.1, -32.6  | 16.0, 15.8, -31.8  | 15.9, 14.0, -29.9   | 15.7, 14.3, -30.0   | 15.7, 14.2, -30.0   |                             |

<sup>a</sup> Individual  $T_{ii}$  components are given for nonaxial tensors. <sup>b</sup> Experimental values are taken from the sources cited in the footnotes to Tables 8 and 10. <sup>c</sup> In Ne or Ar matrix, respectively. <sup>d</sup> Hyperfine tensor components are given in order: (1) along the metal–ligand bond, (2) normal to the metal–ligand bond, in the molecular plane, and (3) along the molecular  $z$ -axis. <sup>e</sup> Anisotropy experimentally not well defined, cf. discussion in ref 18. <sup>f</sup> Hyperfine tensor components are given in order: (1) along the metal–ligand bond, (2) normal to the metal–ligand bond and parallel to the  $xy$  plane, and (3) perpendicular to directions 1 and 2.

agreement with experiment than pure GGAs. A relatively large dependence on  $\nu_c$  is also apparent for MnF and MnF<sub>2</sub>.

A large dependence on  $\nu_x$  is seen for the isotropic <sup>13</sup>C HFCCs of the axial ligands in <sup>2</sup>[Mn(CO)<sub>5</sub>] and <sup>2</sup>[Fe(CO)<sub>5</sub>]<sup>+</sup>. The exchange–correlation potential affects mainly the valence-shell spin polarization, and the direct SOMO contribution. The (smaller) dependencies on  $\nu_x$  and  $\nu_c$  for VO, TiN, and TiF<sub>3</sub> are also due to the valence-shell polarization and to SOMO contributions. Particularly large dependence on  $\nu_{xc}$  is found in all cases with significant spin contamination problems, e.g., for MnO<sub>3</sub>. Thus, the very large dependence of  $A_{\text{iso}}(\text{O})$  in MnO<sub>3</sub> on  $\nu_x$  is probably an artifact of the large spin contamination with BH-type hybrid functionals (cf. section 7 and Table 9). Other examples are <sup>13</sup>C and nitrosyl <sup>14</sup>N HFCCs in [Mn(CN)<sub>5</sub>NO]<sup>2-</sup>, <sup>13</sup>C and nitride <sup>14</sup>N HFCCs in [Mn(CN)<sub>4</sub>N]<sup>-</sup>, and <sup>13</sup>C HFCCs in [Co(CO)<sub>4</sub>] (Table 10).

For most of the present systems, the theoretical values for  $A_{\text{dip}}$  of the ligands are very small, and often results with different functionals differ by less than 1 MHz. Agreement with the sparse experimental data appears reasonable in these cases. A larger dependence on  $\nu_{xc}$  is seen for TiF<sub>3</sub>, MnO, and MnF<sub>2</sub> (and also for cases with large spin contamination, cf. above). Thus, the ligand dipolar couplings in <sup>6</sup>MnO and <sup>6</sup>MnF<sub>2</sub> increase when adding exact exchange.

## 9. Conclusions

The present study shows that the quantitative calculation of hyperfine coupling constants for transition metal systems is still a challenge to quantum chemistry, more so than for organic radicals. None of the density functionals investigated here may be considered to provide acceptable results for the whole range of transition metal species studied. For a number of particularly difficult systems, essentially none of the functionals provides satisfactory results.

There are various reasons why the HFCCs of transition metal systems present such difficulties. One of them is the very delicate core–shell spin polarization, which is in many cases the dominant pathway to create spin density at the metal nucleus. Even for an isolated transition metal atom (consider Mn<sup>+</sup> in section 5), we may understand why this type of spin polarization is so difficult to describe by present-day functionals. The spin polarization is mainly due to exchange interactions between singly occupied metal 3d orbitals and the outermost doubly occupied 3s- and 2s-type core shells. It is clear that these exchange interactions are strongly nonlocal (specific examples will be discussed elsewhere<sup>25</sup>) and thus difficult to account for with approaches derived from the local density approximation.<sup>94</sup> It is also clear that the description of such subtle spin-polarization effects is very different from the energy quantities that are currently used to fit the free parameters in the exchange–correlation functionals. The description of spin polarization is already nontrivial for organic  $\pi$ -radicals.<sup>13,15,83</sup> The spin polarization mechanisms in transition metal complexes are even more variable, and they involve not only the valence shell but also to a large extent the outermost core shells of the metal.

A second difficulty is connected to spin contamination. In several of the examples studied here, spin contamination became significant when exact exchange was mixed into  $\nu_x$ . This led to a significant deterioration of the results. In some cases where spin polarization was underestimated at the GGA level, and where exact-exchange mixing would thus have been desirable to increase it, the dramatic onset of spin contamination made it impossible to improve the results with hybrid functionals. In some of the “limiting cases” discussed toward the end of section

7, spin contamination is already significant with pure GGA-type functionals. The spin contamination for the hybrid functionals is closely related to the well-known bias of unrestricted Hartree–Fock wave functions for higher spin multiplicities. Obviously, the spin contamination may be very pronounced for transition metal complexes (particularly so for 3d-metals!) due to the presence of low-lying excited states.

It is not clear how the magnitude of the spin polarization could be increased while avoiding significant spin contamination.<sup>95</sup> However, one may speculate that improved functionals might give increased core–shell spin polarization without exceedingly large valence-shell spin polarization (and thus spin contamination). Obviously, the description of valence spin polarization is also not trivial, even in cases with low spin contamination (cf. section 7). It seems likely that the desired functional would have to incorporate significantly less than 50% exact exchange. Generally, hyperfine coupling constants, in particular for transition metal systems, may turn out to be a particularly fruitful testing ground for new DFT (or alternative) approaches. In addition to the appreciable literature on organic molecules,<sup>13,15,31</sup> the hyperfine coupling constants of the 21 complexes studied in the present work should be useful as a benchmark set against which to calibrate new methods.

On the other hand, we should not judge even the present situation too pessimistically. For a significant number of complexes, the ca. 10–15% agreement with experimental isotropic metal HFCCs we were aiming for has been achieved with essentially all of the functionals (e.g., for ScO, TiN, TiO, VO, MnO, or MnF). In other subsets of molecules, the analysis of the electronic structure suggests the range of functionals (GGAs, B3-type, or BH-type hybrids) that might be most appropriate (as shown by the various examples discussed in this work). Careful selection of functionals is thus still expected to allow useful chemical applications in many areas, even though such an approach is obviously not completely satisfactory from a theoretical point of view. We expect that spin contamination is less pronounced for 4d or 5d transition metal complexes, and thus the choice of functional may also be somewhat less critical (on the other hand, relativistic effects will definitely have to be considered for heavy-atom systems, and we are presently developing approaches to do so).

The coupled cluster calculations we carried out for a subset of systems appear to be less influenced by such problems. Even in cases of significant spin contamination the results appeared to remain relatively stable. On the other hand, the computational effort involved presently makes such coupled-cluster approaches prohibitive for larger systems. Even for those di-, tri-, and tetraatomic complexes studied here, the large demand on the computational resources has not allowed us to truly saturate the basis sets with regard to higher angular momentum functions. There remains thus an urgent need for more economical approaches, and more accurate density functionals might offer the most practical route for improvement.

The present calculations also show conclusively that spin-polarization effects are nonnegligible for the metal dipolar couplings. This contrasts to the situation for main group compounds, where it is usually sufficient to take account of the direct SOMO spin densities to obtain good results for dipolar couplings.<sup>13</sup> The importance of spin polarization for transition metal dipolar hyperfine couplings arises from the presence of strongly polarizable semicore p-type orbitals (mainly the 3p orbitals for first-row transition metals), which have a very similar radial extent as the valence d-type SOMO orbitals. The importance of spin polarization for dipolar coupling constants

of the metal had already been noted by Belanzoni et al., in their careful study of  $\text{TiF}_3$ .<sup>17</sup> In view of the importance of spin polarization, the widely used simplified models that derive the d or s character of the SOMO directly from the dipolar coupling constants should be viewed with caution in transition metal systems. More detailed analyses of spin-polarization mechanisms for transition metal hyperfine coupling constants will be given elsewhere.<sup>25</sup>

**Acknowledgment.** This work has been supported by Deutsche Forschungsgemeinschaft and by Fonds der Chemischen Industrie. Part of this work benefitted also from the graduate college "Moderne Methoden der magnetischen Resonanz" at Universität Stuttgart. We are grateful to Vladimir G. Malkin, Olga L. Malkina (Bratislava), Pavel Kubáček (Brno), and Dominik Munzar (Stuttgart) for helpful discussions. Jürgen Gauss (Mainz) kindly provided assistance with the ACES-II code. We also thank Evert-Jan Baerends (Amsterdam) for a preprint of ref 18 and Ernest R. Davidson for informing us about an error in ref 21 (cf. section 7).

## References and Notes

- (1) Abragam, A.; Bleaney, B. *Electron Paramagnetic Resonance of Transition Ions*; Clarendon Press: Oxford, 1970.
- (2) Symons, M. C. R. *Chemical and Biochemical Aspects of Electron-Spin Resonance Spectroscopy*; Van Nostrand: New York, 1978.
- (3) Atherton, N. M. *Principles of Electron Spin Resonance*; Prentice Hall: New York, 1993.
- (4) Weil, J. A.; Bolton, J. R.; Wertz, J. E. *Electron Paramagnetic Resonance: Elementary Theory and Practical Applications*; Wiley & Sons: New York, 1994.
- (5) Carrington, A.; McLachlan, A. D. *Introduction to Magnetic Resonance with Applications to Chemistry and Chemical Physics*; Harper & Row: London, 1969.
- (6) Weltner, W., Jr. *Magnetic Atoms and Molecules*; Van Nostrand: New York, 1983.
- (7) McGarvey, B. R. In *Transition Metal Chemistry: A Series of Advances*; Carlin, R. L., Ed.; Marcel Dekker: New York, 1966; Vol 3., pp 89–201.
- (8) Mabbs, F. E.; Collison, D. *Electron Paramagnetic Resonance of d Transition Metal Compounds*; Elsevier: Amsterdam, 1992.
- (9) Mattar, S. M.; Hamilton, W. D.; Kingston, C. T. *Chem. Phys. Lett.* **1997**, *271*, 125.
- (10) Mattar, S. M.; Kennedy, C. *Chem. Phys. Lett.* **1995**, *238*, 230.
- (11) Mattar, S. M.; Doleman, B. J. *Chem. Phys. Lett.* **1993**, *216*, 369.
- (12) Knight, L. B.; Babb, R.; Ray, M.; Banisaukas, T. J. III; Russon, L.; Dailey, R. S.; Davidson, E. R. *J. Chem. Phys.* **1996**, *105*, 10241.
- (13) Engels, B.; Eriksson, L.; Lunell, S. *Adv. Quantum Chem.* **1996**, *27*, 297.
- (14) Barone, V.; Fournier, R.; Mele, F.; Russo, N.; Adamo, C. *Chem. Phys. Lett.* **1995**, *237*, 189.
- (15) Barone, V. In *Recent Advances in Density Functional Theory*; Chong, D. P., Ed.; World Scientific: Singapore, 1995; Part 1, p 287.
- (16) Aarnts, M. P.; Wilms, M. P.; Peelen, K.; Fraanje, J.; Goubitz, K.; Hartl, F.; Stufkens, D. J.; Baerends, E. J.; Vlcek, A., Jr. *Inorg. Chem.* **1996**, *35*, 5468.
- (17) Belanzoni, P.; Baerends, E. J.; van Asselt, S.; Langewen, P. B. *J. Phys. Chem.* **1995**, *99*, 13094.
- (18) Belanzoni, P.; Baerends, E. J.; Gribnau, M. *J. Phys. Chem. A* **1999**, *103*, 3732.
- (19) van Lenthe, E.; van der Avoird, A.; Wormer, P. E. S. *J. Chem. Phys.* **1998**, *108*, 4783.
- (20) Swann, J.; Westmoreland, T. D. *Inorg. Chem.* **1997**, *36*, 5348.
- (21) Knight, L. B.; Kaup, J. G.; Petzoldt, B.; Ayyad, R.; Ghanty, T. K.; Davidson, E. R. *J. Chem. Phys.* **1999**, *110*, 5658.
- (22) Geurts, P. J. M.; Bouten, P. C. P.; van der Avoird, A. *J. Chem. Phys.* **1980**, *73*, 1306.
- (23) Case, D. A.; Karplus, M. *J. Am. Chem. Soc.* **1977**, *99*, 6182.
- (24) Weber, J.; Goursot, A.; Pénigault, E.; Ammeter, J. H.; Bachmann, J. *J. Am. Chem. Soc.* **1982**, *104*, 1491.
- (25) Munzarová, M.; Kaupp, M., in preparation.
- (26) Harriman, J. E. *Theoretical Foundations of Electron Spin Resonance*, Academic Press: New York, 1978.
- (27) Childs, W. J. *Phys. Reports* **1992**, *211*, 114.
- (28) Childs, J.; Steimle, T. C. *J. Phys. Chem.* **1988**, *88*, 6168.
- (29) Fletcher, D. A.; Surlock, C. T.; Jung, K. Y.; Steimle, T. C. *J. Chem. Phys.* **1993**, *99*, 4288.
- (30) Carrington, A. *Microwave Spectroscopy of Free Radicals*; Academic Press: New York, 1974.
- (31) Malkin, V. G.; Malkina, O. L.; Eriksson, L. A.; Salahub, D. R. In *Modern Density Functional Theory: A Tool for Chemistry, Vol. 2 of Theoretical and Computational Chemistry*; Politzer, P., Seminario, J. M., Eds.; Elsevier: Amsterdam, The Netherlands, 1995; pp 273–347.
- (32) Kasai, P. H. *J. Chem. Phys.* **1968**, *49*, 4979.
- (33) Cheung, A. S.-C.; Hansen, R. C.; Merer, A. J. *J. Mol. Spectrosc.* **1982**, *91*, 165.
- (34) Weltner, W., Jr.; McLeod, D., Jr.; Kasai, P. *J. Chem. Phys.* **1967**, *46*, 3172.
- (35) Baumann, C. A.; Van Zee, R. J.; Weltner, W., Jr. *J. Phys. Chem.* **1982**, *86*, 5084.
- (36) Namiki, K.; Saito, S. *J. Chem. Phys.* **1997**, *107*, 8848.
- (37) Varberg, D.; Field, R. W.; Merer, A. J. *J. Chem. Phys.* **1991**, *95*, 1563.
- (38) Morton, J. R.; Preston, K. F. *J. Chem. Phys.* **1984**, *81*, 5775.
- (39) Frisch, M. J.; Trucks, G. W.; Schlegel, H. B.; Gill, P. M. W.; Johnson, B. G.; Robb, M. A.; Cheeseman, J. R.; Keith, T.; Petersson, G. A.; Montgomery, J. A.; Raghavachari, K.; Al-Laham, M. A.; Zakrzewski, V. G.; Ortiz, J. V.; Foresman, J. B.; Peng, C. Y.; Ayala, P. Y.; Chen, W.; Wong, M. W.; Andres, J. L.; Replogle, E. S.; Gomperts, R.; Martin, R. L.; Fox, D. J.; Binkley, J. S.; Defrees, D. J.; Baker, J.; Stewart, J. P.; Head-Gordon, M.; Gonzalez, C.; Pople, J. A. *Gaussian 94* (revision E.2); Gaussian, Inc.: Pittsburgh, PA, 1995.
- (40) Dolg, M.; Wedig, U.; Stoll, H.; Preuss, H. *J. Chem. Phys.* **1987**, *86*, 866.
- (41) (a) Bergner, A.; Dolg, M.; Küchle, W.; Stoll, H.; Preuss, H. *Mol. Phys.* **1993**, *80*, 1431. (b) d-Type polarization functions have been taken from: *Gaussian Basis Sets for Molecular Calculations*; Huzinaga, S., Ed.; Elsevier: New York, 1984.
- (42) Dunning, T. H.; Hay, H. In *Methods of Electronic Structure Theory, Vol. 3 of Modern Theoretical Chemistry*; Schaefer, H. F., III, Ed.; Plenum Press: New York, 1977.
- (43) Ehlers, A. W.; Böhme, M.; Dapprich, S.; Gobbi, A.; Höllwarth, A.; Jonas, V.; Köhler, K. F.; Stegmann, R.; Veldkamp, A.; Frenking, G. *Chem. Phys. Lett.* **1993**, *208*, 111.
- (44) DeVore, C.; Weltner, W., Jr. *J. Am. Chem. Soc.* **1977**, *99*, 4700.
- (45) Ferrante, F.; Wilkerson, J. L.; Graham, W. R. M.; Weltner, W., Jr. *J. Chem. Phys.* **1977**, *67*, 5904.
- (46) Kasai, P. H.; Jones, P. M. *J. Am. Chem. Soc.* **1985**, *107*, 818.
- (47) Chenier, J. H. B.; Hampson, C. A.; Howard, J. A.; Mile, B. *J. Phys. Chem.* **1989**, *93*, 114.
- (48) Hastie, J. W.; Hauge, R. H.; Margrave, L. *J. Chem. Phys.* **1969**, *51*, 2648.
- (49) Huber, H.; Kündig, E. P.; Moskovits, M.; Ozin, G. A. *J. Am. Chem. Soc.* **1975**, *97*, 2097.
- (50) Fairhurst, S. A.; Morton, J. R.; Preston, K. F. *J. Magn. Res.* **1983**, *55*, 453.
- (51) Morton, J. R.; Preston, K. F. *J. Chem. Phys.* **1984**, *81*, 5775.
- (52) Fairhurst, S. A.; Morton, J. R.; Preston, K. F. *Chem. Phys. Lett.* **1984**, *104*, 112.
- (53) Buschmann, W. E.; Arif, A. M.; Miller, J. S. *Angew. Chem., Int. Ed. Engl.* **1998**, *110*, 813.
- (54) Symons, M. C. R. *Organometallics* **1982**, *1*, 834.
- (55) Lionel, T.; Morton, J. R.; Preston, K. F. *J. Chem. Phys.* **1982**, *76*, 234.
- (56) Rosa, A.; Ehlers, A. W.; Baerends, E. J.; Snijders, J. G.; te Velde, G. *J. Phys. Chem.* **1996**, *100*, 5690.
- (57) Ricca, A.; Bauschlicher, C. W., Jr. *J. Phys. Chem.* **1994**, *98*, 12899.
- (58) Bendix, J.; Meyer, K.; Weyhermüller, T.; Bill, E.; Metzler-Nolte, N.; Wieghart, K. *Inorg. Chem.* **1998**, *37*, 1767.
- (59) Pink, M.; Billig, R. *Z. Kristallogr.* **1996**, *211*, 203.
- (60) Becke, A. D. *Phys. Rev. A* **1988**, *38*, 3098.
- (61) Lee, C.; Yang, W.; Parr, G. R. *Phys. Rev. B* **1988**, *37*, 785. Miehlich, B.; Savin, A.; Stoll, H.; Preuss, H. *Chem. Phys. Lett.* **1989**, *157*, 200.
- (62) Perdew, J. P.; Wang, Y. *Phys. Rev. B* **1986**, *33*, 8822. Perdew, J. P.; Wang, Y. *Phys. Rev. B* **1986**, *34*, 7406.
- (63) Perdew, J. P. *Physica B* **1992**, *172*, 1. Perdew, J. P. In *Electronic Structure of Solids '91*; Ziesche, P., Eschring, H., Eds.; Akademie Verlag: Berlin, 1991. Perdew, J. P.; Wang, Y. *Phys. Rev. B* **1992**, *45*, 13244.
- (64) Becke, A. D. *J. Chem. Phys.* **1993**, *98*, 5648.
- (65) Becke, A. D. *J. Chem. Phys.* **1993**, *98*, 1372.
- (66) Gianturco, A.; de Larra-Castels, M. P.; *Chem. Phys.* **1996**, *208*, 25. Braid, B.; Hiberty, P. C.; Savin, A. *J. Phys. Chem. A* **1988**, *102*, 7872.
- (67) Holthausen, M. C.; Heinemann, C.; Cornehl, H. H.; Koch, W.; Schwarz H. *J. Chem. Phys.* **1995**, *102*, 4931.
- (68) Stanton, J. F.; Gauss, J.; Watts, J. D.; Lauderdale, W. J.; Bartlett, R. J.; ACES-II program; University of Florida: Gainesville, 1994. Prof. J. Gauss (Universität Mainz) provided a modified version. For the underlying relaxed-density matrix MBPT/CC approach, see, e.g., Salter, E. A.; Trucks,

- G. W.; Bartlett, R. J. *J. Chem. Phys.* **1989**, *90*, 1752. Perreira, S. A.; Watts, J. D.; Bartlett, R. J. *J. Chem. Phys.* **1994**, *100*, 1425.
- (69) Schäfer, A.; Horn, H.; Ahlrichs, R. *J. Chem. Phys.* **1992**, *97*, 2571.
- (70) Kutzelnigg, W.; Fleischer, U.; Schindler, M. In *NMR—Basic Principles and Progress*; Springer-Verlag: Heidelberg, 1990; Vol. 23, p 165.
- (71) Pou-Amerigo, R.; Merchan, M.; Nebot-Gil, I.; Widmark, P. O.; Roos, B. *Theor. Chim. Acta* **1995**, *92*, 149, based on the (20s, 12p, 9d) primitives of Partridge, H. *J. Chem. Phys.* **1989**, *90*, 1043.
- (72) Bauschlicher, C. W., Jr.; Langhoff, S. R.; Barnes, L. A. *J. Chem. Phys.* **1989**, *91*, 2399.
- (73) Cf. *Extensible Computational Chemistry Environment Basis Set Database, Version 1.0*; Molecular Science Computing Facility: Pacific Northwest Laboratory.
- (74) Pyykkö, P.; Pajanne, E.; Inokuti, M. *Int. J. Quantum Chem.* **1973**, *7*, 785.
- (75) Harriman, J. E. *Theoretical Foundations of Electron Spin Resonance*; Academic Press: New York, 1978.
- (76) Abragam, A.; Pryce, M. H. L. *Proc. R. Soc. London A* **1951**, *205*, 135.
- (77) Purvis, G. D., III; Sekino, H.; Bartlett, R. J. *Collect. Czech. Chem. Commun.* **1988**, *53*, 2203.
- (78) Laidig, W. D.; Purvis, G. D., III; Bartlett, R. J. *Int. J. Quantum Chem. Symp.* **1982**, *16*, 561.
- (79) Eriksson, L. A.; Malkina, O. L.; Malkin, V. G.; Salahub, D. R. *J. Chem. Phys.* **1994**, *100*, 5066. Eriksson, L. A.; Malkina, O. L.; Malkin, V. G.; Salahub, D. R. *Int. J. Quantum Chem.* **1994**, *52*, 879.
- (80) See also, e.g., Chipman, D. M. *J. Chem. Phys.* **1989**, *91*, 5455. Chipman, D. M. *Theor. Chim. Acta* **1989**, *76*, 73. Engels, B.; Peyerimhoff, S. D. *J. Phys. B: At. Mol. Opt. Phys.* **1988**, *21*, 3459. Engels, B.; Peyerimhoff, S. D. *Mol. Phys.* **1989**, *67*, 583.
- (81) We note that the metal 3s-shell provides a positive core-shell spin-polarization contribution to the metal HFCC, whereas the 2s-shell provides an even larger negative contribution. This is consistent with previous interpretations, see refs 1 and 3. Compare also: Freeman, A. J.; Watson, R. E. In *Magnetism*; Rado, G. T., Suhl, H., Eds.; Academic Press: New York, 1965; Volume IIA, p 167. Watson, R. E.; Freeman, A. J. In *Hyperfine Interactions*; Freeman, A. J., Fraenkel, R. D., Eds.; Academic Press: New York, 1967; p 53, as well as refs 23 and 24.
- (82) These  $\langle S^2 \rangle$  values pertain to the Kohn–Sham wave function, i.e., to the noninteracting reference system rather than to the real system. Such data are nevertheless expected to give a reasonable and useful representation

for the real system as well (see, e.g., Baker, J.; Scheiner, A.; Andzelm, J. *Chem. Phys. Lett.* **1993**, *216*, 380).

(83) Suter, H. U.; Pless, V.; Ernzerhof, M.; Engels, B. *Chem. Phys. Lett.* **1994**, *230*, 398.

(84) Note, however, that there may be significant differences even between different GGA functionals.<sup>13,15,31,83</sup>

(85) Note however, that for  $\pi$ -type radicals spin polarization is important.<sup>13–15,83</sup> Indeed, it appears that in many cases even B3LYP underestimates this spin polarization. See also, e.g., Carmichael, I. *J. Phys. Chem. A* **1997**, *101*, 4633.

(86) We note that a similar situation pertains presently for the application of DFT methods to the calculation of NMR chemical shifts for transition metal nuclei. For reviews see, e.g., Bühl, M.; Kaupp, M.; Malkin, V. G.; Malkina, O. L. *J. Comput. Chem.* **1999**, *20*, 91. Kaupp, M.; Malkina, O. L.; Malkin, V. G. In *Encyclopedia of Computational Chemistry*; Schleyer, P. v. R., Ed.; Wiley-Interscience: New York, 1998, pp 1857ff.

(87) Davidson, E. R., personal communication.

(88) [Co(CO)<sub>4</sub>] may be considered a typical case of a Jahn–Teller distortion within a nonrelativistic framework.<sup>88a</sup> Spin–orbit coupling is, however, expected to lift the degeneracy of the ground state.<sup>88b</sup> (a) See, e.g., Burdett, J. K. *J. Chem. Soc., Faraday Trans. 2* **1974**, *70*, 1599. (b) See, e.g., Hanlan, L. A., Huber, H.; Kündig, E. P.; McGarvey, B. R.; Ozin, G. A. *J. Am. Chem. Soc.* **1975**, *97*, 7054.

(89) Hippe, D.; Peyerimhoff, S. D. *Mol. Phys.* **1992**, *76*, 293.

(90) a) Salahub, D. R.; Fournier, R.; Mlynarski, P.; Papai, I.; St-Amant, A.; Ushio, J. In *Density Functional Methods in Chemistry*; Labanowski, J., Andzelm, J., Eds.; Springer: New York, 1991. (b) St-Amant, A.; Salahub, D. R. *Chem. Phys. Lett.* **1990**, *169*, 387.

(91) Langhoff, S. R.; Bauschlicher, C. W., Jr. *Chem. Phys. Lett.* **1986**, *124*, 241.

(92) Huber, K. P.; Herzberg, G. *Molecular Spectra and Molecular Structure. IV. Constants of Diatomic Molecules*; Van Nostrand: New York, 1979.

(93) Bauschlicher C. W., Jr.; Maitre, P. *Theor. Chim. Acta* **1995**, *90*, 189.

(94) In this study we have concentrated on GGA exchange functionals derived from Becke's 1986 *ansatz*. Some differences may already be expected when using other GGA approaches.<sup>31,79</sup>

(95) In principle, one might remove the spin contaminants by spin projection techniques. However, the justification for doing so is doubtful. For a lucid discussion, see e.g., Chipman, D. M. *Theor. Chim. Acta* **1992**, *82*, 93.

*The only justification for our concepts is that they serve to represent the complex of our experience; beyond this they have no legitimacy.*

*Albert Einstein (1879-1955)*

## **6 Density Functional Calculations of Electronic $g$ -Tensors for Transition Metal Complexes: A Validation Study**

### *Introduction*

The electronic  $g$ -tensor is a characteristic part of any EPR spectrum and can provide information on the identity, as well as electronic and molecular structure of the paramagnetic species present. The fundamental physical laws that determine the  $g$ -tensor are well understood. However, serious computational difficulties had largely prevented a rigorous first-principles prediction of this quantity. Thus, in contrast to the treatment of EPR hyperfine coupling constants that already do have an appreciable history of first principles theoretical treatments, quantitative calculations of electronic  $g$ -tensors by nonempirical quantum chemistry have become possible only very recently. The first accurate calculations at the HF and multireference configuration interaction (MRCI) levels of theory are due to Lushington et al.<sup>1,2</sup> Vahtras and coworkers<sup>3</sup> have employed HF and multiconfigurational self-consistent-field (MCSCF) linear response functions. Recently, two different DFT implementations of  $g$ -tensor calculations within the Amsterdam density-functional code have been reported by Schreckenbach and Ziegler<sup>4</sup> and by van Lenthe et al.<sup>5</sup>

The following paper reports an alternative DFT implementation of electronic  $g$ -tensors within the deMon code including all relevant perturbation operators. A main feature of the new approach is the use of two types of accurate yet efficient approximations to the full one- and two-electron molecular spin-orbit operators. The new method has been validated on a number of species, including a detailed analysis of different contributions to  $g$ -shifts. The author of this thesis contributed to the paper by performing validation calculations on a set of  $3d$ -transition metal complexes. The

corresponding results are summarized in Table 10, Figure 2, and the relevant discussion in Part 6 (“Further Validation Calculations“) of the paper. The two sections given below, *Results* and *Conclusions*, refer to the work done by the author of this thesis.

### *Results*

Table 10 in the following paper gives results obtained with the VWN functional, and, in addition to the accurate atomic mean-field treatment of the  $\Delta g_{\text{SO/OZ}(1e)}$  and  $\Delta g_{\text{SO/OZ}(2e)}$  terms, contains also results that neglect the  $\Delta g_{\text{SO/OZ}(2e)}$  terms altogether. Additional results obtained by the author that have not been included in the paper are presented in Table 5.1. The latter table contains information on the effect of the density functional (VWN/BP86) and inclusion of the “SOS-DFPT” correction on the  $g$ -tensor components.

In contrast to the good performance for main-group species (cf. Figure 1 of the paper), the results obtained for  $3d$  transition metal complexes are less satisfactory. The graphical comparison of the theoretical and experimental results in Figure 2 indicates that the proper inclusion of the two-electron SO terms deteriorates the agreement with experiment significantly. The two-electron terms reduce the overall  $g$ -shifts by  $\sim 40$ - $50\%$ , so that a linear fit with slope 0.59 is obtained when including both the one-electron and the two-electron terms in the calculation. This observation corresponds strikingly to observations obtained recently by Bühl et al.,<sup>6,7</sup> when testing GGA-DFT approaches in calculations of nuclear shieldings of  $3d$  transition metal nuclei. UDFT-GIAO calculations with GGA functionals gave slopes of  $\sim 0.6$  in comparison with experiment. This corresponds to a significant underestimate of the paramagnetic contributions to shielding. Bühl found that the slope could be improved to almost 1.0 by using hybrid functionals (B3LYP or B3PW91).<sup>7</sup> In view of the close similarity of nuclear shielding tensor and electronic  $g$ -tensor, we expect that the origin of the failure of the GGA functionals in both cases is related, and that the inclusion of Hartree-Fock exchange should improve the performance also for the  $g$ -tensor.



**Table 5.1** Comparison of Computed and Experimental  $\Delta g$ -Tensor Components (ppt) for a Series of 3d Transition Metal Complexes<sup>a</sup>

| complex                              | com<br>p.              | VWN,<br>UDFT,<br>with<br>$\Delta g_{SO/OZ(2e)}$ | VWN,<br>SOS -<br>DFPT <sup>b</sup> ,<br>with<br>$\Delta g_{SO/OZ(2e)}$ | VWN,<br>UDFT,<br>without<br>$\Delta g_{SO/OZ(2e)}$ | VWN,<br>SOS-<br>DFPT <sup>b</sup> ,<br>without<br>$\Delta g_{SO/OZ(2e)}$ | BP86,<br>UDFT,<br>without<br>$\Delta g_{SO/OZ(2e)}$ | BP86,<br>SOS-<br>DFPT <sup>b</sup> ,<br>without<br>$\Delta g_{SO/OZ(2e)}$ | Exp. <sup>c</sup>          |
|--------------------------------------|------------------------|---|--|--|--|---|---|----------------------------|
| TiF <sub>3</sub>                     | $\Delta g_{\perp}$     | -28.3   | -23.2  | -79.4  | -61.8  | -62.1   | -50.7   | -111.3<br>-121.5<br>-123.7 |
| Mn(CN) <sub>5</sub> NO <sup>2-</sup> | $\Delta g_{\parallel}$ | -1.9  | -1.4   | -1.2   | -0.3   | -5.2  | -4.2  | -10.1                      |
| TiF <sub>3</sub>                     | $\Delta g_{\parallel}$ | -1.2  | -1.2   | -1.8   | -1.8   | -1.8  | -1.9  | -11.1<br>-11.1<br>-3.7     |
| Mn(CO) <sub>5</sub>                  | $\Delta g_{\parallel}$ | -0.9  | -1.0   | -1.2   | -1.3   | -1.6  | -1.7  | -1.7<br>-2.3               |
| [Fe(CO) <sub>5</sub> ] <sup>+</sup>  | $\Delta g_{\parallel}$ | -0.9  | -0.9   | -0.6   | -0.6   | -1.0  | -1.0  | -1.5<br>-1.4               |
| ScO                                  | $\Delta g_{\perp}$     | 0.0   | 0.0  | -0.9   | -0.8   | -1.2  | -1.2  | -0.5(3)<br>-2.8(5)         |
| ScO                                  | $\Delta g_{\parallel}$ | -0.1  | -0.1   | -0.2   | 0.2  | 0.2   | 0.2   | -0.5(3)<br>-0.8(7)         |
| MnO <sub>3</sub>                     | $\Delta g_{\parallel}$ | 4.3   | 4.2  | 6.3  | 6.9  | 1.9   | 1.3   | 1.3                        |
| Ni(CO) <sub>3</sub> H                | $\Delta g_{\parallel}$ | 1.3   | 1.2  | 2.7  | 2.5  | 2.0   | 1.8   | 1.9                        |
| Co(CO) <sub>4</sub>                  | $\Delta g_{\parallel}$ | 3.3   | 3.1  | 7.1  | 6.8  | 8.1   | 7.4   | 3.6<br>5.0                 |
| MnO <sub>3</sub>                     | $\Delta g_{\perp}$     | 1.9   | 2.4  | 4.2  | 5.8  | 9.4   | 9.2   | 6.1                        |
| Mn(CN) <sub>5</sub> NO <sup>2-</sup> | $\Delta g_{\perp}$     | 17.9  | 15.4   | 36.3   | 31.5   | 27.8  | 24.7  | 28.8                       |
| Mn(CO) <sub>5</sub>                  | $\Delta g_{\perp}$     | 22.6  | 20.4   | 42.6   | 38.4   | 38.0  | 34.8  | 40.7<br>35.7               |
| Cu(acac) <sub>2</sub>                | $\Delta g_{xx}$        | 30.6  | 28.4   | 50.1   | 45.2   | 50.1  | 46.5  | 48.7<br>49.6               |
| Cu(NO <sub>3</sub> ) <sub>2</sub>    | $\Delta g_{xx}$        | 28.2  | 26.3   | 45.1   | 42.2   | 47.3  | 44.2  | 49.9(5)                    |
| Cu(NO <sub>3</sub> ) <sub>2</sub>    | $\Delta g_{yy}$        | 31.0  | 28.9   | 49.3   | 46.0   | 50.8  | 47.4  | 49.9(5)                    |
| Cu(acac) <sub>2</sub>                | $\Delta g_{yy}$        | 34.7  | 31.5   | 55.4   | 49.9   | 55.4  | 50.4  | 48.7<br>52.8               |
| Ni(CO) <sub>3</sub> H                | $\Delta g_{\perp}$     | 39.8  | 36.5   | 65.0   | 59.7   | 67.1  | 61.6  | 65.1                       |
| [Fe(CO) <sub>5</sub> ] <sup>+</sup>  | $\Delta g_{\perp}$     | 48.7  | 43.0   | 89.3   | 78.8   | 77.9  | 70.2  | 81.0, 77.4<br>78.8, 76.6   |
| Co(CO) <sub>4</sub>                  | $\Delta g_{\perp}$     | 79.3  | 68.3   | 137.5  | 118.7  | 120.7   | 106.5   | 127.6<br>126.0             |
| Cu(NO <sub>3</sub> ) <sub>2</sub>    | $\Delta g_{zz}$        | 116.3   | 105.1  | 183.0  | 165.5  | 183.6   | 166.2   | 246.6(3)                   |
| Cu(acac) <sub>2</sub>                | $\Delta g_{zz}$        | 115.5   | 105.8  | 180.2  | 165.5  | 180.2   | 165.8   | 285.2<br>263.8             |

<sup>a</sup>UDFT-IGLO / SOS-DFPT-IGLO with AMFI approximation for  $\Delta g_{SO/OZ(2e)}$ , 9s7p4d metal basis, BIII basis on ligands, BII on remote atoms in Cu(acac)<sub>2</sub>. <sup>b</sup>Including the correction term in the Loc.1 approximation. <sup>c</sup>For references to the literature, see last column of Table 10 of the paper.

### *Conclusions and outlook*

In contrast to the good performance of our DFT approach for main-group species, the present results for a rather diverse set of 3d transition metal complexes indicate that the paramagnetic contributions are underestimated significantly. We expect that the use of exchange-correlation functionals that include some exact exchange will enable more accurate calculations. The present version of our code does not allow the inclusion of the Hartree-Fock exchange. However, hybrid functionals have recently been implemented in a new code of our group. Initial test calculations indicate improved performance for the calculation of  $g$ -tensors of the same series of 3d transition metal complexes.<sup>8</sup>

## References

---

- <sup>1</sup> Lushington, G. H.; Grein, F. *Theor. Chimica Acta* **1996**, *93*, 259. Bruna, P.; Lushington, G. H.; Grein, F. *Chem. Phys.* **1997**, *225*, 1.
- <sup>2</sup> Lushington, G. H. Ph.D. Thesis, The University of New Brunswick, Canada, 1996.
- <sup>3</sup> (a) Engström, M.; Minaev, B.; Vahtras, O.; Ågren, H. *Chem. Phys.* **1998**, *237*, 149. (b) Vahtras, O.; Minaev, B.; Ågren, H. *Chem. Phys. Lett.* **1997**, *281*, 186.
- <sup>4</sup> Schreckenbach, G; Ziegler, T. *J. Phys. Chem. A* **1997**, *101*, 3388.
- <sup>5</sup> van Lenthe, E.; Baerends, E. J.; Snijders, J. G. *J. Chem. Phys.* **1997**, *107*, 2488.
- <sup>6</sup> Bühl, M.; Malkina, O. L.; Malkin, V. G. *Helv. Chim. Acta* **1996**, *79*, 742.
- <sup>7</sup> Bühl, M.; *Chem. Phys. Lett.* **1997**, *267*, 251.
- <sup>8</sup> Reviakine, R.; Malkin, V. G.; Malkina, O. L.; Arbouznikov, A.; Kaupp, M. *unpublished results*.

# Density Functional Calculations of Electronic $g$ -Tensors Using Spin–Orbit Pseudopotentials and Mean-Field All-Electron Spin–Orbit Operators

Olga L. Malkina,<sup>†,‡</sup> Juha Vaara,<sup>§</sup> Bernd Schimmelpfennig,<sup>||</sup> Markéta Munzarová,<sup>⊥</sup> Vladimir G. Malkin,<sup>\*,‡</sup> and Martin Kaupp<sup>\*,#</sup>

Contribution from the Computing Center and Institute of Inorganic Chemistry, Slovak Academy of Sciences, Dubravska Cesta 9, SK-84236 Bratislava, Slovakia, Max-Planck-Institut für Festkörperforschung, Heisenbergstrasse 1, D-70569 Stuttgart, Germany, Institut für Anorganische Chemie, Universität Würzburg, Am Hubland, D-97074 Würzburg, Germany

Received March 20, 2000. Revised Manuscript Received June 29, 2000

**Abstract:** Modern density-functional methods for the calculation of electronic  $g$ -tensors have been implemented within the framework of the deMon code. All relevant perturbation operators are included. Particular emphasis has been placed on accurate yet efficient treatment of the two-electron spin–orbit terms. At an all-electron level, the computationally inexpensive atomic mean-field approximation is shown to provide spin–orbit contributions in excellent agreement with the results obtained using explicit one- and two-electron spin–orbit integrals. Spin–other–orbit contributions account for up to 25–30% of the two-electron terms and may thus be non-negligible. For systems containing heavy atoms we use a pseudopotential treatment, where quasirelativistic pseudopotentials are included in the Kohn–Sham calculation whereas appropriate spin–orbit pseudopotentials are used in the perturbational treatment of the  $g$ -tensors. This approach is shown to provide results in good agreement with the all-electron treatment, at moderate computational cost. Due to the atomic nature of both mean-field all-electron and pseudopotential spin–orbit operators used, the two approaches may even be combined in one calculation. The atomic character of the spin–orbit operators may also be used to analyze the contributions of certain atoms to the paramagnetic terms of the  $g$ -tensors. The new methods have been applied to a wide variety of species, including small main group systems, aromatic radicals, as well as transition metal complexes.

## 1. Introduction

Electron paramagnetic resonance (EPR) spectroscopy is one of the most important experimental techniques of studying compounds containing unpaired electrons. Typical applications encompass biological systems, paramagnetic defects in extended solids, transition metal complexes, or simple organic radicals (e.g., in zeolites). The recent development of high-field EPR spectroscopy (at frequencies of 95 GHz or higher) has significantly widened the scope of the method and of the information that may be extracted. In particular, in modern solid-state EPR experiments the components of the electronic  $g$ -tensor may frequently be resolved.<sup>1</sup> Interpretation of these experiments by quantum chemical calculations has thus become highly desirable. However, in contrast to the treatment of EPR hyperfine coupling constants that already do have an appreciable history of first

principles theoretical treatments,<sup>2</sup> quantitative calculations of electronic  $g$ -tensors by the machinery of nonempirical quantum chemistry have become possible only very recently (for semiempirical calculations, cf. refs 3 and 4; see also ref 5).

The first accurate calculations at the Hartree–Fock (HF) and multireference configuration interaction (MRCI) levels of theory are due to Lushington et al.<sup>6,7</sup> Vahtras and co-workers<sup>8</sup> have employed HF and multiconfiguration self-consistent-field (MCSCF) linear response functions. These ab initio implemen-

(1) See, for example: (a) Möbius, K. In *Biological Magnetic Resonance*; Berliner, L. J., Reuben, J., Eds.; Plenum Press: New York, 1993; Vol. 13, pp 253–274. (b) Prisner, T. F. In *Advances in Magnetic and Optical Resonance*; Warren, W., Ed.; Academic Press: New York, 1997; Vol. 20, pp 245–299.

(2) Engels, B.; Eriksson, L. A.; Lunell, S. *Adv. Quantum Chem.* **1996**, 27, 297.

(3) See, for example: Angstl, R. *Chem. Phys.* **1989**, 132, 435. Plakhutin, B. N.; Zhidomirov, G. M.; Zamaraev, K. I. *J. Struct. Chem.* **1983**, 24, 3.

(4) See, for example: Un, S.; Atta, M.; Fontcave, M.; Rutherford, A. W. *J. Am. Chem. Soc.* **1995**, 117, 10713.

(5) For DFT calculations of  $g$ -tensors with semiempirical SO operators cf., for example: Geurts, P. J. M.; Bouten, P. C. P.; van der Avoird, A. J. *Chem. Phys.* **1980**, 73, 1306. Belanzoni, P.; Baerends, E. J.; van Asselt, S.; Langewen, P. B. *J. Phys. Chem.* **1995**, 99, 13094. Swann, J.; Westmoreland, T. D. *Inorg. Chem.* **1997**, 36, 5348.

(6) Lushington, G. H.; Grein, F. *Theor. Chim. Acta* **1996**, 93, 259. Bruna, P.; Lushington, G. H.; Grein, F. *Chem. Phys.* **1997**, 225, 1.

(7) Lushington, G. H. Ph.D. Thesis, The University of New Brunswick, Canada, 1996.

(8) Engström, M.; Minaev, B.; Vahtras, O.; Ågren, H. *Chem. Phys.* **1998**, 237, 149. Vahtras, O.; Minaev, B.; Ågren, H. *Chem. Phys. Lett.* **1997**, 281, 186.

<sup>†</sup> Computing Center, Slovak Academy of Sciences.

<sup>‡</sup> Institute of Inorganic Chemistry, Slovak Academy of Sciences, E-mail: malkin@savba.sk.

<sup>§</sup> Max-Planck-Institut für Festkörperforschung. Present address: Department of Chemistry, P.O. Box 55 (A.I. Virtasen aukio 1), FIN-00014 University of Helsinki, Finland.

<sup>||</sup> Max-Planck-Institut für Festkörperforschung. Present address: Theoretical Chemistry, Teknikringen 30, Royal Institute of Technology, S-10044 Stockholm, Sweden.

<sup>⊥</sup> Max-Planck-Institut für Festkörperforschung. Present address: Department of Theoretical and Physical Chemistry, Faculty of Science, Masaryk University, Kotlářská 2, CZ-61137 Brno, Czech Republic.

<sup>#</sup> Institut für Anorganische Chemie, Universität Würzburg. Telephone: +49–931-888-5281. Fax: +49–931-888-7135. E-mail: kaupp@mail.uni-wuerzburg.de.

tations include essentially all perturbation operators—at the Breit–Pauli level of treating spin–orbit coupling—which are thought to be relevant for the electronic  $g$ -tensor. Thus, at least for systems containing only light elements, it is in principle possible to converge to the experimental results, by using larger and larger basis sets and by improving the treatment of electron correlation. However, obviously such calculations are at present largely restricted to relatively small systems, as the accurate inclusion of electron correlation becomes very demanding with increasing size of the system.

In case of the NMR nuclear shielding tensor, which is conceptually related to the electronic  $g$ -tensor, it has recently been shown that density-functional theory (DFT) provides a valuable alternative to post-HF treatment, by approximately including electron correlation at lower computational cost.<sup>9–11</sup> Indeed, a recent state-of-the-art DFT implementation of  $g$ -tensor calculations, reported by Schreckenbach and Ziegler (SZ),<sup>12</sup> was based on their previous NMR chemical shift implementation (using gauge-including atomic orbitals, GIAOs) in the Amsterdam density-functional (ADF) program. A different DFT-GIAO implementation (but also in the ADF code), using the two-component zero-order regular approximation (ZORA<sup>13</sup>) to account for spin–orbit (SO) coupling and scalar relativity, has been reported by van Lenthe et al.<sup>14</sup> A two-component UHF approach has been implemented by Jayatilaka.<sup>15</sup>

Here we report an alternative DFT implementation of electronic  $g$ -tensors within the deMon<sup>16,17</sup> code. Our method differs from SZ mainly in the way we deal with spin–orbit coupling. SZ used an effective Kohn–Sham potential to model approximately the two-electron SO terms.<sup>12</sup> This treatment does not include the spin–other–orbit terms, and it also involves a number of other approximations. We have recently shown for calculations of SO corrections to NMR chemical shifts that (1) a mean-field one-center approximation to the full two-electron SO integrals gives results in excellent agreement with an exact treatment, at a small fraction of the computational effort;<sup>18</sup> (2) spin–orbit pseudopotentials (spin–orbit effective-core potentials, SO-ECPs) do also provide a good approximation to the full SO operator, in a valence-only treatment, and they allow easily the simultaneous treatment of SO and scalar relativistic effects.<sup>19</sup> Our new  $g$ -tensor code is based on these efficient and accurate “atomic” treatments of SO coupling. This leads to a number of advantages in the calculations, as well as in the subsequent interpretation of the results, as we will demonstrate.

(9) Kaupp, M.; Malkina, O. L.; Malkin, V. G. In *Encyclopedia of Computational Chemistry*; Schleyer, P. v. R., Ed.; Wiley-Interscience: New York, 1998.

(10) Bühl, M.; Kaupp, M.; Malkin, V. G.; Malkina, O. L. *J. Comput. Chem.* **1999**, *20*, 91.

(11) Schreckenbach, G.; Ziegler, T. *Theor. Chem. Acc.* **1998**, *2*, 71.

(12) Schreckenbach, G.; Ziegler, T. *J. Phys. Chem. A* **1997**, *101*, 3388.

(13) van Lenthe, E.; Baerends, E. J.; Snijders, J. G. *J. Chem. Phys.* **1993**, *99*, 4597.

(14) van Lenthe, E.; Wormer, P. E. S.; van der Avoird, A. *J. Chem. Phys.* **1997**, *107*, 2488.

(15) Jayatilaka, D. *J. Chem. Phys.* **1998**, *108*, 7587.

(16) (a) Salahub, D. R.; Fournier, R.; Mlynarski, P.; Papai, I.; St-Amant, A.; Ushio, J. In *Density Functional Methods in Chemistry*; Labanowski, J., Andzelm, J., Eds.; Springer: New York, 1991. (b) St-Amant, A.; Salahub, D. R. *Chem. Phys. Lett.* **1990**, *169*, 387.

(17) Malkin, V. G.; Malkina, O. L.; Eriksson, L. A.; Salahub, D. R. In *Modern Density Functional Theory: A Tool for Chemistry*; Seminario, J. M., Politzer, P., Eds.; Elsevier: Amsterdam, 1995; Vol. 2.

(18) Malkina, O. L.; Schimmelpfennig, B.; Kaupp, M.; Hess, B. A.; Chandra, P.; Wahlgren, U.; Malkin, V. G. *Chem. Phys. Lett.* **1998**, *296*, 93.

(19) Vaara, J.; Malkina, O. L.; Stoll, H.; Malkin, V. G.; Kaupp, M. Submitted.

## 2. Methods

We define the  $g$ -tensor as

$$\mathbf{g} = g_e \mathbf{1} + \Delta \mathbf{g} \quad (1)$$

and focus on  $g$ -shifts ( $\Delta \mathbf{g}$  components) relative to the free electron  $g$ -value. Throughout this work,  $g$ -shifts are given in ppm for main group radicals and in ppt (parts-per-thousand) for most transition metal systems (more significant digits are typically not available from experiment anyway).

The second-order theory for calculating  $\Delta \mathbf{g}$  within a one-component approach has been presented in several recent reports of modern quantum chemical implementations.<sup>6–8,12,20</sup> Hence, we limit ourselves to recapitulating only the relevant points and give the final expressions used in our present DFT calculations. Here we investigate radicals with doublet electronic ground states only. We look for terms bilinear in the magnetic field  $\mathbf{B}_0$  and effective electronic spin  $\mathbf{s}$  in the molecular energy expression  $E$ ; hence, the Cartesian  $uv$ -component of  $\Delta \mathbf{g}$  is

$$\Delta g_{uv} = \frac{1}{\mu_B} \left. \frac{\partial^2 E}{\partial B_{0,u} \partial s_v} \right|_{\mathbf{B}=\mathbf{s}=0} \quad (2)$$

We shall employ atomic units based on the SI system, where the Bohr magneton  $\mu_B = 1/2$ .

The main contributions to the  $\Delta \mathbf{g}$  tensor up to  $\mathcal{O}(\alpha^2)$  ( $\alpha$  is the fine-structure constant) arise from the SO coupling Hamiltonian

$$H_{\text{SO}} = \frac{\alpha^2}{4} g_e \left[ \sum_M Z_M \sum_i \frac{\mathbf{s}_i \cdot \mathbf{l}_{iM}}{r_{iM}^3} - \sum_{ij} \frac{(\mathbf{s}_i + 2\mathbf{s}_j) \cdot \mathbf{l}_{ij}}{r_{ij}^3} \right] \quad (3)$$

where  $Z_M e$  is the charge of nucleus  $M$ ,  $\mathbf{s}_i$  the spin of electron  $i$ ,  $\mathbf{l}_{iM} = (\mathbf{r}_i - \mathbf{R}_M) \times [-i\nabla_i + \mathbf{A}_0(\mathbf{r}_i)]$  the angular momentum of electron  $i$  with respect to the position of nucleus  $M(\mathbf{R}_M)$ , and  $\mathbf{l}_{ij} = (\mathbf{r}_i - \mathbf{r}_j) \times [-i\nabla_i + \mathbf{A}_0(\mathbf{r}_i)]$  the corresponding angular momentum with respect to the position of electron  $j(\mathbf{r}_j)$ . Here,  $\mathbf{A}_0(\mathbf{r}_i) = 1/2 \mathbf{B}_0 \times (\mathbf{r}_i - \mathbf{O})$  is the vector potential at  $\mathbf{r}_i$  corresponding to the external magnetic field. We note that at the present level of accuracy of both the theory and experiment, it is not necessary to distinguish between  $g_e$  and the  $g$ -factor associated with the SO interaction.<sup>20,21</sup> The field-independent part of  $H_{\text{SO}}$  (arising from the  $-i\nabla_i$  terms in eq 3) couples, in double perturbation theory, with the orbital Zeeman (OZ) interaction

$$H_{\text{OZ}} = \frac{1}{2} \sum_i \mathbf{l}_{iO} \cdot \mathbf{B}_0 \quad (4)$$

to the sum-over-states density-functional perturbation theory (SOS-DFPT)<sup>22</sup> expression for the paramagnetic part of  $\Delta \mathbf{g}$

$$\Delta g_{\text{SO/OZ},uv} = \frac{\alpha^2}{2} g_e \left[ \sum_k^{\text{occ}(\alpha)} \sum_a^{\text{virt}(\alpha)} \frac{\langle \psi_k^\alpha | H_{\text{SO},v} | \psi_a^\alpha \rangle \langle \psi_a^\alpha | l_{O,u} | \psi_k^\alpha \rangle}{\epsilon_k^\alpha - \epsilon_a^\alpha - \Delta E_{k \rightarrow a}^{\text{xc}}} - \sum_k^{\text{occ}(\beta)} \sum_a^{\text{virt}(\beta)} \frac{\langle \psi_k^\beta | H_{\text{SO},v} | \psi_a^\beta \rangle \langle \psi_a^\beta | l_{O,u} | \psi_k^\beta \rangle}{\epsilon_k^\beta - \epsilon_a^\beta - \Delta E_{k \rightarrow a}^{\text{xc}}} \right] \quad (5)$$

Here,  $\psi_k^{\alpha\beta}$  and  $\psi_a^{\alpha\beta}$  are unperturbed occupied and virtual  $\alpha/\beta$  MOs, respectively.  $\epsilon_k$  and  $\epsilon_a$  are the corresponding Kohn–Sham eigenvalues, and  $\Delta E_{k \rightarrow a}^{\text{xc}}$  is the “SOS-DFPT correction” (Loc.1 in the present paper) imposed on the energy denominators.<sup>17,22</sup> We refer to the original papers for details. Leaving the  $\Delta E_{k \rightarrow a}^{\text{xc}}$  term out corresponds to the uncoupled DFT (UDFT) approximation.  $H_{\text{SO},v}$  denotes the  $v$ -component of the spatial part of the field-free SO Hamiltonian (the prefactors  $\alpha^2 g_e/4$  of  $H_{\text{SO}}$  of eq 3 have been absorbed in the prefactor of eq 5). While the

(20) Schreckenbach, G. Ph.D. Thesis, The University of Calgary, Canada, 1996.

(21) Harriman, J. E. *Theoretical Foundations of Electron Spin Resonance*; Academic Press: New York, 1978.

(22) Malkin, V. G.; Malkina, O. L.; Casida, M. E.; Salahub, D. R. *J. Am. Chem. Soc.* **1994**, *116*, 5898.

present formulae are written in terms of a common gauge origin, the choice of individual-gauges-for-localized-orbitals (IGLO<sup>43</sup>) can be trivially read from the nuclear shielding formulae of ref 22.

As mentioned above, an accurate treatment of spin-orbit coupling is particularly critical for quantitative *g*-tensor calculations.<sup>23</sup> We base our implementation on our latest version of the deMon-NMR module for calculating the SO contribution to the nuclear shielding tensor<sup>19</sup> and use three different types of SO integrals in the present calculation: (1) from the full microscopic one- and two-electron SO Hamiltonian of eq 3 using the EAGLE code,<sup>24</sup> (2) from the effective one-electron one-center mean-field approximation for both one- and two-electron SO integrals<sup>25</sup> as implemented in the AMFI software,<sup>26</sup> and (3) from spin-orbit pseudopotentials of the Pitzer-Winter form.<sup>27</sup> The second alternative is a very accurate approximation of the first (as shown below), and allows calculations of much larger molecular systems due to eliminating the need to compute and store a large number of two-electron integrals. Since **g** is largely a valence property, SO-ECPs can be used to reduce the computational effort further by removing the core electrons and to take into account scalar relativistic effects when used in connection with Kohn-Sham valence pseudo-orbitals optimized in the presence of corresponding quasirelativistic ECPs. Furthermore, the implementation allows mixed usage of AMFI and SO-ECP integrals on different atomic centers of the molecule. Hence, it is possible to perform an atomic break-down of the calculated  $\Delta g_{\text{SO/OZ}}$  contributions.

To obtain a consistent account for all the important terms up to  $\mathcal{O}(\alpha^2)$ , one has to additionally consider the bilinear terms of the Breit-Pauli Hamiltonian<sup>21</sup>

$$H_{\text{RMC}} = -\frac{1}{4}\alpha^2 g_e \sum_i p_i^2 \mathbf{s}_i \cdot \mathbf{B}_0 \quad (6)$$

the so-called kinetic energy correction to the spin-Zeeman interaction (taken up to  $\mathcal{O}(B_0)$ , with  $p = -i\nabla$ ), and the part of the SO Hamiltonian arising from the magnetic field dependence of the SO Hamiltonian (the  $\mathbf{A}_0$ -dependent terms in eq 3). After taking the appropriate expectation values, the former leads to a diagonal (isotropic) contribution

$$\Delta g_{\text{RMC},\mu\nu} = -\frac{1}{2}\alpha^2 g_e \delta_{\mu\nu} \sum_{\mu\nu} P_{\mu\nu}^{\alpha-\beta} \langle \nu | p^2 | \mu \rangle \quad (7)$$

where

$$P_{\mu\nu}^{\alpha-\beta} = \sum_k^{\text{occ}(\alpha)} c_k^\mu c_k^{\nu*} - \sum_k^{\text{occ}(\beta)} c_k^\mu c_k^{\nu*} \quad (8)$$

is the spin density matrix in the atomic orbital ( $\mu, \nu$ ) basis and  $c$  are the MO coefficients. The latter term causes diamagnetic gauge correction contributions, whose one-electron term reads

$$\Delta g_{\text{GC}(1e),\mu\nu} = \frac{1}{4}\alpha^2 g_e \sum_{\mu\nu} P_{\mu\nu}^{\alpha-\beta} \left\langle \nu \left| \sum_M \frac{\delta_{\mu\nu}(\mathbf{r}_M \cdot \mathbf{r}_O) - r_{M,\mu} r_{O,\nu}}{r_M^3} Z_M \right| \mu \right\rangle \quad (9)$$

In the present calculations we neglect the corresponding and analogous

(23) A consistent and complete incorporation of spin-orbit coupling into a Kohn-Sham framework is far from trivial. Thus, for example, spin-orbit terms arise strictly only from relativistic contributions to the electron-electron interaction. Rather than resorting to relativistic exchange-correlation potentials, we have in this work preferred to incorporate spin-orbit coupling explicitly via suitably chosen and well-established perturbation operators (see text).

(24) EAGLE is a code for the calculation of integrals of the Breit-Pauli SO Hamiltonian over molecular Cartesian Gaussian functions, written by P. Chandra and B. A. Hess.

(25) Hess, B. A.; Marian, C. M.; Wahlgren, U.; Gropen, O. *Chem. Phys. Lett.* **1996**, 251, 365.

(26) Schimmelpennig, B. *Atomic Spin-Orbit Mean-Field Integral Program*; Stockholms Universitet, Sweden, 1996.

(27) Pitzer, R. M.; Winter, N. W. *J. Phys. Chem.* **1988**, 92, 3061.

two-electron contribution  $\Delta g_{\text{GC}(2e)}$  due to its general smallness (see refs 7 and 12) and the lack of a computationally efficient approximation thereto.

### 3. Computational Details

**3.1. Structures.** For small main group radicals, we used for better comparison with the results of Schreckenbach and Ziegler (SZ) their DFT-optimized structures.<sup>12</sup> Similarly, we employed the DFT (VWN)-optimized structures of Patchkowski and Ziegler (PZ)<sup>28</sup> for a set of  $\text{MX}_4^{m-}$  transition metal complexes. Most of the structures of 3d complexes are those reported in a recent study of hyperfine couplings for these systems<sup>39</sup> (mostly DFT-optimized, in a few cases experimental). Additional 3d complexes are the three vanadyl complexes [*N,N'*-ethylenebis(*o*-*tert*-butyl-*p*-methylsalicylaldiminato)]oxovanadium(IV), bis(*N*-isopropyl-*o*-methylsalicylaldiminato)oxovanadium(IV), and bis(*N*-methyl-*o*-*tert*-butyl-salicylaldiminato)oxovanadium(IV), for which experimental structures<sup>29</sup> were used. Structures of  $\text{Cu}(\text{acac})_2$  and  $\text{Cu}(\text{NO}_3)_2$ , and of phenoxy radicals have been fully optimized with the Gaussian98 code,<sup>30</sup> at the gradient-corrected, unrestricted DFT level (BP86 functional<sup>31,32</sup>). Quasi-relativistic small-core pseudopotentials and (8s7p6d)/[6s5p3d] valence basis sets of the Stuttgart group were employed for the transition metals,<sup>33,34</sup> ECPs<sup>35</sup> with DZP valence basis sets<sup>35-37</sup> for main group atoms. A DZV basis<sup>38</sup> was used for hydrogen. The newly optimized structures are reported as Supporting Information.

**3.2. *g*-Tensor Calculations.** The Kohn-Sham calculations were performed in an unrestricted manner (UKS), using the deMon code,<sup>16</sup> with either local density (VWN<sup>40</sup>) or gradient-corrected (GGA) functionals. We mainly used BP86,<sup>31,32</sup> but PP86<sup>32,41</sup> and PW91<sup>42</sup> functionals were also tested. In most calculations, in particular in our comparison with the results of

(28) Patchkovskii, S.; Ziegler T. *J. Chem. Phys.* **1999**, 111, 5730.

(29) Cornman, C. R.; Geiser-Bush, K. M.; Rowley, S. P.; Boyle, P. D. *Inorg. Chem.* **1997**, 36, 6401.

(30) Frisch, M. J.; Trucks, G. W.; Schlegel, H. B.; Scuseria, G. E.; Robb, M. A.; Cheeseman, J. R.; Zakrzewski, V. G.; Montgomery, J. A. Jr.; Stratmann, R. E.; Burant, J. C.; Dapprich, S.; Millam, J. M.; Daniels, A. D.; Kudin, K. N.; Strain, M. C.; Farkas, O.; Tomasi, J.; Barone, V.; Cossi, M.; Cammi, R.; Mennucci, B.; Pomelli, C.; Adamo, C.; Clifford, S.; Ochterski, J.; Petersson, G. A.; Ayala, P. Y.; Cui, Q.; Morokuma, K.; Malick, D. K.; Rabuck, A. D.; Raghavachari, K.; Foresman, J. B.; Cioslowski, J.; Ortiz, J. V.; Baboul, A. G.; Stefanov, B. B.; Liu, G.; Liashenko, A.; Piskorz, P.; Komaromi, I.; Gomperts, R.; Martin, R. L.; Fox, D. J.; Keith, T.; Al-Laham, M. A.; Peng, C. Y.; Nanayakkara, A.; Gonzalez, C.; Challacombe, M.; Gill, P. M. W.; Johnson, B.; Chen, W.; Wong, M. W.; Andres, J. L.; Gonzalez, C.; Head-Gordon, M.; Replogle, E. S.; Pople, J. A. *Gaussian 98*, revision A.7; Gaussian, Inc.: Pittsburgh, PA, 1998.

(31) Becke, A. D. *Phys. Rev. A* **1988**, 38, 3098.

(32) Perdew, J. P. *Phys. Rev. B* **1986**, 33, 8822.

(33) Andrae, D.; Häußermann, U.; Dolg, M.; Stoll, H.; Preuss, H. *Theor. Chim. Acta* **1990**, 77, 123.

(34) Dolg, M.; Wedig, U.; Stoll, H.; Preuss, H. *J. Chem. Phys.* **1987**, 86, 866.

(35) Nicklaß, A.; Dolg, M.; Stoll, H.; Preuss, H. *J. Chem. Phys.* **1995**, 102, 8942. Bergner, A.; Dolg, M.; Küchle, W.; Stoll, H.; Preuss H. *Mol. Phys.* **1993**, 80, 1431. Dolg, M. Ph.D. Dissertation, Universität Stuttgart, Germany, 1989.

(36) Kaupp, M.; Schleyer, P. v. R.; Stoll, H.; Preuss, H. *J. Am. Chem. Soc.* **1991**, 113, 6012.

(37) d-Type polarization functions have been taken from: *Gaussian Basis Sets for Molecular Calculations*, Huzinaga, S., Ed.; Elsevier: New York, 1984.

(38) Godbout, N.; Salahub, D. R.; Andzelm J.; Wimmer, E. *Can. J. Chem.* **1992**, 70, 560.

(39) Munzarová, M.; Kaupp, M. *J. Phys. Chem. A* **1999**, 103, 9966.

(40) Vosko, S. H.; Wilk, L.; Nusair, M. *Can. J. Chem.* **1980**, 58, 1200.

(41) Perdew, J. P.; Wang, Y. *Phys. Rev. B* **1986**, 33, 8800.

(42) Perdew, J. P. *Physica B* **1992**, 172, 1. Perdew, J. P. In *Electronic Structure of Solids '91*, Ziesche, P., Eschring, H., Eds.; Akademie Verlag: Berlin, 1991. Perdew, J. P.; Wang, Y. *Phys. Rev. B* **1992**, 45, 13244.

SZ for simple main-group radicals and with those of PZ for some  $d^1$  transition metal systems, we will concentrate on the BP86 results. The calculations were performed in two separate steps, (1) the Kohn–Sham SCF calculation, and (2) the computationally inexpensive perturbation calculation, based on the Kohn–Sham orbitals of the previous step. This two-step procedure makes it easy to alter the parameters of the perturbation calculation only, for example, to test different options to treat the gauge problem, different SO operators, or for analysis purposes.

As we employ exchange-correlation functionals that do not depend on the current density, the resulting perturbation calculations are uncoupled (UDFT). In NMR chemical shift calculations on main group compounds with low-lying excited states, it was found previously, that the simple correction term  $\Delta E_{k\rightarrow a}^{xc}$  in eq 5 may be used to reduce the paramagnetic contributions to the shielding tensors, thereby improving in most cases the agreement with experiment.<sup>17,22</sup> In the case of the electronic *g*-tensor, we find that the accuracy of the experimental data available does typically not allow us to judge whether this SOS-DFPT correction term is beneficial to the agreement between theory and experiment. We will thus concentrate on the UDFT results and give SOS-DFPT results for comparison only in a few examples.

Unless noted otherwise, results are reported with the IGLO<sup>43</sup> choice of gauge. Orbitals were typically localized with the Boys procedure.<sup>44</sup> For the heavier main-group compounds and the square pyramidal  $d^1$  complexes, the Pipek–Mezey localization<sup>45</sup> converged better and was used instead. The  $\alpha$  and  $\beta$  MOs were localized separately. For analyses in terms of canonical MOs, a common gauge origin at the center of mass has been employed. *g*-Tensor calculations are known<sup>6–8,12,14</sup> to be less gauge-dependent than, for example, NMR chemical shift computations, and we find that the IGLO and common gauge results typically do not differ much.

All-electron basis sets used for the 3d metals were (15s11p6d)/[9s7p4d] sets designed previously for hyperfine calculations.<sup>39</sup> Basis sets for Mo and Zr were constructed from the primitive set of the well-tempered series of Huzinaga et al.<sup>46</sup> by removing the tightest three *s*-, two *p*- and four *d*-functions and adding the two most diffuse *p*-functions from the ECP basis set.<sup>33</sup> The resulting 24s19p13d sets were used fully uncontracted. Test calculations show that this allows a valid comparison with ECP results. The basis sets BII and BIII (also termed IGLO-II and IGLO-III) of Kutzelnigg et al.<sup>43</sup> (based on the earlier work of Huzinaga<sup>47</sup>) were used for main group atoms. In some cases, smaller DZVP basis sets<sup>38</sup> were also studied (either with or without *p*-polarization functions on hydrogen).

Energy-adjusted ECPs and valence basis sets for 4d and 5d transition metals were the same as those used in the structure optimizations,<sup>33</sup> augmented by appropriate spin–orbit pseudopotentials<sup>33</sup> in the perturbation step of the calculation. Similarly, an ECP treatment of main group atoms (mainly of Kr, Xe, and

**Table 1.** Analysis of Different Contributions to *g*-Shifts (ppm) in  $\text{CO}^+$ <sup>a</sup>

| contribution  | exact<br>SO treatment <sup>b</sup> |                    | atomic<br>mean-field appr. <sup>c</sup> |  | SZ <sup>d</sup>        |                    |
|---|------------------------------------|--------------------|---|--|------------------------|--------------------|
|   | $\Delta g_{\parallel}$             | $\Delta g_{\perp}$ | $\Delta g_{\parallel}$                  | $\Delta g_{\perp}$                             | $\Delta g_{\parallel}$ | $\Delta g_{\perp}$ |
| $\Delta g_{\text{GC}(1e)}$  | 85                                 | 71                 | 85                                      | 71   | 81                     | 119                |
| $\Delta g_{\text{GC}(2e)}$  | -                                  | -                  | -                                       | -  | -34                    | -61                |
| $\Delta g_{\text{RMC}}$   | -180                               | -180               | -180                                    | -180   | -181                   | -181               |
| $\Delta g_{\text{SO/OZ}(1e)}$   | 0                                  | -3668              | 0                                       | -3660  | 0                      | -3678              |
| $\Delta g_{\text{SO/OZ}(2e)}$<br>(SSO <sup>e</sup> , SOO <sup>f</sup> ) | 0                                  | 1271               | 0                                       | 1312<br>(975 <sup>e</sup> , 337 <sup>f</sup> ) | 0                      | 684                |
| total <sup>g</sup>  | -95                                | -2507              | -95                                     | -2458  | -135                   | -3117              |

<sup>a</sup> UDFT results with BP86 functional. Our results with basis BIII and IGLO gauge. Results of SZ with STO basis and GIAO gauge.

<sup>b</sup> Exact calculation of all SO integrals with the EAGLE code. <sup>c</sup> Atomic mean-field approximation. <sup>d</sup> Approximate treatment of two-electron SO terms.<sup>12</sup> <sup>e</sup> Spin–same–orbit contribution. <sup>f</sup> Spin–other–orbit contribution. <sup>g</sup> Gas-phase experiments give -2400 ppm for  $\Delta g_{\perp}$ .

the halogens) employed the same quasirelativistic ECPs as the optimizations, together with SO-ECPs.<sup>35</sup> The valence basis sets were decontracted and extended to TZ + 2P quality. The fitting procedure of the SO-ECPs used differs slightly from that of the quasirelativistic ECPs, as they were obtained by a single-electron fit rather than by a multielectron fit.<sup>33,35</sup> Moreover, the SO-ECPs used in the present work have been fitted to two-component Wood–Boring or averaged four-component Dirac–Fock energies that do not include the Breit interaction. Thus, they do not cover the spin–other–orbit term. Development of improved two-component multielectron-fit ECPs and SO-ECPs adjusted to multiconfiguration Dirac–Fock–Breit energies is presently carried out by Stoll et al.,<sup>48</sup> and we plan to use these more accurate parameters in our future *g*-tensor work. In some cases we also used nonrelativistic ECPs in the Kohn–Sham step for interpretation purposes. Gauge factors arising from the use of ECPs in the IGLO treatment have been neglected in the present work.<sup>49</sup>

#### 4. All-Electron Calculations: The Importance of the Two-Electron SO Terms

For two systems, namely for  $\text{CO}^+$  and for  $\text{H}_2\text{O}^+$ , SZ reported individual contributions to the  $\Delta g$  components from their DFT calculations.<sup>12</sup> This allows us detailed comparison, in particular regarding the different treatment of the two-electron SO terms ( $\Delta g_{\text{SO/OZ}(2e)}$  terms). Table 1 gives the results for  $\text{CO}^+$ , Table 2 for  $\text{H}_2\text{O}^+$ . We give results with either (1) the exact (EAGLE) treatment of all one- and two-electron SO integrals, (2) the one-center and mean-field approximation (AMFI) to these integrals, and (3) the results of SZ, using their approximate treatment of the two-electron SO terms via an effective Kohn–Sham potential. In our mean-field SO calculations, we are furthermore able to separate the two-electron SO terms into contributions from spin–same–orbit (SSO) and spin–other–orbit (SOO) terms. This allows us to estimate the importance of the SOO terms, which were neglected in the approach of SZ. Note that, like SZ, we use the BP86 functional, that is, our calculations differ essentially only in the basis sets used (extended STO basis sets of SZ, extended GTO basis sets in our case), and in the treatment of the two-electron SO terms. The fact that we use IGLO rather than GIAO should not be relevant as we obtain essentially the same results with other choices of gauge origin.

(48) Metz, B.; Schweizer, M.; Stoll, H.; Dolg, M.; Liu, W. *Theor. Chem. Acc.* **2000**, *104*, 22.

(49) For a justification, see: Kaupp, M.; Malkin, V. G.; Malkina, O. L.; Salahub, D. R. *Chem. Phys. Lett.* **1995**, *235*, 382.

(43) Kutzelnigg, W.; Fleischer, U.; Schindler, M. In *NMR-Basic Principles and Progress*; Diehl, P., Fluck, E., Günther, H.; Kosfeld, R., Eds.; Springer-Verlag: Heidelberg, 1990; Vol. 23, pp 165ff.

(44) Edmiston, C.; Ruedenberg, K. *Rev. Mod. Phys.* **1963**, *35*, 457. Edmiston, C.; Ruedenberg, K. *J. Chem. Phys.* **1965**, *43*, 597. See also: Boys, S. F. In *Quantum Theory of Atoms, Molecules and the Solid State*; Löwdin, P.-O., Ed.; Academic Press: New York, 1966; p 253. This procedure is often incorrectly attributed to Foster, S.; Boys, S. F. *Rev. Mod. Phys.* **1963**, *35*, 457.

(45) Pipek, J.; Mezey, P. G. *J. Chem. Phys.* **1989**, *90*, 4916.

(46) Huzinaga, S.; Miguel, B. *Chem. Phys. Lett.* **1990**, *175*, 289. Huzinaga, S.; Klobukowski, M. *Chem. Phys. Lett.* **1993**, *212*, 260.

(47) Huzinaga, S. *Approximate Atomic Functions*; University of Alberta, Canada, 1971.

**Table 2.** Analysis of Different Contributions to  $g$ -Shifts (ppm) in  $\text{H}_2\text{O}^+$  <sup>a</sup>

| contribution                           | atomic mean-field appr. <sup>b,c</sup> |   |  | SZ <sup>d</sup> |                 |                 |
|--|--|---|--|-----------------|-----------------|-----------------|
|  | $\Delta g_{11}$                        | $\Delta g_{22}$                           | $\Delta g_{33}$                            | $\Delta g_{11}$ | $\Delta g_{22}$ | $\Delta g_{33}$ |
| $\Delta g_{\text{GC}(1e)}$             | 138                                    | 172                                       | 183  | 147             | 254             | 216             |
| $\Delta g_{\text{GC}(2e)}$             | -                                      | -   | -  | -54             | -109            | -92             |
| $\Delta g_{\text{RMC}}$                | -312                                   | -312                                      | -312                                       | -310            | -310            | -310            |
| $\Delta g_{\text{SO/OZ}(1e)}$          | 28                                     | 5946                                      | 15993                                      | 0               | 6153            | 16808           |
| $\Delta g_{\text{SO/OZ}(2e)}$          | 5                                      | -2104                                     | -5658                                      | 9               | -1188           | -3165           |
| (SSO <sup>e</sup> , SOO <sup>f</sup> ) | (10 <sup>e</sup> , -5 <sup>f</sup> )   | (-1599 <sup>e</sup> , -505 <sup>f</sup> ) | (-4300 <sup>e</sup> , -1358 <sup>f</sup> ) |                 |                 |                 |
| total <sup>g</sup>                     | -142                                   | 3702                                      | 10205                                      | -209            | 4800            | 13457           |

<sup>a</sup> UDFT results with BP86 functional. Our results with basis BIII and IGLO gauge. Results of SZ with STO basis and GIAO gauge. <sup>b</sup> Mean-field and one-center approximation. <sup>c</sup> The exact treatment of the two-electron SO integrals with the EAGLE code gives the following results:  $\Delta g_{11} = -142$  ppm,  $\Delta g_{22} = 3855$  ppm,  $\Delta g_{33} = 10422$  ppm. <sup>d</sup> Reference 12. <sup>e</sup> Spin-same-orbit contribution. <sup>f</sup> Spin-other-orbit contribution. <sup>g</sup> Gas-phase experiments give  $\Delta g_{11} = 200$  ppm,  $\Delta g_{22} = 4800$  ppm,  $\Delta g_{33} = 18800$  ppm.

We first note that the agreement between the exact (EAGLE) treatment and the one-center mean-field approximation (AMFI) is excellent, both for the  $\Delta g_{\text{SO/OZ}(1e)}$  terms (which include the one-center approximation in AMFI but not in EAGLE), and for the  $\Delta g_{\text{SO/OZ}(2e)}$  terms. Differences are below 7% (typically below 5%) in the two-electron terms, that is, much less for the overall  $g$ -shifts. This confirms the excellent performance of the atomic mean-field SO approximation, as found in many other types of applications.<sup>18,25,50</sup> For systems with heavier atoms, the mean-field approximation is expected to be even more accurate. The computational effort for the atomic mean-field approximation is not much more than for the one-electron SO integrals alone. Therefore, this approach removes effectively any SO-integral bottleneck from our calculations with very little sacrifice in the accuracy, and it enables us to treat large systems.

As shown already by other workers (see, e.g., refs 6 and 7), the  $g$ -shift tensors are usually—except for very light systems or for very small components—dominated by the second-order (paramagnetic)  $\Delta g_{\text{SO/OZ}(1e)}$  and  $\Delta g_{\text{SO/OZ}(2e)}$  terms, while the first-order (diamagnetic) contributions ( $\Delta g_{\text{RMC}}$  and  $\Delta g_{\text{GC}(1e)}$  terms) are small. In both  $\text{CO}^+$  and  $\text{H}_2\text{O}^+$ , our  $\Delta g_{\text{RMC}}$  terms agree quantitatively with the results of SZ. Similarly, the  $\Delta g_{\text{RMC}}$  contributions for these two radicals, as well as for  $\text{NO}_2$  and  $\text{MgF}$ , agree excellently with the MRCI results of Lushington.<sup>7</sup> The  $\Delta g_{\text{GC}(1e)}$  corrections are not directly comparable, due to the different choice of gauge origin. Nevertheless, they are close to the results of SZ and agree also with those of Lushington (we find an even better agreement when using a common gauge origin at the center of mass). We neglect the  $\Delta g_{\text{GC}(2e)}$  corrections. They have been found to be smaller and of the opposite sign to the  $\Delta g_{\text{GC}(1e)}$  terms, that is, small compared to the paramagnetic terms.<sup>7,12</sup> This is expected to cause slight errors for very small components, where the spin-orbit terms are small, but it will not influence much the comparison with experiment.

Interestingly, even the  $\Delta g_{\text{SO/OZ}(1e)}$  contributions to the larger components agree with the results of SZ to within better than 5%. Thus, any significant deviation between the overall results must stem from the treatment of the  $\Delta g_{\text{SO/OZ}(2e)}$  terms. Indeed, in both systems the two-electron SO contributions recovered by SZ account for only ~50% of our results. As a consequence, the overall  $g$ -shifts of SZ are generally somewhat larger than ours, as the partial compensation of the one-electron SO terms by the two-electron terms is underestimated. We have tried to find out to what extent the incomplete recovery of the two-electron terms by SZ is due to either (1) the neglect of the SOO

**Table 3.**  $g$ -Tensor Components (ppm) for Some Light Main Group Radicals<sup>a</sup>

|                        |                        | Lushington             |                 |                     | exp. <sup>e</sup> |           |
|------------------------|------------------------|------------------------|-----------------|---------------------|-------------------|-----------|
|                        |                        | this work <sup>b</sup> | SZ <sup>c</sup> | (MRCI) <sup>d</sup> |                   |           |
| $\text{H}_2\text{O}^+$ | $\Delta g_{11}$        | -142                   | 103             | -292                | 200               | gas phase |
|                        | $\Delta g_{22}$        | 3702                   | 5126            | 4217                | 4800              |           |
|                        | $\Delta g_{33}$        | 10205                  | 13824           | 16019               | 18800             |           |
| $\text{CO}^+$          | $\Delta g_{\perp}$     | -2458                  | -3129           | -2674               | -2400             | gas phase |
|                        | $\Delta g_{\parallel}$ | -93                    | -138            | -178                | -                 |           |
| $\text{HCO}$           | $\Delta g_{11}$        | -224                   | -270            | -                   | 0                 | matrix    |
|                        | $\Delta g_{22}$        | 2275                   | 2749            | -                   | 1500              |           |
|                        | $\Delta g_{33}$        | -7476                  | -9468           | -                   | -7500             |           |
| $\text{C}_3\text{H}_5$ | $\Delta g_{11}$        | -65                    | -115            | -                   | 0                 | matrix    |
|                        | $\Delta g_{22}$        | 497                    | 660             | -                   | 400               |           |
|                        | $\Delta g_{33}$        | 603                    | 769             | -                   | 800               |           |
| $\text{NO}_2$          | $\Delta g_{11}$        | -688                   | -760            | -235                | -300              | gas phase |
|                        | $\Delta g_{22}$        | 3400                   | 4158            | 3806                | 3900              |           |
|                        | $\Delta g_{33}$        | -11229                 | -13717          | -10322              | -11300            |           |
| $\text{NF}_2$          | $\Delta g_{11}$        | -617                   | -738            | -                   | -100              | matrix    |
|                        | $\Delta g_{22}$        | 3928                   | 4678            | -                   | 2800              |           |
|                        | $\Delta g_{33}$        | 6288                   | 7619            | -                   | 6200              |           |
| $\text{MgF}$           | $\Delta g_{\perp}$     | -1869                  | -2178           | -1092               | -1300             | matrix    |
|                        | $\Delta g_{\parallel}$ | 14                     | -60             | -59                 | -300              |           |

<sup>a</sup> UDFT-BP86 results. <sup>b</sup> Basis BIII, UDFT-IGLO, AMFI approximation. <sup>c</sup> UDFT-GIAO.<sup>12</sup> <sup>d</sup> Multireference configuration interaction results.<sup>7</sup> <sup>e</sup> Experimental data as quoted in refs. 7,12.

terms or (2) to the approximations involved in the effective Kohn-Sham potential used. Tables 1 and 2 show that in both systems, the SOO term accounts for ~25% of the total  $\Delta g_{\text{SO/OZ}(2e)}$  terms. Thus, about half of the errors of SZ in the two-electron terms is due to the neglect of the SOO term, the other half must be due to the other approximations mentioned.

Table 3 compares our overall calculated  $g$ -shift components for some small, light main-group compounds to the DFT results of SZ, the CI data of Lushington et al., and experiment (either in the gas phase or in matrix). As expected from the above discussion, our  $g$ -shift components are generally of smaller absolute value than those of SZ, due to the more complete treatment of the two-electron SO terms. As SZ's results often overestimate the absolute values of the experimental  $g$ -shift components, in the majority of cases our data are overall in somewhat closer agreement with experiment (exceptions are  $\Delta g_{33}$  of  $\text{H}_2\text{O}^+$  and  $\text{C}_3\text{H}_5$ , where the experimental value is higher). Figure 1 compares graphically our UDFT-BP86 data for light main-group systems to experiment. The plot includes the data from Table 3 and those for the larger substituted aromatic radicals discussed in section 6. The agreement is reasonable. A notable exception is  $\Delta g_{33}$  of  $\text{H}_2\text{O}^+$ . The MRCI results of Lushington are in much better agreement with experiment. The  $\text{H}_2\text{O}^+$  radical cation may be a particularly difficult case for a Kohn-Sham approach, due to the near-degeneracy between HOMO and SOMO.

(50) See, for example: Ruud, K.; Schimmelpfennig, B.; Ågren, H. *Chem. Phys. Lett.* **1999**, *310*, 215. Maron, L.; Leininger, T.; Schimmelpfennig, B.; Vallet, V.; Heully, J.-L.; Teichteil, Ch.; Gropen, O.; Wahlgren, U. *Chem. Phys. Lett.* **1999**, *244*, 195. Fagerli, H.; Schimmelpfennig, B.; Gropen, O.; Wahlgren, U. *THEOCHEM* **1998**, *451*, 227.



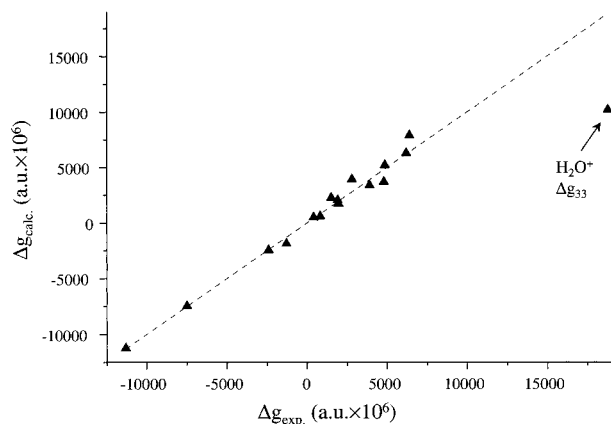


**Figure 1.** Comparison of calculated and experimental  $g$ -shift tensor components (ppm) for first-row compounds (cf. Tables 3, 9; Only components with  $|\Delta g| > 1000$  ppm have been included).

Obviously, the importance of errors in the two-electron SO terms for the overall  $g$ -shifts depends on the relative importance of the  $\Delta g_{\text{SO/OZ}(2e)}$  contributions. In  $\text{CO}^+$  and  $\text{H}_2\text{O}^+$ , the two-electron terms amount to  $\sim 35\%$  of the absolute magnitude of the  $\Delta g_{\text{SO/OZ}(1e)}$  terms (with opposite sign). We find this to be the general behavior for compounds containing atoms from at most the second period. Our results for other systems containing heavier main group atoms indicate that the importance of the two-electron terms decreases to  $\sim 20\%$ ,  $10\%$ ,  $7\%$  for the third, fourth and fifth period, respectively (see, e.g., results for  $\text{CF}_3\text{X}^-$ ;  $\text{X} = \text{Cl}, \text{Br}, \text{I}$ , in Table 4). The same percentages were found previously in both DFT<sup>18</sup> and MCSCF calculations<sup>51</sup> of SO corrections to NMR chemical shifts. Thus, the accurate treatment of the two-electron terms becomes somewhat less important for compounds of heavier main group elements. For light main group, for example, organic radicals, the two-electron SO terms are particularly critical. The SOO term accounts for  $\sim 20\%$  of the two-electron SO terms also for the heavier main group compounds (cf. Table 4).

The relative importance of the different terms changes when transition metals are involved. This is demonstrated for the simple 3d and 4d complexes  $\text{TiF}_3$  and  $\text{ZrH}_3$  in Table 5. In both cases, the spin density is mainly localized on the metal, and the SO coupling at the metal dominates the  $g$ -tensor. For the titanium complex, the  $\Delta g_{\text{SO/OZ}(2e)}$  contributions amount to  $\sim 47\%$  and  $\sim 55\%$  of the magnitude of the  $\Delta g_{\text{SO/OZ}(1e)}$  terms for  $\Delta g_{\parallel}$  and  $\Delta g_{\perp}$ , respectively. For the  $\text{ZrH}_3$  4d model complex the fractions are  $\sim 34\%$  and  $\sim 31\%$ , respectively. In both cases, the two-electron contributions are thus of considerably larger relative importance than with main group elements of the same row (cf.  $\sim 13\%$  for Br,  $\sim 7\%$  for I). This is probably related to the more pronounced penetration of the valence d-orbitals of the transition metals into the core.<sup>52</sup>

Another difference compared to the main group case is seen with the SOO term, which for both  $\text{TiF}_3$  and  $\text{ZrH}_3$  accounts for only  $\sim 10\text{--}12\%$  of the  $\Delta g_{\text{SO/OZ}(2e)}$  contribution, that is, it is only about half as important as in the main group cases we have looked at above. Good agreement with the perturbational UKS results (obtained with the SZ code) of van Lenthe et al.<sup>14</sup> for  $\text{TiF}_3$  may be obtained by reducing our  $\Delta g_{\text{SO/OZ}(2e)}$  contributions by  $\sim 50\%$ . This suggests that the main difference is in their incomplete treatment of the two-electron terms. On the other

(51) Vaara, J.; Ruud, K.; Vahtras, O.; Ågren, H.; Jokisaari, J. *J. Chem. Phys.* **1998**, *109*, 1212.

(52) The fact that the 3d shell is the first shell with  $l = 2$  and thus particularly compact, may be responsible for the particularly large  $\Delta g_{\text{SO/OZ}(2e)}$  contributions for 3d systems (similar arguments apply to the 2p shell).

**Table 4.** Analysis of Different Contributions to  $g$ -Shifts (ppm) in  $\text{CF}_3\text{X}^-$  ( $\text{X} = \text{Cl}, \text{Br}, \text{I}$ )<sup>a</sup>

| $\text{CF}_3\text{Cl}^-$   |  | $\Delta g_{\parallel}$                | $\Delta g_{\perp}$                         |
|----------------------------|--|---------------------------------------|--|
| all-el. <sup>a</sup>       | $\Delta g_{\text{GC}(1e)}$             | 130                                   | 96   |
|                            | $\Delta g_{\text{RMC}}$                | -315                                  | -315                                       |
|                            | $\Delta g_{\text{SO/OZ}(1e)}$          | -482                                  | 17891                                      |
|                            | $\Delta g_{\text{SO/OZ}(2e)}$          | 134                                   | -3474                                      |
|                            | (SSO <sup>b</sup> , SOO <sup>c</sup> ) | (93 <sup>b</sup> , 41 <sup>c</sup> )  | (-2768 <sup>b</sup> , -707 <sup>c</sup> )  |
| total all-el. <sup>a</sup> | -532                                   | 14198                                 |  |
| ECP-QR(Cl) <sup>d</sup>    | -390                                   | 12961                                 |  |
| SZ NR <sup>e,f</sup>       | -609                                   | 14573                                 |  |
| SZ QR <sup>e,g</sup>       | -610                                   | 15112                                 |  |
| exp. <sup>h</sup>          | -200                                   | 4700                                  |  |
| $\text{CF}_3\text{Br}^-$   |  | $\Delta g_{\parallel}$                | $\Delta g_{\perp}$                         |
| all-el. <sup>a</sup>       | $\Delta g_{\text{GC}(1e)}$             | 167                                   | 401  |
|                            | $\Delta g_{\text{RMC}}$                | -313                                  | -313                                       |
|                            | $\Delta g_{\text{SO/OZ}(1e)}$          | -475                                  | 57833                                      |
|                            | $\Delta g_{\text{SO/OZ}(2e)}$          | 151                                   | -5663                                      |
|                            | (SSO <sup>b</sup> , SOO <sup>c</sup> ) | (117 <sup>b</sup> , 34 <sup>c</sup> ) | (-4583 <sup>b</sup> , -1080 <sup>c</sup> ) |
| total all-el. <sup>a</sup> | -470                                   | 52258                                 |  |
| ECP-QR(Br) <sup>d</sup>    | -353                                   | 53680                                 |  |
| SZ NR <sup>e,f</sup>       | -635                                   | 67273                                 |  |
| SZ QR <sup>e,g</sup>       | -637                                   | 70229                                 |  |
| exp. <sup>h</sup>          | -1300                                  | 18900                                 |  |
| $\text{CF}_3\text{I}^-$    |  | $\Delta g_{\parallel}$                | $\Delta g_{\perp}$                         |
| all-el. <sup>a</sup>       | $\Delta g_{\text{GC}(1e)}$             | 196                                   | -56  |
|                            | $\Delta g_{\text{RMC}}$                | -303                                  | -303                                       |
|                            | $\Delta g_{\text{SO/OZ}(1e)}$          | -452                                  | 137144                                     |
|                            | $\Delta g_{\text{SO/OZ}(2e)}$          | 112                                   | -9455                                      |
|                            | (SSO <sup>b</sup> , SOO <sup>c</sup> ) | (76 <sup>b</sup> , 36 <sup>c</sup> )  | (-7833 <sup>b</sup> , -1622 <sup>c</sup> ) |
| total all-el. <sup>a</sup> | -447                                   | 127330                                |  |
| ECP-QR(I) <sup>d</sup>     | -291                                   | 138056                                |  |
| SZ NR <sup>e,f</sup>       | -581                                   | 146759                                |  |
| SZ QR <sup>e,g</sup>       | -571                                   | 161466                                |  |
| exp. <sup>h</sup>          | -2100                                  | 46000                                 |  |

<sup>a</sup> UDFT-IGLO results with BP86 functional and AMFI approximation. All-electron results with basis BII. <sup>b</sup> Spin-same-orbit terms only. <sup>c</sup> Spin-other-orbit terms only. <sup>d</sup> Quasirelativistic ECP/SO-ECP and TZ+2P valence basis on all halogen atoms, BII on C. <sup>e</sup> DFT-GIAO, ref 12. <sup>f</sup> Without scalar relativistic effects. <sup>g</sup> With scalar relativistic effects included. <sup>h</sup> In tetramethylsilane matrix (Hasegawa, A.; Williams, F. *Chem. Phys. Lett.* **1977**, *46*, 66). These anions are expected to experience increasing interactions with the environment from  $\text{X} = \text{Cl}$  through  $\text{X} = \text{I}$ . Therefore, the experimental data are probably not well-suited to be compared with calculations on the isolated anions.

hand, their restricted Kohn-Sham (ROKS) calculations (both perturbational and two-component treatment) give much larger  $\Delta g_{\perp}$  than the UKS treatment, i.e., spin polarization does seem to be important. Here the ROKS data are closer to experiment, probably due to error compensation, cf. section 6.

The previous examples were relatively simple, as the spin-orbit coupling arose mainly from one (the heaviest) atom, and from only a few molecular orbitals. Obviously, things may be much more complicated, if several heavy atoms are involved, and if several MOs may contribute. As an illustration, Table 6 compares the analyses for the two square pyramidal complexes  $\text{CrOF}_4^-$  and  $\text{CrOCl}_4^-$ . In the case of  $\text{CrOF}_4^-$ , things are still relatively straightforward. The  $\Delta g_{\text{SO/OZ}(2e)}$  terms amount to about half of the  $\Delta g_{\text{SO/OZ}(1e)}$  terms ( $\sim 51\%$  for  $\Delta g_{\parallel}$ ,  $\sim 45\%$  for  $\Delta g_{\perp}$ ), and the SOO term to about 11–14% of the  $\Delta g_{\text{SO/OZ}(2e)}$  contribution. However, in the case of  $\text{CrOCl}_4^-$ ,  $\Delta g_{\perp}$  behaves “normally” ( $\sim 45\%$  magnitude of the two-electron terms,  $\sim 10\%$  fraction of SOO terms), but  $\Delta g_{\parallel}$  is atypical. Here the  $\Delta g_{\text{SO/OZ}(2e)}$  terms are very small ( $\sim 2\%$ ; with  $\sim 35\%$  SOO contribution). An MO analysis (section 7) indicates that at least two occupied MOs contribute significantly to  $\Delta g_{\parallel}$ , with opposite signs. The

**Table 5.** Analysis of Different Contributions to *g*-Shifts (ppm) in TiF<sub>3</sub> and ZrH<sub>3</sub><sup>a</sup>

| contribution                           | TiF <sub>3</sub>                         |   | ZrH <sub>3</sub>                          |   |
|--|--|---|---|---|
|  | $\Delta g_{\parallel}$                   | $\Delta g_{\perp}$                          | $\Delta g_{\parallel}$                    | $\Delta g_{\perp}$                          |
| $\Delta g_{GC(1e)}$                    | +203                                     | +371  | +227                                      | +484  |
| $\Delta g_{RMC}$                       | -320                                     | -320  | -255                                      | -255  |
| $\Delta g_{SO/OZ(1e)}$                 | -1924                                    | -58669                                      | -6007                                     | -250046                                     |
| $\Delta g_{SO/OZ(2e)}$                 | +907                                     | +32043                                      | +2037                                     | +77658                                      |
| (SSO <sup>b</sup> , SOO <sup>c</sup> ) | (+783 <sup>b</sup> , +124 <sup>c</sup> ) | (+28199 <sup>b</sup> , +3844 <sup>c</sup> ) | (+1833 <sup>b</sup> , +204 <sup>c</sup> ) | (+69864 <sup>b</sup> , +7795 <sup>c</sup> ) |
| total all-el.                          | -1124                                    | -26577                                      | -3998                                     | -172160                                     |
| ECP-NR(Zr) <sup>d</sup>                |  |   | -3377                                     | -160070                                     |
| ECP-QR(Zr) <sup>e</sup>                |  |   | -2673                                     | -146534                                     |
| van Lenthe UKS <sup>f</sup>            | -1700                                    | -42800                                      |   |   |
| van Lenthe ROKS <sup>g</sup>           | +100                                     | -73300                                      |   |   |
| van Lenthe 2-comp. <sup>h</sup>        | -1000                                    | -79700                                      |   |   |
| exp.                                   | -11100 <sup>i</sup>                      | -111900 <sup>i</sup>                        |   |   |
|  | -3700 <sup>j</sup>                       | -123700 <sup>j</sup>                        |   |   |

<sup>a</sup> Present all-electron calculations at UDFT-IGLO level. The AMFI approximation, 9s7p4d basis on Ti, 24s19p13d basis on Zr, and BII on H, BIII on F. <sup>b</sup> Spin-same-orbit contribution. <sup>c</sup> Spin-other-orbit contribution. <sup>d</sup> Nonrelativistic ECP in the KS calculation. <sup>e</sup> Quasirelativistic ECP in the KS calculation. <sup>f</sup> Reference 14. With the perturbational approach of SZ, unrestricted KS wave function. <sup>g</sup> Reference 14. With the perturbational approach of SZ, restricted KS wave function. <sup>h</sup> Reference 14. Two-component ZORA calculation, spin-restricted. <sup>i</sup> Average of two sites in Ne matrix. <sup>j</sup> Ar matrix result.<sup>62</sup>

**Table 6.** Analysis of Different Contributions to *g*-Shifts (ppm) in CrOF<sub>4</sub><sup>-</sup> and CrOCl<sub>4</sub><sup>-</sup><sup>a</sup>

| contribution                           | CrOF <sub>4</sub> <sup>-</sup>              |   | CrOCl <sub>4</sub> <sup>-</sup>          |   |
|--|---|---|--|---|
|  | $\Delta g_{\parallel}$                      | $\Delta g_{\perp}$                          | $\Delta g_{\parallel}$                   | $\Delta g_{\perp}$                          |
| $\Delta g_{GC(1e)}$                    | +549  | +472  | +505                                     | +482  |
| $\Delta g_{RMC}$                       | -701  | -701  | -657                                     | -657  |
| $\Delta g_{SO/OZ(1e)}$                 | -27513                                      | -39331                                      | +20900                                   | -32848                                      |
| $\Delta g_{SO/OZ(2e)}$                 | +14073                                      | +17741                                      | -407                                     | +14955                                      |
| (SSO <sup>b</sup> , SOO <sup>c</sup> ) | (+12471 <sup>b</sup> , +1602 <sup>c</sup> ) | (+15216 <sup>b</sup> , +2525 <sup>c</sup> ) | (-266 <sup>b</sup> , -141 <sup>c</sup> ) | (+13399 <sup>b</sup> , +1556 <sup>c</sup> ) |
| total                                  | -13592                                      | -21811                                      | +20341                                   | -18067                                      |
| PZ <sup>d</sup>                        | -19000                                      | -29000                                      | +18000                                   | -21000                                      |
| exp. <sup>e</sup>                      | -43000                                      | -34000                                      | -10000                                   | -25000                                      |

<sup>a</sup> UDFT-IGLO results with BP86 functional. AMFI approximation, 9s7p4d basis on Cr, BII on all other atoms. <sup>b</sup> Same-orbit contribution. <sup>c</sup> Other-orbit contribution. <sup>d</sup> UDFT-GIAO results, ref 28. Data given only in ppt accuracy. <sup>e</sup> Experimental references as compiled in ref 28.

$\Delta g_{SO/OZ(2e)}$  contributions from these two MOs compensate each other to a large extent. Thus, obviously the importance of the two-electron terms, as well as the relative contributions from the SSO and SOO terms to them may differ significantly from system to system, and for different tensor components within one system. It is therefore not justified to use a simple scaling procedure to correct for a neglect of certain two-electron SO terms.

We may again ask to what extent the differences of our results relative to those of Ziegler et al. are due to their incomplete treatment of the  $\Delta g_{SO/OZ(2e)}$  terms. If we simply reduce our two-electron terms by half, we obtain roughly -20000 ppm and -30000 ppm for  $\Delta g_{\parallel}$  and  $\Delta g_{\perp}$ , respectively, in CrOF<sub>4</sub><sup>-</sup>, in much better agreement with the results of Patchkovski and Ziegler.<sup>28</sup> The same procedure applied to CrOCl<sub>4</sub><sup>-</sup> produces more negative  $\Delta g_{\perp}$  (~-25000 ppm), whereas  $\Delta g_{\parallel}$  is not affected much, due to the smallness of the two-electron terms in this case.

## 5. ECP Calculations: Validation of Spin-Orbit Pseudopotentials

Table 7 compares all-electron (AE) and pseudopotential (ECP/SO-ECP) treatments of  $\Delta g$  components for NF<sub>2</sub>, KrF, XeF, and MoOF<sub>4</sub><sup>-</sup>. Table 3 includes the same comparison for CF<sub>3</sub>X<sup>-</sup> (X = Cl, Br, I), and Table 5 for ZrH<sub>3</sub>. The results of Ziegler et al., with an approximate treatment of the  $\Delta g_{SO/OZ(2e)}$  terms, are included in Tables 4 and 7 as well, and experimental data are given for completeness. However, at least the data for KrF, XeF, and particularly those for the anions CF<sub>3</sub>X<sup>-</sup>, are probably influenced significantly by environmental effects (cf. below).

We will thus only compare the different theoretical approaches. For easier comparison, the ECP calculations use ECPs and SO-ECPs only for the heaviest atoms, whereas the all-electron AMFI treatment is kept for the lighter atoms (as discussed in section 2, this combination of methods is allowed, due to the atomic nature of the SO operators involved).

As the SO-ECPs used here have been adjusted to atomic calculations that did not include the Breit interaction, they do not cover the SOO term. The ECP results might therefore be expected to slightly overestimate the  $\Delta g_{SO/OZ}$  contributions, typically by ~10–15% for NF<sub>2</sub>, by less than half of this for the heavier main group and transition metal species (cf. section 4). On the other hand, the direct comparison between all-electron and ECP-NR results has to be viewed with some caution, as the use of nonrelativistic ECPs with the relativistically adjusted SO-ECPs is not completely consistent.

Inspecting the data of Tables 5 and 7, the ECP-NR results are found to be both high or low relative to the all-electron data. However, agreement is found generally within a few percent. The differences are significantly smaller than, for example, differences between local or gradient-corrected density functionals, and also smaller than differences relative to the approximate treatment of the SO integrals by SZ. This indicates that the combination of ECPs in the Kohn-Sham step with SO-ECPs in the perturbation treatment provides a useful valence-only approximation to the all-electron calculations. In all cases, our *g*-shifts are lower than those of SZ.

Comparison of the ECP-NR and ECP-QR results for KrF and XeF (Table 7) suggests an increase of  $\Delta g_{\perp}$  due to scalar

**Table 7.** Comparison of All-Electron and ECP/SO-ECP Results for *g*-Shift Components (ppm)<sup>a</sup>

|                                |                         | $\Delta g_{11}$ | $\Delta g_{22}$    | $\Delta g_{33}$ |
|--------------------------------|-------------------------|-----------------|--------------------|-----------------|
| NF <sub>2</sub>                | all-el. <sup>b</sup>    | -617            | 3928               | 6288            |
|                                | ECP-QR(F) <sup>c</sup>  | -774            | 3980               | 6699            |
|                                | SZ <sup>d</sup>         | -738            | 4678               | 7619            |
|                                | exp. <sup>e</sup>       | -100            | 2800               | 6200            |
|                                |                         | $\Delta g_{  }$ | $\Delta g_{\perp}$ |                 |
| KrF                            | all-el. <sup>b</sup>    | -246            | 49494              |                 |
|                                | ECP-NR(Kr) <sup>f</sup> | -166            | 48303              |                 |
|                                | ECP-QR(Kr) <sup>f</sup> | -164            | 50857              |                 |
|                                | SZ NR <sup>d,g</sup>    | -335            | 60578              |                 |
|                                | SZ QR <sup>d,h</sup>    | -345            | 61851              |                 |
|                                | exp. <sup>e</sup>       | -2000           | 66000              |                 |
| XeF                            | all-el. <sup>b</sup>    | -184            | 127288             |                 |
|                                | ECP-NR(Xe) <sup>f</sup> | -91             | 130003             |                 |
|                                | ECP-QR(Xe) <sup>f</sup> | -93             | 134302             |                 |
|                                | SZ NR <sup>d,g</sup>    | -340            | 151518             |                 |
|                                | SZ QR <sup>d,h</sup>    | -346            | 158083             |                 |
|                                | exp. <sup>e</sup>       | -28000          | 124000             |                 |
| MoOF <sub>4</sub> <sup>-</sup> | all-el. <sup>b</sup>    | -51855          | -46733             |                 |
|                                | ECP-NR(Mo) <sup>f</sup> | -48633          | -47293             |                 |
|                                | ECP-QR(Mo) <sup>f</sup> | -50557          | -47646             |                 |
|                                | PZ QR <sup>i</sup>      | -62000          | -57000             |                 |
|                                | exp. <sup>j</sup>       | -167000         | -76000             |                 |

<sup>a</sup> UDFT-IGLO results with BP86 functional and AMFI approximation. <sup>b</sup> All-electron basis sets 24s19p13d for Mo, BIII basis for F in NF<sub>2</sub>, KrF, XeF, BII for all other atoms. <sup>c</sup> ECP and TZ+2P valence basis on F, BII on N. <sup>d</sup> Reference 12. <sup>e</sup> As cited in ref 12. <sup>f</sup> Non-relativistic and quasi-relativistic ECP, respectively, on the heavy atom, with all-electron treatment for the light atoms. <sup>g</sup> Non-relativistic. <sup>h</sup> With scalar relativistic effects included. <sup>i</sup> Reference 28. <sup>j</sup> Sunil, K. K.; Rogers, M. T. *Inorg. Chem.* **1981**, *20*, 3283.

relativistic effects (more so for XeF than for KrF). This is consistent with the increase of the *g*-shifts upon inclusion of scalar relativistic effects by SZ (at the first-order Breit-Pauli level). Moreover, the relative increase is of comparable magnitude, suggesting that the comparison of NR-ECP and QR-ECP results provides a reasonable estimate of the influence of scalar relativistic effects.

In the case of the anions CF<sub>3</sub>X<sup>-</sup> (X = Cl, Br, I; Table 4), the ECP calculations use quasirelativistic ECPs and SO-ECPs for X (no appropriate nonrelativistic ECPs have been available for comparison). The QR-ECP results for  $\Delta g_{\perp}$  in CF<sub>3</sub>Cl<sup>-</sup> are ~9% lower than the all-electron results. In contrast, the QR-ECP calculations give ~3% and ~8% larger values for CF<sub>3</sub>Br<sup>-</sup> and CF<sub>3</sub>I<sup>-</sup>, respectively, probably in part due to the inclusion of scalar relativistic effects in the ECP calculations (cf. comparison between nonrelativistic and relativistic results of SZ). Again, our  $\Delta g_{\perp}$  components are somewhat smaller than those of SZ. The experimental data were obtained in a solid matrix of tetramethylsilane and are probably not strictly comparable to the free-anion calculations. The increasing discrepancy from X = Cl through X = I may be due either (1) to potential problems with the perturbation treatment of SO coupling for the heavier halogens, as suggested by SZ, or (2) to an increasingly diffuse nature of the SOMO (which corresponds to a  $\sigma^*$  (C–X) MO and does exhibit small positive energies in our Kohn–Sham calculations) and thus increasing interactions with the environment. The second possibility, which we find more likely, could be tested by calculations that simulate the matrix environment. This is beyond the scope of the present study.

ECP and all-electron results for the 4d model system ZrH<sub>3</sub> may be compared in Table 5. The ECP–NR calculations give ~7% too positive  $\Delta g_{\perp}$ . Scalar relativistic effects appear to reduce further significantly the absolute value. In contrast, for

**Table 8.** Comparison of First-Order Corrections (ppm) from All-Electron and ECP/SO-ECP Calculations<sup>a</sup>

|                                 |            | $\Delta g_{\text{RMC}}$ | $\Delta g_{\text{GC}(1e)}$ <sup>b</sup> |
|---------------------------------|------------|-------------------------|---|
| NF <sub>2</sub>                 | all-el. NR | -314                    | 126,232,225                             |
|                                 | ECP-QR(F)  | -316                    | 127,233,226                             |
| KrF                             | all-el. NR | -429                    | 179,491                                 |
|                                 | ECP-NR(Kr) | -351                    | 170,472                                 |
|                                 | ECP-QR(Kr) | -349                    | 170,473                                 |
| XeF                             | all-el. NR | -414                    | 228,598                                 |
|                                 | ECP-NR(Xe) | -303                    | 211,567                                 |
|                                 | ECP-QR(Xe) | -304                    | 209,569                                 |
| CF <sub>3</sub> Cl <sup>-</sup> | all-el. NR | -315                    | 144,82                                  |
|                                 | ECP-QR(Cl) | -244                    | 135,59                                  |
| CF <sub>3</sub> Br <sup>-</sup> | all-el. NR | -313                    | 181,200                                 |
|                                 | ECP-QR(Br) | -229                    | 170,179                                 |
| CF <sub>3</sub> I <sup>-</sup>  | all-el. NR | -303                    | 212,293                                 |
|                                 | ECP-QR(I)  | -209                    | 195,270                                 |
| ZrH <sub>3</sub>                | all-el. NR | -247                    | 251,455                                 |
|                                 | ECP-NR(Zr) | -118                    | 220,421                                 |
|                                 | ECP-QR(Zr) | -117                    | 219,419                                 |
| MoOF <sub>4</sub> <sup>-</sup>  | all-el. NR | -555                    | 797,531                                 |
|                                 | ECP-NR(Mo) | -283                    | 715,472                                 |
|                                 | ECP-QR(Mo) | -278                    | 708,470                                 |

<sup>a</sup> UDFT-BP86 results. Basis sets and ECPs as in Tables 3, 5, and 7.  $\Delta g_{\text{GC}(1e)}$  terms with common gauge at center of mass. <sup>b</sup>  $\Delta g_{11}$ ,  $\Delta g_{22}$ , and  $\Delta g_{33}$  for NF<sub>2</sub>,  $\Delta g_{||}$  and  $\Delta g_{\perp}$  for the other compounds.

the more complicated 4d complex MoOF<sub>4</sub><sup>-</sup> (Table 7), the scalar relativistic effects appear to be modest.

Table 8 compares  $\Delta g_{\text{RMC}}$  contributions obtained with all-electron and ECP approaches. While the agreement is excellent for the light NF<sub>2</sub> molecule, the ECP results increasingly underestimate the all-electron results for increasingly heavy atoms. It appears that the ECP calculations miss some core–shell contributions to this term. However, in view of the dominance of SO terms, errors in the  $\Delta g_{\text{RMC}}$  term will typically introduce only negligible errors in the overall computed *g*-shifts. The  $\Delta g_{\text{GC}(1e)}$  contributions are more difficult to compare directly, due to their gauge dependence. Table 8 includes results with a common gauge at the center of mass. Again, it seems that the ECP calculations underestimate these terms moderately for the heavier systems, whereas the core contribution from the fluorine 1s-orbitals in NF<sub>2</sub> apparently is negligible.

## 6. Further Validation Calculations

In this section, we validate the performance of the present DFT approach for a somewhat larger set of species, including also larger main group and transition metal systems. Table 9 gives *g*-shift tensors for some phenoxyl radicals (see Scheme 1), which have received appreciable attention due to the paramount importance of the tyrosyl radical in biological systems.<sup>53</sup> In addition to the free, unsubstituted phenoxyl radical, for which no experimental data appear to be available, we have also studied the substituted 2,4,6-tris- *t*-Bu-C<sub>6</sub>H<sub>2</sub>O radical, as well as the tyrosyl radical itself. The *g*-tensor of the tyrosyl radical has been studied by semiempirical calculations,<sup>4</sup> but to our knowledge not by first-principles methods. We have used the neutral rather than the zwitter-ionic form of the amino acid residue.

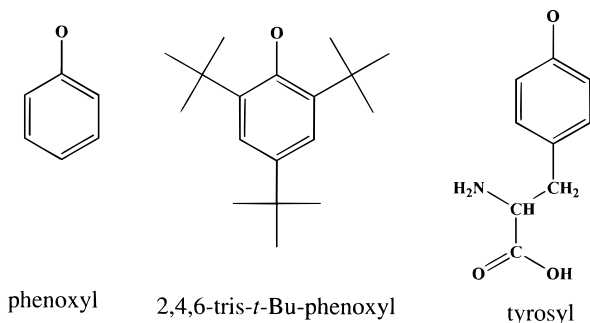
We take the parent phenoxyl radical as an example to test the basis set dependence of the DFT results, and to compare different exchange–correlation functionals (Table 9). The  $\Delta g_{22}$

(53) See, for example: (a) Ivancich, A.; Mattioli, T. A.; Un, S. *J. Am. Chem. Soc.* **1999**, *121*, 5743. (b) Allard, P.; Barra, A. L.; Andersson, K. K.; Schmidt, P. P.; Atta, M.; Gräslund, A. *J. Am. Chem. Soc.* **1996**, *118*, 895. (c) van Dam, P. J.; Willems, J.-P.; Schmidt, P. P.; Pötsch, S.; Barra, A.-L.; Hagen, W. R.; Hoffman, B. M.; Andersson, K. K.; Gräslund, A. *J. Am. Chem. Soc.* **1998**, *120*, 5080.

**Table 9.** Effects of Basis Sets and Functionals on Computed *g*-Shift Components (ppm) for Phenoxy Radicals<sup>a</sup>

| basis   |                   | $\Delta g_{\text{iso}}$ | $\Delta g_{11}$ | $\Delta g_{22}$ | $\Delta g_{33}$    |
|---|-------------------|-------------------------|-----------------|-----------------|--------------------|
| phenoxy                                       |                   |                         |                 |                 |                    |
| VWN, UDFT                                     | DZVD <sup>b</sup> | 3156                    | -139            | 363             | 9243               |
| VWN, UDFT                                     | DZVP              | 4429                    | -150            | 2145            | 11292              |
| VWN, UDFT                                     | BII               | 4505                    | -85             | 2249            | 11351              |
| VWN, UDFT                                     | BIII              | 4543                    | -83             | 2292            | 11419              |
| PP86, UDFT                                    | BII               | 3388                    | -91             | 2125            | 8130               |
| PW91, UDFT                                    | BII               | 3548                    | -89             | 2117            | 8617               |
| BP86, UDFT                                    | DZVD <sup>b</sup> | 2333                    | -146            | 319             | 6825               |
| BP86, UDFT                                    | DZVP              | 3355                    | -160            | 2031            | 8194               |
| BP86, UDFT                                    | BII               | 3405                    | -91             | 2117            | 8188               |
| BP86, UDFT                                    | BIII              | 3461                    | -85             | 2170            | 8299               |
| BP86, SOS-DFPT <sup>c</sup>                   | BIII              | 2980                    | -85             | 2133            | 6891               |
| ROHF <sup>d</sup>                             | cc-pVDZ           | 24200                   | 100             | 5200            | 67400              |
| MCSCF <sup>d</sup>                            | cc-pVDZ           | 2500                    | 200             | 2400            | 5000               |
| <i>t</i> -Bu-substituted phenoxy <sup>e</sup> |                   |                         |                 |                 |                    |
| VWN, UDFT                                     | DZVP              | 2721                    | 42              | 1834            | 6285               |
| BP86, UDFT                                    | DZVP              | 2314                    | -4              | 1734            | 5213               |
| BP86, SOS-DFPT <sup>c</sup>                   | DZVP              | 2093                    | -7              | 1721            | 4565               |
| exp.  |                   | 2297                    | 70              | 1960            | 4860               |
| tyrosyl                                       |                   |                         |                 |                 |                    |
| VWN, UDFT                                     | DZVP              | 4263                    | -167            | 2177            | 10480              |
| BP86, UDFT                                    | DZVP              | 3264                    | -181            | 2064            | 7908               |
| BP86, SOS-DFPT <sup>c</sup>                   | DZVP              | 2827                    | -195            | 2037            | 6639               |
| exp. ( <i>E. coli</i> RNR) <sup>f</sup>       |                   | 2670                    | -300            | 1900            | 6400               |
| exp. ( <i>S. typh.</i> RNR) <sup>g</sup>      |                   | 2848 ( $\pm 70$ )       | -200            | 2000            | 6600               |
| exp. ( <i>N</i> -Ac-L-TyrO) <sup>h</sup>      |                   | 3200 ( $\pm 200$ )      |                 |                 | 7000 ( $\pm 200$ ) |

<sup>a</sup> DFT results with IGLO gauge and AMFI approximation. <sup>b</sup> Without polarization functions on hydrogen. <sup>c</sup> Including correction term in Loc.1 approximation. <sup>d</sup> Results with common gauge at center of mass.<sup>54</sup> Only a limited number of digits were given. <sup>e</sup> Results for 2,4,6-tris-*t*-Bu-C<sub>6</sub>H<sub>2</sub>O. Experimental data in frozen toluene solution (145 K) from Bresgunov, A. Y.; Dubinsky, A. A.; Poluektov, O. G.; Lebedev, Y. S.; Prokov'ev, A. I. *Mol. Phys.* **1992**, *75*, 1123. <sup>f</sup> Experimental data for the tyrosyl radical in *E. coli* RNR. (Hoganson, C. W.; Sahlin, M.; Sjöberg, B.-M.; Babcock, G. T. *J. Am. Chem. Soc.* **1996**, *118*, 4672; see also ref 4). <sup>g</sup> Experimental data for the tyrosyl radical in *S. typhimurium* RNR (ref 53 b). <sup>h</sup> Irradiated crystal of *N*-acetyl-L-tyrosine (Mezzetti, A.; Maniero, A. L.; Brustolon, M.; Giacometti, G.; Brunel, L. C. *J. Phys. Chem. A* **1999**, *103*, 9636).

**Scheme 1.** Three Phenoxy Radicals Studied

and  $\Delta g_{33}$  components change relatively little in going from DZVP to the larger BII and BIII basis sets (this holds for both VWN and BP86 functionals). Only the DZVD basis, that is, omission of polarization p-functions on hydrogen, leads to a rather dramatic deterioration of the results, mainly for  $\Delta g_{22}$ . Closer inspection indicates that without the polarization functions, too much spin density is accumulated on the hydrogen atoms and withdrawn from the heavy atoms. In going from the local VWN to the gradient-corrected BP86 functional, the *g*-shifts decrease moderately but nonnegligibly. On the other hand, differences between different GGA functionals (BP86, PP86, PW91) are small. This is our general experience and the reason for concentrating mostly on one functional (BP86) throughout this work. An only modest dependence on the functional was also noted by Ziegler and co-workers,<sup>12,28</sup> and similar conclusions pertain to NMR chemical shift calculations on main-group nuclei.<sup>17</sup>

We may compare our results for the phenoxy radical to the ROHF and MCSCF calculations of Engström et al.<sup>54</sup> They found

(54) Engström, M.; Vahtras, O.; Ågren, H. *Chem. Phys.* **1999**, *243*, 263.

that electron correlation is extremely important for the description of the *g*-tensor of the phenoxy radical. This may be seen from the dramatically overestimated  $\Delta g_{22}$  and  $\Delta g_{33}$  components at the ROHF level (Table 9). Much lower *g*-shifts were obtained at the MCSCF level (Table 9). Our DFT results (e.g., UDFT-IGLO with BP86 functional and BIII basis) are much closer to the MCSCF than to the ROHF data but give ~65% larger  $\Delta g_{33}$  than the former.

The good agreement with the experimental result for the 2,4,6-tris-*t*-Bu-C<sub>6</sub>H<sub>2</sub>O radical has been taken as evidence for the good quality of the CASSCF wave function for the phenoxy radical.<sup>54</sup> While the substituted radical was too large to be studied at the MCSCF level, our DFT approach is easily applicable also to the larger system. Interestingly, the computed *g*-shifts are considerably reduced by the substitution (Table 9). In particular,  $\Delta g_{33}$  is much lower. On the other hand, our computed results for the tyrosyl radical are much closer to those for the unsubstituted phenoxy radical. *tert*-Butyl substituents in ortho position have obviously a rather significant effect on the spin density within the system (in particular on that for oxygen, which dominates the *g*-tensor; cf. below), but the amino acid moiety in para position of the tyrosyl radical oxygen atom affects the spin density distribution much less. Thus, while the free phenoxy radical is not a very good model to study quantitatively the *g*-tensor of the 2,4,6-tris-*t*-Bu-C<sub>6</sub>H<sub>2</sub>O radical, it serves as a very good model for the biologically relevant tyrosyl system (as previously concluded from spin-density calculations<sup>55</sup>). Notably, the present DFT approach reproduces rather accurately the experimental differences between the two substituted radicals. This suggests that substituent influences on the *g*-tensor in aromatic radicals may now be studied with good accuracy. We note in passing that, in contrast to the ring

(55) Qin, Y.; Wheeler, R. A. *J. Am. Chem. Soc.* **1995**, *117*, 6083.

protons, the neglect of polarization *p*-functions on the *t*-butyl hydrogen atoms in the 2,4,6-tris-*t*-Bu-C<sub>6</sub>H<sub>2</sub>O radical has a negligible effect on the computed *g*-shifts.

In addition to our UDFT-IGLO results with various functionals and basis sets, Table 9 also includes SOS-DFPT results with the BP86 functional. As is well-known from NMR chemical shift calculations, the SOS-DFPT correction term reduces to some extent the paramagnetic contributions and thus the overall shift components.<sup>17,22,56</sup> No experimental data are available to judge the performance of the different approaches for the free phenoxyl radical. For the 2,4,6-tris-*t*-Bu-C<sub>6</sub>H<sub>2</sub>O radical, the UDFT and SOS-DFPT results with the BP86 functional bracket the experimental value for  $\Delta g_{33}$ , whereas  $\Delta g_{22}$  is underestimated slightly in both calculations. The latter point is probably a basis set effect, cf. the basis set study for the free phenoxyl radical in Table 9. For the tyrosyl radical, the lower SOS-DFPT values appear to be somewhat closer to the available experimental data (we have chosen experimental numbers for tyrosyl radicals where hydrogen bonding to the phenoxyl oxygen is thought to be absent). From the present data it is difficult to decide whether the SOS-DFPT correction terms improve the results significantly for main group radicals. We have therefore concentrated on UDFT-BP86 results throughout this study. In any case, the results in Table 9 indicate that DFT approaches are significantly superior to Hartree–Fock calculations for phenoxyl radicals, comparable in quality to the (modest) MCSCF wave functions of ref 54. The advantage of DFT is the relatively low computational effort, and thus the possibility to treat large systems. Indeed, we are presently studying *g*-tensors for much larger radicals. This requires also a very efficient treatment of the spin–orbit operators, such as demonstrated in this work.

Less favorable performance of DFT was noted by PZ for *g*-tensors of transition metal complexes (a number of square pyramidal d<sup>1</sup> complexes were studied, see below) compared to main-group radicals.<sup>28</sup> This has been attributed to deficiencies of the currently used exchange–correlation functionals. Table 10 gives our results for a more diverse set of 3d complexes. In addition to the accurate atomic mean-field treatment of the  $\Delta g_{\text{SO/OZ}(1e)}$  and  $\Delta g_{\text{SO/OZ}(2e)}$  terms, we have also included results which neglect the  $\Delta g_{\text{SO/OZ}(2e)}$  contributions altogether. Figure 2 compares the results graphically to experiment. Some care has to be exercised in this comparison, due to the varying quality and nature of the experimental data. Nevertheless, the graphical comparison indicates that, rather disappointingly, the proper inclusion of the two-electron SO terms deteriorates the agreement with experiment significantly. Neglecting the three extreme outliers ( $\Delta g_{zz}$  of Cu(NO<sub>3</sub>)<sub>2</sub> and of Cu(acac)<sub>2</sub>, and  $\Delta g_{\perp}$  of TiF<sub>3</sub>), we arrive at a linear fit with slope 0.59 and  $R = 0.99378$ . The complete neglect of the two-electron SO terms improves the slope to 1.06 ( $R = 0.99381$ ). This is not surprising, as the two-electron terms reduce the overall *g*-shifts by ~40–50% (cf. section 4). Neglect of the two-electron terms does in this case correspond to a scaling by a factor of ~1.8. The three outliers mentioned are at particularly large (negative or positive)  $\Delta g$  values.

The slope of ~0.59 we find upon exact treatment of the SO operators corresponds strikingly to observations made recently by Bühl et al.<sup>57,58</sup> when testing DFT approaches in calculations of nuclear shieldings of 3d transition metal nuclei (in particular

of <sup>57</sup>Fe, but similar observations apply to <sup>59</sup>Co<sup>59</sup>). UDFT-GIAO calculations with GGA functionals gave slopes of ~0.6 in comparison with experiment, with one extreme outlier (ferrocene).<sup>57</sup> This corresponds to a significant underestimate of the paramagnetic contributions to shielding. Bühl found that the slope could be improved to almost 1.0 by using hybrid functionals (B3LYP or B3PW91).<sup>58</sup> In view of the close similarity of nuclear shielding and electronic *g*-tensor, we expect that the origin of the failure of the “pure” GGA functionals in the two cases is related (most likely, the usual functionals do not describe accurately local excitations at the metal<sup>60</sup>). Thus, the inclusion of Hartree–Fock exchange (and of the resulting coupling terms) should improve the performance also for the *g*-tensor. In the present version of our code we cannot include Hartree–Fock exchange. However, we are presently implementing a new program which will allow this to be done. Then more accurate calculations of *g*-tensors should also become possible for transition metal compounds.<sup>61</sup> Until then, a simple multiplicative scaling of the SO contributions may be considered as a short-term improvement. This result contrasts somewhat with the conclusions of PZ, based on a less diverse set of complexes. PZ argued that a simple, additive constant shift (different for 3d, 4d, and 5d systems) might be used to correct the computed results.<sup>28</sup> We expect less problems for complexes where the spin density is largely concentrated on the ligands. In fact, GGA functionals perform excellently for nuclear shieldings of ligand atoms in transition metal systems.<sup>9,10,11</sup>

Finally, Table 11 compares our results and those of PZ for a number of 4d<sup>1</sup> and 5d<sup>1</sup> complexes. The agreement of our calculations with experiment is again not satisfactory, actually even somewhat worse than for those of PZ. This is probably due to some error compensation in the results of PZ, related to the incomplete treatment of the SO operators. The paramagnetic contributions to the nuclear shielding of 4d transition metal nuclei are known to be underestimated less dramatically by GGA functionals than in the case of 3d metals (e.g., the slope for Rh shieldings at the GIAO–BPW91 level was found to be ~0.8<sup>57,58</sup>). One might thus expect 4d systems to be less critical also for *g*-tensor calculations. This is not borne out by the limited set of data given in Table 11. More calculations on a larger set of more diverse 4d complexes will be needed to settle this question.

## 7. Separation of *g*-Tensors into Atomic Contributions

As already mentioned, our use of a superposition of effective atomic spin–orbit operators does also offer advantages in terms of analyses of *g*-tensors. In this way we obtain a particularly straightforward separation of the  $\Delta g_{\text{SO/OZ}}$  terms into atomic SO contributions. This is shown as an example for the phenoxyl radical in Table 12. We first note that the relative weights of  $\Delta g_{\text{SO/OZ}(1e)}$  and  $\Delta g_{\text{SO/OZ}(2e)}$  terms, as well as of SOO and SSO contributions to the latter, are essentially just as discussed above for CO<sup>+</sup> and H<sub>2</sub>O<sup>+</sup>.

The atomic analysis is performed by carrying out a number of separate calculations (which employ the same Kohn–Sham wave function and thus do not require much extra computational effort), in which atomic mean-field SO operators are only used

(59) See, for example: Chan, C. C. J.; Au–Yeung, S. C. F.; Wilson, P. J.; Webb, G. A. *J. Mol. Struct.* **1996**, 365, 125. Godbout, N.; Oldfield, E. *J. Am. Chem. Soc.* **1997**, 119, 8065.

(60) Schreckenbach, G. *J. Chem. Phys.* **1999**, 110, 11936.

(61) Alternative functionals may also be envisioned, in which exact exchange is simulated rather than treated explicitly (see, e.g.: Becke, A. D. *J. Chem. Phys.* **2000**, 112, 4020).

(62) DeVore, C.; Weltner, W., Jr. *J. Am. Chem. Soc.* **1977**, 99, 4700.

(56) Olsson, L.; Cremer, D. *J. Chem. Phys.* **1996**, 105, 8995.

(57) Bühl, M.; Malkina, O. L.; Malkin, V. G. *Helv. Chim. Acta* **1996**, 79, 742.

(58) Bühl, M. *Chem. Phys. Lett.* **1997**, 267, 251.

**Table 10.** Comparison of Computed and Experimental *g*-Shift Tensor Components (ppt) for a Series of 3d Transition Metal Complexes<sup>a</sup>

| complex                                       | component              | without $\Delta g_{\text{SO/OZ}(2e)}$ | with $\Delta g_{\text{SO/OZ}(2e)}$ | exp.       | lit (exp.)   |
|---|------------------------|---------------------------------------|------------------------------------|------------|--------------|
| TiF <sub>3</sub>                              | $\Delta g_{\perp}$     | -79.4                                 | -28.3                              | -111.3     | <i>b</i> (1) |
|   |                        |                                       |                                    | -121.5     | <i>b</i> (2) |
|   |                        |                                       |                                    | -123.7     | <i>b</i> (3) |
| VO(L <sup>3</sup> ) <sub>2</sub> <sup>c</sup> | $\Delta g_{zz}$        | -55.6                                 | -25.7                              | -55.3      | <i>c</i>     |
| VO(L <sup>2</sup> ) <sub>2</sub> <sup>c</sup> | $\Delta g_{zz}$        | -48.8                                 | -24.6                              | -51.3      | <i>c</i>     |
| VO(L <sup>1</sup> ) <sub>2</sub> <sup>c</sup> | $\Delta g_{zz}$        | -58.2                                 | -28.6                              | -49.3      | <i>c</i>     |
| VO(L <sup>3</sup> ) <sub>2</sub> <sup>c</sup> | $\Delta g_{yy}$        | -31.5                                 | -15.4                              | -23.3      | <i>c</i>     |
| VO(L <sup>2</sup> ) <sub>2</sub> <sup>c</sup> | $\Delta g_{yy}$        | -29.1                                 | -14.5                              | -21.3      | <i>c</i>     |
| VO(L <sup>1</sup> ) <sub>2</sub> <sup>c</sup> | $\Delta g_{yy}$        | -24.1                                 | -12.2                              | -21.3      | <i>c</i>     |
| VO(L <sup>3</sup> ) <sub>2</sub> <sup>c</sup> | $\Delta g_{xx}$        | -17.4                                 | -8.8                               | -18.3      | <i>c</i>     |
| VO(L <sup>2</sup> ) <sub>2</sub> <sup>c</sup> | $\Delta g_{xx}$        | -20.2                                 | -10.3                              | -19.3      | <i>c</i>     |
| VO(L <sup>1</sup> ) <sub>2</sub> <sup>c</sup> | $\Delta g_{xx}$        | -19.1                                 | -9.7                               | -19.3      | <i>c</i>     |
| Mn(CN) <sub>5</sub> NO <sup>2-</sup>          | $\Delta g_{\parallel}$ | -1.2                                  | -1.9                               | -10.1      | <i>d</i>     |
| TiF <sub>3</sub>                              | $\Delta g_{\parallel}$ | -1.8                                  | -1.2                               | -11.1      | <i>b</i> (1) |
|   |                        |                                       |                                    | -11.1      | <i>b</i> (2) |
|   |                        |                                       |                                    | -3.7       | <i>b</i> (3) |
| Mn(CN) <sub>4</sub> N <sup>-</sup>            | $\Delta g_{\parallel}$ | 9.8                                   | 3.9                                | -3.3       | <i>e</i>     |
| Mn(CO) <sub>5</sub>                           | $\Delta g_{\parallel}$ | -1.2                                  | -0.9                               | -1.7       | <i>f</i> (1) |
|   |                        |                                       |                                    | -2.3       | <i>f</i> (2) |
| Fe(CO) <sub>5</sub> <sup>+</sup>              | $\Delta g_{\parallel}$ | -0.6                                  | -0.9                               | -1.5       | <i>g</i> (1) |
| ScO   | $\Delta g_{\perp}$     | -0.9                                  | 0.0                                | -1.4       | <i>g</i> (2) |
|   |                        |                                       |                                    | -0.5(3)    | <i>h</i> (1) |
| ScO   | $\Delta g_{\parallel}$ | -0.2                                  | -0.1                               | -2.8(5)    | <i>h</i> (2) |
|   |                        |                                       |                                    | -0.5(3)    | <i>h</i> (1) |
| MnO <sub>3</sub>                              | $\Delta g_{\parallel}$ | 6.3                                   | 4.3                                | -0.8(7)    | <i>h</i> (2) |
|   |                        |                                       |                                    | 1.3        | <i>i</i>     |
| Ni(CO) <sub>3</sub> H                         | $\Delta g_{\parallel}$ | 2.7                                   | 1.3                                | 1.9        | <i>j</i>     |
| Mn(CN) <sub>4</sub> N <sup>-</sup>            | $\Delta g_{\perp}$     | 4.7                                   | 2.1                                | 2.2        | <i>e</i>     |
| Co(CO) <sub>4</sub>                           | $\Delta g_{\parallel}$ | 7.1                                   | 3.3                                | 3.6        | <i>k</i> (1) |
|   |                        |                                       |                                    | 5.0        | <i>k</i> (2) |
| MnO <sub>3</sub>                              | $\Delta g_{\perp}$     | 4.2                                   | 1.9                                | 6.1        | <i>i</i>     |
| Mn(CN) <sub>5</sub> NO <sup>2-</sup>          | $\Delta g_{\perp}$     | 36.3                                  | 17.9                               | 28.8       | <i>d</i>     |
| Mn(CO) <sub>5</sub>                           | $\Delta g_{\perp}$     | 42.6                                  | 22.6                               | 40.7       | <i>f</i> (1) |
|   |                        |                                       |                                    | 35.7       | <i>f</i> (2) |
| Cu(acac) <sub>2</sub>                         | $\Delta g_{xx}$        | 50.1                                  | 30.6                               | 48.7       | <i>l</i> (1) |
|   |                        |                                       |                                    | 49.6       | <i>l</i> (2) |
| Cu(NO <sub>3</sub> ) <sub>2</sub>             | $\Delta g_{xx}$        | 45.1                                  | 28.2                               | 49.9(5)    | <i>m</i>     |
| Cu(NO <sub>3</sub> ) <sub>2</sub>             | $\Delta g_{yy}$        | 49.3                                  | 31.0                               | 49.9(5)    | <i>m</i>     |
| Cu(acac) <sub>2</sub>                         | $\Delta g_{yy}$        | 55.4                                  | 34.7                               | 48.7       | <i>l</i> (1) |
| Ni(CO) <sub>3</sub> H                         | $\Delta g_{\perp}$     | 65.0                                  | 39.8                               | 65.1       | <i>j</i>     |
| Fe(CO) <sub>5</sub> <sup>+</sup>              | $\Delta g_{\perp}$     | 89.3                                  | 48.7                               | 81.0, 77.4 | <i>g</i> (1) |
|   |                        |                                       |                                    | 78.8, 76.6 | <i>g</i> (2) |
| Co(CO) <sub>4</sub>                           | $\Delta g_{\perp}$     | 137.5                                 | 79.3                               | 127.6      | <i>k</i> (1) |
|   |                        |                                       |                                    | 126.0      | <i>k</i> (2) |
| Cu(NO <sub>3</sub> ) <sub>2</sub>             | $\Delta g_{zz}$        | 183.0                                 | 116.3                              | 246.6(3)   | <i>m</i>     |
| Cu(acac) <sub>2</sub>                         | $\Delta g_{zz}$        | 180.2                                 | 115.5                              | 285.2      | <i>l</i> (1) |
|   |                        |                                       |                                    | 263.8      | <i>l</i> (2) |

<sup>a</sup> UDFT-IGLO with AMFI approximation for  $\Delta g_{\text{SO/OZ}(2e)}$ , 9s7p4d metal basis, BIII on ligands (DZVD basis on remote atoms in VO(L<sup>n</sup>)<sub>2</sub>; BII on remote atoms in Cu(acac)<sub>2</sub>). <sup>b</sup> Reference 62: (1) Neon, site a; (2) Neon, site b; (3) Argon. Estimated error of  $\Delta g$ :  $\pm 0.2$  ppt. <sup>c</sup> The complexes are: VO(L<sup>1</sup>)<sub>2</sub> = [*N,N'*-ethylenebis(*o*-*tert*-butyl-*p*-methylsalicylaldiminato)]oxovanadium(IV); VO(L<sup>2</sup>)<sub>2</sub> = bis(*N*-methylsalicylaldiminato)oxovanadium(IV); VO(L<sup>3</sup>)<sub>2</sub> = bis(*N*-methyl-*o*-*tert*-butyl-*p*-methylsalicylaldiminato)oxovanadium(IV). Experimental data from ref 29. Estimated error of  $\Delta g$ :  $\pm 1$  ppt. EPR on polycrystalline substance. <sup>d</sup> Manoharan, T.; Gray, H. B. *Inorg. Chem.* **1966**, *5*, 823; single-crystal EPR in a host lattice of Na<sub>2</sub>Fe(CN)<sub>5</sub>NO $\cdot$ 2H<sub>2</sub>O. <sup>e</sup> Bendix, J.; Meyer, K.; Weyhermüller, T.; Bill, E.; Metzler-Nolte, N.; Wieghart, K. *Inorg. Chem.* **1998**, *37*, 1767; EPR in frozen CH<sub>3</sub>CN. <sup>f</sup> (1) Symons, M. C. R. *Organometallics* **1982**, *1*, 834; EPR in Ar matrix. Estimated error of  $\Delta g$ :  $\pm 10$  ppt. (2) EPR in C<sub>6</sub>D<sub>6</sub> matrix: Howard, J. A.; Morton, J. R.; Preston, K. F. *Chem. Phys. Lett.* **1982**, *83*, 1226. Estimated error of  $\Delta g$ :  $\pm 3$  ppt. <sup>g</sup> EPR in Cr(CO)<sub>6</sub> host crystal, Lionel, T.; Morton, J. R.; Preston, K. F. *J. Chem. Phys.* **1982**, *76*, 234. (1) site a, (2) site b. For the perpendicular components, experimental  $\Delta g_{xx}$ ,  $\Delta g_{yy}$  are given. <sup>h</sup> Knight, L. B.; Kaup, J. G.; Petzoldt, B.; Ayyad, R.; Ghanty, T. K.; Davidson, E. R. *J. Chem. Phys.* **1999**, *110*, 5658; (1) EPR in Ne matrix, (2) EPR in Ar matrix. <sup>i</sup> Ferrante, F.; Wilkerson, J. L.; Graham, W. R. M.; Weltner, W., Jr. *J. Chem. Phys.* **1977**, *67*, 5906. EPR in Ne matrix. Estimated error of  $g$ :  $\pm 0.8$  ppt. <sup>j</sup> Morton, J. R.; Preston, K. F. *J. Chem. Phys.* **1984**, *81*, 5775. EPR in Kr matrix. Estimated error of  $g$ :  $\pm 0.2$  ppt. <sup>k</sup> (1) EPR in solid Kr; Fairhurst, S. A.; Morton, J. R.; Preston, K. F. *J. Magn. Reson.* **1983**, *55*, 453; (2) EPR in CO matrix, Hanlan, L. A., Huber, H.; Kündig, E. P.; McGarvey, B. R.; Ozin, G. A. *J. Am. Chem. Soc.* **1975**, *97*, 7054. Estimated error of  $\Delta g$ :  $\pm 10$  ppt. <sup>l</sup> (1) Wilson, R.; Kivelson, D. *J. Chem. Phys.* **1966**, *44*, 4445. Radicals trapped in chloroform glass. (2) Maki, A. H.; McGarvey, B. R. *J. Chem. Phys.* **1958**, *29*, 31, 35. EPR in host crystal of Pd[(CH<sub>3</sub>CO)<sub>2</sub>CH]<sub>2</sub>. <sup>m</sup> Kasai, P. H.; Whipple, E. B.; Weltner, W., Jr. *J. Chem. Phys.* **1966**, *44*, 2581. EPR in Ne matrix.

on specific atoms or sets of atoms. The sums of these contributions do in all cases studied correspond closely to the overall  $\Delta g_{\text{SO/OZ}}$  results, as they should. The analysis for the phenoxyl radical shows, as expected in this case,<sup>54</sup> that SO coupling at the oxygen atom dominates the  $\Delta g_{22}$  and  $\Delta g_{33}$  components. The other atomic contributions are much smaller but not always negligible. Thus, for example, contributions from SO coupling at the ortho carbon atoms reduce  $\Delta g_{33}$  but enhance

$\Delta g_{22}$ . We may go one step further and decompose also individual molecular orbital contributions into their atomic SO constituents. Table 12 shows this as an example for the in-plane  $\pi$  b<sub>1</sub> HOMO. The coupling of the  $\beta$ -part of this MO (cf. Figure 3a) with the unoccupied  $\beta$ -part of the out-of-plane  $\pi$  b<sub>2</sub> SOMO (Figure 3b) is known<sup>54</sup> to dominate  $\Delta g_{33}$  (contributions from several occupied MOs with  $\sigma$ (C–O) bonding character dominate  $\Delta g_{22}$ ). This is confirmed by the entry in Table 12. The further

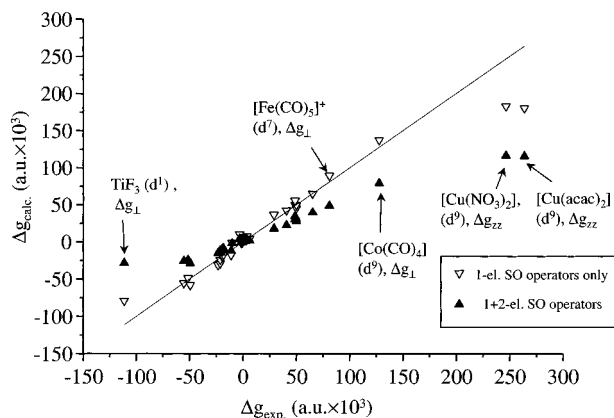


**Figure 2.** Comparison of calculated and experimental  $g$ -shift tensor components (ppt) for 3d transition metal complexes (cf. Table 10).

**Table 11.**  $g$ -Shift Tensor Results (ppt) for Some Square Pyramidal  $4d^1$  and  $5d^1$  Complexes

|                                  | ECP-SO <sup>a</sup> |                    | PZ <sup>b</sup> |                    | exp. <sup>c</sup> |                    |
|----------------------------------|---------------------|--------------------|-----------------|--------------------|-------------------|--------------------|
|                                  | $\Delta g_{  }$     | $\Delta g_{\perp}$ | $\Delta g_{  }$ | $\Delta g_{\perp}$ | $\Delta g_{  }$   | $\Delta g_{\perp}$ |
| MoOF <sub>4</sub> <sup>-</sup>   | -59                 | -51                | -62             | -57                | -107              | -76                |
| MoOCl <sub>4</sub> <sup>-</sup>  | +12                 | -38                | +6              | -43                | -37               | -55                |
| MoOBr <sub>4</sub> <sup>-</sup>  | +119                | -29                | +142            | -31                |                   |                    |
| MoNCl <sub>4</sub> <sup>2-</sup> | -35                 | -6                 | -47             | -9                 | -96               | -18                |
| WOCl <sub>4</sub> <sup>-</sup>   | -31                 | -120               | -68             | -139               |                   |                    |
| TcNF <sub>4</sub> <sup>-</sup>   | -43                 | -15                | -41             | -16                | -107              | -12                |
| TcNCl <sub>4</sub> <sup>-</sup>  | +47                 | +8                 | +43             | +6                 | +6                | -2                 |
| TcNBr <sub>4</sub> <sup>-</sup>  | +187                | +64                | +212            | +75                | +145              | +32                |
| ReOF <sub>4</sub>                | -123                | -156               | -132            | -177               |                   |                    |
| ReOCl <sub>4</sub>               | +106                | -117               | +80             | -141               | -28               | -294               |
| ReOBr <sub>4</sub>               | +253                | -84                | +257            | -117               | +168              | -237               |
| ReNF <sub>4</sub> <sup>-</sup>   | -189                | -57                | -187            | -70                | -353              |                    |
| ReNCl <sub>4</sub> <sup>-</sup>  | +46                 | -7                 | +9              | -17                | -88               | -57                |
| ReNBr <sub>4</sub> <sup>-</sup>  | +185                | +40                | +174            | +33                | +67               | -29                |

<sup>a</sup> This work, UDFT-IGLO, BP86. Quasirelativistic ECP/SO-ECP calculations. <sup>b</sup> UDFT-GIAO, BP86, ref. 28. <sup>c</sup> Experimental data as compiled in ref 28.

atomic decomposition of the HOMO contribution shows again clearly the dominance of oxygen SO coupling, but also the negative contributions from the ortho carbon atoms, which reduce the  $\Delta g_{33}$  component.

While the dominance of oxygen SO coupling has been obvious in the previous example, Table 13 shows two examples, CrOF<sub>4</sub><sup>-</sup> and CrOCl<sub>4</sub><sup>-</sup>, in which several atoms contribute nonnegligibly. We may first examine the atomic break-down of the total  $g$ -shift components. In both cases, SO coupling from the metal dominates the negative  $\Delta g_{\perp}$ . In contrast, halogen SO coupling contributes positively to  $\Delta g_{||}$ . While the negative metal contribution is larger and dominates in CrOF<sub>4</sub><sup>-</sup>, the halogen contribution in CrOCl<sub>4</sub><sup>-</sup> dominates, and a relatively small, positive  $\Delta g_{||}$  results (experimentally, this component is also small but negative, cf. Table 6).

MO analyses of the  $g$ -tensors for these types of  $C_{4v}$ -symmetrical  $d^1$  complexes have already been discussed in detail,<sup>28</sup> and we refer the reader to that work for the MO notation. In Table 13, we go a step further and decompose the most important MO contributions into their atomic constituents. The above-mentioned compensation between metal and halogen SO coupling for  $\Delta g_{||}$  arises in an interesting manner. Metal SO coupling contributes negatively via the SOMO but positively via the  $b_1$  MO, and in the case of CrOCl<sub>4</sub><sup>-</sup> also via the  $e$  MOs. Halogen SO coupling contributes positively through all three MOs. In contrast, metal SO coupling dominates  $\Delta g_{\perp}$  mainly via the negative SOMO contribution. These results are just

**Table 12.** Break-Down of  $g$ -Shift Tensor (ppm) for the Phenoxy Radical<sup>a</sup>

|   | $\Delta g_{11}$                     | $\Delta g_{22}$                           | $\Delta g_{33}$                            |
|---|-------------------------------------|---|--|
| $\Delta g_{GC(1e)}$                                     | 188                                 | 268                                       | 186  |
| $\Delta g_{RMC}$  | -198                                | -198                                      | -198                                       |
| $\Delta g_{SO/OZ(1e)}$                                  | -95                                 | 3574                                      | 13110                                      |
| $\Delta g_{SO/OZ(2e)}$                                  | 97                                  | -1410                                     | -4729                                      |
| (SSO <sup>b</sup> , SOO <sup>c</sup> )                  | (97 <sup>b</sup> , 0 <sup>c</sup> ) | (-1087 <sup>b</sup> , -323 <sup>c</sup> ) | (-3638 <sup>b</sup> , -1091 <sup>c</sup> ) |
| total   | -8                                  | 2234                                      | 8369                                       |
| break-down into atomic contributions <sup>d</sup>       |                                     |   |  |
| O   | 3                                   | 1734                                      | 8685                                       |
| C <sub>ipso</sub>                                       | 0                                   | 48  | -4   |
| C <sub>ortho</sub> (2x)                                 | 0                                   | 283                                       | -358                                       |
| C <sub>meta</sub> (2x)                                  | 4                                   | -42                                       | -92  |
| C <sub>para</sub>                                       | -3                                  | 141                                       | 150  |
| H (5x)  | 0                                   | 0   | 0  |
| $\Sigma$  | 2                                   | 2164                                      | 8381                                       |
| total $\Delta g_{SO/OZ}$                                | 2                                   | 2164                                      | 8381                                       |
| HOMO contribution                                       | 40                                  | -8  | 7748                                       |
| atomic break-down of the HOMO contribution <sup>d</sup> |                                     |   |  |
| O   | 41                                  | -1  | 8178                                       |
| C <sub>ipso</sub>                                       | 0                                   | -1  | 123  |
| C <sub>ortho</sub> (2x)                                 | 4                                   | -5  | -620                                       |
| C <sub>meta</sub> (2x)                                  | -5                                  | -5  | -24  |
| C <sub>para</sub>                                       | 0                                   | -1  | 94   |
| H (5x)  | 0                                   | -1  | 1  |
| $\Sigma$  | 40                                  | -14                                       | 7752                                       |

<sup>a</sup> UDFT-BP86 calculations with common gauge at center of mass, BIII basis, and AMFI approximation. <sup>b</sup> Spin-same-orbit contribution. <sup>c</sup> Spin-other-orbit contribution. <sup>d</sup> Atomic mean-field SO operators were employed only on the specified atoms in each case (see text).

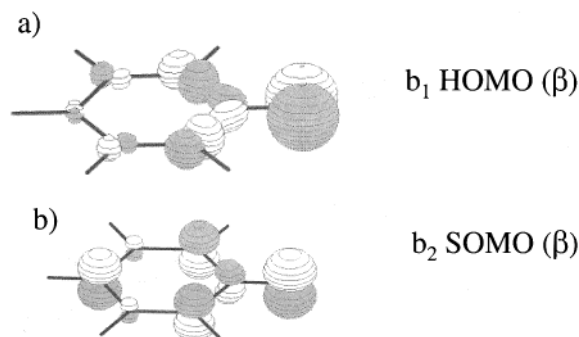


**Figure 3.** Display of Kohn-Sham orbitals for the phenoxy radical as isosurface ( $\pm 0.1$  au). (a)  $\beta$ -component of HOMO ( $b_1$ ). (b)  $\beta$ -component of SOMO ( $b_2$ ).

illustrative examples of the additional insight that is provided by the use of SO operators which are accurate and yet atomic in nature. Analyses of this type should become useful for a large variety of questions related to the interpretation of electronic  $g$ -tensors.

## 8. Conclusions

We have implemented and validated DFT calculations of the electronic  $g$ -tensor of EPR spectroscopy including all the relevant perturbation operators and IGLO gauge origins. The main advantage of the present approach lies in the treatment of spin-orbit coupling. To our knowledge, both the all-electron atomic mean-field approximation to the complete Breit-Pauli SO operators and the combination of quasirelativistic ECPs with SO-ECPs have been used here for the first time in  $g$ -tensor calculations. Both approximations provide an inexpensive but accurate way to include SO coupling. Agreement of the mean-field SO treatment with the full-blown explicit treatment of all

**Table 13.** Break-Down of  $g$ -Shift Tensor (ppt) for  $\text{CrOX}_4^-$  ( $X = \text{F}, \text{Cl}$ )<sup>a</sup>

|   | $\text{CrOF}_4^-$      |                    | $\text{CrOCl}_4^-$     |                    |
|---|------------------------|--------------------|------------------------|--------------------|
|   | $\Delta g_{\parallel}$ | $\Delta g_{\perp}$ | $\Delta g_{\parallel}$ | $\Delta g_{\perp}$ |
| break-down into atomic contributions <sup>b</sup>           |                        |                    |                        |                    |
| Cr  | -25                    | -21                | -11                    | -18                |
| X   | 10                     | 0                  | 30                     | 1                  |
| O   | 0                      | -1                 | 0                      | -1                 |
| $\Sigma$  | -15                    | -22                | 19                     | -18                |
| total $\Delta g_{\text{SO/OZ}}$                             | -15                    | -22                | 19                     | -18                |
| atomic break-down of dominant MO contributions <sup>c</sup> |                        |                    |                        |                    |
| SOMO ( $b_2$ , "d <sub>xy</sub> ")                          |                        |                    |                        |                    |
| Cr  | -34                    | -20                | -28                    | -16                |
| X   | 7                      | -1                 | 19                     | 0                  |
| O   | 0                      | 0                  | 0                      | 0                  |
| $\Sigma$  | -27                    | -21                | -9                     | -16                |
| $\sigma$ -MO ( $b_1$ )                                      |                        |                    |                        |                    |
| Cr  | 12                     | 0                  | 10                     | 1                  |
| X   | 5                      | 0                  | 5                      | 3                  |
| O   | 0                      | 0                  | 0                      | 0                  |
| $\Sigma$  | 17                     | 0                  | 15                     | 4                  |
| $\pi(\text{Cr-O})$ MOs ( $e$ )                              |                        |                    |                        |                    |
| Cr  | -3                     | 0                  | 6                      | -2                 |
| X   | 0                      | 0                  | 10                     | -2                 |
| O   | 0                      | 0                  | 0                      | 0                  |
| $\Sigma$  | -3                     | 0                  | 16                     | -4                 |

<sup>a</sup> UDFT-BP86 results with BII basis, AMFI approximation, and common gauge at the center of mass. Cf. Table 6 for the IGLO results (and for a decomposition into first- and second-order terms). <sup>b</sup> Atomic mean-field SO operators were employed only on the specified atoms in each case (see text). <sup>c</sup> Cf. ref 28 for a more detailed discussion of the MO contributions.

one- and two-electron SO integrals is essentially quantitative at a small fraction of the computational cost of the latter, as found previously in other applications of this approach. In turn, SO-ECPs approximate well the mean-field all-electron approach, with the additional advantage of a very efficient simultaneous inclusion of scalar relativistic effects. The pseudopotential approximation is particularly fruitful for a property like the  $g$ -tensor, which is to a large extent a property of the valence electrons. Due to the atomic nature of both all-electron mean-field operators and SO-ECPs, the two approaches may furthermore be combined in one calculation. In addition to a significant improvement in computational efficiency, this fact simplifies the analysis of  $g$ -tensors by allowing a separation into atomic SO contributions.

Having been able to include SO coupling accurately for larger systems, we could evaluate the performance of DFT approaches for the calculation of  $g$ -tensors without significant errors to be expected from approximate SO operators. We find that gradient-corrected exchange-correlation functionals perform very well for main-group species. This opens the way to quantitative calculations of  $g$ -tensors in a wide variety of applications, for example, for phenoxyl or semiquinone radicals or for other spin labels in biological systems. Larger discrepancies found for some compounds of heavier atoms (e.g., for the anions  $\text{CF}_3\text{X}^-$ , see Table 4) may partly be due to the neglect of environmental effects.

In contrast to the good performance for main-group species, the results obtained for transition metal complexes are much less satisfactory. We agree with Patchkowski and Ziegler<sup>28</sup> in attributing this less favorable performance for transition metal systems to deficiencies in the gradient-corrected functionals. The present results for a rather diverse set of 3d transition metal complexes indicate that the paramagnetic ( $\Delta g_{\text{SO/OZ}}$ ) contributions are underestimated systematically. A simple multiplicative scaling of these terms improves the overall agreement with experiment but is certainly not satisfactory from a theoretical point of view. We have also pointed out that similar problems have been observed by Bühl et al. for NMR chemical shifts of transition-metal nuclei.<sup>57,58</sup> In the latter case, the use of exchange-correlation functionals that include some exact, non-local exchange, enabled much more accurate calculations. We expect this to be the case also for  $g$ -tensor calculations on systems in which the spin density is mainly localized on a transition metal. We are thus presently implementing a code which will allow such hybrid functionals to be used also for the calculation of  $g$ -tensors.

A further potential source of errors stems from the first-order perturbation theoretical treatment of SO coupling. This may affect the results for systems with very heavy atoms. Therefore, our ongoing work involves also a two-component relativistic approach that covers SO coupling variationally. Despite the obvious need for further methodological improvements, the present approach should provide a very powerful tool to study electronic  $g$ -tensors in a large variety of areas ranging from materials research to biochemistry.

**Acknowledgment.** We thank Drs. H. Stoll (Stuttgart), H.-J. Flad (Leipzig), and P. Pyykkö (Helsinki) for helpful discussions. V.G.M. and O.L.M. gratefully acknowledge financial support from the Slovak Grant Agency VEGA (Grant No. 2/7203/00) and from the COST chemistry program (Project D9/0002/97), and they thank the Computing Center of the Slovak Academy of Sciences for computational resources. J.V. is on leave from the University of Oulu, Department of Physical Sciences, Oulu, Finland, and has been supported by the Marie Curie program (Contract No. ERBFMBICT982911) of the European Commission. Further support has been provided within the Graduiertenkolleg "Moderne Methoden der magnetischen Resonanz" in Stuttgart (scholarship to B.S. and travel costs), by Deutsche Forschungsgemeinschaft (Heisenberg scholarship to M.K. and Schwerpunktprogramm "Relativistische Effekte in der Chemie und Physik schwerer Elemente"), and by the Fonds der Chemischen Industrie.

**Supporting Information Available:** Tables S1–S5 give optimized Cartesian coordinates for the phenoxyl, 2,4,6-tris-*t*-Bu-C<sub>6</sub>H<sub>2</sub>O and tyrosyl radicals, as well as for Cu(acac)<sub>2</sub> and Cu(NO<sub>3</sub>)<sub>2</sub> (PDF). This material is available free of charge via the Internet at <http://pubs.acs.org>.

JA000984S



*...Why they are as they are, and not otherwise*

*Johannes Kepler (1571-1630)*

## **7 Mechanisms of EPR Hyperfine Coupling in Transition Metal Complexes**

### *Introduction*

The density-functional and coupled-cluster study of EPR hyperfine coupling in 21 transition metal complexes (Chapter 5) has not only validated the existing computational methods but also aroused the curiosity of the author to understand the underlying mechanisms of the hyperfine interactions. The problematic performance of DFT for some of the HFCCs has lead us to an analysis of orbital contributions to the hyperfine coupling. Both the striking order observed in the core-polarization contributions and the large variability in the valence-shell polarization became a motivation for a detailed study of mechanisms of EPR hyperfine coupling that is presented in the following paper.

The latter work concentrates on the qualitative aspects of hyperfine coupling in transition metal compounds and attempts to provide a detailed understanding of the different spin polarization mechanisms. The interpretations are based on the molecular DFT calculations of Chapter 5 but are augmented by detailed UHF and ROHF analyses of the relevant exchange, Coulomb, and one-electron integrals for some atomic systems. The author of this thesis performed all of the calculations included in the study, most of the interpretational work, and contributed significantly to the preparation of the manuscript.

### *Results*

The detailed analysis of the spin polarization in atomic systems has shown that the contributions from the metal 2s and 3s orbitals to  $A_{\text{iso}}$  and from the metal 2p and 3p orbitals to  $A_{\text{dip}}$  have opposite signs due to the orthogonality requirement between orbitals of the same angular momentum. While spin polarization enhances the exchange interaction of the 2s and 2p shells with the singly occupied orbitals, the 3s and 3p orbitals are forced to lose some of their exchange to stay orthogonal to their respective penultimate shell. The core-shell spin-polarization contributions to the isotropic hyperfine couplings have been found to be proportional to the spin population in the metal 3d orbitals and relatively independent of other details of the bonding. The valence-shell spin-polarization, however, depends strongly on the electronic structure of the system. Particularly large valence-shell spin-polarization contributions to both isotropic and dipolar coupling constants are found for systems in which the SOMO overlaps significantly with certain high-lying doubly occupied valence orbitals. These are the same cases in which our previous study found dramatic spin contamination effects to plague unrestricted Kohn-Sham calculations with hybrid functionals. In contrast to the assumptions implicit in many qualitative and quantitative schemes in current use by experimentalists, both core- and valence-shell spin polarization may significantly contribute to transition-metal dipolar coupling constants.

### *Conclusions and outlook*

The present work provides basic insight into the mechanisms of spin polarization in 3d transition metal systems. The results obtained may also be used to pinpoint the weaknesses of certain theoretical approaches for the calculation of HFCCs and hopefully also to develop improved methods. It is the wish of the author to extend the study undertaken in this paper to 4d and 5d systems, including a detailed analysis of valence-shell spin polarization, and of the mechanisms that transfer the spin density to the ligands. In the author's opinion, this study illustrates that the combination of the DFT approach and qualitative molecular-orbital thinking is a very powerful analytical tool that once again emphasises the great potential of one-electron approximations for understanding chemistry.

# Mechanisms of EPR Hyperfine Coupling in Transition Metal Complexes

Markéta L. Munzarová,<sup>†,‡</sup> Pavel Kubáček,<sup>†</sup> and Martin Kaupp<sup>\*,‡</sup>

Contribution from the Department of Theoretical and Physical Chemistry, Faculty of Science, Masaryk University, Kotlářská 2, CZ-61137 Brno, Czech Republic, and Institut für Anorganische Chemie, Universität Würzburg, Am Hubland, D-97074 Würzburg, Germany

Received June 9, 2000. Revised Manuscript Received August 25, 2000

**Abstract:** A detailed quantum chemical analysis of the underlying principles of hyperfine coupling in 3d transition metal complexes has been carried out. The explicit evaluation of one- and two-electron integrals for some atomic systems has been used to understand the spin polarization of the core shells. While spin polarization enhances the exchange interaction of the 2s and 2p shells with the singly occupied orbitals, the opposite spin polarization of the 3s and 3p shells arises from the required orthogonality to the 2s and 2p shells, respectively. Core-shell spin polarization in molecules is found to be proportional to the spin population in the valence 3d orbitals but to depend little on other details of bonding. In contrast, the spin polarization of the valence shell depends crucially on the overlap between the singly occupied and certain doubly occupied valence orbitals. Large overlap leads to pronounced spin polarization of these orbitals and, among other things, likely to spin contamination when using UHF wave functions or hybrid density functionals. The role of core- and valence-shell spin polarization for dipolar hyperfine couplings in transition metal complexes is discussed. It is demonstrated that great care should be exercised in deriving spin populations or even orbital compositions from dipolar couplings alone.

## 1. Introduction

The early history of EPR spectroscopy is closely connected to the study of transition metal complexes.<sup>1–8</sup> Already during the 1950s, the concept of spin polarization was used in the discussion of the hyperfine coupling constants (HFCCs) to transition metal nuclei (cf. section 2). Transition metal systems have thus been adequately represented in early, qualitative theoretical studies of EPR hyperfine couplings. In contrast, modern applications of quantum chemical methods to calculate hyperfine couplings more quantitatively have largely concentrated on organic radicals,<sup>9,10</sup> due to the various practical difficulties presented by the more complicated transition metal systems.<sup>11</sup>

We recently reported a systematic study,<sup>11</sup> in which various density functional theory (DFT) and coupled cluster approaches were critically compared in calculations of hyperfine coupling

tensors for a representative set of 21 3d transition metal complexes. Complexes with significant metal 4s orbital contributions to the singly occupied molecular orbital(s) (SOMO) may be treated adequately with essentially any of the state-of-the-art density functionals. In contrast, it is much more difficult to reproduce experimentally derived HFC tensors in systems in which the spin density at the metal arises largely from spin polarization. Gradient-corrected functionals tend to underestimate the important spin polarization of the 2s and 3s core orbitals. While admixture of exact exchange in “hybrid functionals” helps to enhance the core-shell spin polarization in some cases, the related spin contamination may deteriorate significantly the quality of the results in other systems. Overall, no functional was found to perform satisfactorily for all systems, and for some systems, none of the functionals studied was acceptable.<sup>11</sup> The general quantitative study of HFC tensors for transition metal systems remains thus a challenge to quantum chemistry.

A better understanding of the detailed relation between electronic structure and hyperfine couplings should aid in looking for improved approaches for their calculation. Apart from the validation of existing methods, the detailed study of 21 complexes<sup>11</sup> has provided us with considerable qualitative insight into the mechanisms of spin polarization in transition metal systems. As expected, the underlying interactions can be much more variable than those in organic radicals. For example, not only s-type but also p- and d-type metal orbitals may be

\* Corresponding author: (e-mail) kaupp@mail.uni-wuerzburg.de.

<sup>†</sup> Masaryk University.

<sup>‡</sup> Universität Würzburg.

(1) Abragam, A.; Bleaney, B. *Electron Paramagnetic Resonance of Transition Ions*; Clarendon Press: Oxford, 1970.

(2) Symons, M. C. R. *Chemical and Biochemical Aspects of Electron-Spin Resonance Spectroscopy*; Van Nostrand: New York, 1978.

(3) Atherton, N. M. *Principles of Electron Spin Resonance*; Prentice Hall: New York, 1993.

(4) Weil, J. A.; Bolton, J. R.; Wertz, J. E.; *Electron Paramagnetic Resonance: Elementary Theory and Practical Applications*; Wiley & Sons: New York, 1994.

(5) Carrington, A.; McLachlan, A. D. *Introduction to Magnetic Resonance with Applications to Chemistry and Chemical Physics*; Harper & Row: London, 1969.

(6) Weltner, W., Jr. *Magnetic Atoms and Molecules*; Van Nostrand: New York, 1983.

(7) McGarvey, B. R. In *Transition Metal Chemistry: A Series of Advances*; Carlin, R. L., Ed.; New York, 1966; Vol. 3, pp 89–201.

(8) Mabbs, F. E.; Collison, D. *Electron Paramagnetic Resonance of d-Transition Metal Compounds*; Elsevier: Amsterdam, 1992.

(9) Engels, B.; Eriksson, L.; Lunell, S. *Adv. Quantum Chem.* **1996**, 27, 297.

(10) Malkin, V. G.; Malkina, O. L.; Eriksson, L. A.; Salahub, D. R. In *Modern Density Functional Theory: A Tool for Chemistry*; Theoretical and Computational Chemistry Vol. 2; Politzer, P., Seminario, J. M., Eds.; Elsevier: Amsterdam, The Netherlands, 1995; pp 273–347.

(11) Munzarová M.; Kaupp, M. *J. Phys. Chem. A* **1999**, 103, 9966.

involved, and both core and valence shells of the transition metal may be polarized significantly. The present work concentrates on these more qualitative aspects of hyperfine coupling in transition metal compounds and attempts to provide a detailed understanding of the different spin polarization mechanisms. Our interpretations are based on the molecular DFT calculations of ref 11 but will be augmented by detailed UHF and ROHF analyses of the relevant exchange, Coulomb, and one-electron integrals for some atomic systems. The geometrical and electronic structures of the molecular complexes studied, as well as the relevant available experimental data, have already been discussed.<sup>11</sup> Therefore, with the exception of few systems that will be discussed in more detail, the reader is referred to ref 11 for further information.

## 2. The Spin Polarization Model: Previous Work

The general theoretical background of EPR hyperfine coupling is documented in many textbooks.<sup>1-8</sup> The isotropic hyperfine coupling is directly proportional to the spin density at the point of the corresponding nucleus ( $\rho_N^{\alpha-\beta}$ , in the following abbreviated as  $\rho_N$ ). In traditional interpretations,  $\rho_N$  is frequently approximated by the density of the singly occupied orbital(s). However, for the majority of systems studied by EPR spectroscopy, this simple approach is not sufficient. The unpaired electron, by virtue of its different interactions with electrons of different spin, spin-polarizes the electron distribution in the closed shells. This process can add significant spin density at the position of the nuclei. The inadequacy of the spin-restricted theory of the hyperfine interaction has been noted since 1933 for various main-group atoms.<sup>12,13</sup> In the 1950s, the spin polarization model turned out to be very important for the early qualitative interpretation of EPR spectra for the transition metal ions. In many of these, the unpaired electrons occupy metal d-type orbitals. Although these orbitals have a node at the nucleus, substantial isotropic hyperfine splittings from metal nuclei were observed. Abragam et al.<sup>14</sup> suggested that the isotropic hyperfine splitting in  $Mn^{2+}$  resulted from the spin polarization of the outermost occupied core shell (3s in the case of 3d metal ions).

Later, Watson and Freeman<sup>15</sup> showed by UHF calculations for several 3d ions that the polarized 2s shell contributes even more to the hyperfine coupling than the outermost 3s shell, but with the opposite (negative) sign.<sup>16</sup> Polarization of the 1s orbital provided also a negative, albeit very small, spin density at the nucleus. It was concluded that in the 1s and 2s shells, which exhibit radial density maximums at much smaller radii than the 3d orbital (cf. Figure 1), the  $\alpha$ -spin electrons are "attracted" outward, leaving a region of negative spin density near the nucleus<sup>17</sup> (similar arguments have been used to describe the core polarization in 4d metal complexes<sup>18</sup>). The usual argument given is that exchange reduces the electron repulsion between  $2s^\alpha$  and the  $3d^\alpha$  SOMO and thus allows these electrons

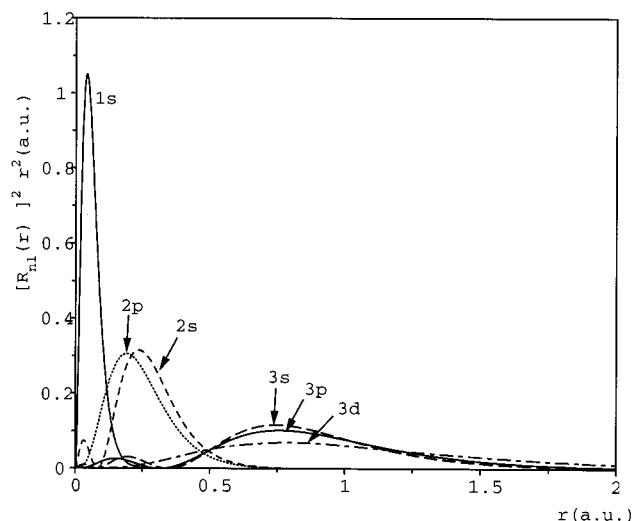


Figure 1. ROHF radial distribution functions  $[R_{nl}(r)]^2 r^2$  for  $Mn^{2+}$ .

to get closer. This would correspond to an "effective attraction" of like-spin electrons. However, what happens with the 3s orbital? All of its radial maximums are also located closer to the nucleus than the 3d radial maximum (cf. Figure 1). Nevertheless, the 3s shell is polarized in the direction opposite from the 1s and 2s orbitals, as if the  $3s^\alpha$  orbital were "repelled"<sup>1</sup> from the 3d-type SOMO. Watson and Freeman interpreted this as a result of the large overlap between 3s and 3d shells, leading to "competing tendencies" in the spin polarization.<sup>15</sup> We will show below that the requirement of orthogonality between 2s and 3s shells is responsible for these seemingly paradoxical observations.

In main-group chemistry, spin polarization dominates the hyperfine couplings for some 2p atoms and ions, for some small  $\pi$ -radicals (e.g., NO,  $CO^+$ ,  $H_2O^+$ ), and for the larger class of organic planar  $\pi$ -radicals. In these cases, the spin polarization of the 1s and 2s orbitals is known to transfer spin density to the nuclei. Just as for transition metal ions, spin polarization of the valence orbitals contributes with a positive sign to  $\rho_N$ , spin polarization of the core (1s) orbitals with a negative sign.<sup>19,20</sup> Unlike for transition metals, the positive outer-shell contributions dominate, providing an overall positive  $\rho_N$ .<sup>21</sup> The traditional interpretation of these observations is analogous to the model of Watson and Freeman. The  $\alpha$ -component of the 1s orbital is attracted outward, leaving negative spin density at the nucleus. The  $2s^\alpha$  orbital, which has its outermost maximum at slightly larger radius than 2p (Figure 2), is attracted inward and thus provides more  $\alpha$ -spin density at the nucleus. This "exchange attraction" of electrons with the same spin is often viewed as a manifestation of Hund's rule of maximum multiplicity.<sup>24</sup>

In the past, the concept of spin polarization has been used exclusively to rationalize isotropic hyperfine couplings. However, recent theoretical work shows that dipolar hyperfine coupling in transition metal systems may also be influenced significantly by spin polarization.<sup>11,22</sup> In 3d complexes, large contributions to the metal dipolar coupling may come from the

(12) Fermi, E.; Segrè, E. *Rend. Accad. Nazl. Lincei* **1933**, *4*, 18; *Z. Phys.* **1933**, *82*, 729.

(13) Sternheimer, R. M. *Phys. Rev.* **1952**, *86*, 316.

(14) Abragam, A.; Horowitz, M.; Pryce, M. H. L. *Proc. R. Soc. A* **1955**, *230*, 169.

(15) Watson, R. E.; Freeman, A. J. *Phys. Rev.* **1961**, *123*, 2027.

(16) Negative contributions to  $\rho_N$  of metal 2s orbitals and positive contributions of metal 3s orbitals have been reported also: (a) Case, D. A.; Karplus, M. *J. Am. Chem. Soc.* **1977**, *99*, 6182. (b) Weber, J.; Gourso, A.; Pénigault, E.; Ammeter, J. H.; Bachmann, J. *J. Am. Chem. Soc.* **1982**, *104*, 1491.

(17) Freeman, A. J.; Watson, R. E. In *Magnetism*; Rado, G. T., Suhl, H., Eds.; Academic Press: New York, 1965; Vol. IIA, p 167.

(18) Watson, R. E.; Freeman, A. J. In *Hyperfine Interactions*, Freeman, A. J., Frankel, R. B., Eds.; Academic Press: New York, 1967; p 53.

(19) See, for example: (a) Karplus, M.; Fraenkel, G. K. *J. Chem. Phys.* **1961**, *35*, 1312. (b) Chang, S. Y.; Davidson, E. R.; Vincow, G. *J. Chem. Phys.* **1970**, *52*, 1741. (c) Chipman, D. M. *J. Chem. Phys.* **1983**, *78*, 3112. (d) Ishii, N.; Shimizu, T. *Phys. Rev. A* **1993**, *48*, 1691. (e) Engels, B.; Peyerimhoff, S. D. *Mol. Phys.* **1989**, *67*, 583.

(20) Chipman, D. M. *Theor. Chim. Acta* **1992**, *82*, 93.

(21) In contrast, the spin density at the hydrogen nuclei in planar  $\pi$  radicals is negative.<sup>24</sup>

(22) Belanzoni, P.; Baerends, E. J.; van Asselt, S.; Langewen, P. B. *J. Phys. Chem.* **1995**, *99*, 13094.

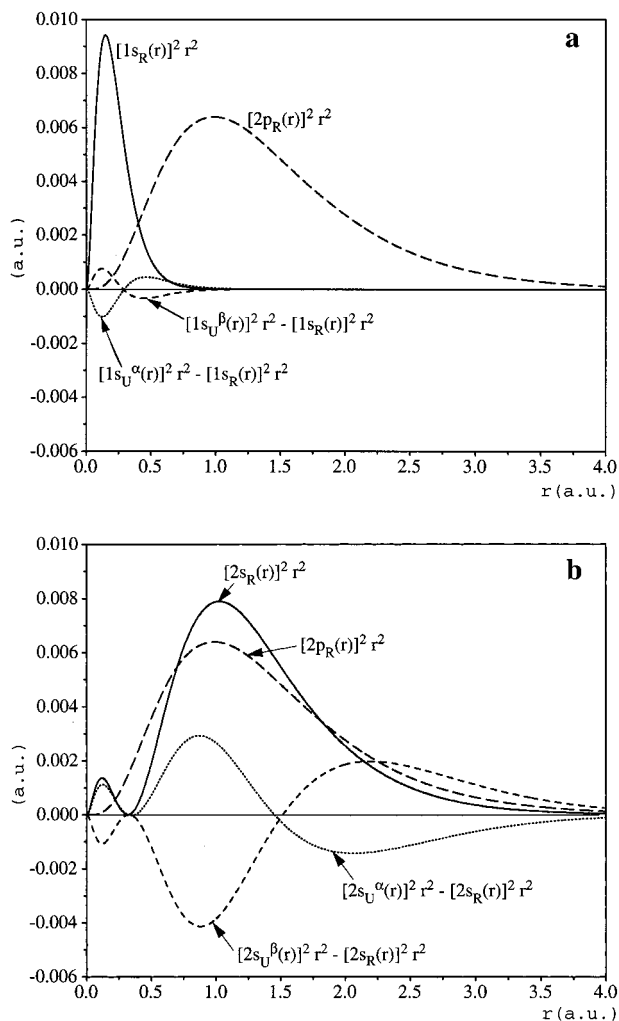


**Figure 2.** ROHF radial distribution functions  $[R_n(r)]^2 r^2$ , and differences between UHF and ROHF radial distributions in  ${}^4\text{N}$ . (a) 1s (ROHF radial distribution scaled by  $1/30$ ). (b) 2s (ROHF radial distribution scaled by  $1/8$ ). For comparison, the ROHF radial distribution function of the 2p SOMOs (scaled by  $1/8$ ) is also plotted (cf. discussion in section 5).

spin-polarized 2p and 3p orbitals. This viewpoint will be strengthened and extended to valence-shell contributions by the present work. Note that, for magnetic nuclei in an electronic environment of axial symmetry (i.e., those located on an at least 3-fold symmetry axis), as is the case for all transition metal nuclei studied here, the dipolar coupling tensor may be brought to the form  $(-A_{\text{dip}}, -A_{\text{dip}}, 2A_{\text{dip}})$ , where  $A_{\text{dip}}$  is the so-called dipolar hyperfine coupling constant.

### 3. Computational and Methodological Details

**Calculations and MO Analyses of HFCCs.** In the following discussion, we will neglect (spin-orbit or scalar) relativistic corrections to the HFCCs (which have been estimated in ref 11). The selection of experimental data for most of the systems used here, and the conversion between different representations of HFCCs, have been summarized in our previous work.<sup>11</sup> The computed and experimental molecular structures used are also those described in ref 11. We will concentrate on all-electron unrestricted Kohn-Sham calculations, mainly on results obtained with the gradient-corrected BP86<sup>23</sup> functional. This “pure” generalized gradient approximation has the advantage that spin

contamination is typically very small.<sup>11</sup> Calculations and analyses of isotropic hyperfine coupling constants (at the Hartree-Fock and DFT level) were done with the Gaussian94 program.<sup>24</sup> Applying the CUBE program option, the values of the individual orbitals at the transition metal nuclei have been determined and they were used for the analysis of the contributions to  $\rho_N$ . DFT calculations of the dipolar hyperfine coupling constants have additionally been carried out with a modified version of the deMon-EPR code,<sup>10,25</sup> where a routine for the analysis of the orbital contributions to  $A_{\text{dip}}$  has been implemented.

The medium-sized (15s11p6d)/[9s7p4d] metal basis sets constructed in ref 11 (based on the work of Schäfer et al.<sup>26</sup>) were used together with basis sets BIII of Kutzelnigg et al. (also known as IGLO-III<sup>27</sup>) for main-group atoms. In the Gaussian94 DFT calculations, the default integration grids (int = finegrid option<sup>24</sup>) of the program have been used. In deMon calculations, additional auxiliary basis sets (5,5;5,5) for the metal and (5,2;5,2) for the ligand have been used to fit the density and the exchange-correlation potential (in this case, an extra iteration without fit of the potential and with extended grid was carried out after SCF convergence). For the numerical integration in deMon, we have employed a nonrandom FINE angular grid with 128 radial shells.<sup>10,28</sup>

**Hartree-Fock Analysis of One- and Two-Electron Integrals.** The total energy corresponding to a Hartree-Fock wave function may be written as<sup>29</sup>

$$E_0 = \sum_i^{N^\alpha} h_{ii}^\alpha + \sum_i^{N^\beta} h_{ii}^\beta + \frac{1}{2} \sum_i^{N^\alpha} \sum_j^{N^\alpha} (J_{ij}^{\alpha\alpha} - K_{ij}^{\alpha\alpha}) + \frac{1}{2} \sum_i^{N^\beta} \sum_j^{N^\beta} (J_{ij}^{\beta\beta} - K_{ij}^{\beta\beta}) + \sum_i^{N^\alpha} \sum_j^{N^\beta} J_{ij}^{\alpha\beta} \quad (1)$$

with  $\alpha$  and  $\beta$  denoting spin.

The one-electron term

$$h_{ii} = \int d\mathbf{r}_1 \psi_i^*(\mathbf{r}_1) \left( -\frac{1}{2} \nabla_1^2 - \sum_A \frac{Z_A}{r_{1A}} \right) \psi_i(\mathbf{r}_1) \quad (2)$$

represents the average kinetic and nuclear-attraction energy of an electron described by the orbital  $\psi_i(\mathbf{r}_1)$ ; the two-electron Coulomb integral

$$J_{ij} = \langle ij|ij \rangle = \int d\mathbf{r}_1 d\mathbf{r}_2 |\psi_i(\mathbf{r}_1)|^2 r_{12}^{-1} |\psi_j(\mathbf{r}_2)|^2 \quad (3)$$

expresses the classical Coulomb repulsion between the charge

(24) Frisch, M. J.; Trucks, G. W.; Schlegel, H. B.; Gill, P. M. W.; Johnson, B. G.; Robb, M. A.; Cheeseman, J. R.; Keith, T.; Petersson, G. A.; Montgomery, J. A.; Raghavachari, K.; Al-Laham, M. A.; Zakrzewski, V. G.; Ortiz, J. V.; Foresman, J. B.; Peng, C. Y.; Ayala, P. Y.; Chen, W.; Wong, M. W.; Andres, J. L.; Replogle, E. S.; Gomperts, R.; Martin, R. L.; Fox, D. J.; Binkley, J. S.; Defrees, D. J.; Baker, J.; Stewart, J. P.; Head-Gordon, M.; Gonzalez, C.; Pople, J. A. *Gaussian 94* (revision E.2); Gaussian, Inc.: Pittsburgh, PA, 1995.

(25) a) Salahub, D. R.; Fournier, R.; Mlynarski, P.; Papai, I.; St-Amant, A.; Ushio, J. In *Density Functional Methods in Chemistry*; Labanowski, J., Andzelm, J., Eds.; Springer: New York, 1991. (b) St-Amant, A.; Salahub, D. R. *Chem. Phys. Lett.* **1990**, *169*, 387.

(26) Schäfer, A.; Horn, H.; Ahlrichs, R. *J. Chem. Phys.* **1992**, *97*, 2571.

(27) Kutzelnigg, W.; Fleischer, U.; Schindler, M. In *NMR—Basic Principles and Progress*; Vol. 23, Springer-Verlag: Heidelberg, 1990; Vol. 23, p 165.

(28) Daul, C. A.; Goursot, A.; Salahub, D. R. In *NATO ARW Proceedings on Grid Methods in Atomic and Molecular Quantum Calculation*; Vol. C412, Cerjan, C., Ed.; Kluwer: Dordrecht, 1993; Vol. C412.

(29) Szabo, A.; Ostlund, Neil S. *Modern Quantum Chemistry*; Dover: New York, 1996.

(23) Perdew, J. P.; Wang, Y. *Phys. Rev. B* **1986**, *33*, 8822. Perdew, J. P.; Wang, Y. *Phys. Rev. B* **1986**, *34*, 7406.

**Table 1.** Spin Densities at the Metal Nuclei (au) for a Series of Manganese Complexes<sup>a</sup>

| molecule  | contributions <sup>b</sup> |       |      |       |      |       | total                      | exp <sup>c</sup> | 3s/2s |
|---|----------------------------|-------|------|-------|------|-------|----------------------------|------------------|-------|
|   | core                       |       |      | VS    | SOMO |       |                            |                  |       |
|   | 1s                         | 2s    | 3s   |       |      |       |                            |                  |       |
| <sup>2</sup> [Mn(CO) <sub>5</sub> ]                 | 0.00                       | -0.18 | 0.09 | 0.04  | 0.06 | 0.00  | 0.00...0.01                | -0.50            |       |
| <sup>2</sup> MnO <sub>3</sub>                       | 0.01                       | -0.33 | 0.18 | -0.58 | 2.54 | 1.82  | 1.46                       | -0.55            |       |
| <sup>2</sup> [Mn(CN) <sub>4</sub> N] <sup>-</sup>   | 0.00                       | -0.39 | 0.20 | 0.04  | 0.00 | -0.15 | -0.25                      | -0.51            |       |
| <sup>2</sup> [Mn(CN) <sub>5</sub> NO] <sup>2-</sup> | -0.01                      | -0.50 | 0.24 | 0.13  | 0.00 | -0.13 | -0.20                      | -0.48            |       |
| <sup>6</sup> MnO                                    | 0.01                       | -1.40 | 0.64 | -0.43 | 3.56 | 2.39  | 2.17                       | -0.46            |       |
| <sup>6</sup> [Mn(CN) <sub>4</sub> ] <sup>2-</sup>   | -0.03                      | -1.60 | 0.71 | 0.46  | 0.00 | -0.45 | -0.60                      | -0.44            |       |
| <sup>6</sup> MnF <sub>2</sub>                       | 0.00                       | -1.62 | 0.72 | -0.22 | 2.45 | 1.33  | 0.47...0.61                | -0.44            |       |
| <sup>7</sup> MnH                                    | 0.01                       | -1.69 | 0.72 | -0.84 | 3.86 | 2.07  | 1.52                       | -0.43            |       |
| <sup>7</sup> MnF                                    | 0.01                       | -1.70 | 0.74 | -0.12 | 3.68 | 2.61  | 2.40                       | -0.44            |       |
| <sup>6</sup> Mn                                     | -0.01                      | -1.78 | 0.78 | 0.93  | 0.00 | -0.07 | -0.35 <sup>d</sup>         | -0.44            |       |
| <sup>7</sup> Mn <sup>+</sup>                        | 0.04                       | -1.79 | 0.76 | 0.00  | 5.30 | 4.31  | 4.12                       | -0.43            |       |
| <sup>6</sup> Mn <sup>2+</sup>                       | -0.01                      | -1.85 | 0.79 | 0.00  | 0.00 | -1.07 | -0.76...-1.24 <sup>e</sup> | -0.43            |       |

<sup>a</sup> DFT results with the BP86 functional. <sup>b</sup> Contributions from the core-shell spin polarization (1s,2s,3s), valence-shell spin polarization (VS), and singly occupied orbital(s) (SOMO). <sup>c</sup> From ref 11, unless stated otherwise. <sup>d</sup> Kasai, P. H. *Acc. Chem. Res.* **1971**, *4*, 329. Ar-matrix isolation. <sup>e</sup> Values obtained in different host crystals; see ref 1.

**Table 2.** Spin Densities at the Metal Nuclei (au) for a Series of First-Row Transition Metal Complexes<sup>a</sup>

| molecule   | contributions <sup>b</sup> |       |      |       |      |       | total                      | exp <sup>c</sup> | 3s/2s |
|--|----------------------------|-------|------|-------|------|-------|----------------------------|------------------|-------|
|  | core                       |       |      | VS    | SOMO |       |                            |                  |       |
|  | 1s                         | 2s    | 3s   |       |      |       |                            |                  |       |
| <sup>3</sup> TiO                                 | 0.03                       | -0.24 | 0.02 | -0.12 | 2.31 | 1.99  | 1.91                       | -0.08            |       |
| <sup>2</sup> TiF <sub>3</sub>                    | 0.01                       | -0.17 | 0.03 | -0.09 | 1.07 | 0.86  | 0.70...0.73                | -0.18            |       |
| <sup>3</sup> VN                                  | 0.03                       | -0.34 | 0.07 | -0.27 | 2.87 | 2.37  | 2.23                       | -0.21            |       |
| <sup>4</sup> VO                                  | 0.02                       | -0.58 | 0.17 | -0.25 | 2.74 | 2.09  | 1.98                       | -0.29            |       |
| <sup>6</sup> Cr <sup>+</sup>                     | 0.00                       | -1.38 | 0.42 | 0.00  | 0.00 | -0.97 |                            | -0.30            |       |
| <sup>6</sup> [Cr(CO) <sub>4</sub> ] <sup>+</sup> | -0.01                      | -1.20 | 0.39 | 0.35  | 0.00 | -0.47 | -0.82                      | -0.33            |       |
| <sup>6</sup> Fe <sup>3+</sup>                    | -0.03                      | -2.30 | 1.19 | 0.00  | 0.00 | -1.14 | -0.81...-1.05 <sup>d</sup> | -0.52            |       |
| <sup>2</sup> [Fe(CO) <sub>5</sub> ] <sup>+</sup> | -0.01                      | -0.33 | 0.19 | 0.05  | 0.10 | 0.00  | -0.02                      | -0.58            |       |
| <sup>2</sup> [Co(CO) <sub>4</sub> ]              | 0.00                       | -0.38 | 0.23 | 0.05  | 0.10 | 0.00  | -0.05                      | -0.61            |       |
| <sup>2</sup> [Ni(CO) <sub>3</sub> H]             | -0.02                      | -0.18 | 0.12 | 0.00  | 0.01 | -0.06 | -0.02                      | -0.67            |       |

<sup>a</sup> DFT results with the BP86 functional. <sup>b</sup> Contributions from the core-shell spin polarization (1s,2s,3s), valence-shell spin polarization (VS), and singly occupied orbital(s) (SOMO). <sup>c</sup> From ref 11, unless stated otherwise. <sup>d</sup> Values obtained in different host crystals; see ref 1.

clouds  $|\psi_i(\mathbf{r}_1)|^2$  and  $|\psi_j(\mathbf{r}_2)|^2$ ; the two-electron exchange integral

$$K_{ij} = \langle ij|ji \rangle = \int d\mathbf{r}_1 d\mathbf{r}_2 \psi_i^*(\mathbf{r}_1)\psi_j(\mathbf{r}_1)r_{12}^{-1}\psi_j^*(\mathbf{r}_2)\psi_i(\mathbf{r}_2) \quad (4)$$

represents the exchange correlation of the two electrons ( $\mathbf{r}_i$  denotes the coordinates of electron  $i$ ).<sup>30</sup>

At the unrestricted Hartree–Fock (UHF) level of theory, the spatial parts of the  $\psi_i^\alpha$  and  $\psi_j^\beta$  orbitals are allowed to differ, while at the restricted-open-shell Hartree–Fock (ROHF) level they are required to be identical for every  $i \leq N^\beta$ . In the following, we will discuss also the overlap integral

$$S_{ij} = \langle ij| \rangle = \int d\mathbf{r} \psi_i^*(\mathbf{r})\psi_j(\mathbf{r}) \quad (5)$$

UHF and ROHF wave functions have been compared in terms of energies and spin density distributions for a number of spherical 3d<sup>5</sup> cations (Cr<sup>+</sup>, Mn<sup>2+</sup>, Fe<sup>3+</sup>), and for the nitrogen atom, using the Gaussian94 code, and basis sets as described above. Using the CUBE option, the radial wave functions have been extracted. Applying standard methods of two-electron integral calculations for atomic systems,<sup>31</sup> the values of Coulomb and exchange integrals, nuclear attraction integrals, and overlap between radial wave functions (cf. below) have been determined. For the numerical calculation of the Slater–Condon parameters, a radial grid of 10<sup>-3</sup> au has been employed over a radius of 10 au from the nucleus. Summation over all electrons and pairs of electrons gives the total nuclear attraction energy and electron repulsion energy (cf. eq 1). The total kinetic energy has been extracted from the Gaussian94 output.

Below we refer to the sum of all Coulomb integrals from eq 1 as the total Coulomb energy ( $E_C$ ) and to the sum of all exchange integrals from eq 1 as the total (negative) exchange energy ( $E_X$ ). Note that the summations in eq 1 are not restricted to pairs of different spin–orbitals. Therefore, the (unphysical) electrostatic interaction of an electron with itself is accounted for in the Coulomb part and again subtracted in the exchange part (ref 32 p 180). This allows a unique orbital breakdown of the total electron repulsion energy into exchange and Coulomb parts.<sup>33</sup> The Coulomb part may be interpreted as a classical electrostatic energy of a charge cloud of density  $\rho(r)$ , whereas the exchange part includes all nonclassical effects, (ref 32, pp 34 and 39).

#### 4. Analysis of Contributions to $\rho_N$

Table 1 gives a breakdown of the DFT results for the spin density at the metal nucleus into MO contributions in a series of manganese complexes (and in three atomic systems). Table

(30) In this work, the notation for one- and two-electron integrals pertains to integration over the spatial parts of the corresponding spin–orbitals only.

(31) Weissbluth, M. *Atoms and Molecules*; Academic Press: New York, 1980.

(32) Parr, R. G.; Yang, W. *Density-functional theory of atoms and molecules*; Oxford University Press: New York, 1989.

(33) When self-interaction is not accounted for, the decomposition of electron repulsion energy into Coulomb and exchange parts may be arbitrary. For example, for a p shell fully occupied with six electrons, both the total Coulomb and the total exchange energy depend on the orbital basis (angular momentum eigenfunctions or real functions). The reason is that  $\langle p_x p_y | p_x p_y \rangle = \langle p_x p_z | p_x p_z \rangle = \langle p_y p_z | p_y p_z \rangle = \langle p_x p_0 | p_x p_0 \rangle = \langle p_y p_0 | p_y p_0 \rangle \neq \langle p_x p_1 | p_x p_1 \rangle$ . An analogous relation holds for the corresponding exchange integrals.

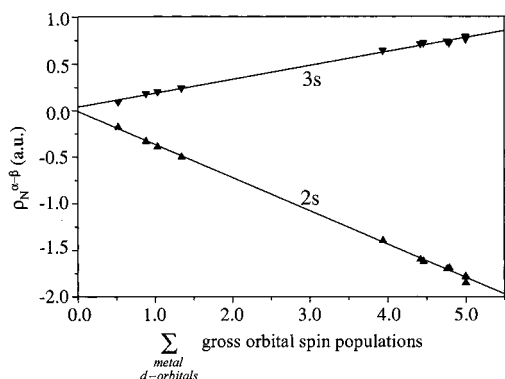


**Figure 3.** Correlation between Mulliken gross d-orbital spin populations and core-shell spin polarization for a series of manganese complexes. BP86 results.

2 provides the same analysis for other 3d complexes. In addition to the 1s, 2s, and 3s core contributions (i.e., contributions from MOs with predominantly metal core character), we summarize under “valence” contributions arising from the spin polarization of the doubly occupied valence MOs. The direct contribution(s) from the SOMO(s) is(are) also given (for cases such as MnH or MnF<sub>2</sub>, where more than one SOMO possesses s-character, their contributions have been summed up). Spin densities derived from experimental hyperfine coupling constants<sup>11</sup> are included for comparison.

While contributions from valence-shell spin polarization vary in both their signs and magnitudes, the core contributions depend much less on the detailed bonding situation (compare, e.g., [Mn(CN)<sub>4</sub>]<sup>2-</sup> and MnF<sub>2</sub>).<sup>34</sup> The negative 2s contributions dominate, whereas the 3s contributions are smaller and positive. The 1s contributions are very small. Both 2s and 3s contributions increase with increasing spin multiplicity of the system. However, the ratio between 2s and 3s (3s/2s ratio in Tables 1 and 2) remains close to  $-0.5$  for all Mn complexes (Table 1). A more detailed analysis indicates that both the 2s and 3s contributions exhibit a remarkable proportionality to the total 3d spin population (Figure 3). Neither the specific bonding situation nor the spin population of the metal 4s orbitals influence the 2s and 3s contributions appreciably. For example, we may compare the 2s and 3s contributions to  $\rho_N$  for the <sup>6</sup>Mn atom ( $-1.78$  and  $0.78$  au), the <sup>7</sup>Mn<sup>+</sup> cation ( $-1.79$  and  $0.76$  au), and the <sup>6</sup>Mn<sup>2+</sup> cation ( $-1.85$  and  $0.79$  au).

Interestingly, the 3s/2s ratio is influenced more by nuclear charge than by anything else (Tables 1 and 2). It becomes more negative when moving toward the right end of the 3d series. This is seen best when comparing the isoelectronic high-spin d<sup>5</sup> ions <sup>6</sup>Cr<sup>+</sup>, <sup>6</sup>Mn<sup>2+</sup>, and <sup>6</sup>Fe<sup>3+</sup>, for which the 3s/2s ratio is computed to be  $-0.30$ ,  $-0.43$ , and  $-0.52$ , respectively. Intuitively, it is not clear whether this is just a consequence of a change in the relative magnitudes of the (spin-averaged) 3s and 2s orbitals at the nucleus or of an increasing spin polarization of the 3s orbital with increasing nuclear charge. As will be shown below, the latter interpretation is to be preferred. In the following, the spatial parts of the spin-orbitals  $\psi_{2s}^{\alpha}(\mathbf{r})\alpha(\sigma)$ ,  $\psi_{2s}^{\beta}(\mathbf{r})\beta(\sigma)$ ,  $\psi_{3s}^{\alpha}(\mathbf{r})\alpha(\sigma)$ , and  $\psi_{3s}^{\beta}(\mathbf{r})\beta(\sigma)$  will be abbreviated as  $2s^{\alpha}(r)$ ,  $2s^{\beta}(r)$ ,  $3s^{\alpha}(r)$ , and  $3s^{\beta}(r)$ , respectively (subscripts U and R will indicate unrestricted or restricted orbitals). For s-type orbitals, the angular part of the wave function is constant and equal to 1. Therefore, we will in the

(34) The low sensitivity of spin polarization contributions to  $\rho_N$  in organic radicals on the particular bonding situation has been discussed. The proportionality between the 1s and 2s contributions for CH<sub>3</sub> over a wide range of conditions (out-of-plane bending) has also been reported.

following refer to the radial wave functions only (hence, the scalar argument  $r$  is used, rather than the vector  $\mathbf{r}$ ). A given pair of spin-polarized orbitals  $2s_U^{\alpha}$  and  $2s_U^{\beta}$  contributes to  $\rho_N$  like  $(2s_U^{\alpha}(0))^2 - (2s_U^{\beta}(0))^2$ . The function  $(2s_U^{\alpha}(r))^2 - (2s_U^{\beta}(r))^2$  may be divided into two parts corresponding to (i) the polarization of the  $2s^{\alpha}$  orbital and (ii) the polarization of the  $2s^{\beta}$  orbital, relative to the corresponding orbitals in the restricted (Hartree–Fock or Kohn–Sham) calculation. We may thus expand the function as

$$(2s_U^{\alpha}(r))^2 - (2s_U^{\beta}(r))^2 = [(2s_U^{\alpha}(r))^2 - (2s_R(r))^2] + [(2s_R(r))^2 - (2s_U^{\beta}(r))^2] = [2s_U^{\alpha}(r) + 2s_R(r)][2s_U^{\alpha}(r) - 2s_R(r)] + [2s_R(r) + 2s_U^{\beta}(r)][2s_R(r) - 2s_U^{\beta}(r)] \quad (6)$$

If we denote  $[2s_U^{\alpha}(r) - 2s_R(r)]$  as  $\Delta 2s^{\alpha}$  and  $[2s_U^{\beta}(r) - 2s_R(r)]$  as  $\Delta 2s^{\beta}$ , eq 6 may be rewritten as

$$(2s_U^{\alpha}(r))^2 - (2s_U^{\beta}(r))^2 = [2(2s_R(r)) + \Delta 2s^{\alpha}(r)]\Delta 2s^{\alpha}(r) - [2(2s_R(r)) + \Delta 2s^{\beta}(r)]\Delta 2s^{\beta}(r) = 2(2s_R(r))(\Delta 2s^{\alpha}(r) - \Delta 2s^{\beta}(r)) + (\Delta 2s^{\alpha}(r))^2 - (\Delta 2s^{\beta}(r))^2 \quad (7)$$

Both  $\Delta 2s^{\alpha}(r)$  and  $\Delta 2s^{\beta}(r)$  are much smaller than  $2s_R(r)$ . The quadratic terms  $(\Delta 2s^{\alpha}(r))^2$ ,  $(\Delta 2s^{\beta}(r))^2$  may therefore be neglected. Furthermore, to a large extent  $(\Delta 2s^{\alpha}(r))^2$  is compensated by  $-(\Delta 2s^{\beta}(r))^2$  (cf. section 5). The left side of eq 7 may thus be approximated as

$$(2s_U^{\alpha}(r))^2 - (2s_U^{\beta}(r))^2 \approx 2(2s_R(r))(\Delta 2s^{\alpha}(r) - \Delta 2s^{\beta}(r)) \quad (8)$$

Analogously we obtain for the contribution from the 3s orbitals

$$(3s_U^{\alpha}(r))^2 - (3s_U^{\beta}(r))^2 \approx 2(3s_R(r))(\Delta 3s^{\alpha}(r) - \Delta 3s^{\beta}(r)) \quad (9)$$

The ratio between the 3s and 2s orbital contributions is thus to a good approximation

$$\frac{(3s_U^{\alpha}(r))^2 - (3s_U^{\beta}(r))^2}{(2s_U^{\alpha}(r))^2 - (2s_U^{\beta}(r))^2} \approx \frac{3s_R(r) \Delta 3s^{\alpha}(r) - \Delta 3s^{\beta}(r)}{2s_R(r) \Delta 2s^{\alpha}(r) - \Delta 2s^{\beta}(r)} \quad (10)$$

Each of the orbital contributions to  $\rho_N^{\alpha-\beta}(r)$  is therefore roughly proportional to the difference between the restricted and unrestricted orbitals, but also to the absolute value of the restricted orbital. As a consequence, the much larger value of the 2s orbital at the nucleus results in the larger 2s orbital contribution to  $\rho_N^{\alpha-\beta}(0)$ , although  $\Delta 3s^{\alpha}(0) - \Delta 3s^{\beta}(0) > \Delta 2s^{\alpha}(0) - \Delta 2s^{\beta}(0)$ . The ratio  $3s_R(0)/2s_R(0)$  changes only slightly throughout the 3d series: for Cr<sup>+</sup>, Mn<sup>2+</sup>, and Fe<sup>3+</sup>, we obtain the ratios  $-0.373$ ,  $-0.377$ , and  $-0.383$ , respectively (BP86 results). In contrast,  $\Delta 3s^{\alpha}(0) - \Delta 3s^{\beta}(0)/\Delta 2s^{\alpha}(0) - \Delta 2s^{\beta}(0)$  changes from  $-0.821$  for Cr<sup>+</sup> through  $-1.138$  for Mn<sup>2+</sup>, to  $-1.348$  for Fe<sup>3+</sup> (extracted from ROB86 and UBP86 results). An interpretation of this trend is given in section 5.

While the valence-shell spin polarization contributions to  $\rho_N$  appear to be irregular at first sight, we find a relation between their sign and the character of the SOMO: The valence contribution to  $\rho_N$  is positive only when there is no metal 4s admixture into the SOMO (e.g., in <sup>6</sup>Mn<sup>0</sup>, <sup>6</sup>[Mn(CN)<sub>4</sub>]<sup>2-</sup>, <sup>6</sup>[Cr(CO)<sub>4</sub>]<sup>+</sup>) or when the admixture is very small (<sup>2</sup>[Mn(CO)<sub>5</sub>], <sup>2</sup>[Fe(CO)<sub>5</sub>]<sup>+</sup>).<sup>35</sup> In the presence of significant metal 4s contribu-

(35) For main-group systems with 2p-type SOMOs, that for symmetry reasons may not mix with the bonding MOs, valence-shell spin polarization always contributes positively to  $\rho_N$  (at the given main-group center).<sup>19</sup>

**Table 3.** Spin Densities at the Metal Nuclei (au) for a Series of Atomic Systems with Five Singly Occupied 3d Orbitals<sup>a</sup>

| atom/ion                      | contribution <sup>b</sup> |       |      |      |      |       | exp <sup>c</sup> | 3s/2s |
|-------------------------------|---------------------------|-------|------|------|------|-------|------------------|-------|
|                               | core                      |       |      |      |      | total |                  |       |
|                               | 1s                        | 2s    | 3s   | VS   | SOMO |       |                  |       |
| <sup>6</sup> Cr <sup>+</sup>  | -0.04                     | -2.11 | 0.51 | 0.00 | 0.00 | -1.64 |                  | -0.24 |
| <sup>6</sup> Mn               | -0.04                     | -2.71 | 1.31 | 1.08 | 0.00 | -0.36 | -0.33            | -0.48 |
| <sup>6</sup> Mn <sup>2+</sup> | -0.08                     | -2.82 | 1.34 | 0.00 | 0.00 | -1.57 | -1.24...         | -0.76 |
| <sup>6</sup> Fe <sup>3+</sup> | -0.12                     | -3.56 | 2.21 | 0.00 | 0.00 | -1.48 | -0.81...         | -1.05 |

<sup>a</sup> UHF results. <sup>b</sup> Contributions from the core-shell spin polarization (1s,2s,3s), valence-shell spin polarization (VS), and singly occupied orbital(s) (SOMO). <sup>c</sup>Cf. Tables 1 and 2 for references.

tions to the SOMO (and thus of large direct, positive SOMO contributions to  $\rho_N$ ), the spin polarization of the valence shell always contributes negatively to  $\rho_N$  (cf. MnH, MnO, MnO<sub>3</sub>, and TiF<sub>3</sub> in Tables 1 and 2).

The signs of the individual MO contributions in Tables 1 and 2 remain the same with the other gradient-corrected and hybrid functionals compared in ref 11, or even at the UHF level. From a quantitative point of view, the contributions change only relatively little for different correlation functionals tested but change significantly upon inclusion of Hartree–Fock exchange into the exchange functional. This is easily understandable, as UHF calculations overestimate spin polarization considerably and thus lead to much larger negative core-shell contributions to  $\rho_N$ . In contrast, gradient-corrected functionals tend to underestimate the core-shell spin polarization.<sup>11</sup> Admixture of (the right amount of) Hartree–Fock exchange frequently brings the results into better agreement with experiment. Negative contributions from valence-shell spin polarization are also often overestimated at the UHF level. In all cases studied, the UHF spin densities at the metal are lower than the DFT results (due to the core-shell contributions) and too low compared to experiment (cf. ref 11).

As an example, UHF results for a series of atomic high-spin d<sup>5</sup> systems are shown in Table 3. All qualitative aspects (sign and relative magnitude of the orbital contributions) are the same for UHF as for DFT (BP86, cf. Tables 1 and 2). We note that the increase in the 3s/2s ratio along the 3d series (cf. discussion above) is also present, albeit somewhat overestimated, at the UHF level. Referring to eq 10,  $3s_R(0)/2s_R(0)$  changes from -0.362 for Cr<sup>+</sup> through -0.367 for Mn<sup>2+</sup> to -0.373 for Fe<sup>3+</sup>, and  $\Delta 3s^\alpha(0) - \Delta 3s^\beta(0) / \Delta 2s^\alpha(0) - \Delta 2s^\beta(0)$  changes from -0.667 for Cr<sup>+</sup>, through -1.290 for Mn<sup>2+</sup>, to -1.348 for Fe<sup>3+</sup> (ROHF and UHF results, respectively). The qualitative similarity of the DFT and HF results justifies our use, in the following section 5, of HF wave functions in the detailed analysis of spin polarization in atoms. We note that spin contamination is negligible for the high-spin atomic systems studied, even with UHF wave functions.

## 5. Analysis of Spin Polarization in Atomic Systems

We will start our discussion with a comparison of spin-restricted and spin-polarized orbitals for Mn<sup>2+</sup>. In its <sup>6</sup>Mn<sup>2+</sup> ground state, the cation has five unpaired electrons, all of them occupying metal 3d orbitals. The maximum of the 3d radial distribution is located at only slightly larger radius than the outermost maximums of the doubly occupied 3s and 3p semicore orbitals (Figure 1). The 2s and 2p orbitals are much more contracted and well separated from the M shell.

**Spin Polarization of 2s vs 3s and 2p vs 3p Core Shells.** Panels a–d of Figure 4 show radial distributions of the 2s, 2p, 3s, and 3p ROHF orbitals of <sup>6</sup>Mn<sup>2+</sup>, respectively, as well as

the associated differences between the UHF and ROHF distributions. The area confined between  $[\psi_U(r)]^2 r^2 - [\psi_R(r)]^2 r^2$  and the x axis may be interpreted as a measure of spin-density redistribution within a given spin–orbital, due to spin polarization. We find that (a) in areas where the spin polarization increases the magnitude of the  $\alpha$  spin–orbital, the magnitude of the corresponding  $\beta$  spin–orbital is decreased and vice versa; (b) close to the nucleus (within  $\sim 0.3$  au), the spin density of the 2s <sup>$\alpha$</sup>  orbital decreases whereas that of the 3s <sup>$\alpha$</sup>  orbital increases (see Figure 4a,c). The same holds for the relation between the 2s <sup>$\beta$</sup>  and 3s <sup>$\beta$</sup>  curves. Furthermore, the 2p <sup>$\alpha$</sup>  and 3p <sup>$\alpha$</sup>  curves, as well as the 2p <sup>$\beta$</sup>  and 3p <sup>$\beta$</sup>  curves, exhibit the same kind of complementarity in the core region (cf. Figure 4b,d). This suggests that the relation between the 2s and 3s contributions to  $\rho_N$ , in particular their opposite sign (as well as the relation between 2p and 3p contributions to the dipolar coupling, cf. section 7), is due to the orthogonality required between the orbitals of the M and L shells.

To gain deeper insight into this relation, we examine in Table 4 the influence of spin polarization on the values of two-electron integrals between the SOMO(s) and the (spin-polarized) doubly occupied orbitals. We discuss first the exchange integrals. Each of them has been calculated (a) for both electrons occupying ROHF orbitals, (b) for the unpaired electron in a ROHF orbital and the “paired” electron in a UHF orbital, and (c) for both electrons in spin-relaxed (unrestricted) orbitals. This allows us to compare the energy gain/loss due to the spin polarization of the doubly occupied orbital and the effect of the relaxation (contraction) of the SOMO. The spin polarization of the 2s and 2p orbitals increases their exchange interaction with the SOMO, and the SOMO relaxation enhances this interaction further, so that the exchange stabilization may be understood as a driving force of 2s and 2p spin polarization. Exchange stabilization correlates with an increase in the overlap of the radial wave functions (Table 4, Figure 4a,b). In the following, we will refer to this type of overlap integral as *radial overlap*, as opposed to the more common overlap integral defined in eq 5. The exchange of the 3s or 3p orbitals with the 3d SOMO is decreased by core-shell spin polarization and is accompanied by a decrease in the radial overlap (Table 4). Relaxation of the SOMO recovers only part of the radial overlap and of the exchange interaction. Obviously, the redistribution of spin density does not enhance the exchange interaction with the SOMO for all orbitals.

This may be not too surprising, as not only exchange with the SOMO but also Coulomb repulsion with the SOMO, exchange and Coulomb repulsion with the other electrons, and electron–nuclear attraction and kinetic energy change upon going from the ROHF to the UHF wave function. Indeed, the absolute value of the exchange energy is roughly 1 order of magnitude smaller than these other terms. Note, also, that changes in the exchange and Coulomb interactions for the  $\alpha$  spin–orbital are partly compensated by the corresponding, complementary changes in the  $\beta$  component (Table 4). Spin polarizations of individual orbitals are obviously not independent processes.

What is the driving force for the spin polarization of the 3s (and 3p) orbitals? To understand this we have to be aware that the optimized orbitals for an atom have to be orthogonal. This may be realized (a) by the spin parts, (b) by the angular parts, or (c) by the radial parts of the wave functions. For two s-type  $\alpha$  spin–orbitals, condition c applies; i.e., the radial functions have to be orthogonal, both for the ROHF and UHF wave functions. In other words, the area between the function  $f =$



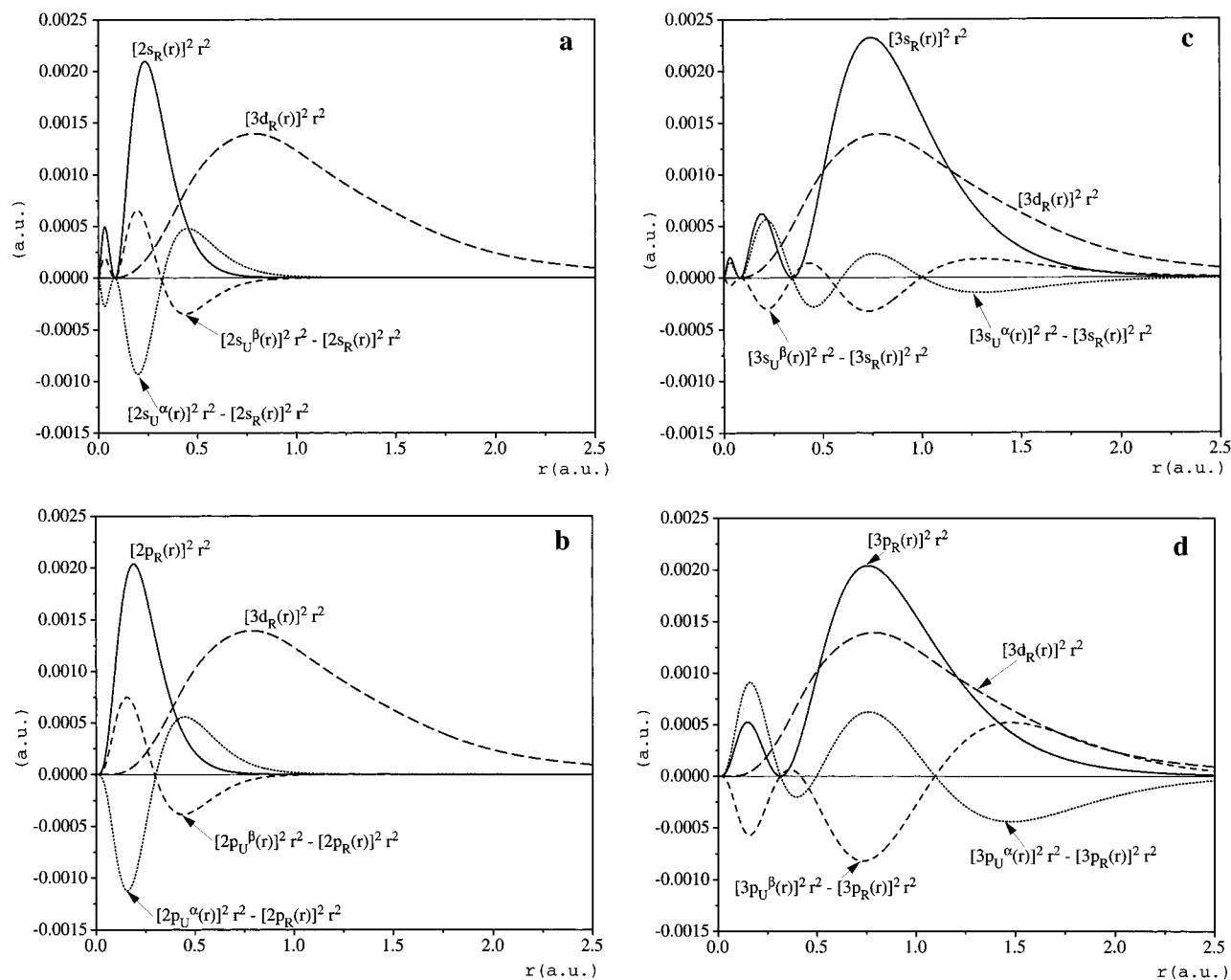


**Figure 4.** ROHF radial distribution functions  $[R_n(r)]^2 r^2$  (scaled by  $1/150$ ), and difference between UHF and ROHF radial distributions for Mn<sup>2+</sup>. (a) 2s, (b) 2p, (c) 3s, (d) 3p. For comparison, the ROHF radial distribution function of the singly occupied 3d orbitals (scaled by  $1/50$ ) is also shown. See text also.

$2s(r)3s(r) r^2$  and the  $x$  axis in regions where  $f$  is positive to be equal to the area in regions where  $f$  is negative. This is demonstrated in Figure 5 for the spin-restricted case. If we now, for example, allow the  $2s^\alpha$  orbital to be polarized (decontracted to larger  $r$ , cf. Figure 4a), the negative area under  $f$  decreases, whereas the positive area increases. The orthonormality between  $2s^\alpha$  and  $3s^\alpha$  has been lost. To recover it, the polarization of the  $3s^\alpha$  orbital must again enhance the negative area and reduce the positive area; i.e., it has to contract. Changes of the  $2s^\beta$  and  $3s^\beta$  spin-orbitals behave analogously, with opposite directions. The same conditions apply to the  $2p^\alpha/3p^\alpha$  and  $2p^\beta/3p^\beta$  pairs; i.e., their radial functions must also remain orthogonal. Thus, orthogonality requires complementary polarizations of the L and M shells. This orthogonality does not hold strictly for molecular systems. However, as the nature of the core orbitals does not change much in molecules, we expect that the same mechanisms apply (see further below).

From this we conclude that the 2s orbital is spin-polarized to enhance the exchange interaction with the SOMO. The 3s orbital has to stay orthogonal on 2s, even if this means a reduced exchange interaction with the SOMO. Why does the spin polarization of the 2s orbital dominate? The reason is that the energy gain in the exchange interaction between the 2s and the 3d SOMO is much larger than the energy loss due to the exchange interaction between the 3s and the 3d SOMO (Table 4). If we were to optimize the exchange between 3s and the

SOMO, the reduced exchange interaction between 2s and the SOMO would overcompensate the gain. This is best illustrated in Figure 4.  $2s^\alpha$  is well separated from 3d and clearly enhances its interaction with the SOMO upon radial expansion (Figure 4a). In contrast, spin polarization of  $3s^\alpha$  is much less effective, as areas with increased and reduced overlap will partly compensate each other (Figure 4c). The same arguments may be applied to the spin polarization of the 2p and 3p orbitals (Figure 4b,d). The polarization of  $2s^\alpha$ ,  $3s^\alpha$ , and  $3d^\alpha$  orbitals is of course not an isolated process but is accompanied by the polarization of all other orbitals of either spin. Besides the exchange interaction, Coulomb repulsion and electron-nucleus attraction also come into play. This will be discussed in more detail below.

The requirement of orthogonality between the 3s and 2s orbitals helps us also to understand better the dependence of their contributions to  $\rho_N$  on nuclear charge. From the orthogonality of  $2s_U^\alpha(r)$  and  $3s_U^\alpha(r)$  follows:

$$\langle 2s_U^\alpha(r) | 3s_U^\alpha(r) \rangle = \langle 2s_R(r) | 2s_R(r) \rangle + \langle 2s_R(r) | \Delta 3s^\alpha(r) \rangle + \langle \Delta 2s^\alpha(r) | 3s_R(r) \rangle + \langle \Delta 2s^\alpha(r) | \Delta 3s^\alpha(r) \rangle = 0 \quad (11)$$

The first term in the middle of (11) vanishes, since the ROHF 2s and 3s orbitals are also orthogonal. The fourth term is negligible with respect to the second and third terms, since  $\Delta 2s^\alpha(r)$

**Table 4.** Exchange, Coulomb, and Radial Overlap Integrals between the SOMO and the Doubly Occupied Orbitals for  ${}^6\text{Mn}^{2+}$  (au)<sup>a</sup>

| exchange integrals   | 1s          | 2s          | $\Sigma 2p$ | 3s         | $\Sigma 3p$ |
|--|-------------|-------------|-------------|------------|-------------|
| $\langle \psi_R 3d_R   3d_R \psi_R \rangle$  | 0.000 278   | 0.026 949   | 0.079 875   | 0.081 590  | 0.298 482   |
| $\langle \psi_U^\alpha 3d_R   3d_R \psi_U^\alpha \rangle$  | 0.000 278   | 0.027 109   | 0.080 715   | 0.081 478  | 0.298 100   |
| $\langle \psi_U^\alpha 3d_U^\alpha   3d_U^\alpha \psi_U^\alpha \rangle$  | 0.000 278   | 0.027 172   | 0.080 900   | 0.081 553  | 0.298 340   |
| $\langle \psi_U^\alpha 3d_U^\alpha   3d_U^\alpha \psi_U^\alpha \rangle - \langle \psi_R 3d_R   3d_R \psi_R \rangle$                              | 0.000 000   | 0.000 223   | 0.001 025   | -0.000 037 | -0.000 142  |
| $5 \sum_\psi - [\langle \psi_U^\alpha 3d_U^\alpha   3d_U^\alpha \psi_U^\alpha \rangle] - \langle \psi_R 3d_R   3d_R \psi_R \rangle = -0.005 345$ |             |             |             |            |             |
| Coulomb integrals  | 1s          | 2s          | $\Sigma 2p$ | 3s         | $\Sigma 3p$ |
| $\langle \psi_R 3d_R   \psi_R 3d_R \rangle$  | 1.181 876   | 1.163 092   | 3.503 115   | 0.926 861  | 2.714 807   |
| $\langle \psi_U^\alpha 3d_R   \psi_U^\alpha 3d_R \rangle$  | 1.181 876   | 1.162 929   | 3.502 484   | 0.927 437  | 2.720 802   |
| $\langle \psi_U^\alpha 3d_U^\alpha   \psi_U^\alpha 3d_U^\alpha \rangle$  | 1.182 956   | 1.163 962   | 3.505 616   | 0.927 996  | 2.722 392   |
| $\langle \psi_U^\beta 3d_U^\alpha   \psi_U^\beta 3d_U^\alpha \rangle$  | 1.182 956   | 1.164 224   | 3.506 621   | 0.926 797  | 2.709 494   |
| radial overlap integrals   | 1s          | 2s          | 2p          | 3s         | 3p          |
| $\langle \psi_R   3d_R \rangle^b$  | 0.001 854   | 0.028 223   | 0.025 459   | 0.069 239  | 0.072 500   |
| $\langle \psi_U^\alpha   3d_R \rangle^b$   | 0.001 855   | 0.028 413   | 0.025 748   | 0.069 099  | 0.072 259   |
| $\langle \psi_U^\alpha   3d_U^\alpha \rangle^b$  | 0.001 857   | 0.028 444   | 0.025 776   | 0.069 116  | 0.072 272   |
| nuclear attraction integrals   | 1s          | 2s          | 2p          | 3s         | 3p          |
| $\langle \psi_R   Z/r   \psi_R \rangle$  | 612.889 503 | 131.448 180 | 129.454 856 | 40.539 902 | 37.291 698  |
| $\langle \psi_U^\alpha   Z/r   \psi_U^\alpha \rangle$  | 612.885 311 | 131.191 339 | 129.169 607 | 40.713 359 | 37.617 042  |
| $\langle \psi_U^\beta   Z/r   \psi_U^\beta \rangle$  | 612.892 007 | 131.627 837 | 129.643 564 | 40.433 853 | 37.032 423  |
| $3d$   |             |             |             |            |             |
| $\langle \psi_R   Z/r   \psi_R \rangle$  | 29.548 909  |             |             |            |             |
| $\langle \psi_U^\alpha   Z/r   \psi_U^\alpha \rangle$  | 29.575 906  |             |             |            |             |

<sup>a</sup> Comparison of ROHF and UHF data. All radial wave functions have been normalized to  $1/(4\pi) = 0.079 577 4$ ; see ref 30. <sup>b</sup>  $\langle \psi | \varphi \rangle = \int \psi(r) \varphi(r) r^2 dr$ , where  $\psi(r)$  and  $\varphi(r)$  are radial parts of the orbitals  $\psi(\mathbf{r}, \sigma)$  and  $\varphi(\mathbf{r}, \sigma)$ , respectively.

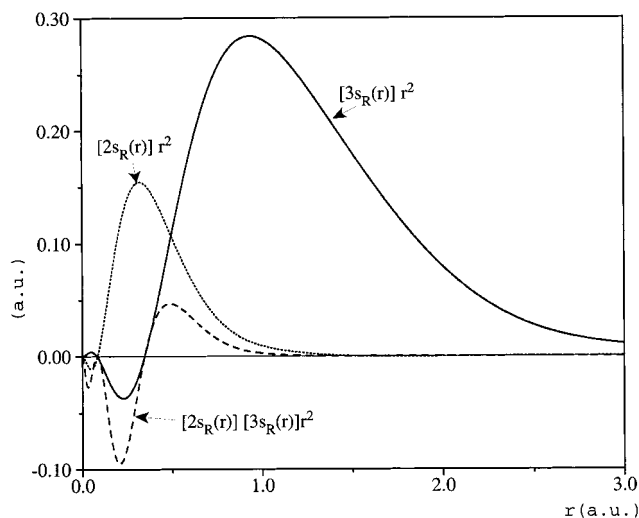


**Figure 5.** Orthogonality of 2s and 3s orbitals in  $\text{Mn}^{2+}$  (ROHF result). The function  $f = 2s(r)3s(r)r^2$  integrates to zero. For comparison, the functions  $2s(r)r^2$  and  $3s(r)r^2$  are also shown. For 2s, the phase convention differs from that used elsewhere.<sup>36</sup>

$\ll 2s_R(r)$  and  $\Delta 3s^\alpha(r) \ll 3s_R(r)$ . Hence,

$$\langle 2s_R(r) | \Delta 3s^\alpha(r) \rangle + \langle \Delta 2s^\alpha(r) | 3s_R(r) \rangle \approx 0 \quad (12)$$

Analogously, it may be shown that

$$\langle 2s_R(r) | \Delta 3s^\beta(r) \rangle + \langle \Delta 2s^\beta(r) | 3s_R(r) \rangle \approx 0 \quad (13)$$

Figure 6 illustrates eq 12 for  $\text{Mn}^{2+}$ . The function  $\Delta 3s^\alpha(r)2s_R(r)r^2$  is positive at most  $r$  values, as  $2s_R(r)$  and  $\Delta 3s^\alpha$

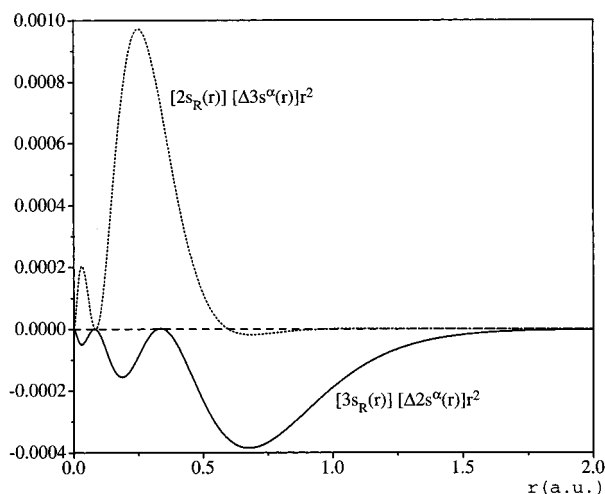


**Figure 6.** Consequences of the orthogonality between 2s and 3s orbitals in  $\text{Mn}^{2+}$ . The function  $\Delta 2s^\alpha(r)3s_R(r)r^2 + \Delta 3s^\alpha(r)2s_R(r)r^2$  integrates to zero; see text.

have equal sign where they overlap significantly. The function  $\Delta 2s^\alpha(r)r^2$  is negative everywhere, as regions of negative  $\Delta 2s^\alpha(r)$  always match those of positive  $3s_R(r)$ , and vice versa.<sup>36</sup> The total area under  $\Delta 2s^\alpha(r)3s_R(r)r^2$  and under  $\Delta 3s^\alpha(r)2s_R(r)r^2$  is calculated to be +0.000 238 and -0.000 238, respectively. The approximation in deriving eq 12 from eq 11 appears thus to be well-justified. The spin polarization contributions

(36) Molecular or atomic orbitals are unique except for a phase factor. Unless noted otherwise, in this work all s-type orbitals are defined as to be positive at the nucleus. The choice of phase does not alter the physical mechanism.

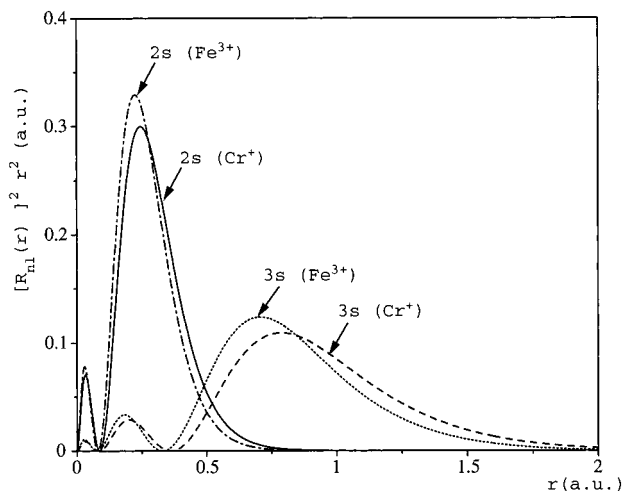


**Figure 7.** Effect of nuclear charge on the 2s and 3s orbitals. Comparison of  $[2s(r)]^2 r^2$  and  $[3s(r)]^2 r^2$  for Cr<sup>+</sup> and Fe<sup>3+</sup> (ROHF results).

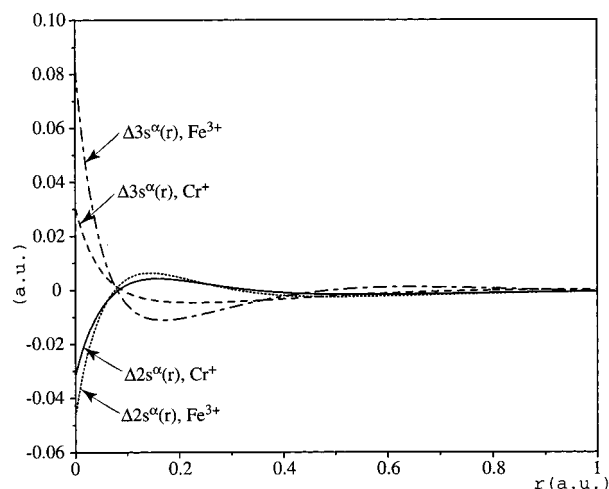


**Figure 8.** Core-shell spin polarization in Cr<sup>+</sup> and Fe<sup>3+</sup>:  $\Delta 2s^\alpha(r)$ ,  $\Delta 3s^\alpha(r)$ .

$\Delta 3s^\alpha(r)$  and  $\Delta 2s^\alpha(r)$  have to match the restricted orbital distributions  $2s_R(r)r^2$  and  $3s_R(r)r^2$ , to fulfill eq 12.

Figure 7 examines the changes in the ROHF 2s and 3s radial distributions upon increasing the nuclear charge by two (the d<sup>5</sup> ions Cr<sup>+</sup> and Fe<sup>3+</sup> are compared). Both 2s and 3s contract and increase their overlap with  $\Delta 3s^\alpha$  and  $\Delta 2s^\alpha$ , respectively. The redistribution of the electron density is more pronounced for the more polarizable 3s orbital. This is seen most clearly when comparing the area confined between the curves  $3s(\text{Fe}^{3+})$  and  $3s(\text{Cr}^+)$  with the area confined between the curves  $2s(\text{Fe}^{3+})$  and  $2s(\text{Cr}^+)$ . The contraction of 3s and 2s will thus enhance  $\langle \Delta 2s^\alpha(r) | 3s_R(r) \rangle$  more than  $\langle \Delta 3s^\alpha(r) | 2s_R(r) \rangle$ . To retain orthogonality in the spin-polarized case,  $\Delta 3s^\alpha(r)$  has to increase relative to  $\Delta 2s^\alpha(r)$ . This is supported by Figure 8: While the absolute value of  $\Delta 2s^\alpha(r)$  increases only slightly from Cr<sup>+</sup> to Fe<sup>3+</sup>,  $\Delta 3s^\alpha(r)$  is significantly enhanced. Consequently, the ratio  $\Delta 3s^\alpha(0)/\Delta 2s^\alpha(0)$  is larger for Fe<sup>3+</sup>. Analogously,  $\Delta 3s^\beta(0)/\Delta 2s^\beta(0)$  is enhanced. As a result, the magnitude of the 3s/2s ratio of core-shell spin polarization contributions to  $\rho_N$  increases with increasing nuclear charge (cf. Tables 2 and 3), due to the requirement of orthogonality between 2s and 3s shells.

**Spin Polarization of the 1s Orbital.** The direction of 1s spin polarization in Mn<sup>2+</sup> is the same as for the 2s orbital: the  $\alpha$  component expands, whereas the  $\beta$  component contracts. Both processes produce a negative contribution to  $\rho_N$  (cf. Tables 1

**Table 5.** Analysis of ROHF and UHF Total Energies of <sup>6</sup>Mn<sup>2+</sup> and <sup>4</sup>N (au)

|  | <sup>6</sup> Mn <sup>2+</sup> | <sup>4</sup> N |
|--|-------------------------------|----------------|
| $E_{\text{tot,ROHF}}^a$                    | -1148.793 015                 | -54.398 026    |
| $E_{\text{tot,UHF}}^a$                     | -1148.795 003                 | -54.401 648    |
| $E_{\text{tot,UHF}} - E_{\text{tot,ROHF}}$ | -0.001 988                    | -0.003 622     |
| $E_{\text{kin,ROHF}}^b$                    | 1148.959 337                  | 54.397 176     |
| $E_{\text{kin,UHF}}^b$                     | 1148.962 479                  | 54.401 243     |
| $E_{\text{kin,UHF}} - E_{\text{kin,ROHF}}$ | 0.003 142                     | 0.004 067      |
| $E_{\text{pot,ROHF}}^c$                    | -2297.752 352                 | -108.795 202   |
| $E_{\text{pot,UHF}}^c$                     | -2297.757 482                 | -108.802 891   |
| $E_{\text{pot,UHF}} - E_{\text{pot,ROHF}}$ | -0.005 130                    | -0.007 689     |
| $E_{\text{Ne,ROHF}}^d$                     | -2717.979 039                 | -128.343 514   |
| $E_{\text{Ne,UHF}}^d$                      | -2718.011 143                 | -128.353 641   |
| $E_{\text{Ne,UHF}} - E_{\text{Ne,ROHF}}$   | -0.032 104                    | -0.010 127     |
| $E_{\text{ee,ROHF}}^e$                     | 420.226 687                   | 19.548 312     |
| $E_{\text{ee,UHF}}^e$                      | 420.253 661                   | 19.550 750     |
| $E_{\text{ee,UHF}} - E_{\text{ee,ROHF}}$   | 0.0269 74                     | 0.0024 38      |
| $E_{\text{C,ROHF}}^f$                      | 511.200 248                   | 31.975 583     |
| $E_{\text{C,UHF}}^f$                       | 511.230 621                   | 31.987 506     |
| $E_{\text{C,UHF}} - E_{\text{C,ROHF}}$     | 0.030 373                     | 0.011 923      |
| $E_{\text{X,ROHF}}^g$                      | -90.973 561                   | -12.427 271    |
| $E_{\text{X,UHF}}^g$                       | -90.976 960                   | -12.436 756    |
| $E_{\text{X,UHF}} - E_{\text{X,ROHF}}$     | -0.003 399                    | -0.009 485     |

<sup>a</sup> Total (kinetic + potential) energy of the system. <sup>b</sup> Total kinetic energy. <sup>c</sup> Total potential energy ( $E_{\text{pot}} = E_{\text{Ne}} + E_{\text{ee}}$ ). <sup>d</sup> Total energy of the electrons due to nuclear attraction. <sup>e</sup> Total electron–electron repulsion energy ( $E_{\text{ee}} = E_{\text{C}} + E_{\text{X}}$ ). <sup>f</sup> The sum of all Coulomb integrals, including self-interactions. <sup>g</sup> The sum of all exchange integrals, including self-interactions.

and 3). Previously the minimization of the electrostatic repulsion with the unpaired electrons had been considered to be the major driving force of the 1s spin polarization.<sup>1,17</sup> According to our calculation, 1s spin polarization does not lead to any significant difference between the  $\alpha$  and  $\beta$  components with respect to exchange and Coulomb interaction with the SOMO, cf. Table 4.<sup>37</sup> From this, and from the small 1s contributions of either sign to  $\rho_N$  in different systems (Tables 1–3), we conclude that the 1s orbital reacts to the spin polarizations of the other doubly occupied orbitals rather than minimizing its repulsion with the SOMO. Note, for example, that the 1s contribution to  $\rho_N$  and the sum of the valence-shell contributions always have opposite signs (cf. also Tables 1 and 2).

**Spin Polarization and Energy Gain.** The gain in exchange energy, due to spin polarization, between the five SOMOs and the doubly occupied orbitals in Mn<sup>2+</sup> (-0.005 345 au; see Table 4) corresponds to 104% of the difference between the total UHF and ROHF potential energies (Table 5). For the <sup>4</sup>N atom, the corresponding gain in exchange energy represents 105% of the total reduction in potential energy ( $E_{\text{pot}}$ , Table 5). This is consistent with the usual interpretation of spin polarization as being due to improved exchange interactions between the SOMO(s) and the doubly occupied orbital(s) in the UHF wave function.

Additionally, the spin polarization creates a new equilibrium between electron–electron repulsion and electron–nuclear attraction. The crucial role of electron–nuclear attraction energy ( $E_{\text{Ne}}$ ) is demonstrated in Table 5. It provides the main energy gain upon going from ROHF to UHF wave functions. This may be rationalized as follows: As the ROHF wave function is not relaxed with respect to exchange interactions between the SOMO and the other  $\alpha$  spin–orbitals, the density is too diffuse. Spin polarization helps to contract the metal 3d $^\alpha$ , 3p $^\alpha$ , and 3s $^\alpha$  orbitals and thus enhances electron–nuclear attraction. Part of this energy gain is compensated by the decontraction of the

(37) The strongly localized 1s shell experiences ~2 orders of magnitude less exchange interactions with 3d than 2s does.

charge density in  $1s^\alpha$ ,  $2s^\alpha$ ,  $2p^\alpha$ , as well as in  $3s^\beta$  and  $3p^\beta$  ( $1s^\beta$ ,  $2s^\beta$ ,  $2p^\beta$  contract and thus lower  $E_{Nc}$ ). Tables 4 and 5 show that the spin polarization improves exchange ( $E_X$ ) but increases the total  $E_{ee}$ . This is also a consequence of an overall more contracted charge density. Nevertheless,  $E_{pot}$  decreases, due to the large contribution from  $E_{Nc}$ . The total kinetic energy ( $E_{kin}$ ) increases, in agreement with the virial theorem.<sup>38</sup>

Table 4 also shows that, due to formal similarity, the exchange integrals and their changes upon spin polarization are closely connected with the radial overlap of the corresponding orbitals. (a) The exchange interaction increases in the series (3d,1s), (3d,2s) and (3d,3s) and so does the radial overlap; (b) the spin polarization increases the exchange integral with the SOMO when the radial overlap with the SOMO increases and vice versa.<sup>39</sup> In contrast, the Coulomb interaction increases along the series (3d,3s), (3d,2s), and (3d,1s), even though the 2s and particularly the 1s maximums are far from the 3d maximum. This implies that  $\langle 1/r_{12} \rangle$  may actually increase with increasing distance between the radial maximums and vice versa. Compared to the 1s wave function, the 3s wave function occupies a larger angular space. Thus, the electrons in 3s and 3d orbitals are on average further apart (despite the large overlap of the corresponding radial wave functions).

Coming back to the historical interpretations of spin polarization in transition metal systems (section 2<sup>1,15</sup>), we conclude that the expansion of the  $2s^\alpha$  orbital reduces its electrostatic repulsion with the SOMO, both by reduced Coulomb interaction (angular correlation) and by improved exchange (radial correlation). This would correspond to the usual “effective attraction” of like-spin electrons on a radial scale. On the other hand, the boundary condition of orthogonality to 2s forces the 3s spin polarization (expansion of  $3s^\alpha$ , contraction of  $3s^\beta$ ), irrespective of the resulting partial energy loss.

**Comparison to the Main-Group Case ( $^4N$ ).** The quartet ground state of the nitrogen atom is a good main-group example to be compared with, as it exhibits a spherical distribution of the three unpaired electrons in the 2p orbitals. The positive 2s contribution to  $\rho_N$  (0.91 au, UHF result) overcompensates the negative 1s contribution ( $-0.74$  au), giving an overall positive  $\rho_N$  (cf. ref 19e). The spin polarization of the nitrogen 1s and 2s orbitals (Figure 2a,b) may be compared to the polarization of the 2s and 3s orbitals in  $Mn^{2+}$  (Figure 4a,c). For nitrogen, the  $1s^\alpha$  and  $2s^\beta$  orbitals expand, whereas the  $1s^\beta$  and  $2s^\alpha$  orbitals contract. Note that, in contrast to the situation for the 3s and 3d orbitals in  $Mn^{2+}$  (see above), the second maximum of the 2s distribution is located at slightly larger radius than the 2p maximum.

The opposite direction of the polarization of the  $1s^\alpha$  and  $2s^\alpha$  orbitals is again required by their mutual orthogonality. However, in contrast to the  $Mn^{2+}$  case, in this case, the spin polarization enhances the exchange interaction with the 2p SOMO for both s orbitals, despite the slight decrease of radial overlap between  $2s^\alpha$  and  $2p^\alpha$  (Table 6). This appears to be due to the dominant role of the second maximum of  $2s^\alpha$ . Spin polarization brings the latter closer to the  $2p^\alpha$  maximum and thus enhances  $2s^\alpha/2p^\alpha$  exchange. The accompanying increase in  $2s^\alpha/2p^\alpha$

(38) Levin, I. N. *Quantum Chemistry*; Allyn and Bacon: Boston, 1975; p 363.

(39) Exchange interactions are more short-ranged than Coulomb repulsion and thus parallel more closely the radial overlap (see, e.g., Bethe, H. A.; Jackiw, R. *Intermediate Quantum Mechanics*; W. A. Benjamin, Inc.: Reading, MA, 1974). In contrast, Coulomb repulsion may also be large for two nonoverlapping pointlike charge distributions, provided their distance is not too large. Of course, even the exchange interactions may deviate from the behavior of the radial overlap integrals, due to the influence of the  $r_{12}^{-1}$  factor in the integrand of eq 4 (cf. also discussion for  $^4N$ ).

**Table 6.** Exchange, Coulomb, and Radial Overlap Integrals between the SOMO and the Doubly Occupied Orbitals for  $^4N$  (au)<sup>a</sup>

| exchange integrals   | 1s         | 2s           |
|--|------------|--------------|
| $\langle \psi_R 2p_R   2p_R \psi_U \rangle$  | 0.028 820  | 0.137 305    |
| $\langle \psi_U^\alpha 2p_U   2p_U \psi_U^\alpha \rangle$  | 0.029 190  | 0.138 789    |
| $\langle \psi_U^\alpha 2p_U^\alpha   2p_U^\alpha \psi_U^\alpha \rangle$  | 0.029 505  | 0.139 322    |
| $\langle \psi_U^\alpha 2p_U^\alpha   2p_U^\alpha \psi_U^\alpha \rangle - \langle \psi_R 2p_R   2p_R \psi_U \rangle$                  | 0.000 685  | 0.002 017    |
| $3\Sigma_\phi - [\langle \psi_U^\alpha 2p_U^\alpha   2p_U^\alpha \psi_U^\alpha \rangle - \langle \psi_R 2p_R   2p_R \psi_U \rangle]$ |            | $-0.008 106$ |
| Coulomb integrals  | 1s         | 2s           |
| $\langle \psi_R 2p_R   \psi_R 2p_R \rangle$  | 0.947 366  | 0.668 210    |
| $\langle \psi_U^\alpha 2p_U   \psi_U^\alpha 2p_U \rangle$  | 0.947 209  | 0.677 922    |
| $\langle \psi_U^\alpha 2p_U^\alpha   \psi_U^\alpha 2p_U^\alpha \rangle$  | 0.951 949  | 0.680 044    |
| $\langle \psi_U^\beta 2p_U^\beta   \psi_U^\beta 2p_U^\beta \rangle$  | 0.952 208  | 0.655 545    |
| radial overlap integrals <sup>b</sup>  | 1s         | 2s           |
| $\langle \psi_R   2p_R \rangle^b$  | 0.020 783  | 0.076 279    |
| $\langle \psi_U^\alpha   2p_U \rangle^b$   | 0.021 107  | 0.075 845    |
| $\langle \psi_U^\alpha   2p_U^\alpha \rangle^b$  | 0.021 217  | 0.075 882    |
| nuclear attraction integrals   | 1s         | 2s           |
| $\langle \psi_R   Z/r   \psi_R \rangle$  | 46.584 427 | 7.532 656    |
| $\langle \psi_U^\alpha   Z/r   \psi_U^\alpha \rangle$  | 46.467 873 | 7.803 738    |
| $\langle \psi_U^\beta   Z/r   \psi_U^\beta \rangle$  | 46.669 016 | 7.201 735    |
|  | 2p         |              |
| $\langle \psi_R   Z/r   \psi_R \rangle$  | 6.703 116  |              |
| $\langle \psi_U^\alpha   Z/r   \psi_U^\alpha \rangle$  | 6.737 093  |              |

<sup>a</sup> ROHF and UHF results. <sup>b</sup> See also corresponding footnote to Table 4.

Coulomb repulsion is compensated by reduced  $2s^\beta/2p^\alpha$  repulsion and increased nuclear–electron attraction (Table 6).

**Valence-Shell Spin Polarization in  $Mn^0$ .** As a first step toward a better understanding of valence-shell spin polarization in transition metal systems, we examine the spin polarization of the 4s orbital in the  $^6Mn^0$  atom, comparing ROHF and UHF wave functions and energies. The spin polarization is qualitatively the same as discussed above for the 2s orbital in nitrogen: The  $\alpha$ -component contracts, whereas the  $\beta$  component expands (Figure 9). The exchange interaction between 3d and 4s (0.006 581 au at the ROHF level) is overall less pronounced than between 2s and 3d in  $Mn^{2+}$  (0.026 949 au; cf. Table 4), but the energy gain upon spin polarization is still significant (+0.000 872 au). This is due to the large polarizability of the 4s shell, which also leads to a significant redistribution of spin density (Figure 9) and to a larger spin polarization contribution to  $\rho_N$  from 4s compared to 3s (Table 1). We may also view this, within a configuration–interaction framework,<sup>40</sup> as a consequence of the lower excitation energies of the 4s valence compared to the 3s core orbital (for the same reason, spin contamination is largely connected to valence-shell spin polarization; see below). The same argument holds of course for the comparison between valence-shell 2s vs core-shell 1s spin polarization in nitrogen (see above).

## 6. Valence-Shell Spin Polarization in Molecules

As discussed above, the spin polarization of the core shells does not depend much on the particular bonding situation. It is similar for molecules and for atomic systems (cf. Tables 1 and

(40) Melchior, M. T., *J. Chem. Phys.* **1969**, *50*, 511.

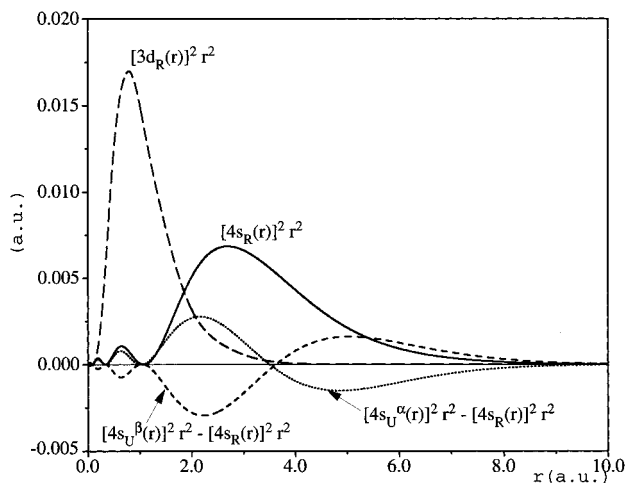


**Figure 9.** ROHF radial distribution function  $[R_{ni}(r)]^2 r^2$  (scaled by  $1/4$ ) and difference between ROHF and UHF radial distributions for the 4s orbital in  $Mn^0$ . For comparison, the radial distribution function of the 3d SOMOs (scaled by  $1/4$ ) is also plotted.

**Table 7.** Orbital Contributions to  $A_{dip}$  for  $TiF_3$  and  $MnO_3$  (au)<sup>a</sup>

| MO        | character  | contribution                    |                      |
|-----------|--|---------------------------------|----------------------|
|           |  | $TiF_3$                         | $MnO_3$              |
| $7a_1'$   | (metal $3d_z^2 + 4s$ , singly occupied MO)             | 0.441                           | 0.640                |
| $3a_2''$  | (ligand $2p_z$ )                                       | 0.012                           | 0.052                |
| $1e''$    | (metal $3d_{xz}, 3d_{yz}$ ; ligand $2p_z$ )            | 0.005                           | 0.147                |
| $6a_1'$   | (metal $4s, 3d_x^2$ ; ligand $2p_x, 2p_y$ )            | 0.013                           | 0.206                |
| $5e'$     | (metal $3d_{xy}, 3d_{x^2-y^2}$ ; ligand $2p_x, 2p_y$ ) | -0.014                          | -0.113               |
| $4e'$     | (ligand 2s)  | 0.051                           | 0.008                |
| $2a_2'$   | (metal $3p_z$ )  | -0.086                          | -0.018               |
| $3e'$     | (metal $3p_x, 3p_y$ )                                  | -0.108                          | -0.152               |
| $1a_2''$  | (metal $2p_z$ )  | -0.067                          | -0.143               |
| $2e'/1e'$ | (metal $2p_x, 2p_y$ )                                  | 0.048                           | 0.108                |
| total     |  | 0.305                           | 0.746                |
| exp       |  | 0.22(1)...0.027(1) <sup>b</sup> | 0.62(2) <sup>b</sup> |
| $<S^2>$   |  | 0.7526                          | 0.7875               |

<sup>a</sup> DFT(BP86) results. All values have been divided by the nuclear  $g$  value. Contributions, which were for both molecules smaller than 0.01 au, have been omitted. <sup>b</sup> Reference 11.

2). In contrast, the spin polarization of the valence shells is characteristic of the specific chemical environment and bonding. We have selected the four examples,  $TiF_3$ ,  $MnO_3$ ,  $[Mn(CO)_5]$ , and  $[Mn(CN)_4N]^-$ , to discuss valence-shell spin polarization contributions to  $\rho_N$ . DFT results obtained with the BP86 functional will be examined (Tables 1 and 2).

These complexes represent a variety of different bonding situations (cf. Tables 7 and 8 for a characterization of the MOs).  $TiF_3$ <sup>22</sup> and  $MnO_3$  are isoelectronic, trigonal planar ( $D_{3h}$ )  $d^1$  complexes. Their SOMO ( $7a_1'$ ) is metal–ligand  $\sigma$  antibonding and is dominated by the metal  $3d_z^2$  orbital, with some 4s character mixed in. While the SOMO in  $TiF_3$  is localized to 94% at the metal (with 76%  $3d_z^2$ , and 18% 4s character<sup>41</sup>), in  $MnO_3$  it is more delocalized (with 49%  $3d_z^2$ , 15% 4s, and 36% ligand character). Three  $\sigma$ -bonding orbitals ( $5e'$ ,  $6a_1'$ ) are formed by the interaction of metal  $3d_{xy}$  and  $3d_{x^2-y^2}$  orbitals ( $e'$ ), a metal  $3d_z^2$  orbital with 4s admixture ( $a_1'$ ), and the appropriate ligand orbital combinations. In addition, two partial  $\pi$  bonds are formed

(41) The orbital compositions and spin populations reported here have been obtained using a Mulliken population analysis of the BP86 Kohn–Sham wave function.

by an interaction of the metal  $3d_{xz}$  and  $3d_{yz}$  orbitals with the appropriate linear combination of ligand  $2p_z$  orbitals ( $1e''$ ). The third linear combination of ligand  $2p_z$  orbitals is nonbonding ( $3a_2''$ ).  $[Mn(CO)_5]$  and  $[Mn(CN)_4N]^-$  adopt square-pyramidal structures ( $C_{4v}$  symmetry).  $[Mn(CO)_5]$  is a low-spin  $d^7$  complex. Its SOMO is composed of metal  $3d_z^2$  and  $4p_z$  orbitals ( $17a_1$ ). The  $4p_z$  admixture reduces the  $\sigma$ -antibonding interaction with the axial ligand by polarizing the SOMO toward the opposite side. The metal 4s contribution to the SOMO is small, giving a small, positive direct SOMO contribution to  $\rho_N$ .  $[Mn(CN)_4N]^-$  is a  $d^1$  complex with a single metal  $3d_{xy}$ -type SOMO ( $2b_1$ ). In both square-pyramidal complexes, two  $\sigma$  bonds in the equatorial plane are formed by an interaction between a metal  $4s/3d_z^2$  hybrid, the metal  $3d_{x^2-y^2}$  orbital, and the corresponding ligand  $\sigma$ -bonding hybrids ( $a_1$  and  $b_2$  MOs). The  $\sigma$  bond to the axial ligand involves mainly the metal  $3d_z^2$  orbital. The metal  $3d_{xy}$  orbital ( $b_1$ ) is partially  $\pi$  bonding to the equatorial ligands, the  $3d_{xz}$ ,  $3d_{yz}$  orbitals ( $e$ ) interact also with the axial ligand. The antibonding counterparts of the latter three orbitals (which may be derived from the well-known  $t_{2g}$  set in octahedral symmetry) correspond to the six nonbonding d electrons of  $[Mn(CO)_5]$ .

The valence-shell spin polarization concentrates  $\alpha$  spin density at the metal (cf. discussion above for the  $Mn^0$  atom and ref 18). An excess of  $\beta$  spin density is left at the ligands. In  $[Mn(CN)_4N]^-$ , the spin polarization increases the atomic spin population of Mn from 0.51 (SOMO contribution) to 1.18 (total spin population<sup>41</sup>). The  $\alpha$  spin density is withdrawn mainly from the axial ligand and added mainly to d-type orbitals of Mn (0.25, 0.10, 0.10, 0.07, and 0.06 electrons to  $d_{xy}$ ,  $d_{xz}$ ,  $d_{yz}$ ,  $d_{x^2-y^2}$ , and  $d_z^2$ , respectively). This likely enhances the overall negative core-shell spin polarization contributions to  $\rho_N$  (cf. section 5). The spin population of the 4s orbital increases also slightly (several metal–ligand bonding orbitals are involved), resulting in a small contribution to  $\rho_N$  of +0.04 au (Table 1). This is much less than the valence-shell contribution in Mn (+0.93 au), where the spin polarization of the fully occupied 4s orbital contributes (note also that  $[Mn(CN)_4N]^-$  has only one unpaired electron whereas Mn has five).

Similarly, spin polarization increases the spin population at the metal in  $Mn(CO)_5$  from 0.58 (SOMO contribution) to 0.82. The increase concentrates mostly in orbitals of e symmetry (the metal  $3d_{xz}$ ,  $3d_{yz}$ ,  $4p_x$ , and  $4p_y$  orbitals, total gain  $\sim 0.13$ ). The spin population in orbitals of  $a_1$  symmetry increases only slightly, by 0.04 for  $3d_z^2$  and by 0.03 for 4s. The increase is only 0.03 and 0.01 for  $3d_{xy}$  and  $3d_{x^2-y^2}$ , respectively (with significant consequences for  $A_{dip}$ , cf. below).

Negative valence-shell contributions to  $\rho_N$  are found for the isoelectronic  $TiF_3$  and  $MnO_3$ , due to an interesting rehybridization mechanism: The spin polarization, mainly of the metal–ligand  $\sigma$ -bonding  $6a_1'$  MO, shifts  $\alpha$  density from the ligands toward the metal. Therefore, the spin population at the metal is enhanced from 0.93 (SOMO contribution) to 1.04 in  $TiF_3$ , and from 0.64 to 1.19 in  $MnO_3$  (the larger effect for the manganese complex is a consequence of the larger covalence of the  $\sigma$  bonds). However, at the same time, the metal contribution to this bonding MO loses 4s character and gains 3d character. Therefore, the overall valence-shell spin polarization contribution to  $\rho_N$  and thus to  $A_{iso}$  is negative (and that to  $A_{dip}$  positive, cf. below), in particular for the very covalent  $MnO_3$ . We also note that, in  $TiF_3$ , the excess  $\alpha$  spin density is distributed almost equally over all five metal d orbitals. In contrast, the excess spin population in  $MnO_3$  pertains mostly to the  $d_z^2$ ,  $d_{xz}$ , and  $d_{yz}$  orbitals (+0.17, +0.13, and +0.13, respectively) and less to the  $d_{xy}$  and  $d_{x^2-y^2}$  orbitals (each +0.05).

**Table 8.** Orbital Contributions to  $A_{\text{dip}}$  for  $[\text{Mn}(\text{CO})_5]$  and  $[\text{Mn}(\text{CN})_4\text{N}]^-$  (au)<sup>a</sup>

| MO in $[\text{Mn}(\text{CN})_4\text{N}]^-/[\text{Mn}(\text{CO})_5]$ | character  | contribution                         |  |
|---|--|--------------------------------------|--|
|   |  | $[\text{Mn}(\text{CN})_4\text{N}]^-$ | $[\text{Mn}(\text{CO})_5]$                 |
| -17a <sub>1</sub>   | (Mn 3d <sub>z<sup>2</sup></sub> , 4p <sub>z</sub> , 4s, SOMO in $[\text{Mn}(\text{CO})_5]$ )                     |                                      | 0.763                                      |
| -11e  | (Mn 3d <sub>xz</sub> , 3d <sub>yz</sub> ; eq ligands 2p <sub>z</sub> )   |                                      | 0.032                                      |
| 2b <sub>1</sub> /2b <sub>1</sub>                                    | (Mn 3d <sub>xy</sub> , eq lig 2p <sub>x</sub> , 2p <sub>y</sub> , SOMO in $[\text{Mn}(\text{CN})_4\text{N}]^-$ ) | -0.669                               | -0.040                                     |
| 13a <sub>1</sub> /14a <sub>1</sub>                                  | (eq ligands sp <sub>x</sub> , sp <sub>y</sub> hybrids; Mn 4s)  | -0.030                               | 0.002                                      |
| 5b <sub>2</sub> /5b <sub>2</sub>                                    | (eq ligands sp <sub>x</sub> , sp <sub>y</sub> hybrids; Mn 3d <sub>x<sup>2</sup>-y<sup>2</sup></sub> )            | -0.015                               | 0.000                                      |
| 1b <sub>1</sub> /1b <sub>1</sub>                                    | (Mn 3d <sub>xy</sub> , eq ligands 2p <sub>x</sub> , 2p <sub>y</sub> )  | -0.273                               | -0.003                                     |
| 6e/10e  | (Mn 3d <sub>xz</sub> , 3d <sub>yz</sub> ; eq ligands 2p <sub>x</sub> , 2p <sub>y</sub> )                         | 0.110                                | 0.021                                      |
| 4b <sub>2</sub> /6b <sub>2</sub>                                    | (Mn 3d <sub>x<sup>2</sup>-y<sup>2</sup></sub> , eq ligands 2s+2p <sub>x</sub> +2p <sub>y</sub> )                 | -0.069                               | -0.013                                     |
| 11a <sub>1</sub> /12a <sub>1</sub>                                  | (Mn 4s+3d <sub>z<sup>2</sup></sub> , eq ligands 2s+2p <sub>x</sub> +2p <sub>y</sub> )                            | 0.018                                | -0.002                                     |
| 8a <sub>1</sub> /9a <sub>1</sub>                                    | (Mn 3p <sub>z</sub> )  | 0.076                                | 0.057                                      |
| 4e/4e   | (Mn 3p <sub>x</sub> , 3p <sub>y</sub> )  | -0.121                               | -0.044                                     |
| 3a <sub>1</sub> /3a <sub>1</sub>                                    | (Mn 2p <sub>z</sub> )  | -0.077                               | -0.094                                     |
| 1e/1e   | (Mn 2p <sub>x</sub> , 2p <sub>y</sub> )  | 0.163                                | 0.048                                      |
| total   |  | -0.882                               | 0.727                                      |
| exp   |  | -0.929 <sup>b</sup>                  | 0.68(6), <sup>b</sup> 0.70(5) <sup>b</sup> |
| <S <sup>2</sup> >   |  | 0.7729                               | 0.7544                                     |

<sup>a</sup> DFT(BP86) results. See also footnote to Table 7. <sup>b</sup> Reference 11.

In both  $[\text{Mn}(\text{CN})_4\text{N}]^-$  and  $\text{MnO}_3$ , the largest valence-shell spin polarization is experienced by doubly occupied orbitals which are the bonding counterparts of the partly antibonding SOMO (this holds at the BP86 level but is altered upon adding Hartree–Fock exchange; see section 8). In  $[\text{Mn}(\text{CN})_4\text{N}]^-$ , this is the 1b<sub>1</sub> orbital which represents  $\pi$  bonding between the metal and the equatorial ligands. In  $\text{MnO}_3$  it is the  $\sigma$ -bonding 6a<sub>1</sub>' orbital. This observation may again be rationalized by a tendency to maximize the exchange interaction with the SOMO; i.e., the  $\alpha$  component of the doubly occupied MO is polarized toward the metal (where the SOMO is largely localized), the  $\beta$  component toward the ligands. Due to the large overlap with the SOMO, the spin polarization is particularly effective in these MOs. The abovementioned rehybridization in the  $\alpha$  and  $\beta$  components of the  $\sigma$ -bonding 6a<sub>1</sub>' MO of  $\text{MnO}_3$  and  $\text{TiF}_3$  may be understood analogously: The SOMO has more 3d<sub>z<sup>2</sup></sub> than 4s character, and thus an increase of the relative d character in the  $\alpha$  component of the bonding MO improves the exchange interaction with the SOMO. In  $\text{TiF}_3$  and  $\text{Mn}(\text{CO})_5$ , the bonding counterparts of the (antibonding) SOMO are not polarized significantly. In  $\text{TiF}_3$ , this is due to the ionic character of the bonds. In  $\text{Mn}(\text{CO})_5$ , the SOMO is polarized away from the ligands (by 4p<sub>z</sub> admixture) and thus has also little overlap with the doubly occupied valence MOs.

## 7. Effect of Spin Polarization on Dipolar Coupling Constants

While spin polarization is usually not considered for the dipolar hyperfine coupling (cf. Introduction), two recent computational studies have shown that in transition metal systems spin polarization may have a significant influence.<sup>11,22</sup> The most important MO contributions to the metal dipolar couplings of our four example systems are summarized in Tables 7 and 8 (again, DFT results with the BP86 functional are compared). As expected, the largest contribution in all cases is the direct one from the SOMO. This is positive for  $\text{TiF}_3$ ,  $\text{MnO}_3$ , and  $[\text{Mn}(\text{CO})_5]$  but negative for  $[\text{Mn}(\text{CN})_4\text{N}]^-$ .<sup>42</sup> However, contri-

butions due to the spin polarization of the doubly occupied orbitals are clearly nonnegligible. We may discriminate again between core- and valence-shell spin polarization.

**Core-Shell Spin Polarization.** A common feature of all four systems are the significant contributions to  $A_{\text{dip}}$  from metal p-type core orbitals. The metal 2p<sub>z</sub> contributions are always negative; the 2p<sub>x</sub> and 2p<sub>y</sub> contributions are always positive. This is consistent with the discussion in section 5: Spin polarization expands the 2p<sup>α</sup> orbitals and contracts the 2p<sup>β</sup> orbitals. Thus, the positive contribution from 2p<sub>z</sub><sup>α</sup> to  $A_{\text{dip}}$  becomes smaller than the negative one from 2p<sub>z</sub><sup>β</sup>, and the negative contributions from 2p<sub>x</sub><sup>α</sup>, 2p<sub>y</sub><sup>α</sup> become smaller than the positive ones from 2p<sub>x</sub><sup>β</sup>, 2p<sub>y</sub><sup>β</sup>. In a system of cubic or higher symmetry, these contributions would cancel exactly. In less symmetric systems, the anisotropy of the 2p spin polarization disturbs the balance between the two contributions. For our four systems, the effect is clearly nonnegligible, corresponding to ~5–10% of the total  $A_{\text{dip}}$ . The 2p<sub>z</sub> orbital dominates the 2p shell contributions in  $\text{TiF}_3$ ,  $\text{MnO}_3$ , and  $[\text{Mn}(\text{CO})_5]$  (the 3d<sub>z<sup>2</sup></sub>-type SOMO affects particularly the 2p<sub>z</sub><sup>α</sup> component), whereas spin polarization contributions from 2p<sub>x</sub> and 2p<sub>y</sub> orbitals are larger in  $[\text{Mn}(\text{CN})_4\text{N}]^-$  (the 3d<sub>xy</sub>-type SOMO affects mostly 2p<sub>x</sub><sup>α</sup> and 2p<sub>y</sub><sup>α</sup>).

The requirement of orthogonality between the 3p and 2p shells for atoms, as stated in section 5, does not hold strictly for molecules. Nevertheless, the 3p<sub>x</sub> and 3p<sub>y</sub> contributions to  $A_{\text{dip}}$  generally have the opposite sign of the 2p<sub>x</sub> and 2p<sub>y</sub> contributions. The 2p<sub>z</sub> and 3p<sub>z</sub> contributions are also of opposite sign for  $[\text{Mn}(\text{CO})_5]$  and  $[\text{Mn}(\text{CN})_4\text{N}]^-$ . Therefore, the positive 3p<sub>z</sub> and the negative 3p<sub>x</sub> and 3p<sub>y</sub> contributions partially cancel, leading to a relatively low overall 3p contribution. In  $\text{TiF}_3$  and  $\text{MnO}_3$ , the presence of the d<sub>z<sup>2</sup></sub>-type SOMO forces both 2p<sub>z</sub><sup>α</sup> and 3p<sub>z</sub><sup>α</sup> orbitals to expand. Therefore, 3p<sub>z</sub> and 3p<sub>x</sub>/3p<sub>y</sub> contributions do not compensate but enhance each other. Therefore, the spin polarization contributions from the 3p shell in  $\text{TiF}_3$  and  $\text{MnO}_3$  are particularly large and amount to ~23% of the total  $A_{\text{dip}}$  in  $\text{MnO}_3$  and even to ~64% in  $\text{TiF}_3$ .<sup>11,22</sup>

**Valence-Shell Spin Polarization.** In the relatively ionic complex  $\text{TiF}_3$ , valence-shell spin polarization contributions to  $A_{\text{dip}}$  are small, with the largest individual MO contribution arising from a nonbonding fluorine 2s orbital combination of 4e' symmetry (this and other results of our analysis for  $\text{TiF}_3$  are consistent with earlier results by Belanzoni et al.<sup>22</sup>). We find larger valence-shell contributions for  $\text{MnO}_3$  (Table 7). The covalency of the Mn–O  $\sigma$  and  $\pi$  bonds enables a significant

(42) The dipolar hyperfine interaction is a vector property and depends on the orientation of the orbitals involved. For a single  $\alpha$  electron in a d<sub>z<sup>2</sup></sub> orbital, the  $(A_{xx}, A_{yy}, A_{zz})$  vector is of the form  $(-B, -B, +2B)$ . For the other d orbitals, the signs are reversed. For d<sub>x<sup>2</sup>-y<sup>2</sup></sub>  $(A_{xx}, A_{yy}, A_{zz}) \approx (B, B, -2B)$ , for d<sub>xz</sub>  $(A_{xx}, A_{yy}, A_{zz}) \approx (B, -2B, B)$ , and so on. Analogous considerations hold for p orbitals. For p<sub>z</sub>  $(A_{xx}, A_{yy}, A_{zz}) \approx (-B, -B, +2B)$ , for p<sub>x</sub>  $(A_{xx}, A_{yy}, A_{zz}) \approx (+2B, -B, -B)$ , and for p<sub>y</sub>  $(A_{xx}, A_{yy}, A_{zz}) \approx (-B, 2B, -B)$ . See, e.g., ref 2 for a detailed discussion.

shift of  $\alpha$  spin density toward the metal (cf. above). Large positive contributions to  $A_{\text{dip}}$  arise from the  $6a'$  and  $1e''$  MOs (involving the metal  $d_{z^2}$  and  $d_{xz}/d_{yz}$  orbitals, respectively), whereas the  $5e'$  MO (involving the metal  $d_{xy}$  and  $d_{x^2-y^2}$  orbitals) contributes negatively. Thus, while the overall negative spin polarization contributions to  $A_{\text{dip}}$  in  $\text{TiF}_3$  involve mainly the core shells (in particular 3p), additional significant, overall positive valence-shell contributions dominate for the more covalent  $\text{MnO}_3$ . This has consequences for the sensitivity to spin contamination (see below).

Valence-shell spin polarization contributions to  $A_{\text{dip}}$  in  $[\text{Mn}(\text{CO})_5]$  are relatively small and partially compensate each other (Table 8). This appears to be a direct consequence of the character of the SOMO, which overlaps very little with the other valence MOs. In contrast, valence-shell contributions in  $[\text{Mn}(\text{CN})_4\text{N}]^-$  are significant. The largest contribution arises from the energetically high-lying, doubly occupied counterpart ( $1b_1$ ) of the  $2b_1$  SOMO. If it were not for its very large, negative contribution, the remaining valence-shell spin polarization contributions would almost cancel each other: A significant positive contribution from the  $\pi$  bonding  $6e$  MO is compensated by negative contributions from equatorially  $\sigma$ -bonding MOs. The significant valence-shell spin polarization contribution to  $A_{\text{dip}}$  (29% of the total value) in  $[\text{Mn}(\text{CN})_4\text{N}]^-$  is thus at least in part due to the presence of a doubly occupied MO that has particularly large overlap with the SOMO.

## 8. Spin Polarization and Spin Contamination

The above discussion shows clearly that the two complexes  $\text{MnO}_3$  and  $[\text{Mn}(\text{CN})_4\text{N}]^-$  exhibit particularly pronounced valence-shell spin polarization, due to the presence of high-lying doubly occupied bonding MOs that overlap strongly with the SOMO. These two systems were also two of the most critical cases in our systematic validation of different density functionals for the calculation of hyperfine coupling constants.<sup>11</sup> In particular, spin contamination turned out to be a problem when hybrid functionals were used. For  $[\text{Mn}(\text{CN})_4\text{N}]^-$ , we found that the spin contamination was related to a mixing in of low-lying excited states that involve  $\pi$ -type orbitals. Upon going from a pure gradient-corrected ("GGA") functional like BP86 to hybrid functionals incorporating exact exchange, the population of each of the metal  $d_{xz}$  and  $d_{yz}$  orbitals increased dramatically, e.g., from 0.08 for BP86 to 0.62 for the "half-and-half" BHP86 functional. At the same time, the  $S^2$  expectation value of the Kohn–Sham wave function<sup>43</sup> indicated a significant increase in spin contamination (BP86:  $\langle S^2 \rangle = 0.773$ ; BHP86:  $\langle S^2 \rangle = 1.784$ ). Similar effects were noted with  $\text{MnO}_3$ .<sup>11</sup> Obviously, the exact-exchange contribution to the hybrid functionals favors excited states of higher spin multiplicity to the extent that the UKS wave functions for the ground state of these types of systems become significantly spin-contaminated.

In both systems, the description of  $A_{\text{dip}}$  deteriorated significantly with hybrid functionals, becoming too positive for  $\text{MnO}_3$  and insufficiently negative for  $[\text{Mn}(\text{CN})_4\text{N}]^-$ . Our present analysis indicates that the spin contamination produces too large spin populations in  $d_{xz}$ - and  $d_{yz}$ -type orbitals and thus too large positive contributions to  $A_{\text{dip}}$  from these orbitals. For similar reasons, hybrid functionals underestimated  $A_{\text{dip}}$  in the related complex  $[\text{Mn}(\text{CN})_5\text{NO}]^{2-}$ .<sup>11</sup> At the same time, the isotropic coupling constants, i.e., the spin density at the metal nuclei,

(43) These  $\langle S^2 \rangle$  values pertain to the noninteracting reference system rather than to the real system. Such data are nevertheless expected to give a reasonable and useful representation for the real system as well (see, e.g.: Baker, J.; Scheiner, A.; Andzelm, J. *Chem. Phys. Lett.* **1993**, *216*, 380).

are also affected significantly by the spin contamination: As the spin population of metal d-type orbitals is exaggerated, the spin polarization of the 3s and 2s core shells becomes too large. Thus, for example, the core-shell spin polarization contribution to  $\rho_{\text{N}}$  in  $[\text{Mn}(\text{CN})_4\text{N}]^-$  increases from  $-0.192$  au with the BP86 functional up to  $-0.566$  au with the BHP86 functional (with very small changes in the valence-shell contributions). Consequently, the BHP86 result for  $A_{\text{iso}}$  ( $-558.5$  MHz) is considerably more negative than the experimental value ( $-219.5$  MHz). Note, in contrast, that for  $\text{TiF}_3$  or  $[\text{Mn}(\text{CO})_5]$  no significant spin contamination was found,<sup>11</sup> consistent with the small valence-shell spin polarization (due to the small overlap between SOMO and doubly occupied valence MOs; see above).

## 9. Conclusions

The present study has shed light from various directions on hyperfine coupling in 3d transition metal complexes. From the detailed analysis of the spin polarization of the metal core shells in atomic systems, we have learned that the opposite contributions from the metal 2s and 3s shells to the spin density at the metal nucleus,  $\rho_{\text{N}}$ , and of the 2p and 3p shells to the dipolar coupling constants,  $A_{\text{dip}}$ , is a consequence of the orthogonality requirement between orbitals of the same angular momentum. While the 2s and 2p orbitals maximize their exchange interaction with the SOMO, the 3s and 3p orbitals are forced to lose some of their exchange to stay orthogonal to their respective penultimate shell. Changes of the ratio between 2s and 3s (and between 2p and 3p) contributions to  $\rho_{\text{N}}$  along the 3d series may be understood from the nodal structure of the orbitals. We expect that similar considerations apply to 4d and 5d systems.

Parts of this analysis are consistent with traditional views of spin polarization, e.g., in main-group compounds, as being due to enhanced exchange between the  $\alpha$  component of the respective doubly occupied orbitals and the SOMO. A complete view, however, has to include the complementary polarization of the  $\beta$  spin-orbitals, as well as changes in Coulomb repulsion and nuclear–electron attraction.

While the core-shell spin polarization contributions to the isotropic hyperfine couplings have been found to be proportional to the spin population in the metal 3d orbitals, they are relatively independent of other details of the bonding. In contrast, the valence-shell spin polarization depends strongly on the electronic structure of the system. Particularly large valence-shell spin polarization contributions to both isotropic and dipolar coupling constants are found for systems in which the SOMO overlaps significantly with certain high-lying doubly occupied valence orbitals. These are the same cases in which our previous study<sup>11</sup> found dramatic spin contamination effects to plague unrestricted Kohn–Sham calculations with hybrid functionals. In addition to providing some basic insight into the mechanisms of spin polarization in transition metal systems, the results of the present work may also be used to pinpoint the weaknesses of certain theoretical approaches for the calculation of hyperfine couplings and thus hopefully also to develop improved methods.

In contrast to the assumptions implicit in many qualitative<sup>2</sup> and quantitative<sup>44,45</sup> schemes in current use by experimentalists, both core- and valence-shell spin polarization may significantly contribute to transition metal dipolar coupling constants. Moreover, for  $\text{TiF}_3$  and  $\text{MnO}_3$ , we have identified an interesting 3d/4s rehybridization of the SOMO upon including spin

(44) Varberg, T. D.; Field, R. W.; Merer, A. J. *J. Chem. Phys.* **1991**, *95*, 1563.

(45) Balfour, W. J.; Merer, A. J.; Niki, H. *J. Chem. Phys.* **1993**, *99*, 3288.

polarization. These features complicate the extraction of spin densities and orbital character from experimental  $A_{\text{dip}}$  values. Explicit quantum chemical analyses are thus to be preferred instead.

**Acknowledgment.** This study has been supported by Deutsche Forschungsgemeinschaft and by Fonds der Chemischen

Industrie. Part of this work benefitted also from the graduate college "Moderne Methoden der magnetischen Resonanz in der Materialforschung" at Universität Stuttgart. We are grateful to Drs. Dominik Munzar (Brno), Bernd Schimmelpfennig (Stockholm), and Vladimir Malkin (Bratislava) for helpful discussions.

JA002062V



*Concepts without factual content are empty; sense data without concepts are blind... . The understanding cannot see. The senses cannot think. By their union only can knowledge be produced.*

*Immanuel Kant (1724-1804)*

## **8 A Density Functional Study of EPR-Parameters for Vanadyl Complexes Containing Schiff Base Ligands<sup>1</sup>**

### *Introduction*

The coordination chemistry of vanadium has recently received increased attention due to the reported biochemical activity of vanadyl complexes. The latter is being related to the interplay between four-coordinate, tetrahedral structures of vanadates(V) and five-coordinate, trigonal bipyramidal structures of vanadyl(IV) or vanadyl(V) complexes. Structural distortions have been found to be reflected characteristically in the EPR spectra of vanadyl(IV) complexes.<sup>2</sup> The following paper reports density functional calculations of electronic  $g$ -tensors and metal hyperfine coupling tensors for a series of four of these vanadyl complexes with structures ranging from nearly trigonal bipyramidal (TBP-5) to nearly square pyramidal (SQP-5). The EPR spectroscopic parameters have been rationalized in terms of electronic and geometrical structures. The author of this thesis performed all of the calculations included in the study, most of the interpretational work, and contributed significantly to the preparation of the manuscript.

### *Results*

The  $\Delta g$ -tensor components are underestimated systematically by ca. 40%. Good agreement with experiment is obtained for hyperfine tensor components calculated with hybrid functionals that account better for the spin polarization of the core orbitals than GGA functionals. The rhombicity of the hyperfine tensor is reproduced well at all levels of theory applied. It is mainly determined by the SOMO composition. The latter explains the increasing rhombicity of the  $A$ -tensor with increasing distortion of the

SQP-5 structures along the series of complexes studied. The orientational dependence of the principal tensor components on the local vanadium coordination is much more pronounced for the  $g$ -tensor than for the  $A$ -tensor.

### *Conclusions and outlook*

The paper provides interpretations of the observed trends in the spin Hamiltonian parameters in terms of the SOMO compositions and of spin-orbit coupling. In addition to the magnitudes of the principal components of both tensors, the calculations provide also their orientations relative to each other, and relative to the molecular framework. Such information is more difficult to obtain experimentally. The orientation of  $A$ - and particularly  $g$ -tensors with respect to the molecular framework, or the experimentally more accessible relative orientations of  $g$ - and  $A$ - tensors appears to be very sensitive probes of the local symmetry and coordination of the oxovanadium group.

Apart from interpretational purposes, the present study has also served as a further validation of DFT approaches for the calculation of EPR-parameters in transition metal complexes. Hybrid functionals provide better agreement with experimental hyperfine tensors than gradient-corrected functionals. Preliminary tests suggest that hybrid functionals may provide better accuracy also for  $\Delta g$ -tensor components that are underestimated systematically within the LDA and GGA approaches.<sup>3</sup>

## References

---

- <sup>1</sup> Munzarová, M. L.; Kaupp, M. *submitted to J. Phys. Chem.*
- <sup>2</sup> Cornman, C. R.; Geiser-Bush, K. M.; Rowley, S. P.; Boyle, P. D. *Inorg. Chem.* **1997**, *36*, 6401-6408.
- <sup>3</sup> Reviakine, R.; Malkin, V. G.; Malkina, O. L.; Arbouznikov, A.; Kaupp, M. *unpublished results.*

## A Density Functional Study of EPR-Parameters for Vanadyl Complexes Containing Schiff Base Ligands

Markéta L. Munzarová<sup>a,b</sup> and Martin Kaupp<sup>b,\*</sup>

<sup>a</sup>National Center for Biomolecular Research, Faculty of Science, Masaryk University, Kotlářská 2, CZ-61137 Brno, Czech Republic, and <sup>b</sup>Institut für Anorganische Chemie, Universität Würzburg, Am Hubland, D-97074 Würzburg, Germany.

**Abstract.** Deviations of the coordination arrangement of vanadyl complexes from a regular square pyramid are thought to influence, among other things, their biological function. Such structural distortions have been found to be reflected characteristically in EPR spectra (Cornman et al. *Inorg. Chem.* **1997**, 36, 6401). In this work, density functional calculations of electronic  $g$ -tensors and metal hyperfine coupling tensors have been carried out for a series of four of these vanadyl complexes with structures ranging from nearly trigonal bipyramidal (TBP-5) to nearly square pyramidal (SQP-5). The EPR spectroscopic parameters have been rationalized in terms of electronic and geometrical structures. Using all relevant perturbation operators together with local or gradient-corrected density functionals,  $\Delta g$ -tensor components are underestimated systematically by ca. 40%. Good agreement with experiment is obtained for hyperfine tensor components calculated with hybrid functionals (B3PW91, BHPW91), which account better for the spin polarization of the core orbitals than GGA functionals like BP86. The rhombicity of the hyperfine tensor is reproduced well at all levels of theory applied. It is mainly determined by the SOMO composition. The latter explains the increasing rhombicity of the  $A$ -tensor with increasing distortion of the SQP-5 structures along the series of complexes studied. The orientational dependence of the principal tensor components on the local vanadium coordination is much more pronounced for the  $g$ -tensor than for the  $A$ -tensor. The principal axes of the  $g$ - and  $A$ -tensors are found to be rotated with respect to each other by as much as  $41^\circ$ .

**Keywords.** Bioinorganic chemistry, density functional theory, EPR hyperfine coupling tensors,  $g$ -tensors, vanadyl complexes.

## 1. Introduction

The coordination chemistry of vanadium has recently received increased attention, due to the discovery of enzymes requiring vanadium for activity,<sup>1</sup> and due to the insulin-like effects elicited by vanadium complexes in diabetic animals.<sup>2</sup> The biochemical activity of vanadium is often related to the interplay between four-coordinate, tetrahedral structures of vanadates(V) and five-coordinate, trigonal bipyramidal (TBP-5) structures of vanadyl(IV) or vanadyl(V) complexes.<sup>3</sup> The TBP-5 coordination appears to be the consequence of significant steric constraints, as square pyramidal (SQP-5) or distorted SQP-5 complexes are formed in the absence of bulky ligands.<sup>4</sup> To probe these constraints, Cornman et. al. have recently prepared a series of vanadyl complexes, in which the coordination arrangement varied from approximately SQP-5 to approximately TBP-5.<sup>5</sup> An angular structural parameter  $\tau$  (ranging from  $\tau=0$  for purely SQP-5 coordination to  $\tau=1$  for purely TBP-5 coordination) has been introduced to quantitatively compare the coordination sphere of the metal. The value of  $\tau$  varied from 0.26 to 0.70 for the complexes studied in ref 5. EPR and pulsed ENDOR studies showed that both hyperfine coupling (HFC) tensor components and nuclear quadrupole coupling constant  $P_{||}$  provide a sensitive measure of changes in the arrangement of the ligands.<sup>5,6,7</sup> In particular, it was noted<sup>5</sup> that the EPR spectra of all complexes are rhombic, and that the rhombicity increases with  $\tau$ .

Our previous systematic applications of density functional theory (DFT) to the calculation of hyperfine tensors in a series of 3d transition metal complexes have taught us, that explicit quantum chemical studies may provide considerably refined interpretations of the observed spectroscopic parameters.<sup>8,9</sup> A recently developed DFT approach<sup>10</sup> for the calculation of electronic  $g$ -tensors allows us furthermore to extend our computational investigations also to this property. Here we report a detailed DFT study of hyperfine coupling and  $g$ -tensors for some of the complexes studied by Cornman et al.,<sup>5</sup> and for bis(2-methylquinoline-8-olate)oxovanadium(IV). For the latter complex, single-crystal EPR studies have provided magnitudes, as well as absolute and relative orientations, of the hyperfine and  $g$ -tensors.<sup>11</sup> We will relate the experimental and computational findings to the distribution of spin density within the complexes studied and will provide an interpretation of the correlation between the rhombicity of the tensors and  $\tau$ .

## 2. Theoretical Formalism and Computational Details

**g-Tensor calculations.** The theoretical background of EPR parameters is covered in detail in text books.<sup>12,13,14,15,16,17</sup> Hence we summarize only the most relevant points and the expressions used in our calculations. The g-tensor is calculated as correction to the free electron value (given in ppm), i.e.

$$\mathbf{g} = g_e \mathbf{1} + \Delta \mathbf{g}, \quad (1)$$

with  $g_e = 2.002322$ . Up to the level of second-order perturbation theory, the g-shift  $\Delta \mathbf{g}$  consists of the relevant Breit-Pauli terms

$$\Delta \mathbf{g} = \Delta \mathbf{g}_{SO/OZ} + \Delta \mathbf{g}_{RMC} + \Delta \mathbf{g}_{GC}, \quad (2)$$

of which the „paramagnetic“ second-order spin-orbit/orbital Zeeman cross term,  $\Delta \mathbf{g}_{SO/OZ}$ , dominates (except for extremely small  $\Delta \mathbf{g}$ -values; we also include  $\Delta \mathbf{g}_{RMC}$  and the  $\Delta \mathbf{g}_{GC}$ (1el.) in the calculations<sup>10</sup>). Within the present uncoupled DFT (UDFT) approach, its cartesian components  $u,v$  are computed as<sup>10,18</sup>

$$\Delta g_{SO/OZ,uv} = \frac{\alpha^2}{2} g_e \left[ \sum_k^{occ(\alpha)} \sum_a^{virt(\alpha)} \frac{\langle \psi_k^\alpha | H_{SO,v} | \psi_a^\alpha \rangle \langle \psi_a^\alpha | l_{O,u} | \psi_k^\alpha \rangle}{\epsilon_k^\alpha - \epsilon_a^\alpha} - \sum_k^{occ(\beta)} \sum_a^{virt(\beta)} \frac{\langle \psi_k^\beta | H_{SO,v} | \psi_a^\beta \rangle \langle \psi_a^\beta | l_{O,u} | \psi_k^\beta \rangle}{\epsilon_k^\beta - \epsilon_a^\beta} \right] \quad (3)$$

We calculate the spin-orbit (SO) operator  $H_{SO}$  in the atomic mean-field approximation (AMFI).<sup>19,20</sup> This approach has been shown<sup>10</sup> to give results to within better than a few percent of the exact Breit-Pauli one- and two-electron SO-Hamiltonian, at a small fraction of the computational effort required for the latter. For comparison, we also report results in which the two-electron spin-orbit contributions have been neglected, and only the one-electron part due to the nuclear charges has been retained. We employed a common gauge at the transition metal nucleus. Unrestricted Kohn-Sham calculations were performed within the local density approximation (VWN functional).<sup>21</sup> Gradient corrected functionals do not improve the results in the case of g-tensors of transition metal complexes.<sup>10</sup> The (15s11p6d)/[9s7p4d] metal basis set employed in our previous studies<sup>8,9,10</sup> has been used. DZVP basis sets<sup>22</sup> were used for the main group atoms. Polarization p-functions have been omitted for hydrogens of the methyl- and *t*-butyl substituents.

**Hyperfine Tensor Calculations.** The hyperfine coupling parameters describe the interactions of unpaired electrons with various magnetic nuclei. The 3×3 hyperfine

interaction tensor  $A$  can be separated into its isotropic and anisotropic (dipolar) components. The isotropic part reflects the spin density at the point of the magnetic nucleus. The anisotropic part yields additional information about the local environment of a paramagnetic center. In the first-order approximation (neglecting spin-orbit effects; cf. below), isotropic hyperfine splittings  $A_{\text{iso}}(N)$  correspond to the Fermi-contact term  $A_{\text{FC}}$ :

$$A_{\text{iso}}(N) = A_{\text{FC}} = \frac{4\pi}{3} \beta_e \beta_N g_e g_N \langle S_Z \rangle^{-1} \sum_{\mu, \nu} P_{\mu, \nu}^{\alpha-\beta} \langle \varphi_\mu | \delta(\mathbf{R}_N) | \varphi_\nu \rangle . \quad (4)$$

Here  $\beta_e$  is the Bohr magneton,  $\beta_N$  the nuclear magneton,  $g_N$  is the  $g$ -value of the nucleus  $N$ ,  $\langle S_Z \rangle$  is the expectation value of the  $z$ -component of the total electronic spin,  $P_{\mu, \nu}^{\alpha-\beta}$  is the spin density matrix, and the summation runs over all occupied molecular orbitals. In the first-order approximation, the components  $T_{ij}$  of the anisotropic tensor are given by:

$$T_{ij}(N) = \frac{1}{2} \beta_e \beta_N g_e g_N \langle S_Z \rangle^{-1} \sum_{\mu, \nu} P_{\mu, \nu}^{\alpha-\beta} \langle \varphi_\mu | \mathbf{r}_N^{-5} (\mathbf{r}_N^2 \delta_{ij} - 3r_{N,i} r_{N,j}) | \varphi_\nu \rangle , \quad (5)$$

where  $\mathbf{r}_N = \mathbf{r} - \mathbf{R}_N$  ( $\mathbf{R}_N$  is the position vector of nucleus  $N$ ). In the following, we will generally refer to the metal hyperfine interaction and argument  $N$  will be omitted.

All-electron unrestricted Kohn-Sham calculations of hyperfine structure were done with the Gaussian98 program.<sup>23</sup> We have used three different combinations of exchange and correlation potentials ( $v_x[\rho]$  and  $v_c[\rho]$ , respectively), abbreviated as BP86, B3PW91, and BHPW91. The BP86 functional combines Becke's generalized-gradient-correction (GGA) functional for exchange<sup>24</sup> (B) with Perdew's 1986 GGA<sup>25</sup> (P86) for correlation. B3PW91 contains Becke's three-parameter hybrid functional for exchange (B3, including ca. 20% Hartree-Fock exchange),<sup>26</sup> while the last combination employs the "half-and-half" hybrid exchange functional (BH), incorporating as much as 50% Hartree-Fock exchange.<sup>27</sup> The latter two exchange functionals have been combined with the GGA for correlation of Perdew and Wang (PW91).<sup>28</sup> Additional BP86 calculations of the dipolar hyperfine coupling constants have been carried out with a modified version of the deMon-EPR code,<sup>29,30</sup> in which we have implemented a routine for the analysis of orbital contributions to  $A_{\text{dip}}$ .

The same vanadium orbital basis set has been used as in the  $g$ -tensor calculations (see above), in combination with the 6-31G(d) basis set for the ligands. The default

integration grids (int=finegrid option<sup>23</sup>) of the Gaussian98 program and tight SCF convergence criteria ( $10^{-7}$  in RMS DM,  $10^{-5}$  in MAX DM) have been applied.

**Relationship between Spin-Hamiltonian Parameters and Electronic Structure.** One of the aims of this study is to relate the spin Hamiltonian parameters obtained from theory/experiment to the electronic and molecular structure of a given paramagnetic center. This can be done along the lines of the classical second-order perturbation theory (PT) approach of Abragam and Pryce,<sup>31</sup> as further discussed by McGarvey<sup>15</sup>, Abragam and Bleaney<sup>12</sup>, and by Mabbs and Collison.<sup>16</sup> This approach also enables us to provide a rough semiempirical estimate of spin-orbit (SO) contributions to the hyperfine coupling which are not explicitly accounted for in our present DFT calculations of hyperfine tensors.

Within the approach of Mabbs and Collison, the components of the  $\Delta g$ -tensor and of the metal hyperfine tensor are given by<sup>16</sup>

$$\Delta g_{ij} = -2\xi_{n,l}\Lambda_{ij} \quad , \quad (6)$$

$$A_{ij} = P \left[ -\kappa\delta_{ij} - 3c l_{ij} - 2\xi_{n,l}\Lambda_{ij} + 3c\xi_{n,l}\Lambda'_{ij} \right] \quad . \quad (7)$$

Here  $P = g_e g_N \beta_e \beta_N \langle \varphi_o | r^{-3} | \varphi_o \rangle$  ( $\varphi_o$  is the singly occupied molecular orbital - SOMO),<sup>32</sup>  $c = 2/[(2l-1)(2l+3)]$  ( $2/21$  for a  $d$  electron), and  $l_{ij} = \langle \varphi_o | \hat{l}_i \hat{l}_j + \hat{l}_j \hat{l}_i | \varphi_o \rangle - \frac{1}{3}l(l+1)\delta_{ij}$ . The  $-\kappa\delta_{ij}$  term accounts for the Fermi contact contribution to the isotropic part of the tensor, whereas the  $-3cPl_{ij}$  term represents the first-order (SOMO) contribution to the anisotropic part of the tensor.  $\xi_{n,l}$  is the spin-orbit coupling constant. The terms  $\Lambda_{ij}$  and  $\Lambda'_{ij}$  are defined as

$$\Lambda_{ij} = \sum_m \frac{\langle \varphi_o | \hat{l}_i | \varphi_m \rangle \langle \varphi_m | \hat{l}_j | \varphi_o \rangle}{\varepsilon_m - \varepsilon_o} \quad , \quad (8)$$



$$\Lambda'_{ij} = -\frac{i}{2} \sum_{t,r} \varepsilon_{itr} \sum_m \frac{\langle \varphi_o | \hat{l}_r | \varphi_m \rangle \langle \varphi_m | \hat{l}_j \hat{l}_t + \hat{l}_t \hat{l}_j | \varphi_o \rangle}{\varepsilon_m - \varepsilon_o} \quad (9)$$

In the latter expression,  $\varepsilon_{itr}$  is 1 (-1) if  $(i,t,r)$  is an even (odd) permutation of  $(x,y,z)$  and 0 otherwise. The summation over  $m$  runs over all virtual  $d$ -type orbitals (cf. below). In the expression (11) for the  $\Delta g$ -tensor,  $\Lambda_{ij}$  approximates the paramagnetic part of  $\Delta g$ , given by eq. 5. In the  $A$ -tensor expression (12), the  $\Lambda_{ij}$  elements account for the cross-terms between orbital Zeeman and spin dipolar operator;<sup>33</sup> the elements  $\Lambda'_{ij}$  represent second-order spin-dipolar contributions. One third of the trace of  $T_{ij}$  gives the second-order “pseudocontact” contribution ( $A_{PC}$ ) to the isotropic coupling.<sup>34</sup>

Equations 6 and 7 are often used either to determine MO compositions from the known spin Hamiltonian parameters or *vice versa*. The elements  $l_{ij}$ ,  $\Lambda_{ij}$  and  $\Lambda'_{ij}$  are expressed in terms of compositions and relative energies of the SOMO,  $\varphi_o$ , and of those virtual MOs,  $\varphi_m$ , which are dominated by metal  $d$ -orbital contributions (cf. ref 16, Chapter 9). The values of  $\varepsilon_m - \varepsilon_o$  and of  $\xi_{n,l}$  are usually estimated experimentally. Beyond interpretation purposes, this approach will in the following be used to estimate SO effects on the hyperfine tensor for the  $\text{VO}(\text{L}^2)_2$  complex. The latter system is a  $d^1$  complex possessing  $C_2$  symmetry. The detailed expressions for the spin Hamiltonian parameters in this point group can be found on pages 384-386 of ref 16 (the reference appears to contain two typing errors<sup>35</sup>). The coefficients of the metal  $d$ -orbitals in MOs  $\varphi_o \varphi_1 \dots \varphi_5$ <sup>36</sup> have been determined from a restricted open-shell BP86 calculation. Each coefficient has been taken as the square root of the Mulliken gross orbital population summed over all basis functions of a given symmetry.<sup>37</sup> The value of the parameter  $P$  has been determined from the same calculation, using the fact that, within the first-order approximation,  $T_{ZZ} = -3c P l_{zz}$ . The relative energies, as well the  $g$ -tensor components - cf. equations (9.248)-(9.252) in ref 16 - have been taken from experiment (ref 5). The value of the SO coupling constant ( $148.4 \text{ cm}^{-1}$ ) has been taken from ref 11.

**Structures.** Figure 1 shows the complexes studied:  $[\text{N,N}'\text{-ethylenebis}(o\text{-tert-butyl-}p\text{-methylsalicylaldiminato})]\text{oxovanadium(IV)} = \text{VOL}^1$  ( $\tau=0.26$ ),  $\text{bis}(N\text{-methylsalicylaldiminato})\text{oxovanadium(IV)} = \text{VO}(\text{L}^2)_2$  ( $\tau=0.55$ ),  $\text{bis}(N\text{-methyl-}o\text{-tert-butyl-}p\text{-methylsalicylaldiminato})\text{oxovanadium(IV)} = \text{VO}(\text{L}^3)_2$  ( $\tau=0.70$ ), and  $\text{bis}(2\text{-methylquinoline-}8\text{-olate})\text{oxovanadium(IV)} = \text{VO}(\text{L}^4)_2$ .

For VOL<sup>1</sup>, VO(L<sup>2</sup>)<sub>2</sub>, and VO(L<sup>3</sup>)<sub>2</sub>, structural data from X-ray diffraction have been used.<sup>5</sup> Of these complexes, only VO(L<sup>2</sup>)<sub>2</sub> has crystallographically imposed symmetry (C<sub>2</sub>). No experimental structural data have been available for VO(L<sup>4</sup>)<sub>2</sub>. We have therefore optimized the structure in unrestricted Kohn-Sham calculations with the B3LYP functional (using the Gaussian98 program<sup>23</sup>). The optimization employed a small-core effective-core potential (ECPs) and (8s7p6d)/[6s5p3d] GTO valence basis set for the metal,<sup>38</sup> ECPs with (4s4p1d)/[2s2p1d] basis sets<sup>39</sup> for the ligand atoms, and a (4s1p)/[2s1p] hydrogen basis.<sup>40</sup> The optimization has been performed within the C<sub>2</sub> symmetry indicated by experiment.<sup>11</sup> The resulting structure parameters are reported as supporting information. The optimized |VO<sub>axial</sub>| bond length for VO(L<sup>4</sup>)<sub>2</sub> (1.59 Å) is (within 0.01 Å) the same as found experimentally for VOL<sup>1</sup>, VO(L<sup>2</sup>)<sub>2</sub>, VO(L<sup>3</sup>)<sub>2</sub>. The optimized |VO<sub>ph</sub>| bond length for VO(L<sup>4</sup>)<sub>2</sub> (1.94 Å) lies also within the range of bond lengths found for the other complexes (1.89-1.94 Å). The optimized |VN| bond length for VO(L<sup>4</sup>)<sub>2</sub> (2.16 Å) is somewhat longer than in the other complexes (2.06-2.10 Å). The distortion parameter  $\tau$  for optimized VO(L<sup>4</sup>)<sub>2</sub> structure, 0.55, is the same as for VO(L<sup>2</sup>)<sub>2</sub>.

**Orientation.** All *g*- and *A*-tensor calculations have been performed for the following standard cartesian coordinate system: The  $\vec{VO}_{axial}$  vector defines the positive *z* direction. For VOL<sup>1</sup>, the *y* axis lies in the  $VO_{ph,1} \leftrightarrow O_{ph,2}$  plane, perpendicular to the *z*-axis.<sup>41</sup> For VO(L<sup>2</sup>)<sub>2</sub>, VO(L<sup>3</sup>)<sub>2</sub>, and VO(L<sup>4</sup>)<sub>2</sub>, the *y* axis is defined in the same way but is additionally rotated by +45° around the  $\vec{VO}_{axial}$  vector. This choice of the coordinate system, shown in Figures 2 and 3, is the same as used by Mabbs and Collison<sup>16</sup> for d<sup>1</sup> complexes possessing genuine or approximate C<sub>2</sub> or C<sub>s</sub> symmetries.

### 3. Results and Discussion

Each of the complexes studied here contains one unpaired electron and may be regarded as a *d*<sup>1</sup> system. The SOMO is generally dominated by a metal *d*<sub>x<sup>2</sup>-y<sup>2</sup>-type orbital (ca. 80%), and the largest ligand contribution corresponds to phenolate oxygen *p* orbitals (ca. 10%). The total spin population at vanadium reaches 1.10 due to the spin polarization of the V=O<sub>axial</sub> bond; a negative spin population of ca. -0.10 is left at the axial oxygen (all numbers refer to Mulliken population analyses of UBP86 results for the four complexes).</sub>

**3.1. *g*-Tensor Calculations.** Computed  $\Delta g$  components with respect to standard and principal axes are given in Tables 1 and 2, respectively. Both tables refer to the accurate atomic mean-field treatment of the  $\Delta g_{\text{SO/OZ}(1e)}$  and  $\Delta g_{\text{SO/OZ}(2e)}$  terms. In Table 2 we have also included results obtained if the  $\Delta g_{\text{SO/OZ}(2e)}$  contributions are neglected. As found previously for a series of 3d complexes,<sup>10</sup> the latter results are in apparently better agreement with experiment than the former, obviously due to a compensation of errors due to the neglect of the  $\Delta g_{\text{SO/OZ}(2e)}$  terms and errors in the DFT treatment. The proper inclusion of both one- and two-electron SO terms leads to a systematic underestimate of all components by ca. 40%. Gradient-corrected functionals also underestimate paramagnetic contributions to <sup>57</sup>Fe or <sup>59</sup>Co NMR chemical shifts by roughly the same relative amount, whereas hybrid functionals perform significantly better.<sup>42</sup> We are therefore presently implementing the calculation of *g*-tensors with hybrid functionals. Preliminary tests suggest that this approach may indeed provide improved accuracy.<sup>43</sup>

After completion of this work, Carl et al. reported on their DFT calculations of *A*- and *g*-tensors of some vanadyl(IV) model complexes, with the aim of interpreting EPR spectra of VO<sup>2+</sup> exchanged zeolites.<sup>44</sup> For their *g*-tensor calculations, they used the two-component ZORA approach of van Lenthe et al.,<sup>45</sup> with the BP86 GGA functional. Carl et al. report significantly larger *g*-shifts than in the present study and conclude that the DFT approach used provides excellent agreement with experiment. Unfortunately, this good performance is fortuitous and is probably due to cancellation of DFT errors with errors resulting from the neglect of spin polarization (and partly from the incomplete treatment of the  $\Delta g_{\text{SO/OZ}(2e)}$  terms<sup>10</sup>) in the two-component ZORA approach used.

The orientations of the *g*-tensors are displayed in Figures 2-5. Table 3 includes the angles between the principal axes of the *g*-tensor and the standard axes. The full specification of principal relative to the standard axes is provided as supporting information. Table 3 shows that for complexes with a trans-arrangement of the phenolate oxygen atoms, the *g*<sub>1</sub> principal axis is either parallel or almost parallel to the *z* axis, whereas *g*<sub>2</sub> and *g*<sub>3</sub> are rotated with respect to *y* and *x*, on average by 30°. For VOL<sup>1</sup>, *g*<sub>2</sub> is almost parallel to the *y* axis whereas *g*<sub>1</sub> and *g*<sub>3</sub> are rotated with respect to *z* and *x* by 12° and 10°, respectively (note that neglect of the  $\Delta g_{\text{SO/OZ}(2e)}$  terms affects the tensor orientation negligibly). For these three systems, there is no experimental information to be compared with regarding the orientation of the *g*-tensor with respect to the molecular framework. We focus therefore on the interpretation of the computational results. We will base our discussion on the perturbational approach discussed in section 2.

We are dealing here with d<sup>1</sup> complexes possessing genuine *C*<sub>2</sub> symmetry (VO(L<sup>2</sup>)<sub>2</sub>, VO(L<sup>4</sup>)<sub>2</sub>), approximate *C*<sub>2</sub> symmetry (VO(L<sup>3</sup>)<sub>2</sub>), or approximate *C*<sub>s</sub> symmetry

(VOL<sup>1</sup>). As a consequence, for VO(L<sup>2</sup>)<sub>2</sub> and VO(L<sup>4</sup>)<sub>2</sub> one of the principal axes ( $g_1$ ) must coincide with the two-fold axis ( $z$ ) for symmetry reasons.<sup>14</sup> In a hypothetical VOL<sup>1</sup> molecule possessing genuine  $C_s$  symmetry, one of the principal axes would have to be perpendicular to the  $xz$  symmetry plane and thus coincident with the  $y$  axis. The actual deviation of  $g_2$  from  $y$  ( $6^\circ$ , cf. Table 3) may thus be considered to be a measure of the distortion from  $C_s$  symmetry. For VO(L<sup>3</sup>)<sub>2</sub>, by analogy, the deviation of  $g_1$  from  $z$  ( $7^\circ$ ) corresponds to the distortion from  $C_2$  symmetry.

The extent of the rotation of the principal axes relative to the standard axes depends upon the values of the off-diagonal tensor elements,<sup>16</sup> but also on the relative sizes of the principal components. For genuinely  $C_2$  symmetrical complexes, it can be shown that the angle  $\varphi$  between  $g_2$  and  $y$  and between  $g_3$  and  $x$  is related to the off-diagonal matrix  $g_{xy}$  element and the principal  $g_{22}$  and  $g_{33}$  components via

$$2g_{xy} = (g_{22} - g_{33}) \sin 2\varphi \quad . \quad (10)$$

The  $g_{xy}$  component is of the same size (cf. Table 1) for VO(L<sup>2</sup>)<sub>2</sub> and VO(L<sup>4</sup>)<sub>2</sub>, but the value of  $|g_{22}-g_{33}|$  is smaller for the former complex (cf. Table 2). Consequently,  $g_2$  and  $g_3$  deviate more from the  $y$  and  $x$  directions, respectively, for VO(L<sup>2</sup>)<sub>2</sub> than for VO(L<sup>4</sup>)<sub>2</sub> (cf. Table 3).

According to Mabbs and Collison,<sup>16</sup> the rotation of  $g_2$  and  $g_3$  relative to  $y$  and  $x$  is dominated by the magnitude of the  $d_x^2 - y^2 \rightarrow d_{xz}$ ,  $d_x^2 - y^2 \rightarrow d_{yz}$  contributions (cf. eqs 9.233 - 9.237 in ref 16), which determine the magnitudes of the  $g_{xx}$ ,  $g_{yy}$ , and  $g_{xy}$  elements. By analogy, the rotation of  $g_1$  and  $g_3$  with respect to  $z$  and  $x$  for VOL<sup>1</sup> is determined mainly by the  $d_x^2 - y^2 \rightarrow d_{xy}$ ,  $d_x^2 - y^2 \rightarrow d_{yz}$  contributions (cf. eqs 9.243 and 9.247 in ref 16).<sup>46</sup> An analysis of different contributions to the calculated  $g$ -shifts shows that the paramagnetic (1-electron and 2-electron SO) contributions represent 99% of the  $g$ -tensor components given in Tables 1 and 2. An analysis of the orbital contributions to  $g$ -tensor elements further reveals that the SO terms corresponding to the excitations from the SOMO greatly dominate the  $g$ -tensor elements. Thus, our results show that the approach of Mabbs and Collison, which emphasizes the SOMO contributions, provides a reasonable insight into the origin of the  $g$ -tensor.

**3.2. A-Tensor Calculations.** Our density-functional results for the hyperfine tensor of vanadium with respect to standard and principal axes are given in Tables 4 and 5, respectively. Part of the information in Table 5 is graphically displayed in Figures 6-8.<sup>47</sup> The SOMO provides a small direct contribution to the isotropic hyperfine coupling

constants (HFCCs), due to a slight mixing-in of the metal 4s orbital. Nevertheless, overall  $A_{\text{iso}}$  is dominated by spin polarization and is thus negative. The anisotropic tensor reflects the composition of the SOMO, having one negative component along the  $z$  axis and two positive components within the  $xy$  plane,<sup>48</sup> pointing between the V-N and V-O<sub>phenolate</sub> bonds. Like the  $g$ -tensor, the  $A$ -tensor deviates from axial symmetry.<sup>49</sup> The smaller of the positive components points into the direction of the chelate ligands, and the larger one points out of the complex.

At the nonrelativistic (first-order) level of theory, the BHPW91 functional provides the best agreement with experiment for both the isotropic and the anisotropic parts of the hyperfine tensor. As has been stressed in our recent study,<sup>8</sup> GGA functionals typically underestimate the spin polarization of  $s$ -type metal core orbitals. The latter is enhanced by exact-exchange mixing into  $v_x$ , frequently leading to improved agreement with experimental  $A_{\text{iso}}$  data with hybrid functionals (provided that spin contamination remains low). Figure 6 illustrates the enhancement of spin polarization by inclusion of exact exchange for three of the vanadyl complexes. It also shows that, for systems with related electronic structures, the deficiencies of the state-of-the-art density functionals are systematic. An underestimate of core-shell spin polarization with the BP86 GGA functional is also apparent from the results of the very recent  $A$ -tensor calculations of Carl et al.<sup>44</sup> for a series of vanadyl model complexes.

Similarly, adequate spin polarization of metal  $p$ -type core orbitals is required to reproduce the hyperfine tensor anisotropy.<sup>8,9,50</sup> The absolute values of the dipolar tensor components are quantitatively reproduced only with the BHPW91 functional (cf. Table 5 and Figure 7). B3PW91, and particularly BP86, underestimate all anisotropic components. On the other hand, all unrestricted DFT approaches applied describe the rhombicity of the hyperfine tensor well. The ( $T_{33} - T_{22}$ ) difference does not suffer from the systematic underestimate of spin polarization, as it is determined mainly by the composition of the singly occupied molecular orbital. The relative magnitudes of spin polarization of the metal  $2p_x$ ,  $3p_x$  and  $2p_y$ ,  $3p_y$  orbitals correspond to the rhombicity of the SOMO contribution to the anisotropic HFC tensor. Thus, while the absolute values of the  $T_{22}$ ,  $T_{33}$  components are significantly affected by the spin-polarization contributions, the asymmetry of the tensor ( $T_{33} - T_{22}$ ) is reduced only slightly by core-shell spin polarization.

The present DFT calculations do not include relativistic corrections, which may be quite important for systems with significant  $g$ -tensor anisotropy. To obtain a simple semiempirical estimate of SO corrections, as well as an improved interpretation of the HFC anisotropy, we have used the PT approach described in section 2 to express the  $A$ -tensor of VO(L<sup>2</sup>)<sub>2</sub>. The first-order (SOMO) contributions to the anisotropic part of the  $A$ -tensor have been estimated as  $-192.8$  ( $T_{zz}$ ),  $80.3$  ( $T_{xx}$ ),  $112.5$  ( $T_{yy}$ ), and  $1.4$  ( $T_{xy} = T_{yx}$ )

MHz. The second-order  $\Lambda_{ij}$  elements provide additional  $-17.9$  ( $T_{zz}$ ),  $-6.7$  ( $T_{xx}$ ), and  $-7.4$  ( $T_{yy}$ ) MHz.<sup>51</sup> Finally, the  $\Lambda'_{ij}$  elements have been estimated as  $-3.4$  ( $T_{zz}$ ),  $-0.6$  ( $T_{xx}$ ),  $-1.0$  ( $T_{yy}$ ),  $-0.1$  ( $T_{xy}$ ), and  $0.2$  ( $T_{yx}$ ) MHz. After summing these contributions and transforming the resulting tensor to its principal axes, we obtain the following components:  $-214.1$  ( $T_{11}$ ),  $75.1$  ( $T_{22}$ ), and  $102.1$  ( $T_{33}$ ) MHz. This tensor has a nonzero trace that, multiplied by a factor of  $1/3$ , gives the pseudocontact contribution to the isotropic HFCC ( $-12.3$  MHz). Subtracting the pseudocontact term from the  $T_{ii}$  components, we obtain a traceless anisotropic HFC tensor in the 2<sup>nd</sup>-order approximation. The components of this tensor are  $-201.8$  MHz,  $87.4$  MHz, and  $114.4$  MHz, of which the 2<sup>nd</sup>-order contributions represent  $-9.0$ ,  $4.6$ , and  $4.4$  MHz, respectively. After subtraction of these contributions from the experimental HFC tensor, the B3PW91 and BHPW91 functionals would appear to describe the 1<sup>st</sup>-order hyperfine coupling about equally well. The former underestimates and the latter overestimates  $A_{iso}$  and all  $T_{ii}$  components.

Besides an estimate of the SO contributions, the perturbation theoretical approach *qualitatively* reproduces and rationalizes the rhombicity of the  $A$ -tensor. As discussed above, the difference  $T_{22}-T_{33}$  arises mainly from the 1<sup>st</sup>-order (SOMO) contribution. The only 1<sup>st</sup>-order term which can account for this is a very small (0.2%) symmetry-allowed mixing of the metal  $d_z^2$  orbital into the SOMO, cf. eqs (9.239)-(9.242) in ref 16.<sup>52</sup> This mixing hybridizes the unpaired electron density outside of the chelate rings (i.e. in the  $x$  direction, cf. Figures 2, 3), so that  $T_{22} < T_{33}$ . This approximate treatment cannot aim at *quantitative* agreement with experiment. The rhombicity of the tensor ( $T_{22}-T_{33}$ ) is overestimated. This is understandable, as explicit restricted (ROBP86) Kohn-Sham calculations, using formula (3), also overestimate  $T_{ii}$  ( $T_{11} = -192.8$  MHz,  $T_{22} = 80.3$  MHz, and  $T_{33} = 112.5$  MHz). The influence of the second-order contributions on the asymmetry of the hyperfine tensor is only minor ( $T_{33} - T_{22}$  is decreased by  $0.2$  MHz), as both  $\Lambda_{ij}$  and the  $\Lambda'_{ij}$  contributions to  $T_{33}$  and  $T_{22}$  have identical sign and similar magnitudes. The rhombicity of the HFC tensor in  $\text{VO}(\text{L}^4)_2$  can be understood along the same lines as for  $\text{VO}(\text{L}^2)_2$ . The situation is more complicated for  $\text{VO}(\text{L}^1)$  and  $\text{VO}(\text{L}^3)_2$ , due to the lack of symmetry.

An interesting observation has been made by Cornman et al. on the correlation of  $A_{33} - A_{22}$  (in their notation  $A_{xx} - A_{yy}$ ) and the distortion parameter  $\tau$  for  $\text{VO}(\text{L}^1)$ ,  $\text{VO}(\text{L}^2)_2$ , and  $\text{VO}(\text{L}^3)_2$ .<sup>5</sup> While one of the components was found to be relatively stable with respect to the distortion, the other experienced significant enhancement (cf. Figure 8). Our calculations allow an unambiguous breakdown of the experimental tensor into its isotropic and dipolar parts. While  $T_{33}$  and  $A_{iso}$  increase with increasing  $\tau$  ( $A_{iso}$  becomes less negative; cf. Figure 6),  $T_{22}$  decreases by approximately the same magnitude (cf.

Figure 7). Due to the combination of these effects,  $A_{22}$  remains constant, whereas  $A_{33}$  changes significantly along the SQP-5→TBP-5 distortion coordinate (Figure 8). Thus, in contrast to the interpretation in ref 5, increasing  $\tau$  affects both in-plane dipolar contributions to a similar extent. The increased difference between  $T_{22}$  and  $T_{33}$  from  $\text{VO}(\text{L}^2)_2$  to  $\text{VO}(\text{L}^3)_2$  may be understood in terms of SOMO composition: i) The metal  $d_{xz}$  and  $d_{yz}$  orbitals mix into the SOMO with different coefficients for  $\text{VO}(\text{L}^3)_2$  but not for  $\text{VO}(\text{L}^2)_2$ , where this is prohibited by symmetry. ii) The vanadium  $d_z^2$  orbital mixes into the SOMO more for  $\text{VO}(\text{L}^3)_2$  than for  $\text{VO}(\text{L}^2)_2$ . Both contributions hybridise the spin density further out of the chelate rings in  $\text{VO}(\text{L}^3)_2$ . In  $\text{VO}(\text{L}^1)_2$ , the metal  $d_{xz}$  and  $d_{yz}$  orbitals mix less into the SOMO than in  $\text{VO}(\text{L}^3)_2$ , and their contribution to the anisotropy in  $T_{22}$  and  $T_{33}$  is compensated by reduced  $d_z^2$  mixing, resulting in a total anisotropy that is similar as in  $\text{VO}(\text{L}^1)$ .

A comparison of the A-tensor results for  $\text{VO}(\text{L}^2)_2$  and  $\text{VO}(\text{L}^4)_2$  (cf. Table 5) reveals that the anisotropic HFC tensor components of both complexes are very close, in agreement with identical distortion parameters  $\tau$  (0.55) and similar  $d_{xy}$ ,  $d_{x^2-y^2}$ ,  $d_z^2$  contributions to the SOMO. Due to a higher 4s orbital contribution to the SOMO for  $\text{VO}(\text{L}^4)_2$ , the isotropic HFCC is less negative than for  $\text{VO}(\text{L}^2)_2$ .

The orientations of the A-tensors are shown in Figures 2-5, together with those of the g-tensors. Table 3 includes the angles between the principal axes of the A- and g-tensors, and the standard axes. The full specification of the principal axes of the A-tensor with respect to the standard axes is given as supporting information. Table 3 shows that  $a_1$  is oriented either parallel or close to parallel to the z axis (rotated from z by maximally 6°). The axes of  $a_2$  and  $a_3$  are rotated with respect to y and x by maximally 12°. This is much less than for the g-tensor axes, due to the fact that the off-diagonal elements of the A-tensor are much smaller with respect to the asymmetry in the principal components than for the g-tensor (cf. eq. 13; Tables 4 and 1). Generally, the hyperfine tensor is controlled by the nature of the ground state wave function. In contrast, the g-tensor reflects also energies and character of the excited states.<sup>16</sup> These appear to be particularly sensitive to the local metal coordination. For the same reason, the SQP-5→TBP-5 distortion influences the A-tensor orientation relatively little, whereas the g-tensor is reoriented significantly.

Only for  $\text{VO}(\text{L}^4)_2$ , experimental information is available on the relative orientation of g- and A- tensors.<sup>11</sup> Single-crystal data indicate that the g-tensor component with the smallest g-shift (in our notation  $g_{33}$ ) is rotated by 27.5° relative to the A-tensor component with the smallest magnitude of the dipolar interaction (in our notation  $A_{22}$ ):  $\angle(a_2, g_3) = 27.5^\circ$ . Our computational results suggest that the  $A_{22}$  orientation is closer to the  $g_{22}$  orientation than to the  $g_{33}$  orientation:  $\angle(a_2, g_2) = 35.7^\circ$ ,

$\angle(a_2, g_3) = 54.3^\circ$  (cf. Table 3). It is possible that deficiencies in our DFT treatment are responsible for the different rotation angles. However, the angle is neither affected significantly by the inclusion or neglect of the  $\Delta g_{SO/OZ(2e)}$  operators nor by the use of local or gradient-corrected density functionals. At the moment we can only state that theory agrees with experiment on a ca.  $30^\circ$  relative rotation of the “perpendicular” principal components of *g*- and *A*-tensors. Further theoretical and/or experimental work is needed to decide which *g*- and *A*-tensor components ( $a_2, a_3, g_2, g_3$ ) have the most similar orientations.

#### 4. Conclusions

The increasing rhombicity of both *A*- and *g*-tensors with increasing deviations of the structures of vanadyl(IV) complexes from a regular square-pyramidal (SQP-5) coordination arrangement is reproduced by our density functional calculations. We could therefore provide improved interpretations of the observed trends in terms of the SOMO compositions and of spin-orbit coupling. In addition to the magnitudes of the principal components of both tensors, the calculations provide also their orientations relative to each other, and relative to the molecular framework. Such information is more difficult to obtain experimentally. In the present series of system, the necessary single-crystal experiments were only available for one of the systems,  $VO(L^4)_2$ . While some discrepancies remain in the designation of the components in this case, all calculations indicate clearly that the *g*-tensor is affected more by the structural distortions of the SQP-5 arrangement than the metal *A*-tensor. This may be rationalized by the fact that the hyperfine tensor depends only on the spin-density distribution of the ground state, whereas the *g*-tensor is a response property and thus also reflects the compositions of excited states. As a consequence, the *A*- and *g*-tensors are non-coaxial in all of the systems studied here. The orientation of *A*- and particularly *g*-tensors with respect to the molecular framework, or the experimentally more accessible relative orientations of *g*- and *A*-tensors, may be very sensitive probes of the local symmetry and coordination of the oxovanadium group. In the case of the *A*-tensor, the increasing rhombicity with increasing SQP-5  $\rightarrow$  TBP-5 distortion arises due to the mixing of metal  $d_z^2$  orbitals (made possible by the transformation from SQP-5 towards TBP-5 coordination), but also of metal  $d_{xz}, d_{yz}$  orbitals (allowed by the deviation from  $C_2$  symmetry), into the  $d_x^2 - d_y^2$ -type SOMO.

Apart from interpretational purposes, the present study has also served as a further validation of DFT approaches for the calculation of EPR-parameters in transition metal complexes. The vanadyl complexes studied here exhibit a SOMO with relatively little



overlap to doubly occupied metal valence orbitals. In agreement with our previous considerations,<sup>8,9</sup> spin contamination with increasing exact-exchange mixing is therefore not a serious problem. Hybrid functionals (B3PW91, BHPW91) provide better agreement with experimental isotropic HFCCs than a GGA functional (BP86), due to an improved description of the spin polarization of metal s-type core shells.<sup>8</sup> All functionals, including the BP86 GGA, reproduce well the experimentally observed trends in the anisotropy of the *A*-tensor with increasing structural distortion (which is dominated by the SOMO composition; cf. above).

As found already in the previous, extensive validation of our DFT approach for the calculation of electronic *g*-tensors,<sup>10</sup> LDA or GGA functionals underestimate the paramagnetic ( $\Delta g_{\text{SO/OZ}}$ ) contributions systematically by ca. 40% for 3d transition metal complexes (whereas a slight overestimate by ca. 10% is typical for main group radicals). In agreement with the suggestions of Patchkowskii and Ziegler,<sup>53</sup> we attribute this to deficiencies of the GGA/LDA functionals in describing both energy denominators and matrix elements in the second-order perturbation theory expressions (cf. eq 3). While a partial or complete neglect of the  $\Delta g_{\text{SO/OZ}}(2e)$  terms improves the agreement with experiment in the 3d complexes, this is certainly no satisfactory approach from a theoretical point of view. Preliminary tests suggest that hybrid functionals may provide better accuracy (cf. section 3.1<sup>43</sup>).

**Acknowledgments.** We thank Drs. Pavel Kubáček, Dominik Munzar (Brno) and Juha Vaara (Helsinki) for helpful discussions. Drs. Olga L. Malkina (Bratislava) and Reinaldo Pis-Diez (UNLP, Argentine) kindly provided us with codes that simplified the analyses carried out. This work has been supported by Deutsche Forschungsgemeinschaft (Schwerpunktprogramm „Hochfeld-EPR“, SPP1051) and by Fonds der chemischen Industrie. Further support came from the graduate college “Moderne Methoden der Magnetischen Resonanz“ at Universität Stuttgart.

## References

\*Correspondence author, e-mail: kaupp@mail.uni-wuerzburg.de

---

- <sup>1</sup> a) Vilter, H. In *Metal Ions in Biological Systems*; Sigel, H., Sigel, A., Eds.; Marcel Dekker: New York, 1995; Vol. 31, pp 325-362. b) Eady, R. R. In *Metal Ions in Biological Systems*; Sigel, H., Sigel, A., Eds.; Marcel Dekker: New York, 1995; Vol. 31, pp 363-405. c) Butler, A.; Walker, J. V. *Chem. Rev.* **1993**, *93*, 1937-1944.
- <sup>2</sup> See, e.g., a) Shechter, Y.; Karlsh, S. J. D. *Nature* **1980**, *284*, 556-558. b) Shechter, Y.; Meyerovitch, J.; Farfel, Z.; Sack, J.; Bruck, R.; Bar-Meir, S.; Amir, S.; Degani, H.; Karlsh, S. J. D. In *Vanadium in Biological Systems*, Chasteen, N. D., Ed.; Kluwer Academic Publishers: Dordrecht, The Netherlands, 1990; pp 129-142. c) Orvig, C.; Thompson, K. H.; Battel, M.; McNeal, J. H. In *Metal Ions in Biological Systems*; Sigel, H., Sigel, A., Eds.; Marcel Dekker: New York, 1995; Vol. 31, pp 575-594.
- <sup>3</sup> Crans, D. C. *Comments Inorg. Chem.* **1994**, *16*, 35-76.
- <sup>4</sup> Morcky, L. M.; Carrano, C. J. *Inorg. Chem.* **1993**, *32*, 6119-6121.
- <sup>5</sup> Cornman, C. R.; Geiser-Bush, K. M.; Rowley, S. P.; Boyle, P. D. *Inorg. Chem.* **1997**, *36*, 6401-6408.
- <sup>6</sup> Grant, C. V.; Geiser-Bush, K. M.; Cornman, C. R.; Britt, R. D. *Inorg. Chem.* **1999**, *38*, 6285-6288.
- <sup>7</sup> Grant, C. V.; Cope, W.; Ball, J. A.; Maresch, G. G.; Gaffney, B. J.; Fink, W.; Britt, R. D. *J. Phys. Chem. B* **1999**, *103*, 10627-10631.
- <sup>8</sup> Munzarová M.; Kaupp, M. *J. Phys. Chem. A* **1999**, *103*, 9966.
- <sup>9</sup> Munzarová, M. L.; Kubáček, P.; Kaupp, M. *J. Am. Chem. Soc.* **2000**, *122*, 11900-11913.
- <sup>10</sup> Malkina, O.L.; Vaara, J.; Schimmelpfennig, B.; Munzarová, M.; Malkin, V. G.; Kaupp, M. *J. Am. Chem. Soc.* **2000**, *122*, 9206-9218.
- <sup>11</sup> Collison, D.; Gahan, B.; Mabbs, F. J. *Chem. Soc. Dalton* **1987**, 111.
- <sup>12</sup> Abragam, A.; Bleaney, B. *Electron Paramagnetic Resonance of Transition Ions*; Clarendon Press: Oxford, 1970.
- <sup>13</sup> Atherton, N. M. *Principles of Electron Spin Resonance*, Prentice Hall: New York, 1993.

- 
- <sup>14</sup> Weil, J. A.; Bolton, J. R.; Wertz, J. E.; *Electron Paramagnetic Resonance: Elementary Theory and Practical Applications*, Wiley & Sons: New York, 1994.
- <sup>15</sup> McGarvey, B. R. In *Transition Metal Chemistry: A Series of Advances, Vol 3.*, Carlin, R. L., Ed.; New York, 1966; pp 89-201.
- <sup>16</sup> Mabbs, F. E.; Collison, D. *Electron Paramagnetic Resonance of d Transition Metal Compounds*, Elsevier: Amsterdam, 1992.
- <sup>17</sup> Harriman, J. E. *Theoretical Foundations of Electron Spin Resonance*, Academic Press: New York, 1978.
- <sup>18</sup> Schreckenbach, G.; Ziegler, T. *J. Phys. Chem. A* **1997**, *101*, 3388.
- <sup>19</sup> Hess, B. A.; Marian, C. M.; Wahlgren, U.; Gropen, O. *Chem. Phys. Lett.* **1996**, *251*, 365.
- <sup>20</sup> The code used is due to: Schimmelpfennig, B. AMFI, *Atomic Spin-Orbit Mean-Field Integral Program*; Stockholms Universitet, Sweden 1996.
- <sup>21</sup> Vosko, S. H.; Wilk, L.; Nusair, M. *Can. J. Chem.* **1980**, *58*, 1200.
- <sup>22</sup> Godbout, N.; Salahub, D. R.; Andzelm, J.; Wimmer, E. *Can. J. Chem.* **1992**, *70*, 560.
- <sup>23</sup> Frisch, M. J.; Trucks, G. W.; Schlegel, H. B.; Scuseria, G. E.; Robb, M. A.; Cheeseman, J. R.; Zakrzewski, V. G.; Montgomery, Jr., J. A.; Stratmann, R. E.; Burant, J. C.; Dapprich, S.; Millam, J. M.; Daniels, A. D.; Kudin, K. N.; Strain, M. C.; Farkas, O.; Tomasi, J.; Barone, V.; Cossi, M.; Cammi, R.; Mennucci, B.; Pomelli, C.; Adamo, C.; Clifford, S.; Ochterski, J.; Petersson, G. A.; Ayala, P. Y.; Cui, Q.; Morokuma, K.; Malick, D. K.; Rabuck, A. D.; Raghavachari, K.; Foresman, J. B.; Cioslowski, J.; Ortiz, J. V.; Baboul, A. G.; Stefanov, B. B.; Liu, G.; Liashenko, A.; Piskorz, P.; Komaromi, I.; Gomperts, R.; Martin, R. L.; Fox, D. J.; Keith, T.; Al-Laham, M. A.; Peng, C. Y.; Nanayakkara, A.; Gonzalez, C.; Challacombe, M.; Gill, P. M. W.; Johnson, B.; Chen, W.; Wong, M. W.; Andres, J. L.; Gonzalez, C.; Head-Gordon, M.; Replogle, E. S.; Pople, J. A. Gaussian 98, (Revision A.7), Gaussian, Inc.: Pittsburgh, PA, 1998.
- <sup>24</sup> Becke, A. D. *Phys. Rev. A* **1988**, *38*, 3098.
- <sup>25</sup> Perdew, J. P.; Wang, Y. *Phys. Rev. B* **1986**, *33*, 8822. *ibid* **1986**, *34*, 7406.
- <sup>26</sup> Becke, A. D. *J. Chem. Phys.* **1993**, *98*, 5648.

- 
- <sup>27</sup> Becke, A. D. *J. Chem. Phys.* **1993**, *98*, 1372.
- <sup>28</sup> Perdew, J. P. *Physica B* **1992**, *172*, 1.. Perdew, J. P. In *Electronic Structure of Solids '91*, Ziesche, P., Eschring, H., Eds.; Akademie Verlag: Berlin, 1991. Perdew, J. P.; Wang, Y. *Phys. Rev. B* **1992**, *45*, 13244.
- <sup>29</sup> Malkin, V. G.; Malkina, O. L.; Eriksson, L. A.; Salahub, D. R. In *Modern Density Functional Theory: A Tool for Chemistry, Vol. 2 of Theoretical and Computational Chemistry*, Politzer, P.; Seminario, J. M.; Eds.; Elsevier: Amsterdam, The Netherlands, 1995; pp. 273-347.
- <sup>30</sup> a) Salahub, D. R.; Fournier, R.; Mlynarski, P.; Papai, I.; St-Amant, A.; Ushio, J. In *Density Functional Methods in Chemistry*, Labanowski, J., Andzelm, J., Eds.; Springer: New York, 1991. b) St-Amant, A.; Salahub, D. R. *Chem. Phys. Lett.* **1990**, *169*, 387.
- <sup>31</sup> Abragam, A.; Pryce, M. H. L. *Proc. Roy. Soc. A.* **1951**, *205*, 135.
- <sup>32</sup> The parameter  $P$  depends on the radial wave function of the metal atom in the field of ligands and is usually treated as an adjustable parameter.
- <sup>33</sup> At this level of theory, the elements of  $-2\xi_{n,l}\Lambda_{ij}$  correspond to the  $\Delta g_{ij}$  elements.
- <sup>34</sup> While the first-order contribution to  $T_{ij}$  is symmetrical and traceless, the  $\Lambda_{ij}$  contribution is symmetrical but not traceless. In general,  $\Lambda'_{ij}$  is neither symmetrical nor traceless. See ref. 12 for a lucid discussion.
- <sup>35</sup> According to our calculation, the correct formulas for coefficients  $C_7$  and  $C_9$  should read:  $C_7 = -3e_3a_1 - 3f_3b_1 - \sqrt{3}e_3c_1$ ;  $C_9 = 3f_3a_1 - 3e_3b_1 - \sqrt{3}f_3c_1$ .
- <sup>36</sup> Formulas (9.248)-(9.252) of ref. 16 have been derived from (3)-(5), restricting the summation over  $m$  to the four MOs with the largest d-orbital contributions. In our calculations, we have therefore chosen the four unoccupied MOs with largest computed metal  $d$ -character.
- <sup>37</sup> For the standard orientation of the molecule, we obtained the following d-orbital mixings:  $\phi_0$  (MO 45a) =  $0.977 d_{xy} + 0.098 d_{x^2-y^2} - 0.040 d_z^2$ ;  $\phi_1$  (47a) =  $0.095 d_{xy} - 0.420 d_{x^2-y^2} + 0.387 d_z^2$ ,  $\phi_2$  (44b) =  $0.000 d_{xz} + 0.764 d_{yz}$ ,  $\phi_3$  (45b) =  $0.721 d_{xz} - 0.108 d_{yz}$ ,  $\phi_4$  (49a) =  $-0.082 d_{xy} + 0.516 d_{x^2-y^2} + 0.274 d_z^2$ .
- <sup>38</sup> Dolg, M.; Wedig, U.; Stoll, H.; Preuss, H. *J. Chem. Phys.* **1987**, *86*, 866.

- 
- <sup>39</sup> a) Bergner, A.; Dolg, M.; Küchle, W.; Stoll, H.; Preuss, H. *Mol. Phys.* **1993**, *80*, 1431. b) d-Type polarization functions have been taken from: *Gaussian Basis Sets for Molecular Calculations*, Huzinaga, S., Ed.; Elsevier: New York, 1984.
- <sup>40</sup> Dunning, T. H.; Hay, H. *In Methods of Electronic Structure Theory, Vol. 3 of Modern Theoretical Chemistry*, Schaefer III, H. F., Ed.; Plenum Press: New York, 1977.
- <sup>41</sup> This definition is unique, unless the  $\text{VO}_{\text{ph},1}^{\leftrightarrow}\text{O}_{\text{ph},2}$  plane is perpendicular to the  $\text{VO}_{\text{axial}}^{\rightarrow}$  vector. This is not the case for any of the complexes studied here.
- <sup>42</sup> Bühl, M. *Chem. Phys. Lett.* **1997**, *267*, 251. See also: Godbout, N.; Oldfield, E. *J. Am. Chem. Soc.* **1997**, *119*, 8065.
- <sup>43</sup> Reviakine, R.; Malkin, V. G.; Malkina, O. L.; Arbouznikov, A.; Kaupp, M. unpublished results.
- <sup>44</sup> Carl, P. J.; Isley, S. L.; Larsen, S. C. *J. Phys. Chem. A* **2001**, *105*, 4563.
- <sup>45</sup> van Lenthe, E.; Wormer, P. E. S.; van der Avoird, A. *J. Chem. Phys.* **1997**, *107*, 2488.
- <sup>46</sup> Turning this line of reasoning around, from the theoretical orientations of the principal axes one can estimate the relative sizes of the individual spin-orbit coupling terms.
- <sup>47</sup> As Figures 6-9 serve the interpretation of the experimental findings in ref 5, we have not included the data for  $\text{VO}(\text{L}^4)_2$ .
- <sup>48</sup> This is rigorously true only for the two complexes possessing  $C_2$  symmetry. For the two other complexes, we observe small deviations from the indicated directions, cf. below.
- <sup>49</sup> For the definition of the asymmetry (rhombicity) parameter, cf. ref 14, p. 116.
- <sup>50</sup> Belanzoni, P.; Baerends, E. J.; van Asselt, S.; Langewen, P. B. *J. Phys. Chem.* **1995**, *99*, 13094.
- <sup>51</sup> The corresponding contributions to  $T_{x'y'}$  and  $T_{y'x'}$  are zero, due to zero non-diagonal elements of the g-tensor (cf. Section 2).

---

<sup>52</sup> We note that the asymmetry of the HFC tensor can be influenced also by mixing of the metal 4s orbital into the SOMO, which is symmetry-allowed. This mixing is not considered in the usual interpretations, cf. refs 12, 15, 16.

<sup>53</sup> Patchkovskii, S.; Ziegler T. *J. Chem. Phys.* **1999**, *111*, 5730.

**Table 1.**  $\Delta g$ - Tensors in Standard Axes System (in ppt). <sup>a, b</sup>

|                                  | $\Delta g_{xx}$ | $\Delta g_{yy}$ | $\Delta g_{zz}$ | $\Delta g_{xy} = \Delta g_{yx}$ | $\Delta g_{xz} = \Delta g_{zx}$ | $\Delta g_{yz} = \Delta g_{zy}$ |
|----------------------------------|-----------------|-----------------|-----------------|---------------------------------|---------------------------------|---------------------------------|
| VOL <sup>1</sup>                 | -10.3           | -12.4           | -27.9           | 0.3                             | -3.2                            | 1.7                             |
| VO(L <sup>2</sup> ) <sub>2</sub> | -11.9           | -13.0           | -24.6           | 2.1                             | 0.0                             | 0.0                             |
| VO(L <sup>3</sup> ) <sub>2</sub> | -10.1           | -14.2           | -25.6           | 2.7                             | 0.7                             | -1.0                            |
| VO(L <sup>4</sup> ) <sub>2</sub> | -10.0           | -13.2           | -29.8           | 2.0                             | 0.0                             | 0.0                             |

<sup>a</sup> UDFT-VWN results with AMFI approximation for  $\Delta g_{SO/OZ(2e)}$ . <sup>b</sup> The actually computed g-matrices are slightly asymmetric. This information is not obtainable from the experiment. It means that the principal-axes system is not strictly an orthogonal one.<sup>14</sup> The values reported here and the principal values reported in Table 2 have been determined using the symmetrization procedure described in ref 14, p. 91 (see also ref 17).

**Table 2.** Principal  $\Delta g$ -Tensor Components (in ppt). <sup>a</sup>

|                                  | with $\Delta g_{SO/OZ(1e)}$ only |                 |                 |                 | with $\Delta g_{SO/OZ(1e)} + \Delta g_{SO/OZ(2e)}$ |                 |                 |                 | experiment       |                     |                     |                     |
|----------------------------------|----------------------------------|-----------------|-----------------|-----------------|--|-----------------|-----------------|-----------------|------------------|---------------------|---------------------|---------------------|
|                                  | $\Delta g_{iso}$                 | $\Delta g_{11}$ | $\Delta g_{22}$ | $\Delta g_{33}$ | $\Delta g_{iso}$                                   | $\Delta g_{11}$ | $\Delta g_{22}$ | $\Delta g_{33}$ | $\Delta g_{iso}$ | $\Delta g_{11}$     | $\Delta g_{22}$     | $\Delta g_{33}$     |
| VOL <sup>1</sup>                 | -33.8                            | -58.2           | -24.1           | -19.1           | -16.8  | -28.6           | -12.2           | -9.7            | -30              | -49 <sup>b</sup>    | -21 <sup>b</sup>    | -19 <sup>b</sup>    |
| VO(L <sup>2</sup> ) <sub>2</sub> | -32.7                            | -48.8           | -29.1           | -20.2           | -16.5  | -24.6           | -14.5           | -10.3           | -30              | -51 <sup>b</sup>    | -21 <sup>b</sup>    | -19 <sup>b</sup>    |
| VO(L <sup>3</sup> ) <sub>2</sub> | -34.8                            | -55.6           | -31.5           | -17.4           | -16.6  | -25.7           | -15.4           | -8.8            | -32              | -55 <sup>b</sup>    | -23 <sup>b</sup>    | -18 <sup>b</sup>    |
| VO(L <sup>4</sup> ) <sub>2</sub> | -35.2                            | -59.7           | -28.3           | -17.5           | -17.7  | -29.8           | -14.2           | -9.0            | -29              | -53 <sup>c</sup>    | -19 <sup>c</sup>    | -14 <sup>c</sup>    |
|                                  |                                  |                 |                 |                 |  |                 |                 |                 | -30              | -55(2) <sup>d</sup> | -21(2) <sup>d</sup> | -15(2) <sup>d</sup> |

<sup>a</sup> UDFT-VWN results. See also footnote b to Table 1. <sup>b</sup> Ref 5, estimated error of  $\Delta g$ :  $\pm 1$  ppt, EPR on polycrystalline substance. <sup>c</sup> EPR on [VO(mquin)<sub>2</sub>] in a dilute crystal of [GaCl(mquin)<sub>2</sub>] (cf. ref 11). <sup>d</sup> Values obtained in pure crystal (cf. ref 11).

**Table 3.** Rotation Angles (in deg) between Principal Axes of  $g$ - and  $A$ - Tensors and the Standard Axes<sup>a</sup>

| complex                          | $\angle(g_1,z)$ | $\angle(a_1,z)$ | $\angle(g_1,a_1)$ | $\angle(g_2,y)$ | $\angle(a_2,y)$ | $\angle(g_2,a_2)$ | $\angle(g_3,x)$ | $\angle(a_3,x)$ | $\angle(g_3,a_3)$ |
|----------------------------------|-----------------|-----------------|-------------------|-----------------|-----------------|-------------------|-----------------|-----------------|-------------------|
| VOL <sup>1</sup>                 | 11.6            | 4.7             | 6.9               | 6.1             | 11.5            | 11.1              | 10.0            | 12.4            | 12.0              |
| VO(L <sup>2</sup> ) <sub>2</sub> | 0.0             | 0.0             | 0.0               | 37.7            | 11.3            | 49.0              | 37.7            | 11.3            | 49.0              |
| VO(L <sup>3</sup> ) <sub>2</sub> | 6.6             | 0.8             | 6.2               | 26.9            | 5.1             | 31.9              | 26.2            | 5.2             | 31.4              |
| VO(L <sup>4</sup> ) <sub>2</sub> | 0.0             | 0.0             | 0.0               | 25.8            | 10.0            | 35.7              | 25.8            | 10.0            | 35.7              |

<sup>a</sup> UDFT-VWN results with AMFI approximation for  $\Delta g_{SO/OZ(2e)}$  ( $g$ -tensor) and UBHPW91 results ( $A$ -tensor). See also footnotes to Table 1.

**Table 4.**  $A$ -Tensors in the Standard Axes (in MHz). <sup>a</sup>

|                                  | $A_{xx}$ | $A_{yy}$ | $A_{zz}$ | $A_{xy}=A_{yx}$ | $A_{xz}=A_{zx}$ | $A_{yz}=A_{zy}$ |
|----------------------------------|----------|----------|----------|-----------------|-----------------|-----------------|
| VOL <sup>1</sup>                 | 107.6    | 98.0     | -205.6   | -1.7            | -24.8           | -1.7            |
| VO(L <sup>2</sup> ) <sub>2</sub> | 112.4    | 93.5     | -205.9   | -3.9            | 0.0             | -3.9            |
| VO(L <sup>3</sup> ) <sub>2</sub> | 119.3    | 83.7     | -202.9   | -3.2            | 1.8             | -3.2            |
| VO(L <sup>4</sup> ) <sub>2</sub> | 114.7    | 90.9     | -205.6   | -4.3            | 0.0             | -4.3            |

<sup>a</sup> UBHPW91 results.



**Table 5.** Principal *A*-Tensor Components (in MHz)<sup>a</sup>

|                                      | BP86                | B3PW91              | BHPW91              | Exp./<br>nominal $\langle S^2 \rangle$ |
|--------------------------------------|---------------------|---------------------|---------------------|--|
| <b>VOL<sup>1</sup></b>               |                     |                     |                     |  |
| $A_{\text{iso}}$                     | -183.0              | -231.7              | -299.6              | -274.3                                 |
| $T_{11}, T_{22}, T_{33}$             | -177.9, 79.0, 98.9  | -193.9, 89.5, 104.4 | -207.8, 97.8, 110.0 | -209.3, 96.8, 112.4                    |
| $\langle S^2 \rangle^b$              | 0.7566              | 0.7618              | 0.7754              | 0.7500                                 |
| <b>VO(L<sup>2</sup>)<sub>2</sub></b> |                     |                     |                     |  |
| $A_{\text{iso}}$                     | -179.0              | -230.1              | -297.8              | -273.9                                 |
| $T_{11}, T_{22}, T_{33}$             | -182.2, 79.6, 102.7 | -194.3, 86.5, 107.8 | -205.9, 92.7, 113.2 | -208.8, 94.0, 114.7                    |
| $\langle S^2 \rangle^b$              | 0.7578              | 0.7661              | 0.7856              | 0.7500                                 |
| <b>VO(L<sup>3</sup>)<sub>2</sub></b> |                     |                     |                     |  |
| $A_{\text{iso}}$                     | -157.6              | -217.0              | -290.4              | -264.3                                 |
| $T_{11}, T_{22}, T_{33}$             | -172.9, 63.8, 109.1 | -189.5, 74.1, 115.4 | -203.0, 83.4, 119.6 | -207.3, 86.2, 121.0                    |
| $\langle S^2 \rangle^b$              | 0.7586              | 0.7655              | 0.7838              | 0.7500                                 |
| <b>VO(L<sup>4</sup>)<sub>2</sub></b> |                     |                     |                     |  |
| $A_{\text{iso}}$                     | -164.3              | -216.8              | -295.8              | -262.9                                 |
| $T_{11}, T_{22}, T_{33}$             | -183.0, 76.7, 106.3 | -194.3, 82.7, 111.7 | -205.6, 90.2, 115.5 | -208.7, 93.2, 115.4                    |
| $\langle S^2 \rangle^b$              | 0.7580              | 0.7645              | 0.7834              | 0.7500                                 |

<sup>a</sup> Unrestricted Kohn-Sham calculations with specified exchange-correlation functionals.

<sup>b</sup> These  $\langle S^2 \rangle$  values pertain to the Kohn-Sham wavefunction, i.e. to the non-interacting reference system rather than to the real system. Such data are nevertheless expected to give a reasonable and useful representation for the real system as well (see, e.g.: Baker, J.; Scheiner, A.; Andzelm, J. *Chem. Phys. Lett.* **1993**, 216, 380).

## Figure Captions.

**Figure 1.** The vanadyl complexes studied. (a)  $\text{VO(L}^1\text{)}$ . (b)  $\text{VO(L}^2\text{)}_2$  ( $\text{R}=\text{H}$ ,  $\text{R}'=\text{H}$ ) and  $\text{VO(L}^3\text{)}_2$  ( $\text{R}=\text{t-Bu}$ ,  $\text{R}'=\text{Me}$ ). (c)  $\text{VO(L}^4\text{)}_2$ .

**Figure 2.** The standard orientation of the coordinate system, and the calculated  $g$ - and  $A$ -tensor for  $\text{VO(L}^1\text{)}$ .

**Figure 3.** The standard orientation of the coordinate system, and the calculated  $g$ - and  $A$ -tensor for  $\text{VO(L}^2\text{)}_2$ .

**Figure 4.** Orientation of the calculated  $g$ - and  $A$ -tensor for  $\text{VO(L}^3\text{)}_2$ .

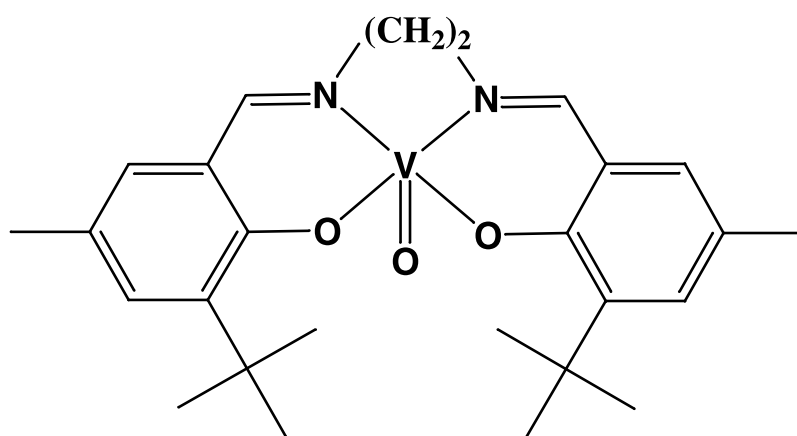
**Figure 5.** Orientation of the calculated  $g$ - and  $A$ -tensor for  $\text{VO(L}^4\text{)}_2$ .

**Figure 6.** Dependence of the isotropic hyperfine coupling constants on the distortion parameter  $\tau$ . BP86, B3PW91, BHPW91, and experimental results are compared for  $\text{VO(L}^1\text{)}$ ,  $\text{VO(L}^2\text{)}_2$ , and  $\text{VO(L}^3\text{)}_2$ .

**Figure 7.** Dependence of the anisotropic hyperfine tensor components on the distortion parameter  $\tau$ . BP86, B3PW91, BHPW91, and experimental results are compared.

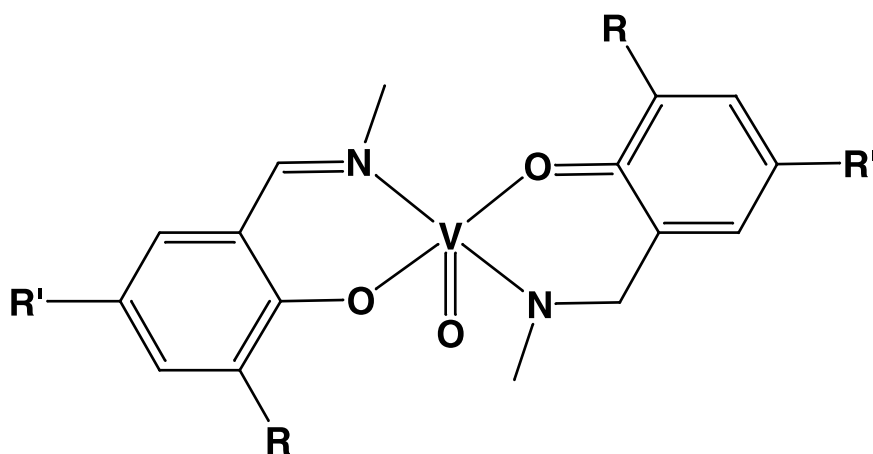
**Figure 8.** Dependence of the total (isotropic+anisotropic) hyperfine tensor components on the distortion parameter  $\tau$ . BHPW91 and experimental results are compared.

Figure 1a



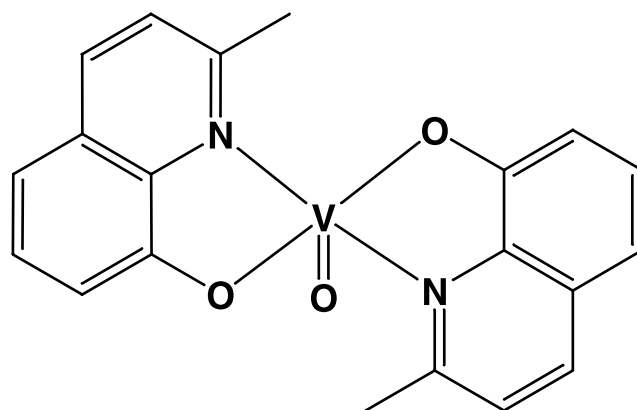
complex VO<sub>L</sub><sup>1</sup>

Figure 1b



|                           |      |    |
|---------------------------|------|----|
| complex                   | R    | R' |
| $\text{VO}(\text{L}^2)_2$ | H    | H  |
| $\text{VO}(\text{L}^3)_2$ | t-Bu | Me |

Figure 1c



complex  $\text{VO}(\text{L}^4)_2$

Figure 2

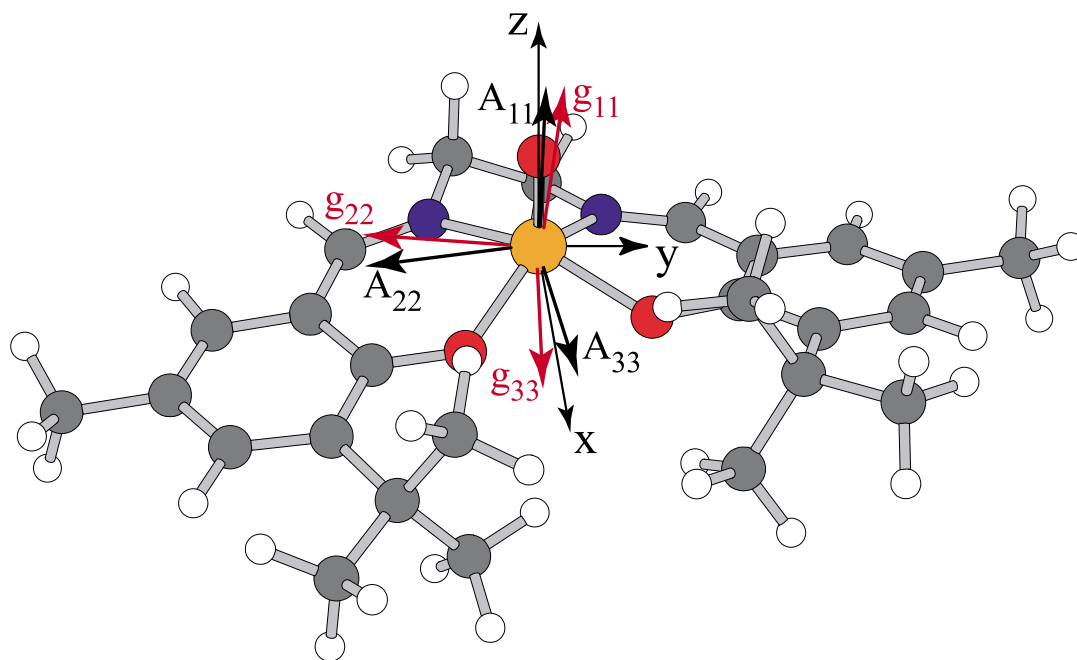


Figure 3

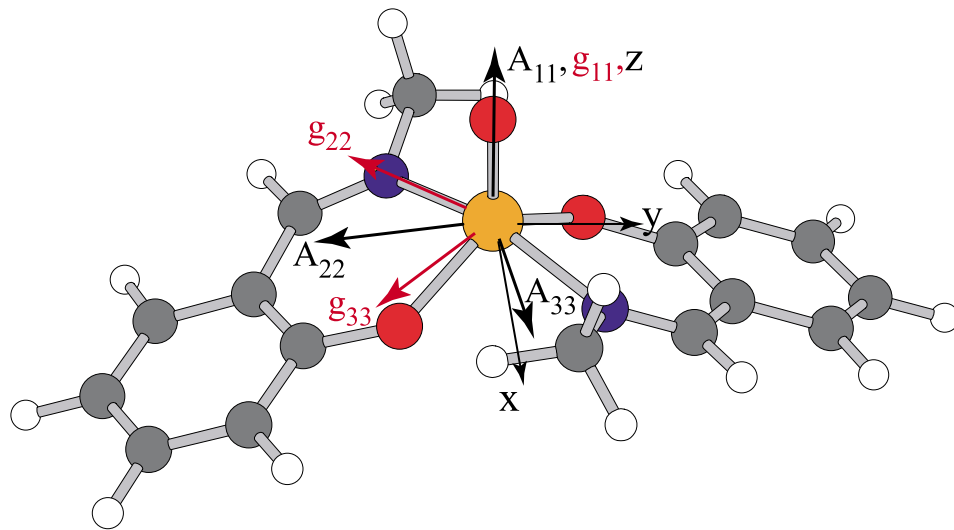


Figure 4

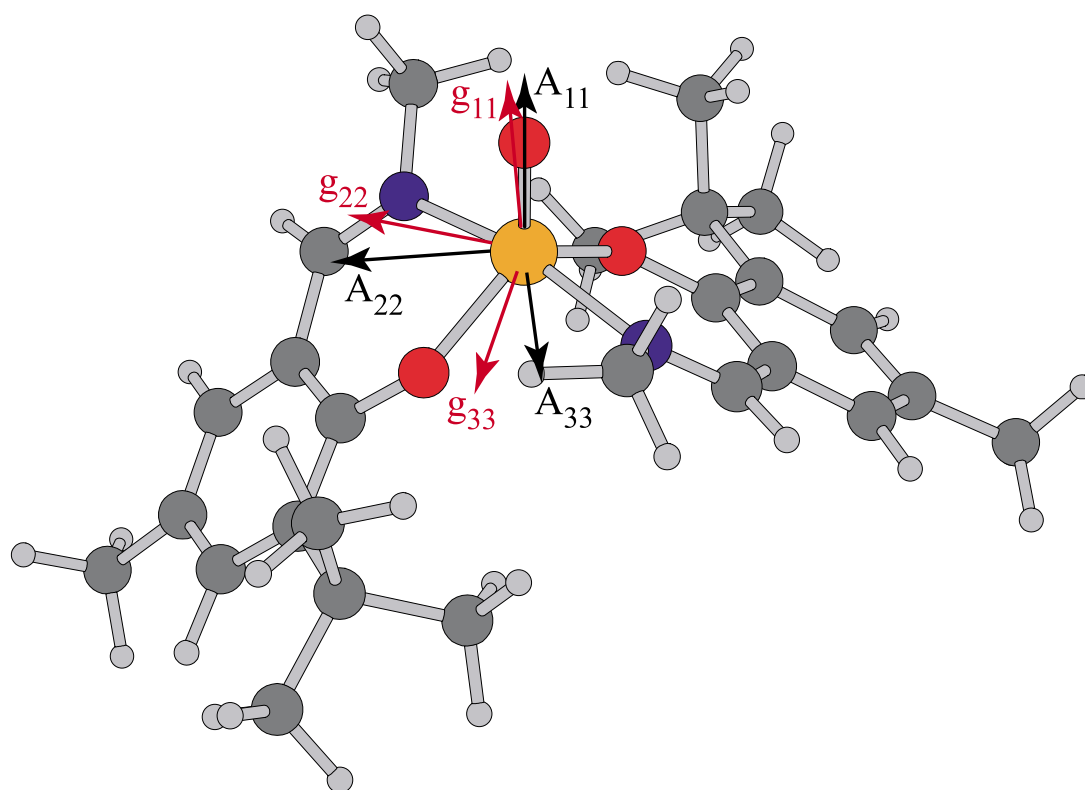




Figure 5

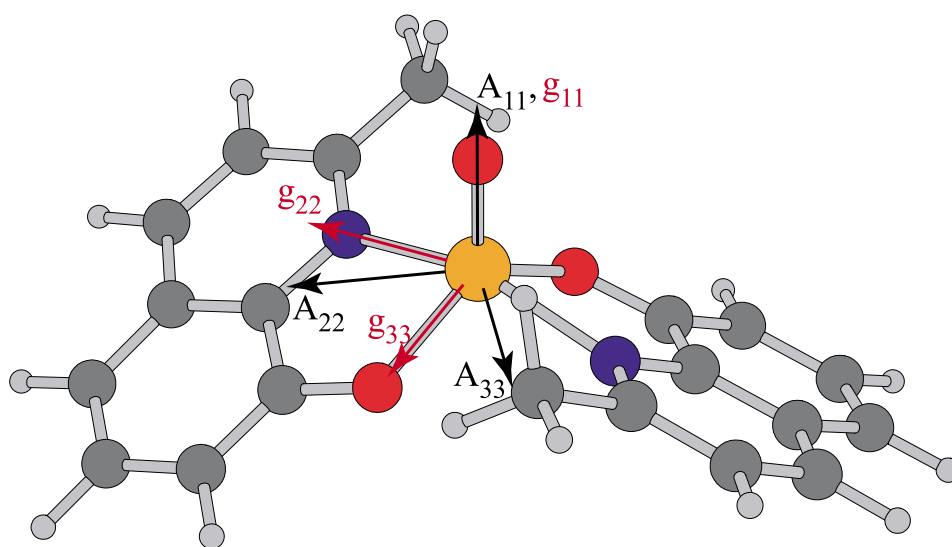


Figure 6

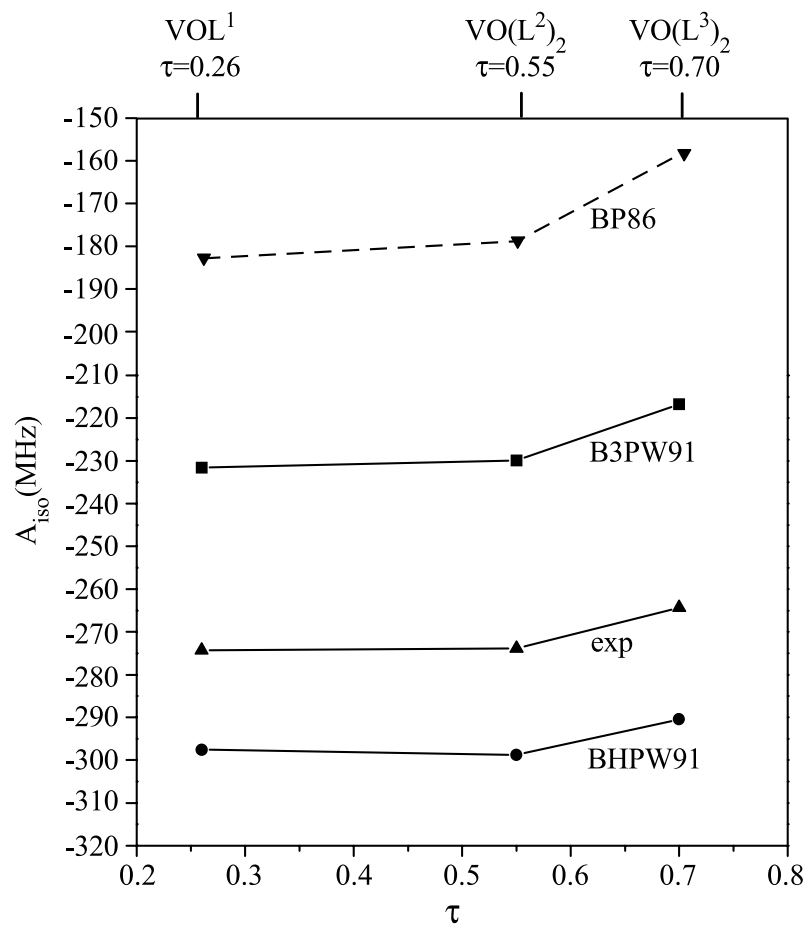


Figure 7

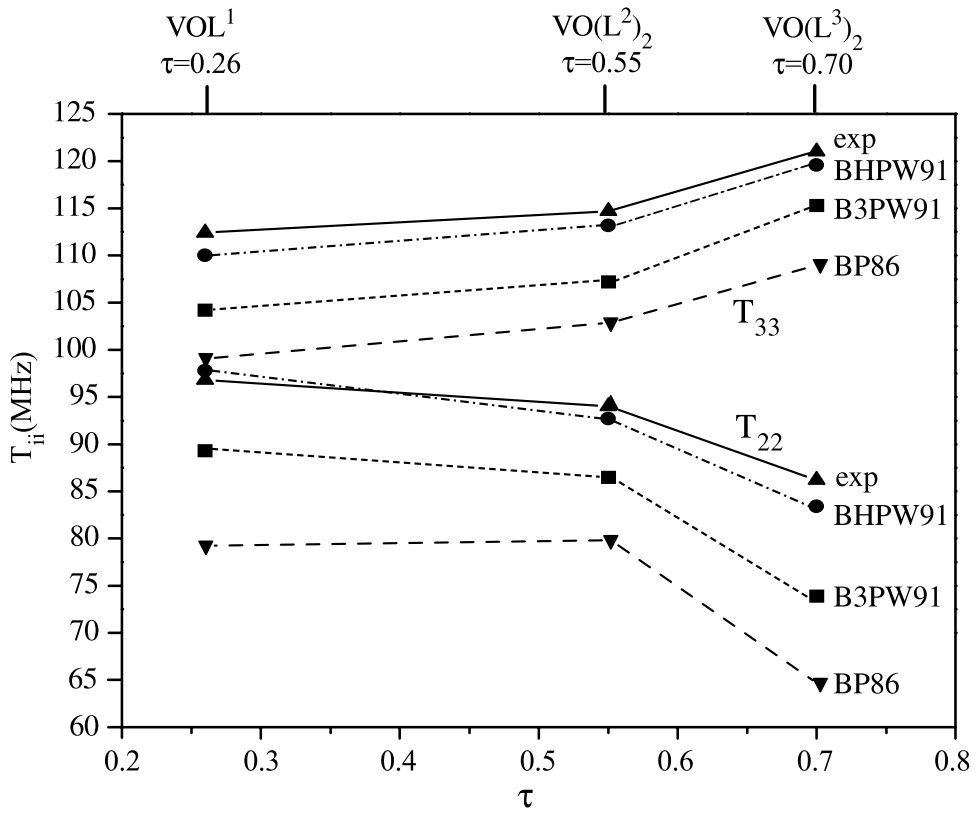
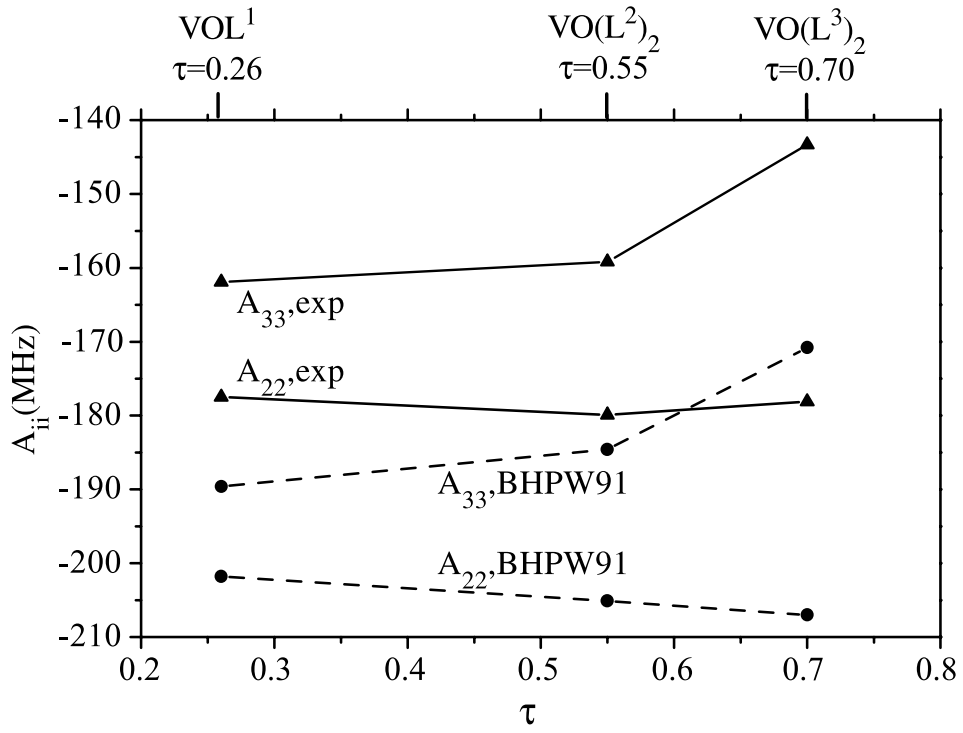


Figure 8



## Supporting Information

### S1. Optimized Structure of *Bis(2-methylquinoline-8-olate)oxovanadium(IV)*<sup>a,b</sup>

| Atom | x         | y         | z         |
|------|-----------|-----------|-----------|
| V    | 0.000000  | 0.000000  | 0.000000  |
| O    | 0.000000  | 0.000000  | 1.591662  |
| O    | 1.713629  | 0.000000  | -0.897952 |
| N    | 0.225038  | -2.104342 | -0.413117 |
| C    | 2.207334  | -1.166282 | -1.292552 |
| C    | 1.416075  | -2.330223 | -1.046147 |
| C    | -0.579510 | -3.123049 | -0.115497 |
| C    | -0.209548 | -4.445380 | -0.472209 |
| C    | 0.981137  | -4.692685 | -1.120524 |
| C    | 1.855563  | -3.623887 | -1.433295 |
| C    | 3.109215  | -3.750888 | -2.087330 |
| C    | 3.864950  | -2.618814 | -2.322834 |
| C    | 3.429683  | -1.330781 | -1.932242 |
| C    | -1.862106 | -2.836929 | 0.611598  |
| H    | -0.886826 | -5.266190 | -0.221466 |
| H    | 1.260256  | -5.716132 | -1.394031 |
| H    | 3.460791  | -4.740312 | -2.394039 |
| H    | 4.833192  | -2.713176 | -2.826086 |
| H    | 4.046529  | -0.449280 | -2.128719 |
| H    | -2.456575 | -2.092443 | 0.057032  |
| H    | -2.452362 | -3.757213 | 0.746648  |
| H    | -1.646410 | -2.401091 | 1.603172  |

<sup>a</sup> B3LYP/ECP optimized structure. <sup>b</sup> Cartesian coordinates in Å. The first two atoms lie on the  $C_2$  symmetry axis (z) which for each of the following atoms defines a symmetry-related counterpart. The latter atoms are omitted from this table.

### S2. Principal Axes of the $g$ -Tensor Relative to the Standard Orientation<sup>a</sup>

| complex                          | $g_{1x}^b$ | $g_{1y}$ | $g_{1z}$ | $g_{2x}$ | $g_{2y}$ | $g_{2z}$ | $g_{3x}$ | $g_{3y}$ | $g_{3z}$ |
|----------------------------------|------------|----------|----------|----------|----------|----------|----------|----------|----------|
| VOL <sup>1</sup>                 | 0.1708     | -0.1052  | 0.9797   | 0.0284   | 0.9944   | 0.1018   | 0.9849   | -0.0104  | -0.1728  |
| VO(L <sup>2</sup> ) <sub>2</sub> | 0.0000     | 0.0000   | 1.0000   | -0.6112  | 0.7915   | 0.0000   | 0.7915   | 0.6112   | 0.0000   |
| VO(L <sup>3</sup> ) <sub>2</sub> | -0.0599    | 0.0969   | 0.9934   | -0.4380  | 0.8918   | 0.1134   | 0.8969   | 0.4419   | 0.0110   |
| VO(L <sup>4</sup> ) <sub>2</sub> | 0.0000     | 0.0000   | 1.0000   | -0.4347  | 0.9006   | 0.0000   | 0.9006   | 0.4347   | 0.0000   |

<sup>a</sup>Both  $\Delta g_{SO/OZ(1e)}$  and  $\Delta g_{SO/OZ(2e)}$  operators have been included. <sup>b</sup>  $g_1$ ,  $g_2$  and  $g_3$  are the axes corresponding to the  $g_{11}$ ,  $g_{22}$  and  $g_{33}$  principal values.

### S3. Principal Axes of the Hyperfine Tensor Relative to the Standard Orientation

| complex                          | $a_{1x}^a$ | $a_{1y}$ | $a_{1z}$ | $a_{2x}$ | $a_{2y}$ | $a_{2z}$ | $a_{3x}$ | $a_{3y}$ | $a_{3z}$ |
|----------------------------------|------------|----------|----------|----------|----------|----------|----------|----------|----------|
| VOL <sup>1</sup>                 | 0.0781     | -0.0285  | 0.9967   | 0.1998   | 0.9798   | 0.0123   | 0.9767   | -0.1981  | -0.0822  |
| VO(L <sup>2</sup> ) <sub>2</sub> | 0.0000     | 0.0000   | 1.0000   | 0.1965   | 0.9805   | 0.0000   | 0.9805   | -0.1965  | 0.0000   |
| VO(L <sup>3</sup> ) <sub>2</sub> | -0.0016    | 0.0016   | 0.9999   | 0.0903   | 0.9960   | -0.0006  | 0.9959   | -0.0902  | 0.0127   |
| VO(L <sup>4</sup> ) <sub>2</sub> | 0.0000     | 0.0000   | 1.0000   | 0.1735   | 0.9849   | 0.0000   | 0.9849   | -0.1735  | 0.0000   |

<sup>a</sup>  $a_1$ ,  $a_2$  and  $a_3$  are the axes corresponding to the  $A_{11}$ ,  $A_{22}$  and  $A_{33}$  principal values.

*I have only knocked on the door of chemistry and I see how much remains to be said.*

*Johannes Kepler (1571-1630)*

## 9 Conclusions

The field of applied quantum chemistry has undergone a major development during the last four decades. The first applications of quantum mechanical methods in inorganic chemistry, introduced in the 1960s mainly by the school of Roald Hoffmann, were based on very simple semi-empirical models. The concepts that arose from these approaches have significantly shaped the ways of understanding the electronic structure and reactivity throughout the whole of chemistry. Over the years, a number of *ab initio* quantum chemistry methods have been developed that enable much higher accuracy than the more qualitative semi-empirical approaches. Nowadays, applications of sophisticated *ab initio* computational methods certainly dominate applied quantum chemistry. Unfortunately, the better agreement with experiment given by these methods is very often being obtained at the cost of reduced understanding of the results. Quantitative calculations easily move one's attention away from the chemical and physical understanding to applied mathematics. However, questions posed at chemical level of complexity should be answered at the same level of complexity.<sup>1</sup> Thus there is a great need for an interplay between the computational and interpretational aspects of applied quantum chemistry. One way of combining these aspects is to derive the general frameworks of understanding on a qualitative level and study the quantitative aspects at a higher level of theory. Two joint works of the author and Roald Hoffmann are an example of this type of approach.<sup>2</sup>

In the author's opinion, the most general outcome of the work reported in this thesis is the illustration of the importance of the opposite approach that starts with performing quantitative calculations and looking for the interpretation of the observed trends. The first step has been undertaken in a critical validation study of density functional approaches for the quantitative calculation of hyperfine tensors for transition

metal complexes (Chapter 5). The second step, the qualitative understanding of the observed trends, is given in the study of mechanisms of EPR hyperfine coupling in transition metal complexes (Chapter 7). The approach adopted in the latter paper is very closely connected to the concept of orbital interactions. It has proven to be particularly fruitful for understanding the physical mechanisms of transfer of spin density within the molecule.

A further important aspect of the studies reported in Chapters 5 and 7 is the identification of density functionals that are appropriate for reproducing and understanding EPR spectra in particular bonding situations. This has been illustrated in the application study reported in Chapter 8. It provides both the reproduction of experimental  $A$ -tensors for systems of chemical (and biological) interest but also interprets the observed trends in terms of spin Hamiltonian parameters.

Finally, the results of the validation studies for both  $A$ - and  $g$ -tensor calculations (Chapters 5 and 7), as well as the interpretational study are important from the point of view of development of density functional approaches. The studies have shown that the desirable, improved functionals should provide sufficiently large spin polarization for core and valence shells without exaggerating it for the latter, and thus introducing spin contamination. Generally, hyperfine coupling constants, in particular for transition metal systems, may turn out to be a particularly fruitful testing ground for new DFT (or alternative) approaches. Another important issue is the account of relativistic effects on the spin Hamiltonian parameters. In the present thesis, this aspect has been touched in some detail for the electronic  $g$ -tensors but only at the semi-empirical level for the hyperfine tensors. The theoretical results for electronic  $g$ -tensors suggest the direction in that further development of density functionals is needed. Furthermore, they illustrate once again the particularly fruitful interaction between experiment and theory that is so characteristic for the field of electron paramagnetic resonance.



## References

---

<sup>1</sup> Hoffmann, R.; in Foreword to *Orbital Interactions in Chemistry*, Albright, T. A.; Burdett, J.; Whangbo, M.-H.; Wiley: New York, 1985.

<sup>2</sup> Munzarová M.; Hoffmann, R. submitted for publication to *J. Am. Chem. Soc.*;  
Munzarová M.; Hoffmann, R.; manuscript in preparation.



## Lebenslauf und Wissenschaftlicher Werdegang

### Mgr. Markéta Munzarová, geb. Bauchnerová

|                   |  |  |
|-------------------|--|--|
| Name              | Mgr. Markéta Munzarová, geb. Bauchnerová                           |  |
| Geboren           | 9. 11. 1973  |  |
| Eltern            | Ing. Eduard Bauchner und Ing. Marie Bauchnerová, geb. Dittingerová |  |
| Familienstand     | verheiratet seit Juni 1996 mit Dr. Dominik Munzar                  |  |
| Schulbildung      | 1980-1988  | Grundschule in Brünn, Tschechische Republik  |
|                   | 1988-1992  | Gymnasium Kapitan Jaroš Straße 14, Brünn<br>Spezialisierung Mathematik und<br>Naturwissenschaften  |
| Studium           | 9/1992-6/1996  | Masaryk Universität in Brünn<br><br>Fach: Lehrberuf von allgemeinen Lehrfächern<br>Mathematik-Chemie<br><br>Diplomarbeit bei Doc. Pavel Kubáček mit dem<br>Thema<br><br><i>‘Didaktik der Orbital-Wechselwirkungen und der<br/>Begriff von Hypervalenz’</i><br><br>11. 6. 1996 Datum des Diplomzeugnisses,<br>Gesamturteil der Staatsprüfung ‘Mit Auszeichnung<br>bestanden’. Erwerbener akademischer Grad<br>‘Magistr’ (Mgr.). |
| Anstellung        | 9/1996-6/1997  | Mittelschulelehrerin, Gymnasium Kapitan Jaroš<br>Straße 14, Brünn  |
| Promotion         | 9/1997-8/2001  | Promotionsstudium unter Betreuung von Prof. Martin<br>Kaupp. Von 9/1997 bis 12/1999 am Max-Planck<br>Institut für Festkörperforschung Stuttgart. Von<br>01/2000 bis 8/2001 an der Masaryk Universität in<br>Brünn.   |
|                   | 10/2000-4/2001   | Auslandsaufenthalt bei Prof. Roald Hoffmann,<br>Department of Chemistry and Chemical Biology,<br>Cornell University, Ithaca, NY, USA.  |
| Stipendien        | 10/2000-4/2001   | ‘Fulbright-Masaryk Fellowship’ der J. W. Fulbright<br>Foundation.  |
| Forschungspreisen | 6/2001   | ‘Prix de Chimie 2001’ der Französischen<br>Botschaft und der Firma Rhodia s.r.o  |

In Brünn, den 15. Juni 2001

Markéta Munzarová